

Resolution enhancement in mask aligner photolithography

Zur Erlangung des akademischen Grades eines
Doktors der Naturwissenschaften
(Dr. rer. nat.)

von der KIT-Fakultät für Physik
des Karlsruher Instituts für Technologie (KIT)

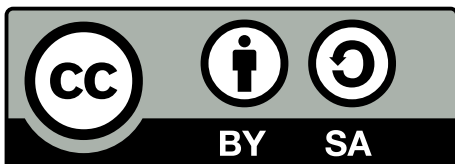
genehmigte Dissertation

von

M. Sc. Andreas Vetter

am Institut für Theoretische Festkörperphysik

Datum der mündlichen Prüfung:	22. November 2019
Referent:	Prof. Dr. Carsten Rockstuhl
Korreferent:	Prof. Dr. Martin Wegener



This document (with the exception of reprinted figures) is licensed under the Creative Commons Attribution-ShareAlike 4.0 International License. To view a copy of this license, visit <https://creativecommons.org/licenses/by-sa/4.0/>.

Abstract

Photolithography is an indispensable tool in the modern microfabrication of integrated electronics and optical devices on several length scales. The task at hand is to replicate a desired pattern, encoded in a photomask, on a photoresist-covered wafer. Recent decades have witnessed an impressive development of photolithographic equipment, enabling a resolution much finer than a micron.

Potentially the simplest photolithographic tool is the mask aligner. It brings the photomask and the wafer in contact or close proximity, with no additional optics in between. Being introduced over 50 years ago, the cost-effective operation renders mask aligner lithography in proximity mode the method of choice for fabricating non-critical layers, with a spatial resolution down to several microns. Mask aligners are used for the manufacturing of microlenses, light-emitting diodes, and microelectromechanical systems. The resolution is ultimately limited by diffraction of the exposure light at the photomask features, resulting in image shape distortions.

In this work, several resolution enhancement technologies for mask aligners in proximity mode are successfully developed, presented, and discussed. This comprises photolithography using a novel light source emitting at deep ultraviolet wavelengths, a rigorously optimized phase-shift mask to print periodic structures, optical proximity correction applied to non-Manhattan geometries, and the design of optical metasurfaces for photomasks in proximity lithography.

Reducing the wavelength reduces the impact of diffraction and directly improves the resolution, but also requires to develop suitable approaches to illumination beam shaping and homogenization. In a holistic approach we discuss mask aligner lithography using a novel frequency-quadrupled continuous wave light source emitting at 193 nm. We successfully demonstrate lithographic prints of test structures with a resolution down to 1.75 μm at a proximity gap of 20 μm . Using the self-imaging effect of Talbot lithography, even sub-micron resolution for periodic structures is achieved.

We discuss the rigorous simulation and optimization of light propagation in and behind phase-shift photomasks under oblique angles. The superposition of individual plane waves illuminating the optimized photomask under three discrete angles allows a demagnification of the photomask period, enabling to print sub-micron structures at relaxed constraints on the photomask fabrication. Furthermore, we introduce a computational approach to optical proximity correction of non-rectangular geometries, so-called non-Manhattan geometries, thus increasing the pattern fidelity in proximity lithography. Both developments are successfully validated in experimental prints.

Wavefront shaping by optical metasurfaces extends the capabilities of photomasks over canonical binary intensity or phase-shift photomasks. We discuss two possible metasurface designs, both covering the full 2π phase range. One design includes a plasmonic absorber enabling enhanced tunability of the transmission coefficient. Furthermore, we implement an algorithm to retrieve photomask layouts to print arbitrary patterns.

Continuous development of mask aligner photolithography is essential to keep up with the ongoing miniaturization in all branches of optics, mechanics, and electronics. Our findings allow to enhance the resolution of proximity printing to face future challenges in photolithography and optical manufacturing.

Zusammenfassung in deutscher Sprache

Photolithographie ist eine unentbehrliche Technologie in der heutigen Mikrofabrikation integrierter elektronischer Schaltungen und optischer Komponenten auf verschiedenen Größenskalen. Die zugrundeliegende Aufgabe ist die Replikation der gewünschten Struktur, die kodiert ist in einer Photomaske, auf einem photolackbedeckten Wafer. In vergangenen Jahrzehnten gab es eine beeindruckende Weiterentwicklung photolithographischer Anlagen, was Auflösungen weit unterhalb eines Mikrometers ermöglicht.

Das einfachste photolithographische Instrument ist der Maskenjustierbelichter, bei dem die Photomaske und der Wafer entweder in Kontakt oder in unmittelbare Nähe gebracht werden (Proximity-Modus), ohne zusätzliche optische Komponenten dazwischen. Vor über 50 Jahren eingeführt bleibt der Maskenjustierbelichter aufgrund seines wirtschaftlichen Betriebs das Instrument der Wahl für die Herstellung unkritischer Schichten, mit einer Auflösung von einigen Mikrometern im bevorzugten Proximity-Modus. Maskenjustierbelichter werden beispielsweise für die Herstellung von Mikrolinsen, lichtemittierende Dioden und mikromechanischen Systemen verwendet. Die erreichbare laterale räumliche Auflösung ist letztlich begrenzt durch die Beugung des Lichts an den Strukturen der Photomaske, was zu Verfälschungen der Abbildung auf dem Photolack führt.

In dieser Arbeit entwickeln, präsentieren und diskutieren wir mehrere Technologien zur Auflösungsverbesserung für Maskenjustierbelichter im Proximity-Modus. Dies umfasst Photolithographie mit einer neuartigen Lichtquelle, die im tiefen Ultraviolett-Bereich emittiert, eine rigoros optimierte Phasenschiebermaske für periodische Strukturen, optische Proximity-Korrektur (Nahbereichskorrektur) angewandt auf nicht-orthogonale Geometrien, und die Anwendung optischer Metaoberflächen als Photomasken.

Eine Reduzierung der Wellenlänge verringert die Auswirkungen der Lichtbrechung und verbessert daher direkt die Auflösung, benötigt aber auch die Entwicklung geeigneter Konzepte für die Strahlformung und Homogenisierung der Beleuchtung. Wir diskutieren die Integration einer neuartigen Lichtquelle, ein frequenzvervierfacher Dauerstrichlaser mit einer Emissionswellenlänge von 193 nm, in einem Maskenjustierbelichter. Damit zeigen wir erfolgreiche Prints von Teststrukturen mit einer Auflösung von bis zu $1,75\ \mu\text{m}$ bei einem Proximity-Abstand von $20\ \mu\text{m}$. Bei Verwendung des selbstabbildenden Talboteffekts wird sogar eine Auflösung weit unterhalb eines Mikrometers für periodische Strukturen erzielt.

Außerdem diskutieren wir die rigorose Simulation und Optimierung der Lichtausbreitung in und hinter Phasenschiebermasken, die unter schrägem Einfall belichtet werden. Mit einem optimierten Photomaskendesign kann dabei die Periode bei Belichtung unter drei diskreten Winkeln verkleinert abgebildet werden. Dies erlaubt es, Strukturen deutlich kleiner als ein Mikrometer abzubilden, wobei die Strukturen auf der Photomaske deutlich größer und damit einfacher herzustellen sind. Zudem betrachten wir eine Simulations- und Optimierungsmethode für die optische Proximity-Korrektur nicht-orthogonaler Strukturen, was deren Formtreue verbessert. Die Wirksamkeit beider Konzepte bestätigen wir erfolgreich in experimentellen Prints.

Die Verwendung optischer Metaoberflächen erweitert die Fähigkeiten zur Wellenfrontformung von Photomasken gegenüber etablierten Intensitäts- oder Phasenschiebermasken. Wir diskutieren zwei Designs für optische Metaoberflächen, die beide den vollen

2π -Phasenbereich abdecken. Ein Design beinhaltet dabei noch einen plasmonischen Absorber, was zusätzliche Möglichkeiten bietet, den Transmissionskoeffizient anzupassen. Desweiteren beschreiben wir einen Algorithmus zur Berechnung des Maskenlayouts für beliebige Strukturen.

Eine kontinuierliche Weiterentwicklung von Maskenjustierbelichtern ist unerlässlich, um Schritt zu halten mit der fortschreitenden Miniaturisierung in allen Bereich der Optik, der Mechanik und der Elektronik. Unsere Forschungsergebnisse ermöglichen es, die Auflösung der optischen Lithographie im Proximity-Modus zu verbessern und sich damit den zukünftigen Herausforderungen der optischen Industrie stellen zu können.

Contents

1	Introduction	1
2	Advanced optical lithography	7
2.1	Optical lithography for the fabrication of integrated circuits and micro-optical components	7
2.2	Review of concepts for high-resolution optical lithography	8
2.2.1	Mask aligner contact and proximity lithography	9
2.2.2	Projection lithography	10
2.3	Basics of optical proximity lithography	11
2.3.1	Light source and illumination shaping	12
2.3.2	Photomask and resist technology	17
2.3.3	Image formation and resolution limits	21
2.4	Resolution enhancement techniques in optical lithography	27
2.4.1	Computational lithographic modeling	28
2.4.2	Non-periodic nanostructures	29
2.4.3	Periodic nanostructures	32
3	Theoretical and computational tools	41
3.1	Introduction to optical simulation methods	42
3.2	Simulation methods for optical proximity lithography	43
3.2.1	The Fourier modal method to simulate periodic structures	43
3.2.2	The angular spectrum method to simulate the propagation of arbitrary field distributions	48
3.2.3	The Rayleigh-Sommerfeld diffraction integral for the efficient simulation of light propagation	50
3.2.4	Ray tracing for simulating macroscopic optical setups	52
4	Mask aligner lithography using a continuous-wave frequency-quadrupled laser emitting at 193 nm	55
4.1	Benefits of continuous-wave laser sources and wavelength reduction for optical lithography	55
4.2	Optical setup and laser beam shaping in the deep ultraviolet	58
4.2.1	Frequency-quadrupled 193 nm light source	58
4.2.2	Controlling the spatial coherence	60
4.2.3	Homogenizing the illumination in the mask plane	62
4.3	Experimental lithographic results	68
4.3.1	Binary intensity photomask in contact and proximity lithography	69
4.3.2	Diffraction phase-shifting photomask for periodic nanostructures	71
4.4	Mask aligner Talbot lithography at 193 nm	72
4.4.1	Near plane wave illumination	73
4.4.2	Aerial image simulation with near plane wave illumination	74
4.4.3	Experimental results of Talbot lithography	75
4.5	Concluding remarks on CW laser lithography at 193 nm	78

5	Rigorously optimized phase-shift mask for creating a dense hexagonal dot pattern	79
5.1	Mask design and optical setup	80
5.2	Simulation of rigorously optimized phase-shifting masks	81
5.3	Experimental results	84
6	Rule-based corner correction of non-Manhattan structures	87
6.1	Incentives and limitations of optical proximity correction in mask aligner photolithography applied to non-Manhattan geometries	87
6.2	Optical proximity correction using the serif bar design	89
6.2.1	Layout of serif bar correction structures	89
6.2.2	Aerial image and resist simulation	89
6.2.3	Figure of merit and optimization	90
6.2.4	Optimization results	91
6.2.5	Retrieving the process window	93
6.3	Optical proximity correction with the pixel-flip design	94
6.3.1	Optimization results	95
6.4	Evaluation and characterization of experimental results	96
6.4.1	Experimental setup	96
6.4.2	Evaluation of serif bar design	98
6.4.3	Iso-dense print bias and the influence of adjacent structures	100
6.4.4	Evaluation of the pixel-flip design	100
6.5	Concluding remarks on optical proximity correction in mask aligner photolithography	102
6.6	Application of pixel-flip algorithm to inverse design in Bloch surface wave devices	103
7	Proximity lithography based on optical metasurfaces	107
7.1	Introduction to optical metasurfaces	108
7.1.1	The physics of optical metasurfaces	108
7.1.2	Wavefront shaping	110
7.1.3	Advantages of all-dielectric metasurfaces in proximity lithography	111
7.2	Layout of metasurface building blocks with complex transmission coefficients and 2π phase coverage working in the deep ultraviolet	112
7.3	Designing lithographic metasurfaces with an iterative soft-quantized propagation algorithm	118
7.4	Concluding remarks on proximity lithography using optical metasurfaces	123
8	Conclusion and outlook	125
	Bibliography	129
	Appendix	155
	Acknowledgments	163
	Curriculum vitae	166

List of Figures

1.1	Shadow printing	2
1.2	Resolution enhancement in optical lithography	3
1.3	Simulated diffraction at photomask features	4
2.1	Process steps in an optical microfabrication cycle	8
2.2	Illustration of a mask aligner	9
2.3	Image shape distortions in optical lithography	10
2.4	Illustration of a projection scanner	11
2.5	Spectrum of electromagnetic waves	12
2.6	Properties of high-pressure mercury arc lamp	13
2.7	Köhler illumination	15
2.8	Sketch of non-imaging and imaging homogenizers	16
2.9	MO Exposure Optics	17
2.10	Schematic of phase-shifting in a photomask	18
2.11	Contrast positive photoresist	22
2.12	Fraunhofer diffraction patterns of single and periodic slits	23
2.13	Threshold model and resolution criteria	24
2.14	Resolution in mask aligner lithography	26
2.15	Properties of light and resolution enhancement techniques	27
2.16	Customized illumination using MOEO	29
2.17	OPC approaches to line-end shortening and corner rounding	31
2.18	Talbot lithography at 193 nm	34
2.19	Talbot distance in mask aligner lithography	36
2.20	Talbot structures for circular and square shapes	37
2.21	Rigorously optimized phase-shift masks	38
3.1	Sketch of a periodic structure composed of several layers	43
3.2	Convergence analysis of the Fourier modal method	47
3.3	Schematic of the angular spectrum method	48
3.4	Comparison of Rayleigh-Sommerfeld diffraction integral and angular spectrum method	52
4.1	Excimer beam profile	56
4.2	Comparison of resolution and depth of focus for different wavelengths	57
4.3	Picture of optical setup	58
4.4	Schematic of the 193 nm light source	59
4.5	Prism coupling of KBBF crystal	59
4.6	Longterm laser stability	60
4.7	Laser beam output	61
4.8	Shaped random diffusers	62
4.9	Non-imaging homogenizer at 193 nm	63
4.10	Optical setup of non-imaging homogenizer	64
4.11	Simulated and measured irradiance distributions for non-imaging homogenizer	65
4.12	Imaging homogenizer for 193 nm	67

4.13	Measured irradiance distribution in homogenization plane for an imaging homogenizer	68
4.14	Aerial image without and with back antireflective coating	69
4.15	Mask design and results for soft contact lithography	70
4.16	SEM micropgraphs in proximity mode, proximity gap 20 μm	71
4.17	SEM micropgraphs of etched Si structures, proximity gap 10 μm	71
4.18	SEM images of patterns structured with phase-shifting mask	72
4.19	Beam profile for near plane wave illumination	73
4.20	Distribution with static and without diffuser	74
4.21	Talbot lithography under ideal and real illumination	75
4.22	Results of Talbot lithography in fractional Talbot plane	76
4.23	Results of Talbot lithography in first Talbot plane	76
4.24	Results of Talbot lithography in higher Talbot plane	77
5.1	Sketch of the RO-PSM design	80
5.2	Simulation of hexagonal ROPSM	81
5.3	Light propagation in the hexagonal RO-PSM	82
5.4	Contrast for the hexagonal RO-PSM	83
5.5	Prints of hexagonal RO-PSM under normal incidence	84
5.6	Prints of hexagonal RO-PSM illuminated by three plane waves	85
5.7	SEM image of the resist cross-section	86
6.1	Optimization routine and serif bar design	88
6.2	Simulated resist contour for unoptimized and optimized corner	90
6.3	Optimization results OPC for serif bar design	91
6.4	Sensitivity to gap variations	92
6.5	Sensitivity to dose variations	93
6.6	Process window	93
6.7	Pixel flip algorithm	94
6.8	Optimization results OPC for pixel-flip design	95
6.9	Interpretation of experimental results	96
6.10	Experimental results on corner optimization for serif bar design	97
6.11	Shape contour	98
6.12	Evaluation of experimental prints	98
6.13	Iso-dense bias	99
6.14	Experimental results on corner optimization for pixel-flip design	101
6.15	FOM of the test structures for pixel-flip design	102
6.16	Sketch of experimental setup to focus Bloch surface waves	103
6.17	Focusing BSWs 5 μm behind the device	104
7.1	Generalized law of refraction and projection lithography using optical metasurfaces	111
7.2	Schematic illustration of a metasurface used in proximity lithography	112
7.3	Performance of a TiO_2 metasurface in the ultraviolet (UV) regime	113
7.4	Design of a TiO_2 metasurface for UV proximity lithography	114
7.5	Field distribution in and around the nanocylinders	115
7.6	Performance of metasurface as a function of the angle of incidence	116
7.7	Metasurface design for complete control over the complex transmission coefficients	117
7.8	Parameter study for complete control over complex transmission coefficients	118
7.9	Iterative propagation algorithm to retrieve the mask configuration	119
7.10	Example of the iterative propagation algorithm results	121
7.11	Simulated test pattern for different gaps	122

8.1	Artistic illustration of a metasurface for zeroth-order cancellation	127
B.1	Tennant's law	156
C.2	Schematic of metal absorber fabrication	160
C.3	Schematic of TiO ₂ metasurface fabrication	161

List of Tables

2.1	Properties of light sources used in optical lithography	12
-----	---	----

List of Acronyms

AFM atomic force microscopy	NIL nanoimprint lithography
ALD atomic layer deposition	NIR near-infrared
ARC anti-reflective coating	OAI off-axis illumination
ASM angular spectrum method	OD optical density
BARC bottom anti-reflective coating	OPC optical proximity correction
BSW Bloch surface wave	OPL optical path length
CAR chemically amplified resist	PAC photoactive compound
CCD charge-coupled device	PAM piezoelectric-actuated mirror
CD critical dimension	PCD prism-coupled device
CGH computer-generated hologram	PDH Pound-Drever-Hall
CW continuous wave	PEB post exposure bake
DLW direct laser writing	PhC photonic crystal
DNQ diazonaphthoquinone	PSM phase-shift mask
DOE diffractive optical element	PSO particle swarm optimization
DOF depth of focus	PVD physical vapor deposition
DPN dip-pen nanolithography	RET resolution enhancement technology
DRIE deep reactive-ion etching	RIE reactive-ion etching
DTL displacement Talbot lithography	RO-PSM rigorously optimized phase-shift mask
DUV deep ultraviolet	
EUV extreme ultraviolet	SE secondary electron
FFT Fast Fourier Transform	SEM scanning electron microscope
FI Faraday isolator	SHG second-harmonic generation
FMM Fourier modal method	Si silicon
FOM figure of merit	SMO source-mask optimization
FWHM full width at half maximum	SNOM scanning near-field optical microscope
GBL Gaussian beam lithography	
HOM Hong-Ou-Mandel	SNR signal-to-noise ratio
IC integrated circuit	SPL scanning probe lithography
ICP inductively coupled plasma	SPP surface plasmon polariton
IFP illumination filter plate	STED stimulated emission depletion
IFTA iterative Fourier transform algorithm	STM scanning tunneling microscope
IR infrared	TA tapered amplifier
KBBF potassium fluoro-beryllate	TE transverse-electric
LBO lithium triborate	TEA thin-element approximation
LED light-emitting diode	TM transverse-magnetic
MLA microlens array	TMM transfer matrix method
MOEO [®] MO Exposure Optics [®]	TPA two-photon absorption
MOPA master-oscillator power-amplifier	UV ultraviolet
MS metasurface	VS variable shaped beam
NA numerical aperture	WLI white light interferometer
NGL next-generation lithography	

Publications

Peer-reviewed scientific journals

Publications presented within this thesis are highlighted in bold letters.

- [1] **A. Vetter**, C. Yan, R. Kirner, T. Scharf, W. Noell, R. Voelkel, & C. Rockstuhl, "Computational rule-based approach for corner correction of non-Manhattan geometries in mask aligner photolithography", *27(22)*, 32523–32535 (2019).
- [2] Y. Yun, A. Vetter, R. Stegmüller, S. Ferrari, W.H.P. Pernice, C. Rockstuhl, & C. Lee, "Superconducting nanowire-based single-photon spectrometer exploiting cascaded photonic crystal cavities", arXiv:1908.01681, 2019.
- [3] S. Ferrari, V. Kovalyuk, A. Vetter, C. Lee, C. Rockstuhl, A. Semenov, G.N. Goltsman, & W.H.P. Pernice, "Analysis of the detection response of waveguide-integrated superconducting nanowire single-photon detectors at high count rate", *Applied Physics Letters* **115**(10), 101104-1 – 101104-4 (2019).
- [4] M. Symeonidis, R.N.S. Suryadharma, R. Grillo, A. Vetter, C. Rockstuhl, T. Bürgi, & T. Scharf, "High-resolution interference microscopy with spectral resolution for the characterization of individual particles and self-assembled meta-atoms", *Optics Express* **27**(15), 20990 – 21003 (2019).
- [5] Y. Augenstein*, A. Vetter*, B.V. Lahijani, H.P. Herzig, C. Rockstuhl, & M.-S. Kim, "Inverse photonic design of functional elements that focus Bloch surface waves", *Light: Science & Applications* **7**, 104 (2018).
- [6] V. Kovalyuk, O. Kahl, S. Ferrari, A. Vetter, G. Lewes-Malandrakis, C. Nebel, A. Korneev, G.N. Goltsman, & W. Pernice, "On-chip single-photon spectrometer for visible and infrared wavelength range", *Journal of Physics: Conf. Series* **1124**, 051045 (2018).
- [7] M. Bagiński, E. Tomczyk, A. Vetter, R.N.S. Suryadharma, C. Rockstuhl, and W. Lewandowski, "Achieving highly stable, reversibly reconfigurable plasmonic nanocrystal superlattices through the use of semifluorinated surface ligands", *Chemistry of Materials* **30**(22), 8201 – 8210 (2018).
- [8] M.-S. Kim*, A. Vetter*, C. Rockstuhl, B.V. Lahijani, M. Häyrynen, M. Kuittinen, M. Roussey, & H.P. Herzig, "Multiple self-healing Bloch surface wave beams generated by a two-dimensional fraxicon", *Nature Communications Physics* **1**(63) (2018).
- [9] **A. Vetter**, R. Kirner, D. Opalevs, M. Scholz, P. Leisching, T. Scharf, W. Noell, C. Rockstuhl, & R. Voelkel, "Printing sub-micron structures using Talbot mask-aligner lithography with a 193 nm CW laser light source", *Optics Express* **26**(17), 22218–22233 (2018).
- [10] J. Münzberg*, A. Vetter*, F. Beutel, W. Hartmann, S. Ferrari, W.H.P. Pernice, & Carsten Rockstuhl, "Superconducting nanowire single-photon detector implemented in a 2D photonic crystal cavity", *Optica* **5**(5), 658–665 (2018).

- [11] R. Kirner*, A. Vetter*, D. Opalevs, C. Gilfert, M. Scholz, P. Leisching, T. Scharf, W. Noell, C. Rockstuhl, & R. Voelkel, "Mask-aligner lithography using a continuous-wave diode laser frequency-quadrupled to 193 nm", *Optics Express* **26**(2), 730–743 (2018).
-

The work on the following publications was performed during the master thesis at the Institute of Nanotechnology and the Institute of Theoretical Solid State Physics, Karlsruhe Institute of Technology, Germany. All publications listed here were published during the PhD period.

- [12] O. Kahl, S. Ferrari, V. Kovalyuk, A. Vetter, G. Lewes-Malandrakis, C. Nebel, A. Korneev, G.N. Goltsman, & W.H.P. Pernice, "Spectrally multiplexed single-photon detection with hybrid superconducting nanophotonic circuits", *Optica*, **4** (5), 557–562 (2017).
- [13] S. Ferrari, V. Kovalyuk, W. Hartmann, A. Vetter, O. Kahl, C. Lee, A. Korneev, C. Rockstuhl, G.N. Goltsman, W.H.P. Pernice, "Hot-spot relaxation time current dependence in niobium nitride waveguide-integrated superconducting nanowire single-photon detectors", *Optics Express* **25**(8), 8739–8750 (2017).
- [14] S. Khasminskaya, F. Pyatkov, K. Słowik, S. Ferrari, O. Kahl, V. Kovalyuk, P. Rath, A. Vetter, F. Hennrich, M.M. Kappes, G.N. Goltsman, A. Korneev, C. Rockstuhl, R. Krupke, & W.H.P. Pernice, "Fully integrated quantum photonic circuit with an electrically driven light source", *Nature Photonics* **10**(11), 727–732 (2016).
- [15] A. Vetter, S. Ferrari, P. Rath, R. Alaei, O. Kahl, V. Kovalyuk, S. Diewald, G.N. Goltsman, A. Korneev, C. Rockstuhl, & W.H.P. Pernice, "Cavity-Enhanced and Ultrafast Superconducting Single-Photon Detectors", *Nano Letters* **16**(11), 7085–7092 (2016).

* denotes an equal contribution by the authors.

Conference contributions

Conference presentations by myself are highlighted in bold letters.

1. C. Rockstuhl, Y. Augenstein, A. Vetter, B.V. Lahijani, H.P. Herzig, and M.-S. Kim, "Controlling the propagation of Bloch Surface Waves", *METANANO*, IV International Conference on Metamaterials and Nanophotonics, 2019.
2. J. Szlachetka, A. Vetter, K. Slowik, C. Rockstuhl, & P. Kolenderski, "Nanostructural beam splitter", *SPIE Optics + Optoelectronics* 11025, Plasmonics: Fundamentals and Applications, 2019 [16].
3. G.N. Goltsman, O. Kahl, S. Ferrari, V. Kovalyuk, A. Vetter, G. Lewes-Malandrakis, C. Nebel, A. Korneev, & W.H.P. Pernice, "Integrated Optical Circuits Enhanced by Single Photon Detectors", *Photonics & Electromagnetics Research Symposium*, PIERS 2019.
4. R. Kirner, A. Vetter, W. Noell, T. Scharf, & R. Voelkel, "Coherent Ray Tracing Simulation of Multi-aperture Elements for Laser Beam-shaping in Mask Aligner Lithography", *11th International Conference on Optics-photonics Design & Fabrication*, ODF 2018.
5. **A. Vetter, R. Kirner, T. Scharf, W. Noell, C. Rockstuhl, & R. Voelkel**, "Resolution enhancement in mask-aligner lithography", *European Optical Society Biennial Meeting (EOSAM) 2018*.
6. **A. Vetter, J. Münzberg, F. Beutel, S. Ferrari, W.H.P. Pernice, & C. Rockstuhl**, "Ultrafast cavity-integrated single-photon detectors", *European Optical Society Biennial Meeting (EOSAM) 2018*.
7. **A. Vetter, R. Kirner, T. Scharf, W. Noell, C. Rockstuhl, & R. Voelkel**, "Improving the Resolution in Mask-Aligner lithography", *2018 International Conference on Optical MEMS and Nanophotonics (OMN)*, IEEE (2018).
8. J. Münzberg, A. Vetter, W. Hartmann, N. Gruhler, F. Beutel, S. Ferrari, C. Rockstuhl, & W.H.P. Pernice, "Cavity-Enhanced Superconducting Single Photon Detectors", *20th International Conference on Transparent Optical Networks*, ICTON (2018) [17].
9. **A. Vetter, R. Kirner, D. Opalevs, M. Scholz, P. Leisching, T. Scharf, W. Noell, C. Rockstuhl, & R. Voelkel**, "Mask-aligner Talbot lithography using a 193 nm CW light source", *Proc. SPIE 10587, Optical Microlithography XXXI, 105870W* (2018). [18]
10. R. Kirner, A. Vetter, D. Opalevs, M. Scholz, P. Leisching, T. Scharf, W. Noell, C. Rockstuhl, & R. Voelkel, "Enabling proximity mask-aligner lithography with a 193nm CW light source", *Proc. SPIE 10587, Optical Microlithography XXXI, 105871F* (2018) [19].
11. D. Opalevs, M. Scholz, J. Stuhler, C. Gilfert, L.J. Liu, X.Y. Wang, A. Vetter, R. Kirner, T. Scharf, W. Noell, C. Rockstuhl, R.K. Li, C.T. Chen, R. Voelkel, & P. Leisching, "Semiconductor-based narrow-line and high-brilliance 193-nm laser system for industrial applications", *Proc. SPIE 10511, Solid State Lasers XXVII: Technology and Devices, 105112C* (2018) [20].
12. S. Ferrari, A. Vetter, P. Rath, & W.H.P. Pernice, "Waveguide integrated superconducting single-photon detectors", *International Conference on Transparent Optical Networks*, ICTON (2016) [21].

Chapter 1

Introduction

For thousands of years, humankind used to paint and to engrave the walls and ceilings of caves [22]. The modern version of ancient cave drawings is the printing industry, with the goal to reproduce images and text in magazines, books, and similar media in large numbers. An important milestone was the invention of *lithography* by Alois Senefelder by the end of the 18th century [23, 24], going back to the Greek words λίθος and γράφειν meaning *stone* and *to write*. Senefelder introduced modifications to the surface of limestone that either accept or repel the printing ink, which allows to transfer the ink to paper using a printing press [25]. This invention represented a significant improvement over gravure and woodblock printing in terms of quality and costs.

In the mid of the last century, another lithographic revolution took place, enabling the development of highly integrated semiconductor electronics, microelectromechanical systems, and optics as we know it today [26]. Almost every modern high-volume manufacturing process of micro-electronic and micro-optical components relies on *photolithography*, a technology adding *light* to the printing process [27]. The underlying idea is simple yet effective: Optical lithography generates a geometric pattern in photosensitive resists on top of a bulk substrate by exposing with light, typically in the ultraviolet regime [28], and developing the exposed resist. The patterns are incorporated in a master called the *photomask*, for example a thin structured chromium layer selectively transmitting or blocking light. In subsequent stages, the pattern is transferred to the substrate by means of etching or deposition. These steps are repeated over and over, with about 50 cycles or more for modern complex integrated circuits (ICs) [26].

Over the years, the resolution of photolithography improved tremendously. Three objectives can be identified as the main driver for this development: Miniaturization allows to integrate more devices on a given area, to shrink the costs for material and fabrication per device, and to reduce the power consumption of electronic components. The first two objectives are commonly described by Moore's law, predicting the number of transistors of dense ICs over time [29]. In 1965 a doubling roughly every two years was observed empirically [30], and adapted to eighteen months in 1975 to keep up with an accelerated development in reality [31]. The third objective is inherently connected to parasitic capacitances, which decrease with shrinking device dimensions, resulting in a reduced power consumption [32].

Optical lithography remains even today a fascinating area of research, as it combines optics on different length scales: From diffraction at features comparable to the wavelength over Fourier optics describing the image transfer to ray optics for designing illumination systems [33]. It also extends to engineer the mechanics of lithographic equipment and the chemistry of the photosensitive material [28]. The goal of lithography can be easily summarized as the correct edge placement of the printed pattern within a predefined



Figure 1.1: Principle of shadow printing.

tolerance [34]. The important performance metrics are the resolution, a dimension that defines the minimum feature size that can be printed, and the overlay accuracy, denoting the positional accuracy of a new pattern on an existing one [28].

Photolithography is tightly connected to photography, and so is their history. It brings us back to Eastern France in the early 19th century, where J.N.Niépce took the first photograph, a lithographic image projection-printed into a tar. This tar, called the *bitumen of Judea*, changes its solubility when exposed to light, but required about 8 h of exposure. The continuous improvement of photoresists resulted in an enhanced sensitivity, starting with dichromated gelatin in the mid-19th century and leading to a photoresist introduced by EASTMAN KODAK in 1953 [35]. This so-called KODAK PHOTORESIST was resistant against acids and allowed the etching of metals [35–37]. It was applied to facilitate the mass production of printed circuit boards, where a layer of copper is structured on top of an insulating substrate.

The fabrication steps resemble the steps of modern photolithography: First, the resist is applied and exposed through a binary mask. In a development step, for a positive photoresist the unexposed volume is removed, and in the unprotected areas the copper is etched away [38]. Negative photoresist act vice versa, i.e., the exposed portion becomes insoluble. The first photomasks were produced from Rubylith[®] by hand, with a resolution of about 100 μm to 200 μm [39]. Andrus and Bond [40] as well as Nall and Lathrop [41] applied the method to fabricate germanium transistors in 1957/1958, and the latter coined the term *photolithography*.

In 1957 Hoerni developed for FAIRCHILD SEMICONDUCTOR the *planar process* [42], which consists of four to five cycles of exposure, etching, and/or layer deposition steps. Shortly after, several transistors were connected to form integrated circuits [43], combining hundreds of electronic components on a single chip and starting the *Silicon Age* [44].

Having several lithographic prints in sequence requires an exposure tool that enables the alignment between subsequent steps. Such a *mask aligner* includes an optical microscope to align the wafer and the photomask with the help of dedicated alignment marks. The photomask and the resist-coated wafer are aligned and brought into contact or remain in close proximity of several tens of micron, followed by the exposure step.

It is important to note that mask aligner photolithography is a parallel full-field printing technique, i.e., the photomask contains the template for the entire wafer. Furthermore,

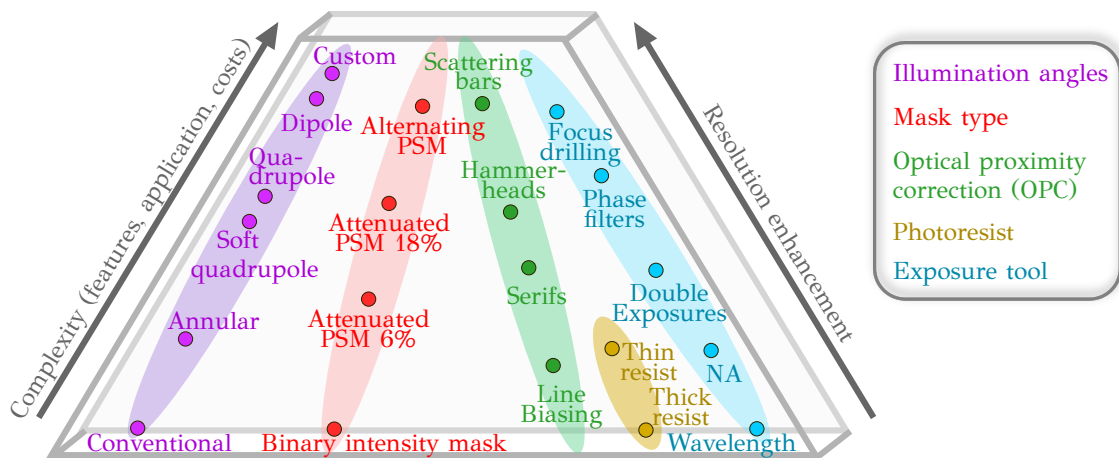


Figure 1.2: Resolution enhancement in optical lithography. Adapted from ASML.

mask aligners typically rely on *shadow printing*, i.e., the photomask selectively either completely blocks or transmits light, as depicted in Fig. 1.1. The best resolution is achieved by bringing the photomask and the wafer into contact, which minimizes the impact of diffraction. However, for high-volume manufacturing, the proximity mode with a gap between photomask and wafer is preferred, as mask contamination and frequent mask cleaning is avoided [45]. The resolution in the proximity mode depends on the gap and the wavelength, and typically amounts to some microns.

In the early 1960s, several companies developed and released mask aligner equipment. The first supplier in Europe was Karl Süss in 1963, including a translation stage to move the wafer relative to the mask, a correction for wedge errors, mechanics to clamp mask and wafer, and a lamp housing [38]. The resolution of optical prints was about 20 μm [38], also limited by the technical possibilities to create photomasks at the time. Since then, the resolution improved, together with the wafer size to 200 mm in diameter nowadays.

The next milestone in photolithography was the advent of projection systems in the 1970s, where the mask is imaged by an optical system to the wafer [46]. Early systems used a 1:1 scanning optics, where only a small part of the photomask is imaged at a time to minimize the optical aberrations [47]. Further resolution enhancement was achieved by reduction systems, introducing a demagnification of the mask features on the wafer [28]. Step-and-repeat systems or short *steppers* expose a small part of the wafer at once, and repeat this exposure over the size of the wafer. In the 1990s, hybrid step-and-scan systems were introduced that allowed to print minimum feature sizes of about 250 nm [28].

Since then, the main development trends strive to improve the resolution by decreasing the exposure wavelength and increasing the numerical aperture, tightly connected to the Abbe diffraction limit commonly applied in microscopy. This development culminated in the rollout of extreme ultraviolet (EUV) lithography, with a light source emitting a wavelength spectrum centered at 13.5 nm, which now enters high-volume manufacturing [48, 49].

Additional resolution enhancement techniques were introduced to optical lithography [50], see Fig. 1.2 for a short summary. This includes the optical systems, implementing structured illumination, phase-shift-masks, and optical proximity correction, as well as improved photoresist and exposure tools. All these techniques combined resulted in an impressive improvement of the resolution down to the single-digit nanometer-scale, and enabled the continuation of Moore's law until recently [51, 52].

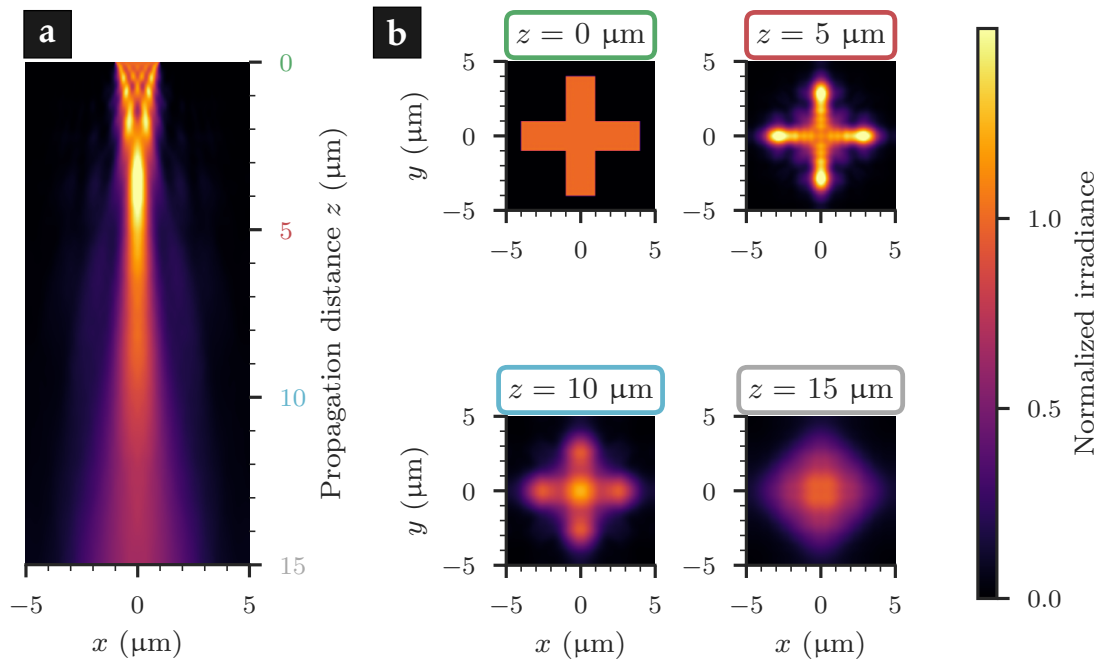


Figure 1.3: Simulated diffraction at photomask features, presented here for a cross-shaped pattern with a bar width of $2 \mu\text{m}$ and using i -line illumination (365 nm) with a constant angular spectrum (maximum half-angle 2.5°). The irradiance is normalized to the incident light.

a Irradiance distribution along the propagation direction z .

b Irradiance distribution in selected planes. Directly behind the photomask at $z = 0 \mu\text{m}$, the mask pattern is perfectly reproduced. For $z > 0 \mu\text{m}$, diffraction affects the image formation, smearing out the cross-shaped pattern.

Here, our short history of mask aligner photolithography could already come to an end. Replaced by the powerful projection lithography offering a better resolution, mask aligners are supposed to be outdated and not required in modern nano- and micro-fabrication. Interestingly, this is not what happened, and mask aligners maintain a decent market share and are actively developed to cope with future challenges. Here, we want to briefly discuss the reasons for this development.

The first argument to justify why mask aligner lithography remains a technology relevant to modern photolithography is less a physical but rather an economical one. As a rule of thumb, the costs of optical lithography amount to about 30% of the total manufacturing costs of an IC [26, 28]. If the resolution of the mask aligner is sufficient for the fabrication process at hand, the greatly reduced capital costs of a mask aligner compared to a stepper enable more cost-efficient operation. In other words, for small- and medium-sized job volumes, the cost of ownership is eventually reduced compared to projection lithography [34]. For this reason, mask aligners are used to fabricate non-critical layers in back end of line fabrication, for instance enabling fan-out packaging in the redistribution layer, i.e., the metal lines connecting individual units on an IC. Further, mask aligners are the prevalent tool for fabricating refractive micro-lenses and arrays, light-emitting diodes, and microelectromechanical systems [53].

Second, mask aligners facilitate rapid prototyping. A mask aligner is a rather simple tool, and shadow printing is a straightforward concept. Hence, photomask design and test prints are comparably simple to perform. In addition, it is possible to implement a new light source and thus to change the exposure wavelength. As a consequence, mask aligners are commonly used to develop technical innovations for steppers, for example

new photoresists [34].

The third argument involves specific applications that cannot use projection lithography for technical reasons. One example is the fabrication of micro-optical components as microlens arrays. The canonical process to fabricate microlenses involves a photoresist that is tens of microns thick. The use of projection lithography for the exposure is precluded by the limited depth of focus [38].

The fourth and final argument involves the ongoing development on mask aligner printing, which is also the impetus for this thesis. Since the early days of optical lithography, the resolution of mask aligners strongly improved. Important aspects concern the non-optical components as well, for example the leveling or the gap metrology [45]. Taken aside the improvements in mechanics and in the photoresist chemistry, also the optical components undergo continuous development. Important examples are the implementation of novel light sources [54], structured illumination [55], and phase-shift masks [56]. Mask aligners that are equipped with such resolution enhancement techniques can eventually replace the use of steppers for non-critical layers in semiconductor and optical manufacturing, which would result in a considerable cost reduction.

Diffraction at the photomask features is the main contribution to image shape distortions in mask aligner lithography (see Fig. 1.3), resulting for example in line-end shortening and corner rounding [50, 57]. In this thesis, we investigate approaches to limit the impact of diffraction or even harness the diffractive effect in order to improve the resolution. For this purpose we heavily rely on the simulation of light propagation to obtain a digital twin of the processes involved [58]. Ultimately, we aim to discover new techniques that extend the application of mask aligner photolithography to new areas not possible before.

Structure of the thesis

We begin in Chapter 2 with a review of state-of-the-art technologies used in mask aligners. We follow the path of light through a mask aligner, starting from a light source and ending with light absorption in a photosensitive material, which includes illumination shaping and photomask technology. Furthermore, we have a look at the inherent properties of light and how it propagates, i.e., the wavelength, the direction, the phase, and the amplitude, and discuss how they can be tweaked to improve the resolution.

Chapter 3 deals with important tools later used in the thesis to describe the light propagation in homogeneous and structured isotropic media. Four methods are introduced: The Fourier Modal Method, the Angular Spectrum Method, the Rayleigh-Sommerfeld diffraction integral, and ray tracing. In addition, we discuss the accuracy and the inherent limitations of these methods. Afterwards we discuss in devoted chapters the different approaches we have pursued in order to improve the resolution in mask aligner photolithography.

One particular method to improve the resolution is to reduce the wavelength of the light source used for the exposure. In Chapter 4 we examine the application of a novel continuous wave light source emitting at 193 nm. In a holistic approach, we discuss the concept of light generation, beam steering and homogenization, and lithographic printing both in simulations and in experiments. Furthermore, we demonstrate the benefits for Talbot lithography that allows to print periodic features with sub-micron resolution.

Chapter 5 extends the concept of phase-shift photomask to a rigorous design. Studying accurate simulations of light propagation in and behind three-dimensional mask structures allows to design photomasks with an improved resolution and extended depth of focus even at proximity gaps of tens of micron. We apply this principle to create a dense hexagonal periodic dot pattern with sub-micron lateral dimensions.

The printing of arbitrary patterns suffers from several types of image shape distortions. In Chapter 6 we apply an optical proximity correction method to mask aligner lithography, based on computational approaches to simulate the resist contour. By introducing dedicated correction structures to the mask design we demonstrate an improvement of the pattern fidelity for non-Manhattan geometries, i.e., corners with an inner angle that is different from 90° .

A novel class of photomasks for mask aligner photolithography is proposed in Chapter 7. Optical metasurfaces enable unprecedented opportunities to control wavefronts and their propagation at the nanoscale. We discuss two platforms based on all-dielectric and hybrid plasmonic-dielectric structures as well as their performance and limitations. In addition, we demonstrate how to encode the pattern in the metasurface.

In a final Chapter 8 we summarize our findings and provide an outlook for further developments in the field of mask aligner photolithography.

Advanced optical lithography

This chapter reviews the basic techniques and major developments for achieving high-resolution optical lithography. We focus here on mask aligner proximity lithography. The task at hand is to replicate any desired pattern inscribed in a photomask to a photosensitive layer on top of a wafer. The most important performance indicator is the resolution of the image transferred to the wafer, that means the ability of the lithographic system to transfer structures that are close to each other. The achievable resolution sensitively hinges on a complex interplay between the illumination optics, the pattern on the photomask, and the photoresist response. Common to all optical lithographic systems used in modern fabrication environments is the application of several resolution enhancement techniques, which we introduce in this chapter.

In general, optical lithography is a mature branch of semiconductor industry with over fifty years of research history. The review at hand aims to introduce the most important concepts, ideas, and technologies with the goal to understand the work presented in later chapters on mask aligner proximity lithography. For an exhaustive introduction to optical lithography in general, the interested reader is referred to existing literature [26–28, 34]. In an extension, Appendix B discusses alternative nanolithographic techniques and their relation to optical lithography.

2.1 Optical lithography for the fabrication of integrated circuits and micro-optical components

In modern top-down micro- and nanofabrication, the manufacturer typically has a pretty good notion of how the perfect device should look like. Consider an IC or a micro-lens: The operation can in theory be tailored to the specific application in mind, for example by relying on simulations of the underlying physics. The first and foremost step in fabrication is hence the transfer of this perfect device layout to a functional layer, made from suitable materials and eventually already containing patterns from previous steps.

The role of optical lithography is to implement a pattern transfer with high fidelity, at high resolution and throughput [34]. In the lithographic step, exposure light introduces a modification in a photosensitive layer. In the development step, either the exposed or the unexposed photoresist is removed, creating a masking structure for subsequent fabrication steps, as illustrated in Fig. 2.1. Additional constraints are a high yield, corresponding to a low defect rate, and a cost-effective operation. In reality, lithography becomes interesting while deviating from the perfect world, and it is rather difficult to incorporate all the aforementioned conditions in one single technique (compare Appendix B).

In the course of time, optical lithography emerged as the predominant pattern transfer technique, due to its versatility and adaptability to a variety of substrates and patterns, at high throughput and low defect density. But it is crucial to keep in mind that optical lithography is only one step in a chain of pattern transfer steps. All these steps are repeated

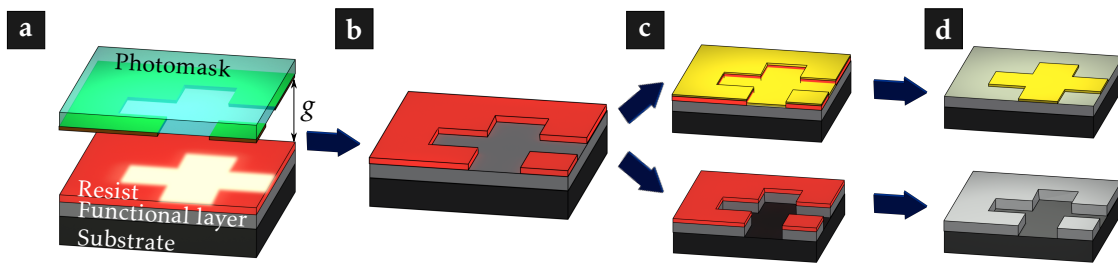


Figure 2.1: Process steps in an optical microfabrication cycle. The main steps are presented, and in reality additional process steps are required. The upper row illustrates an additive pattern transfer, the lower row depicts a subtractive pattern transfer. Such steps are iterated to generate the desired final structure.

a Mask aligner lithography, transferring the pattern from a photomask to a photoresist layer on a substrate. A chromium layer on the mask contains the structural information.

b For a positive photoresist, the exposed area is removed in a development step.

c Subsequently, the pattern is transferred to the functional layer, by depositing material for instance via atomic layer deposition (ALD) or physical vapor deposition (PVD) (top row), or removing material, for instance using reactive-ion etching (RIE) (bottom row).

d The photoresist is removed, for example using a solvent (for a lift-off, top row) or in an oxygen plasma after etching (bottom row).

over and over. To transfer the pattern from the photoresist to the functional layer, for instance etching, material deposition, or ion implantation is used to fabricate ICs and micro-optical components. Obviously, the photoresist chemistry has to be adapted to the individual process, which adds yet another constraint for the lithographic step.

2.2 Review of concepts for high-resolution optical lithography

The field of optical lithography underwent an impressive evolution since its infancy, from simple contact printing to sophisticated projection lithography used for modern front-end-of-line fabrication. The concern of lithography is the correct edge placement, that means to locate the edge of a feature at a nominal position within a tight tolerance window. Two important aspects that limit the edge placement can be distinguished, namely the overlay accuracy and the control of the feature shape [34]. The overlay is a metric that expresses how well subsequent process steps can be aligned. This task belongs to the field of metrology and will not be discussed further. In this thesis, we are concerned with controlling the shape and size of features, both in an isolated and a densely packed environment.

We introduce the idea of *resolution* as the minimum feature size that we can print with a given lithographic system, as we will discuss in detail in Section 2.3.3. For a periodic grating, two quantities are of interest, the grating period and the linewidth. The period that can be transferred by means of optical lithography is fundamentally limited by the underlying Abbe criterion that applies to the specific imaging process. The linewidth, however, can become arbitrarily small in principle. It is crucial to keep this distinction in mind.

Nevertheless, the performance of lithographic equipment has to be quantified in terms of resolution, and for this purpose several metrics - besides the resolution - have been introduced. Most frequently used are the *critical dimension (CD)*, *node*, *gate length*, and

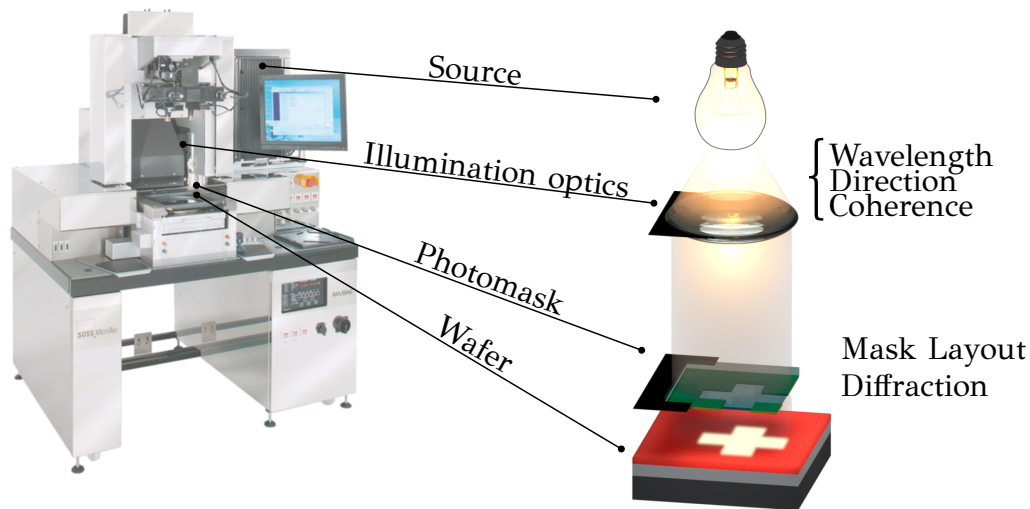


Figure 2.2: Illustration of a mask aligner, here a MA/BA8 from SUSS MicroTec. The light bulb schematically illustrates the source, which is discussed in Section 2.3.1. The task of illumination optics, schematically illustrated by a single lens, is to create a uniform illumination across the entire mask. The graph to the right is not to scale - the proximity gap between mask and wafer is typically only some tens of micron.

*half-pitch*¹. Being used synonymously in the early days of lithography, these quantities are neither uniquely defined nor reliably correspond to a measurable quantity [59]. For assessing the resolution in the work presented here, we typically refer to the linewidth as a CD of the process and to the period of the pattern, if applicable. Occasional exceptions are denoted.

2.2.1 Mask aligner contact and proximity lithography

Having covered the historical perspective of mask aligner lithography in Chapter 1, we aim to give an overview of the main ideas and requirements, before discussing the operation principle in detail in Section 2.3.

As already mentioned, the typical implementation of a mask aligner lithographic system performs shadow printing: The photomask contains the pattern that selectively either completely blocks or transmits the exposure light, for instance using a chrome-on-glass layer. Mask aligner lithography typically uses the emission lines of a mercury arc lamp with wavelengths around 400 nm. The mask is either in contact with the photoresist layer or situated at a small distance, called the proximity gap, in the order of several tens of microns [55]. During pattern transfer, the mask is flood-exposed from the top side using dedicated illumination optics, and the transmitted light subsequently exposes the photosensitive layer on the wafer. Figure 2.2 schematically illustrates this process and shows a picture of a commercially available mask aligner. There is no space for additional optical elements between photomask and wafer. In this configuration, mask aligner lithography is necessarily limited to full-field printing, i.e., the mask features are replicated 1:1 in the photoresist [26].

This works like a charm as long as the features are several wavelengths in size. However, for a feature size in the micron or even sub-micron range, light transmitted through the

¹As an example, for a microprocessor fabricated in 2009, Intel reports on a node of 32 nm, a gate length of 29 nm, and a half-pitch of 52 nm [59].

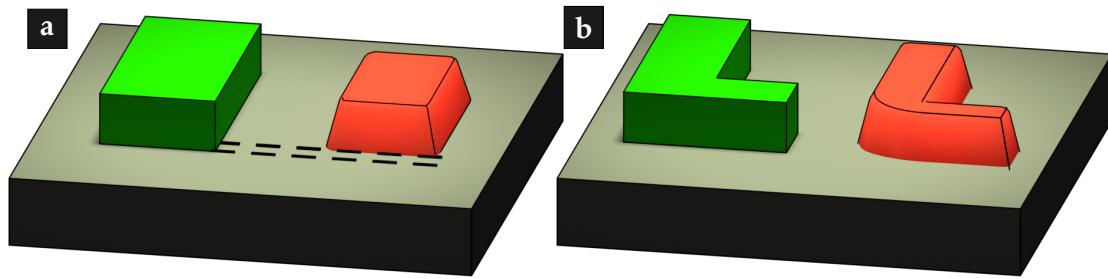


Figure 2.3: Common image shape distortions in optical lithography. **a** Line shortening, illustrated here for a rectangular pattern, and **b** corner rounding for a *L*-shaped pattern [50]. The green structure on the left show the desired ideal case, and the red structures on the right illustrate the impact of distortions.

mask is subject to considerable diffraction. Being a wave-optical phenomenon, the term diffraction was coined by A. Sommerfeld as [60, 61] "any deviation of light rays from rectilinear paths which cannot be interpreted as reflection or refraction". It arises from a wave confinement in a size around the order of a wavelength [61].

Figure 2.3 illustrates common image shape distortions introduced by diffraction at mask structures, line shortening and corner rounding. Large parts of this thesis are dedicated to explore how the impact of diffraction on image formation can be limited or how it can be leveraged.

The obvious solution to the diffraction problem is to bring mask and resist-coated wafer into intimate contact. In this modus operandi, the optical near-field is fully exploited, and the resolution is in principle only limited by diffraction over the finite thickness of the photoresist. However, there is no free lunch: the mechanical contact between mask and photoresist increases the risk of damage. Resist fragments may adhere to the mask and lead to contamination, which requires frequent mask cleaning or even replacement, if structural damage is introduced by the cleaning. In addition, pre-structured wafers already possessing some surface topography deny intimate contact and hence limit the applicability of contact lithography. For these reasons, contact mask aligner lithography is a niche application, not used in modern semiconductor fabrication [26, 34].

Having ruled out contact lithography for large volume manufacturing, we focus our considerations on proximity lithography, where a gap is introduced between mask and wafer. The wafer warp and structures already present on the wafer from previous process steps impose a lower limit on the proximity gap g that is mostly around $20\ \mu\text{m}$. The upper limit is about $100\ \mu\text{m}$, driven by the need to achieve a high resolution [55]. The resolution in mask aligner shadow printing is a function of both wavelength and proximity gap.

To state it once clearly: This thesis focuses on mask aligner lithography. However, for selected topics, we desire to draw comparisons between mask aligner and projection lithography, the prevalent manufacturing technique in modern optical lithography. The following Section 2.2.2 provides a glimpse at the fundamental ideas, without going too deep into detail.

2.2.2 Projection lithography

The main difference between mask aligner and projection photolithography is an additional imaging system between mask and wafer (see Fig. 2.4). This imaging optics renders the setup more complex with regard to aberration control, numerical aperture

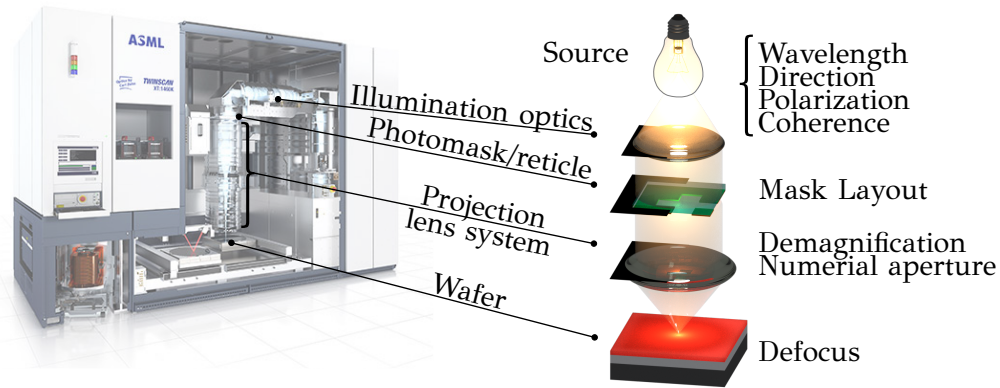


Figure 2.4: Illustration of a projection scanner, here a high-NA immersion scanner from ASML. The image to the left is reproduced with permission from ASML. The simplified graph to the right is not to scale.

(NA), alignment, and metrology, but it solves two problems associated to mask aligner lithography: the limited resolution in the preferred proximity mode and the lack of reduction capability, i.e., the possibility to enlarge mask features and subsequently transfer the de-magnified image onto the wafer [34]. In the early days of projection lithography, when feature sizes continuously shrank below $1.5\ \mu\text{m}$, it became more and more challenging to meet mask specifications at 1X replication, i.e., equal mask and image size. Replication systems were developed with a typical reduction ratio of 4. This development relaxed the requirements on mask resolution. Nowadays, with superior resolution in mask fabrication using e-beam lithography, it enables the implementation of sub-resolution features as part of a resolution enhancement technology (RET).

Relying on specially developed optical materials, dedicated fabrication methods, and with help from computational optics, projection systems are diffraction-limited [28]. We see once again that diffraction effects dictate the performance of lithographic systems. Common to all projection systems is monochromatic operation to avoid chromatic aberrations, whereas in mask aligners also sources with an emission bandwidth of several nanometers are employed.

Full-field exposure systems, exposing entire wafers in a single step, turned out to be impractical when the wafer size and the NA of the optics started to rise. Consequently, the development culminated in two categories, scanning and step-and-repeat solutions. Scanners rely on catadioptric optics, and only a part of the mask is projected onto the wafer at a time. By moving mask and wafer, the complete mask is imaged onto the photoresist. For step-and-repeat, the step field covers only a fractional part of the wafer size, and the entire field is projected from a typically 4X reduction mask at a time. Afterwards, the wafer is moved ("stepped"), and the next field is exposed ("repeat"), until the entire wafer is filled. Combining both methods, step-and-scan technology was developed, with even higher demands on optics and mechanics [26]. At the same time, the NA increased, with immersion lithography as a major development and key enabler. Since the advent of projection lithography in the 1970s, the exposure wavelength in high-volume optical photolithography decreased, culminating in the development of extreme ultraviolet (EUV) lithography.

2.3 Basics of optical proximity lithography

The goal of this section is to introduce the field of mask aligner illumination optics and discuss the concepts of pattern transfer as well as its inherent limitations. To understand

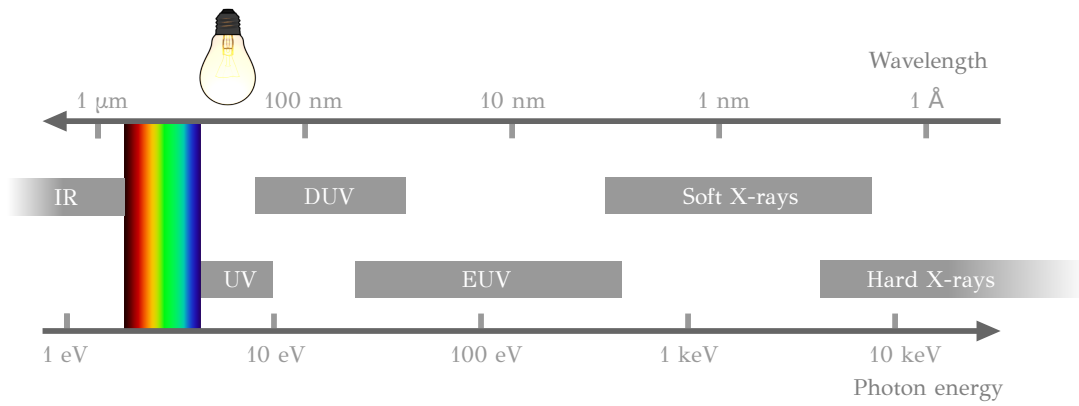


Figure 2.5: Spectrum of electromagnetic waves used in photolithography. Throughout this thesis, relevant wavelengths are in a range of 150 nm to 450 nm.

the mask aligner system, we, in a certain sense, follow the light propagation from the beginning to its end: We start by discussing established light sources and techniques to shape the illumination, then proceed by deriving the fundamental resolution limits, and discuss photomask and photoresist interaction with the illumination light towards the end.

2.3.1 Light source and illumination shaping

Starting point for photolithography is a high-power light source, with its emission spectrum influencing the choice of materials for illumination optics and photochemistry. In this section, we also discuss the possibility to change the properties of the illumination, for instance the angular spectrum or the coherence.

We have to keep in mind that a lower wavelength reduces the impact of diffraction effects for a given feature size (see Section 2.3.3), hence the integration of novel light sources is one approach to address resolution enhancement. Figure 2.5 shows the spectrum of electromagnetic waves relevant for optical lithography. In the infrared (IR) region, pulsed near-infrared (NIR) light sources are employed in multi-photon direct laser writing (DLW), as discussed in Appendix B.

Table 2.1: Properties of light sources used in optical lithography. Additional linewidth narrowing can significantly reduce the bandwidth. Regarding the mercury lamp, the *i*-line intensity amounts to about 40% of the total intensity in the range of 320 nm to 460 nm. For the pulsed solid state laser, the bandwidth is estimated from the pulse width of 35 ns. Data partly reprinted from [28].

Light source	Center wavelength (nm)	Unnarrowed bandwidth (nm)
High-pressure mercury lamp, <i>g</i> -line	435.8	5
High-pressure mercury lamp, <i>h</i> -line	404.7	5
High-pressure mercury lamp, <i>i</i>-line	365.0	6
UV light-emitting diode (LED) [62, 63]	365.0	9.0
Diode-pumped solid state laser [64]	355.0	$< 10^{-5}$
KrF excimer laser	248.4	0.30
ArF excimer laser	193.3	0.45
F ₂ excimer laser	157.6	$2 \cdot 10^{-3}$

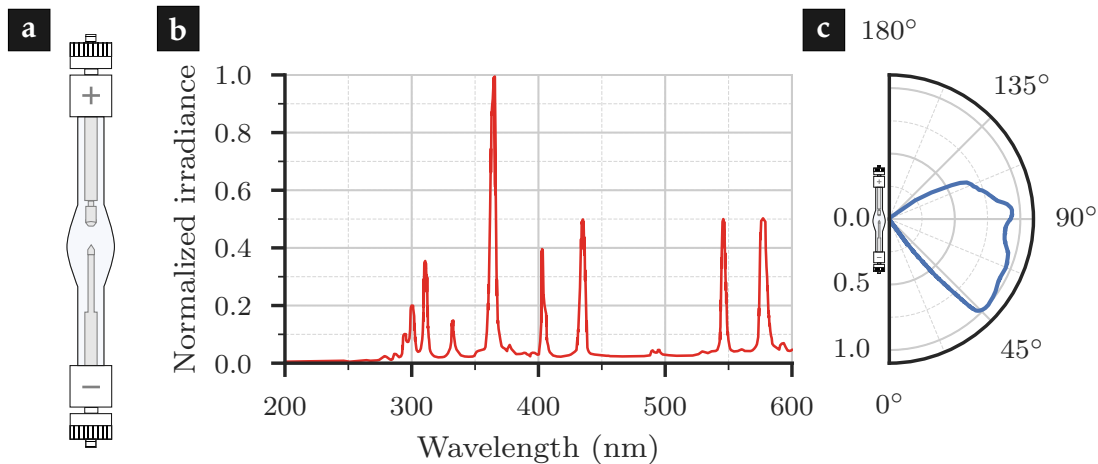


Figure 2.6: Properties of high-pressure mercury arc lamp.

a Schematic illustration of a discharge arc lamp, as used in *SUSS* mask aligners. The overall length amounts to 240 mm.

b Spectral distribution of an *i*-line lamp. The emission lines of mercury used for lithography are clearly visible (compare Table 2.1). Adapted from [67].

c The axial luminous intensity distribution of a mercury arc lamp, shown for one half-space. Adapted from [67].

Towards the right end of Fig. 2.5, large volume fabrication using EUV lithography at 13.5 nm is currently ramping up. We provide a brief summary on the main aspects of EUV lithography in Appendix B.1.

X-ray lithography at even shorter wavelengths has been around for quite some time, and was considered a strong candidate for next-generation lithography (NGL) [65]. However, X-ray lithography lacks the reduction capabilities of modern projection systems due to the unavailability of suitable X-ray optics. Photomasks require thick absorber layers, since adequate materials enabling thin layers are not developed to this day. Also, the rather high photon energy (compare Fig. 2.5) leads to the generation of high-energy secondary electrons (SEs) upon absorption, diminishing the contrast (see Section 2.3.2.2). Thus, X-ray lithography is mostly used for high aspect ratio structures [66].

Within the scope of this thesis, we deal with a narrow region in the UV and deep ultraviolet (DUV), in essence between 150 nm to 450 nm. A list of light sources for this spectral range is provided in Table 2.1.

The workhorse of proximity lithography to this day is the high pressure mercury arc lamp, with three main emission wavelengths (*g*, *h*, and *i*-lines). Figure 2.6a shows a schematic illustration of an arc lamp used in *SUSS* mask aligners [67]. The arc discharge between two tungsten electrodes excites ions and atoms of the mercury vapor. The spectrum of the lamp is essentially composed of single emission lines of the excited mercury ions and atoms. Impact broadening leads to a finite spectral width of the emission lines and a continuum background [68], resulting in the spectrum shown in Fig. 2.6b.

We will repeatedly make use of mercury *i*-line illumination at 365 nm, either in simulation, in experiments, or as a reference. In Section 4.1, we introduce the ArF excimer laser, the prevalent source in projection lithography. We compare its performance in mask aligner lithography [54] to a continuous wave (CW) laser source, emitting at 193 nm as well.

The generation of UV light is comparably efficient in terms of optical power (about 10.5% for the 1 kW lamp used in *SUSS* mask aligners) [67]. The lamp house of mask aligners contains an elliptic reflective mirror to enhance the light collection efficiency. However,

after spectral filtering, only 1 – 2% of the optical power ends up being used for printing. Lifetimes are limited to some 500 h to 1000 h, and they require around a quarter of an hour to reach stable working conditions, as the mercury has to vaporize, and hence typically run in non-stop operation. For all these reasons, considerable effort was dedicated to replace mercury lamps by light-emitting diodes (LEDs) [62, 69–73] or laser sources [64], with the emission close to the canonical g, h, i -lines.

A light source emitting from a small area under small solid angles is crucial for efficient beam shaping. The corresponding physical quantity that can measure this is the *étendue*² G , defined as

$$G = n^2 \int_{A'} \int_{\theta'} dA \cos \theta d\Omega \quad (2.1)$$

with n the refractive index of the medium in which we determine G . dA is an infinitesimal surface element of the source, θ is the half angle of the aperture seen from dA , and Ω is the solid angle. We integrate over the emission area A' and the emission angles θ' of the source.

The *étendue* measures essentially the the spread of the illumination in space and angle. One can show that G is - assuming an optical system in the absence of losses, scattering, or absorption - constant along the propagation of light [74]. Another picture to describe the *étendue* is the phase space representation of an ray, which represents the ray distribution in position and angle in optical systems [68]. In this representation, the conservation of G corresponds to the preservation of the phase space volume during propagation according to the Liouville theorem, with the invariant

$$A \cdot \Omega = \text{const.} \quad (2.2)$$

In simple words, the *étendue* expresses lower limit for converting beam width into an angular spread. A lossless conversion of the light source output into a small angular spectrum and simultaneously into a small space is only possible for a correspondingly small G of the source. For beam shaping this means that a low G allows efficient beam shaping, without the need to block light, for instance emitted into large angles. The luminous intensity distribution along the line between cathode and anode of mercury arc lamps shows a distinct maximum at the cathode tip [67], resulting in a high *étendue*.

The axial distribution of the mercury arc lamp is sketched in Fig. 2.6c. We recognize that the emission of the lamp cannot be used directly for mask aligner lithography, and prior homogenization is required. The task of beam shaping is to achieve a uniform and collimated irradiance distribution in the mask plane, allowing full-field exposure with low inhomogeneity in the irradiance over the field and hence enabling a high critical dimension uniformity. Crucial performance metrics are the non-uniformity of the irradiance and of the angular spectrum in the mask plane.

Historically relevant beam homogenization concepts started with critical illumination, imaging the light source directly into the object plane where a homogenization is desired, in our case the photomask plane. Hence even small non-uniformities of the light source contribute visibly.

An improved illumination scheme was developed for optical microscopy by August Köhler and presented in 1893 [77]. The basic idea is that each point of a macroscopic source shall illuminate the entire object plane, diminishing the impact of local variations in the source intensity. This can be accomplished using two spherical lenses and two diaphragms

²The *étendue* goes by many names in literature, for instance the literal translation 'extent', Lagrange invariant, acceptance, or light gathering capacity [74].

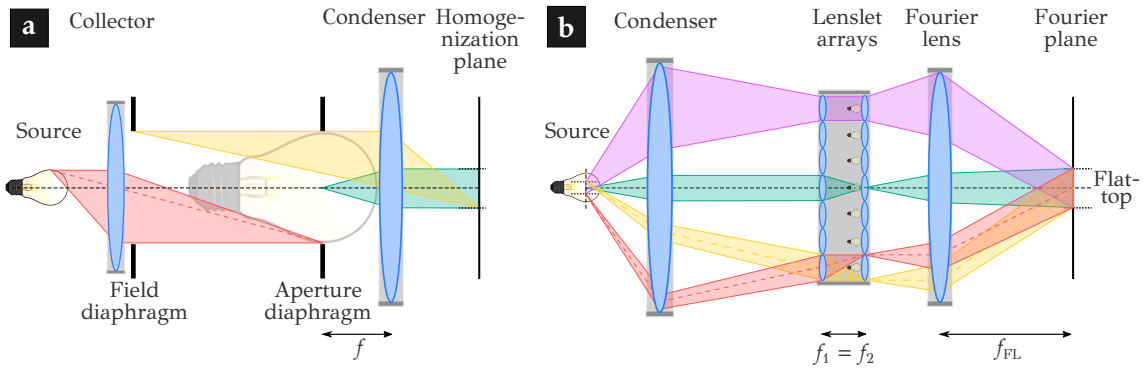


Figure 2.7: **a** Köhler illumination and **b** micro-optical Köhler integrator. The basic idea is that each part of the light source is supposed to illuminate the entire object plane, averaging over non-uniformities. Further improvement is achieved by subdividing the condenser lens into individual channels, as depicted in **b** using microlens arrays (MLAs). Adapted from [75] and [76].

(variable apertures), as illustrated in Fig. 2.7a. The first, so-called field diaphragm is located directly behind the first lens, the collector. A so-called aperture diaphragm is situated in the front focal plane of the second lens, the condenser [75].

In Köhler illumination, every point in the field diaphragm is imaged to the object plane (yellow), and every point in the aperture diaphragm is imaged to infinity (turquoise). One problem emerges: The angular spectrum in the aperture diaphragm dictates the attainable uniformity in the object plane, since different angles end up in different locations.

To further improve the concept of Köhler illumination, a multi-aperture Köhler integrator³ can be used, as illustrated in Fig. 2.7b. Two aspects are now essential to build an integrator: a microlens array (MLA), subdividing the input into individual channels, and an integrator lens, superposing the individual channels in the object plane [78].

Common to all types of integrators presented in this section is the fact that the distance between the integrator lens and the object plane is equal to one focal length f_{FL} . This corresponds to a Fourier transform of the field amplitude behind the MLA [61], and consequently the integrator lens is called the Fourier lens.

Depending on the properties of the light source and the application, two categories of micro-optical homogenizers can be identified, namely non-imaging and imaging homogenizers. The micro-optical elements introduce Fresnel diffraction effects [79], which can be significant, depending on the dimensions and the coherence of the light source. To estimate the impact of diffraction, we consider the one-dimensional Fresnel number FN [80]

$$FN \simeq \frac{P_{MLA} \cdot D_{FT}}{4 \cdot \lambda \cdot f_{FL}} \quad (2.3)$$

P_{MLA} is the period of the MLA, D_{FT} the dimension of the flat-top in the homogenized plane, λ the illumination wavelength, and f_{FL} the focal length of the Fourier lens (compare Fig. 2.8). The larger the Fresnel numbers, the sharper the edges of the image, and the smaller the contribution of diffraction effects ('near-field'). Literature suggests that for $FN \gtrsim 10$ non-imaging homogenizers can be used, corresponding to a source showing high spatial coherence over every sub-aperture [78].

³Again, many terms exist: fly's eye condenser, faceted Köhler integrator, and optical integrator [75].

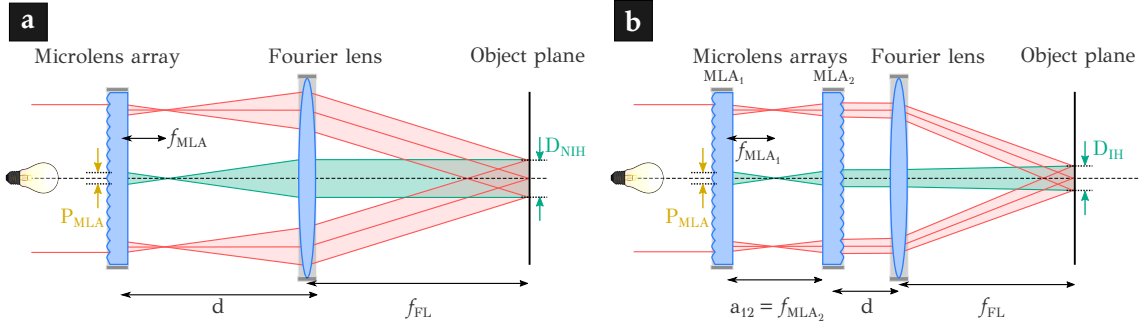


Figure 2.8: Sketch of two types of homogenizers, which are applied throughout this thesis.

a Non-imaging homogenizer.

b Imaging homogenizer. The size of the homogenized object field is D and P_{MLA} is the period of the MLA. The light bulb indicates the illumination with a collimated beam, with a point light source at infinity. Adapted from [75,78,80].

The optical setup of a non-imaging homogenizer is depicted in Fig. 2.8a. A single MLA splits the light into individual beamlets, which are superposed in the object plane. Aberrations of the MLA are the main source of non-uniformities in the object plane [75,80].

We can calculate the size of the homogenized area, considering Fig. 2.8a [80], as

$$D_{\text{NIH}} = \left| \frac{P_{\text{MLA}} \cdot f_{\text{FL}}}{f_{\text{MLA}}} \right|. \quad (2.4)$$

Note that D_{NIH} is independent of the separation d between MLA and Fourier lens.

In contrast to the non-imaging homogenizer, the imaging optical integrator requires two MLAs. With the setup depicted in Fig. 2.8b, the beam uniformity typically improves. As for the case of the non-imaging homogenizer, the first MLA subdivides the beam. Now, the second MLA and the Fourier lens work as an imager, superposing all beamlets on the object plane. The dimensions of the object plane are calculated in paraxial approximation, considering Fig. 2.8b and the thin lens equation [80]:

$$D_{\text{IH}} = \frac{P_{\text{MLA}} \cdot f_{\text{FL}}}{f_{\text{MLA}_1} \cdot f_{\text{MLA}_2}} \left[f_{\text{MLA}_1} + f_{\text{MLA}_2} - a_{12} \right] \quad (2.5)$$

with $f_{\text{MLA}_1} < a_{12} < f_{\text{MLA}_1} + f_{\text{MLA}_2}$.

To image now the sub-apertures of the first MLA by the second MLA and the Fourier lens, the focal length f_{MLA_2} has to be equal to the separation between the MLAs. With $a_{12} = f_{\text{MLA}_2}$, Eq. (2.5) simplifies to [75]

$$D_{\text{IH}} = \frac{P_{\text{MLA}} \cdot f_{\text{FL}}}{f_{\text{MLA}_2}}. \quad (2.6)$$

Throughout the thesis, we use identical MLAs to build up an imaging homogenizer, with $f_{\text{MLA}_1} = f_{\text{MLA}_2}$.

In the following, we discuss two possible problems for imaging homogenizers. First, when the size of the beamlets illuminating the second MLA surpass P_{MLA} , the apertures are overfilled. The resulting crosstalk would result in multiple images, shifted laterally with respect to the desired field distribution [75].

Second, when using coherent laser beams for illumination, the periodic MLAs act as

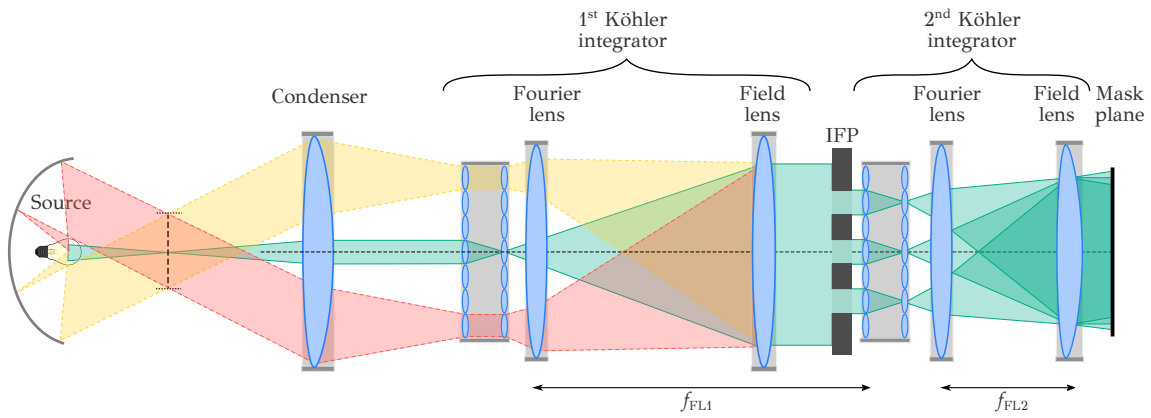


Figure 2.9: MO Exposure Optics[®] (MOEO[®]), consisting of two Köhler integrators in sequence. The first integrator uniformly illuminates the second integrator, resulting in a uniform spatial **and** angular field distribution in the object plane. An illumination filter plate (IFP) selectively blocks light and allows to shape the angular spectrum. The two field lenses ensure telecentric illumination. For the sake of clarity, we show only the turquoise rays behind the field lens of the first integrator. Adapted from [83].

diffraction gratings. The period Λ_{diff} of the diffraction effect in the object plane is

$$\Lambda_{\text{diff}} = \frac{\lambda \cdot f_{\text{FL}}}{P_{\text{MLA}}}. \quad (2.7)$$

Up to now, we discussed only spatial uniformity. For RETs, it is required to have also control over the distribution of illumination angles. Let us consider again the underlying principle of a Köhler integrator: The spatial field distribution in the plane of the MLAs defines the illumination angle, as the Fourier lens performs a Fourier transformation (compare Fig. 2.8). By combining two integrators, one behind the other, both spatial and angular uniformity can be achieved. The concept was presented by SUSS MicroTec in the 1970s, using an array of micro-pyramids. Relying on micro-optical MLAs, SUSS introduced in 2009 the MO Exposure Optics[®] (MOEO[®]), which is depicted in Fig. 2.9 [55, 81].

The first integrator ensures spatially uniform illumination of the second integrator, whereas an illumination filter plate (IFP) allows to selectively modify the illuminated area of the 2nd integrator and thus to shape the angular spectrum. Field lenses facilitate telecentric illumination, i.e., the chief rays behind the Fourier lens enter the object plane perpendicularly [55, 68]. The telecentric system avoids a lateral displacement of the mask pattern.

Using mercury lamp illumination, the non-uniformity of the irradiance in the mask plane is typically well below 3% [82]. We discuss the application and the benefits of MO Exposure Optics[®] (MOEO[®]) to mask aligner lithography in Sections 2.4.2.1 and 2.4.3.3.

2.3.2 Photomask and resist technology

In this section, we introduce the technology and principles behind photomasks and photoresist in optical proximity lithography. The photomask modifies the electric field of the exposure light in amplitude and phase. The field propagates over the proximity gap, and the image is recorded in the photoresist. This process depends on the irradiance, which is proportional to the absolute square of the electric field. For modeling the development process, the interested reader is referred to corresponding literature [28].

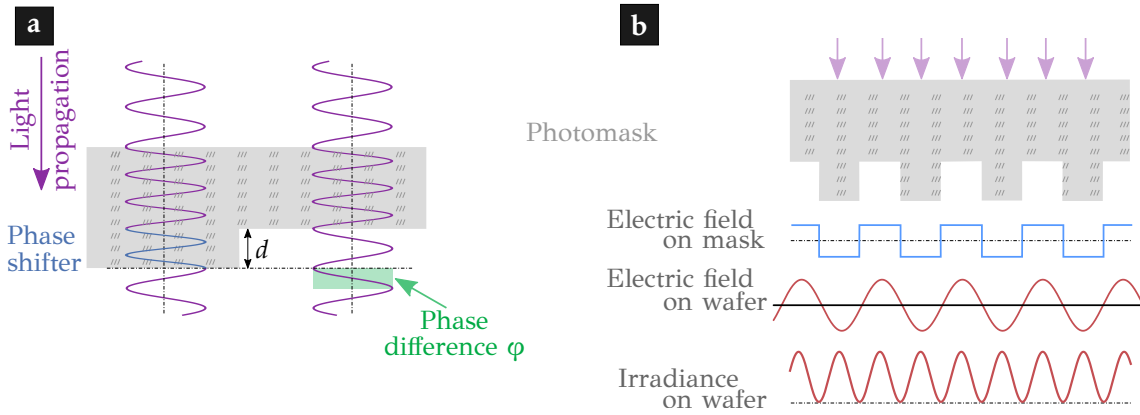


Figure 2.10: Schematic of phase-shifting in a photomask.

a Mask cross-section, showing a part of the mask substrate and an additional phase-shifting layer with thickness d . A phase-shift between light traversing through the phase shifter and light in air arises (depicted in green).

b Frequency doubling in chromeless PSMs under coherent illumination.

2.3.2.1 Photomasks in optical lithography

Photomasks⁴ are an essential part of the lithographic apparatus, as they contain the individual information on the pattern to be replicated. A photomask inherently consists of structures modifying the amplitude and/or phase of light, by incorporating phase shifters and/or patterned absorbers on an otherwise transparent substrate. Fused silica is the substrate of choice, due to its low thermal expansion coefficient of about $\alpha = 0.53 \times 10^{-6}/\text{K}$ [84] and its transparency over the entire visible spectrum down below 200 nm [34]. Soda Lime glass is also widely applied, but shows a higher thermal expansion coefficient and is opaque in the DUV [85].

Concerning the absorber material, in the early days an emulsion mask absorber was implemented [38]. It was quickly replaced by a chromium layer due to its high optical density (OD) enabling thin layers and its hardness required for contact lithography. An OD of 3 is typically sufficient for proximity lithography [28]. The photomasks used throughout this thesis are ordered from a commercial photomask supplier, relying on e-beam lithography for patterning the mask structures.

A further improvement over binary intensity masks is anticipated using transparent mask structures with a well-defined topography, allowing to modify the phase of transmitted light [86]. In combination with partial or complete absorber structures, phase-shift masks (PSMs) give total control over the complex transmitted electric field [28]. By traversing through an extra layer, as depicted in Fig. 2.10a, the phase is shifted with respect to free-space propagation. Combined with partly or completely absorbing layers, a myriad of PSM types exist. We restrict our considerations here to binary and multi-level PSMs. Having no absorbing structures, these types are often referred to as unattenuated or chromeless PSM.

Under coherent illumination, i.e., a plane wave under normal incidence, PSMs use the interference between transmitted fields with differently imposed phase. This leads to a higher resolution and an extended depth of focus (DOF) [34], as we will discuss in more detail on analytical grounds in Section 2.3.3. The exposure light picks up a phase shift φ when traversing through an additional layer on the substrate, compared to the propagation

⁴In former times, the term *recticle* was used for reduction masks in step-and-repeat lithography. Nowadays, both terms are interchangeable [28].

through air (see Fig. 2.10). With a given thickness d for the phase shifter, it follows

$$\varphi = 2\pi \frac{d}{\lambda} (n - 1) \quad (2.8)$$

with n the refractive index, describing the evolution of a plane wave in the phase shifter. In case of a binary PSM, the phase shift of interest is typically π . This corresponds to a minimum additional thickness of

$$d = \frac{\lambda}{2(n - 1)}. \quad (2.9)$$

As a rule of thumb, $n \sim 1.5$ for SiO_2 , and hence $d \sim \lambda$. This means that the thickness of the phase shifter has to be approximately the free-space wavelength of light to achieve a phase shift of π .

What advantage does a PSM offer? First, combining coherent illumination and a periodic PSM, the irradiance on the wafer drops to zero at the transition between shifted and unshifted areas, see Fig. 2.10b. Hence, the contrast in the aerial image, i.e., the modulation between minimum and maximum irradiance, increases. Second, the spatial frequencies propagating through the system are halved, compared to a binary intensity mask with an opening at the position of each phase shifter and the space in between. Thus, the electric field is less affected by the imaging lens in projection lithography. In the wafer plane, the period is halved with respect to the PSM period, corresponding to a frequency doubling (compare both red graphs in Fig. 2.10b).

Multi-level PSMs combine multiple phase levels in one mask, in analogy to diffractive optical elements (DOEs). PSMs are widely used in projection lithography, and their prospects for resolution enhancement in mask aligners have been demonstrated as well, clearly showing a resolution enhancement over binary intensity masks [56, 87]. To create the phase-shifting elements on a full mask size, with wavelength-scale periods, requires tremendous effort and renders mask fabrication expensive. In addition, coherent plane wave illumination is required. For this reason, PSMs are rarely used in mask aligner lithography.

In summary, the photomask is an essential component since it contains the structural information about the pattern to be transferred. Binary intensity masks simply consist of a light-absorbing chromium layer on a polished mask substrate, selectively blocking light propagation through the mask. In contrast, PSMs also offer control over the phase of the exposure light. We will exploit both concepts in the course of the following chapters.

2.3.2.2 Interaction of light with the photoresist

The exposure light behind the mask contains the structural information, and is absorbed by the photoresist. In this light-sensitive component, a chemical reaction is induced upon illumination, in our case with light in the UV regime. Generally speaking, the dissolution rate is different in exposed and unexposed regions. That means, using a suitable solvent called the developer, the photoresist is removed at different rates. The chemistry and modeling of photoresists is not discussed here for brevity, with good reviews provided in [26, 28].

Two polarities of photoresists are available, namely positive and negative resist. In positive photoresists, the exposed regions in the resist become more soluble in the developer than unexposed regions, and vice versa for negative photoresists, where exposed regions become inert. In the realm of this thesis, we consider positive resists only, due to their relevance for fabricating especially micro-optical elements [88].

In general, positive photoresists for g,h,i -line exposure have three main ingredients: a base polymer (resin) for structural integrity, a photoactive compound (PAC) also termed sensitizer, and a solvent to render the resist liquid for spin coating. For the base polymer P typically polymers with a low molecular weight such as Novolaks are used. The PAC, for instance diazonaphthoquinone (DNQ), is light-sensitive, and changes from the sensitizer M to exposure products E during UV exposure. After spin coating, a large portion of the solvent S is removed in a prebake step [28].

Taken all together, the absorption in the photoresist is described by a coefficient α following Beer's law $I(z) = I_0 \exp(-\alpha z)$, with the contribution of individual components i contained in the photoresist. Depending on the concentration C_i and the molar absorption coefficient a_i , the absorption coefficient is

$$\alpha = \sum_i a_i C_i = a_P P + a_M M + a_E E + a_S S \quad (2.10)$$

The working principle is understood as follows: The base polymer alone is soluble in an alkaline developer, but the dissolution is inhibited by the sensitizer. Upon exposure, the reaction products show the opposite behavior, increasing the dissolution rate in the developer. Hence, the exposure process creates a difference in the dissolution rates of exposed and unexposed⁵ portions of the photoresist, leading to removed and remaining structures in the resist.

Upon UV exposure, the DNQ loses nitrogen and reacts to an indene. Subsequently, in air humidity, it rehydrates to a carboxylic acid, the end product. This change in chemistry is accompanied by modified optical properties, as the sensitizer concentration changes from an initial value M_0 , and the exposure products are generated, $E = M_0 - M$. Following the Dill model of exposure, it is insightful to rewrite Eq. (2.10) as [28]

$$\alpha = A \cdot m + B$$

$$\text{with } A = (a_M - a_E)M_0 \quad (2.11)$$

$$B = a_E M_0 + a_P P + a_S S$$

$$\text{and } m = \frac{M}{M_0}.$$

Following these definitions, A and B describe the absorption coefficients for the unexposed (unbleached) and completely exposed (bleached) region of the photoresist, respectively. To determine A and B , the absorbance of photoresists are measured, for a fully exposed resist with $M = m = 0$ and an unexposed resist with $m = 1$ [28]:

$$B = \alpha_{\text{exposed}} \quad (2.12)$$

$$A = \alpha_{\text{unexposed}} - \alpha_{\text{exposed}}.$$

To describe the change in the photoresist upon exposure, we establish a relationship between the relative sensitizer concentration m and the intensity I , resulting in [28]

$$\frac{dm}{dt} = -C I m \quad (2.13)$$

with the standard exposure rate constant C . These ABC or *Dill* parameters describe the optical properties of the photoresist upon exposure, and are provided by the manufacturer.

For photoresists in the DUV, for instance at a wavelength of 193 nm, new resist concepts were required. The conventional DNQ-based photoresists are highly absorbing and show

⁵Unexposed regions are still removed by the developer, just with a greatly reduced rate. This *dark erosion* has to be taken into account when choosing the developing time.

a low sensitivity in the DUV regime, not suited to cope with the initially low power of the light sources. Wilson, Fréchet, and Ito developed a novel scheme with higher sensitivity, called chemically amplified resists (CARs) [89–91]. The photochemistry is designed in a way that an acid, i.e., single protons, are produced upon light absorption. Such a proton catalyzes the conversion of the base resin, without being depleted. Thus, a single generated proton can be used extensively, amplifying the chemical process. To initiate the conversion, the wafer is typically heated in a post exposure bake (PEB) step following the exposure. In Chapter 4, we use a CAR for the DUV experiments at 193 nm.

Taking all this properties of photoresists into account, the essential key performance indicator for photoresists is the contrast, as depicted in Fig. 2.11a. It shows the ratio d/d_0 of remaining film thickness for a positive resist after development. For a perfect contrast, the dependence on the exposure dose is a step function - either the resist remains unaltered or is completely removed above a certain threshold, the dose to clear D_C (compare Fig. 2.13a). Real resists show a dark erosion at low doses, resulting in $d/d_0 < 1$, and a finite slope at the transition. Hence, there are gray areas in the resist, receiving and reacting on an intermediate dose. The slope of the logarithmic decay is a measure for the contrast γ ,

$$\gamma = \left(\log_{10} \left[\frac{D_C}{D_0} \right] \right)^{-1}. \quad (2.14)$$

Figure 2.11b shows schematically the resist contour for one low and one high contrast after development. When the development rate of the resist would rise for instance linearly with the exposure dose, neither steep sidewalls nor high resolution could be achieved. It is crucial to mention that the contrast is not a function of the resist only, but rather depends in a complex fashion on the process steps, the environment, the developer, and many more parameters.

One detrimental effect with implications on the lithographic performance is the formation of standing waves in the resist [93,94], depending sensitively on the resist thickness. When two waves travel in opposite direction with a fixed phase relation, they interfere and form standing waves [28]. Counter-propagating waves arise through multiple reflections at the interface air/resist and resist/substrate, depending on the respective material combination. The consequence of standing waves is non-uniform light absorption in the photoresist, strongly depending on the local resist thickness, and hence jagged resist profiles. The periodicity Λ_s of the standing waves, with illumination under normal incidence, is a function of the exposure wavelength λ and the refractive index of plane wave propagation in the resist n_{res} [28,34],

$$\Lambda_s = \frac{\lambda}{2n_{\text{res}}}. \quad (2.15)$$

To prevent the formation of standing waves, one common approach is to apply additional layers to reduce the reflectivity at interfaces, resulting in either a top anti-reflective coating at the interface air/resist or a bottom anti-reflective coating (BARC) at the interface resist/substrate. Commercially available solutions exist for example for *i*-line illumination.

2.3.3 Image formation and resolution limits

To retrieve minimum resolvable features from optical simulation and to analyze the dependence of the resolution on external parameters such as wavelength or proximity gap, we require to develop suitable criteria. The main idea is to decompose the pattern into its spatial frequencies, and each component is investigated separately. The resolution limit is the minimum resolvable period, corresponding to the largest spatial frequency, transferred by the optical system [57].

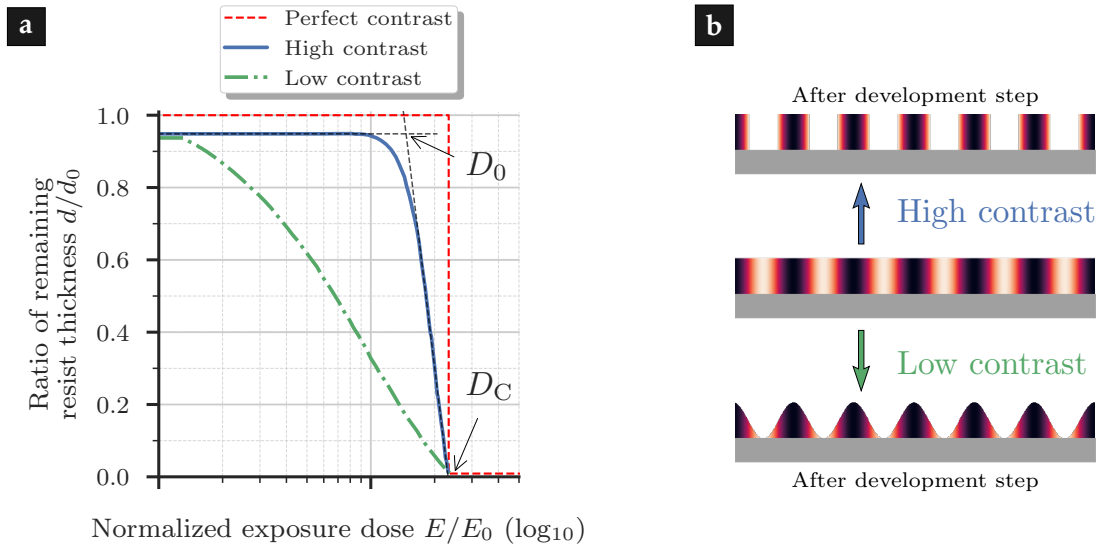


Figure 2.11: Contrast of a positive photoresist.

a Contrast curve, showing the ratio of the remaining resist to the initial resist thickness as a function of the exposure dose on a log-scale. As an example, three contrast curves are presented, with the perfect curve follows a step function. From the intersection of the two asymptotes D_0 and the dose to clear D_C , the contrast parameter γ is retrieved from the logarithmic slope, compare Eq. (2.14). A resist with high contrast exhibits a stronger variation as a function of the exposure dose close to the step, compared to a resist with low contrast. For simplicity, we assume an equal D_C .

b The contrast describes how the latent image transforms to the photoresist topography upon development. Here, we assume a $\sin^2(x)$ irradiance distribution (middle), as obtained by a binary PSM. The color indicates the dose absorbed in the photoresist, and the contour the topography after development. A high contrast resist (top) leads to well-defined structures with vertical sidewall angles, whereas a low contrast resist (bottom) results in the typically undesired reduction in sidewall steepness. Adapted from [92].

Depending on the properties of wave propagation between mask and wafer, we develop a fundamental resolution criterion for projection and proximity lithography. Here, we assume fully coherent illumination, and neglect the vectorial nature of light by considering only scalar fields.

The most relevant contribution to image shape distortions in optical lithography is diffraction [28], i.e., light propagation under the influence of boundaries, as the apertures on a mask. Derived from Maxwell's equations and the Helmholtz wave equation, Kirchhoff and Rayleigh-Sommerfeld diffraction integrals allow to calculate the impact of diffraction in scalar approximation behind the mask. Along the propagation over a distance z , further simplification leads to Fresnel and finally Fraunhofer diffraction in the far-field. Fraunhofer approximation is valid for $z \gg k\xi^2/2$, with the wavevector $k = 2\pi/\lambda$ and the aperture size ξ [61]. The far-field is - besides from phase factors - equal to the Fourier transform of the transmission function of the mask.

To be clear: We can crudely simplify Maxwell's equations in order to facilitate a fast method to assess light propagation, for example over a range of illumination angles. The key task is to rigorously simulate the mask features for a specific polarization and spectrum of plane waves. To investigate binary intensity masks, in the following we apply the TEA, i.e., assuming a binary transmission function. We will discuss in Section 2.4.3.3 the limitations of this assumption with regard to PSMs.

We consider now the image formation behind two distinct apertures, a single slit and a

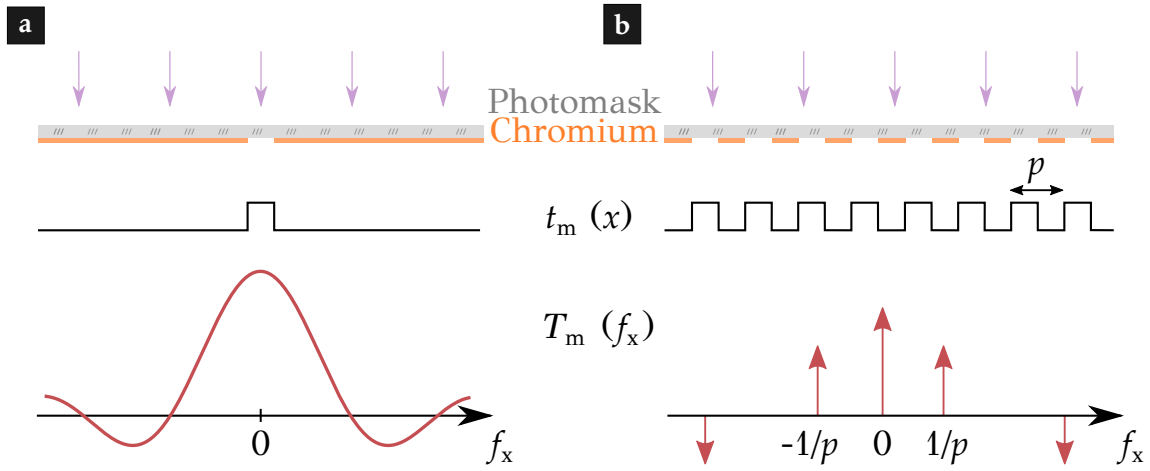


Figure 2.12: Diffraction at a **a** single and **b** periodic slits with period p under plane wave illumination. The figure illustrates the mask with a metallic absorber layer (top), the transmitted electric field t_m in thin-element approximation (TEA) (middle), and the electric field T_m of the Fraunhofer diffraction patterns in the far-field (bottom). The patterns are assumed to be invariant normal to the page. m denotes the diffraction order. Adapted from [28].

grating consisting of lines & spaces, in Fraunhofer approximation, as depicted in Fig. 2.12. For the isolated slit in Fig. 2.12a, we observe a continuous energy distribution across the spatial frequencies f_x . The irradiance distribution in the far-field is described by a *sinc* function, the Fourier transform of the rectangular-shaped transmittance.

The resolution is fundamentally limited only by the sensitivity of the 'sensor', in our case the photoresist: In a simplified threshold model, Fig. 2.13a, all resist is exposed and subsequently removed in a development step when irradiated by a dose above a certain threshold level, and remains unaltered below this level. Here, only linear processes play a role. By varying the exposure dose, the curve scales linearly, and the printing of arbitrarily small isolated features is possible when the applied dose only just surpasses the threshold.

From a perspective of optics, the resolution for printing a single slit is fundamentally limited only by adjacent features, introducing image shape distortions. In Figs. 2.13b and 2.13c, we consider the incoherent superposition of two adjacent slit openings in the Fraunhofer regime, with the intensity I_i of each slit in the far-field [95]

$$I_i(x) = I_0 \cdot [\text{sinc}(x)]^2 = I_0 \cdot \left[\frac{\sin(\pi x)}{\pi x} \right]^2 \quad (2.16)$$

$$\text{with } x = \frac{ak}{2} \sin(\theta) \approx \frac{ak}{2} \tan(\theta) = \frac{ak\delta}{2g}$$

where a denotes the linewidth of the slit, $k = \frac{2\pi}{\lambda}$, and δ the lateral extension of the image when propagating over a distance g . The first minimum occurs at $\delta_1 = \frac{2g}{ak}$, and the total field is the incoherent superposition $I_{\text{total}} = I_0 + I_1$.

When applying for instance the Rayleigh criterion, the maximum irradiance of one slit falls onto the first minimum of the adjacent slit, as depicted in Fig. 2.13b. The dip in the total irradiance (green) of the individual slits (red and blue) allows in general resolvable features. This requires to choose an exposure dose where the threshold is between minimum and maximum, as indicated by the black line in Fig. 2.13b.

By shifting the objects closer to each other, the dip vanishes when the Sparrow criterion is

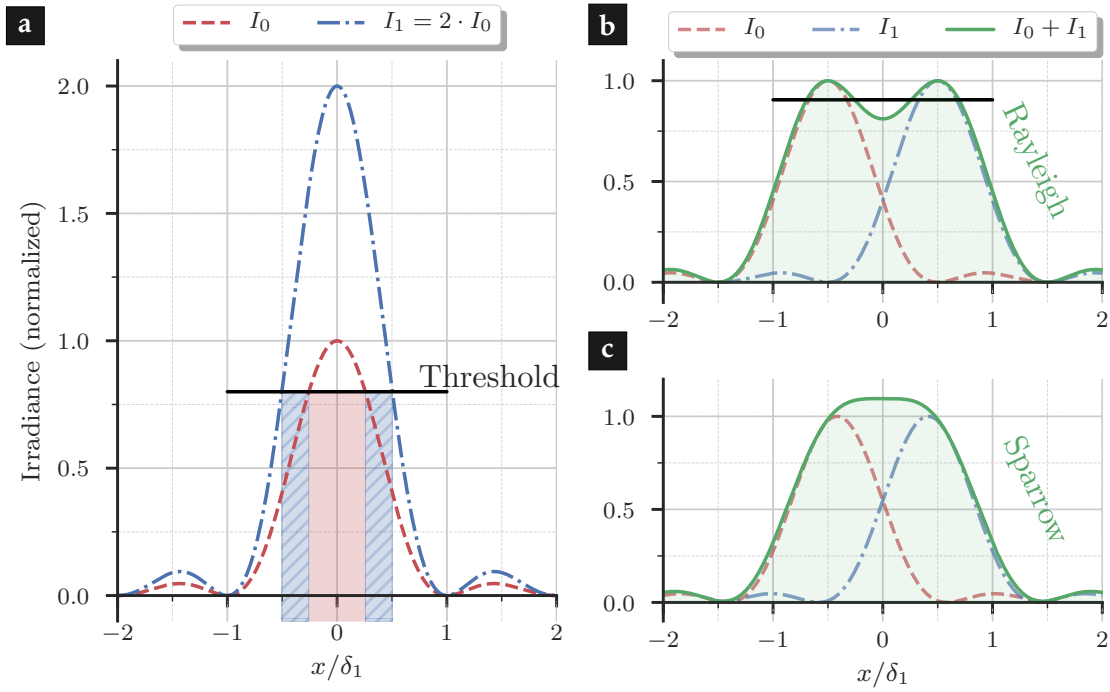


Figure 2.13: Threshold model and resolution criteria, assuming incoherent plane wave illumination [95].

a Threshold behavior, as often applied to thin photoresists, shown for a single slit. A threshold, here 0.8, defines the resist response upon illumination. A higher exposure dose (here indicated as an intensity, blue) leads to larger features. By adapting the exposure dose, an almost arbitrary feature size is achievable.

b Rayleigh and **c** Sparrow resolution criteria for two adjacent slits, assuming incoherent illumination. Applying the threshold model, two separable features can be obtained for a mutual separation of one Rayleigh distance. In contrast, the Sparrow distance fundamentally limits the minimum feature size, as no dip is visible.

met (see Fig. 2.13c), defined as a vanishing second derivative of the irradiance

$$\left[\frac{d^2 I_{\text{total}}(x)}{dx^2} \right]_{x=0} = 0. \quad (2.17)$$

For two adjacent slits, the resolvable separation following the Sparrow criterion is $0.83 \delta_1$ [95].

Up to now, we considered only two adjacent slits, infinitely extended, under plane wave illumination in the far-field. From this simple example, it becomes clear that it is impossible to develop a universally applicable resolution criterion: Resolution is a complex interplay between the exact definition, the diffraction regime under consideration, the properties of illumination source, and the photoresist contrast.

Let us now consider a periodic structure under normal incidence. A grating gives rise to discrete diffraction orders (see Fig. 2.12b), with the envelope defined by the spatial frequencies of a single slit. Following the Abbe resolution criterion, we require at least both first diffraction orders to superpose in the image plane, with the zeroth order only adding a global background.

This condition already suffices to define a resolution criterion in projection lithography: Only light under an angle smaller than the maximum half-angle θ_{max} propagates through the apertures of the projection optics. The lens acts as a low-pass filter for the spatial

frequency components of the mask, corresponding to a NA of

$$\text{NA} = n \cdot \sin \theta_{\max} \quad (2.18)$$

with the refractive index n describing the propagation of a plane wave in the output medium, for instance air in conventional lithography or water in immersion lithography [96].

As introduced before, we investigate the grating in terms of its spatial frequency. We use now the grating equation for a wavelength λ to connect the angle of the first diffraction orders to their spatial frequency [68],

$$f_x = \pm \frac{n \cdot \sin \theta}{\lambda}. \quad (2.19)$$

The condition of at least the first diffraction orders propagating through the system under normal incidence illumination corresponds to $f_x = 1/p_{\min}$, with the minimum grating period p_{\min} (see Fig. 2.12b). Combining Eqs. (2.18) and (2.19), we retrieve a condition for the minimum period

$$p_{\min} = \frac{\lambda}{\text{NA}}. \quad (2.20)$$

This equation is often written as a general resolution criterion in paraxial approximation, taking into account the exact definition of resolution, the influence of different illumination, and other RETs (see Section 2.4), as

$$p_{\min} = k_1 \frac{\lambda}{\text{NA}} \quad (2.21)$$

with k_1 being a process-related factor that summarizes all these additional aspects. Using PSMs, the theoretical lower limit for k_1 is 0.5 using two-beam illumination [28, 50], with typical values for illumination under normal incidence of ~ 0.7 [57]. The main message is the following: an improvement in the resolution (smaller feature size) of projection lithography requires a wavelength reduction and/or an increased NA of the imaging system, for instance using immersion lithography. Further insight is obtained from analyzing the modulation transfer function that is also a function of the spatial coherence σ . Such additional discussion is omitted here for the sake of brevity.

For completeness, we also introduce the DOF, i.e., the deviation from an optimal focus that still leads to acceptable results [28]

$$\text{DOF} = k_2 \frac{\lambda}{\text{NA}^2}, \quad (2.22)$$

with the dimensionless constant k_2 . Improving the resolution following Eq. (2.21) tightens the DOF. A better resolution requires that more spatial frequencies contribute to the image formation, but under defocus they deviate in phase. The DOF is an important concept in projection lithography, as it describes the maximum defocus and hence the sensitivity of the image transfer to resist thickness and variations in the wafer position. Conventional proximity lithography has no DOF, as no focus exists. However, we revisit the DOF in the context of the Talbot effect in Section 2.4.3.2.

Turning to proximity lithography, no aperture between mask and wafer restricts the spatial frequencies. Revisiting the idea of the Rayleigh criterion, we investigate how the image of an individual slit interferes with contributions that are diffracted from the remaining part of the grating [57]. In essence, this concerns the interference between the shadow image of the slit with the \pm first orders of the remaining grating, neglecting the contribution of higher orders.

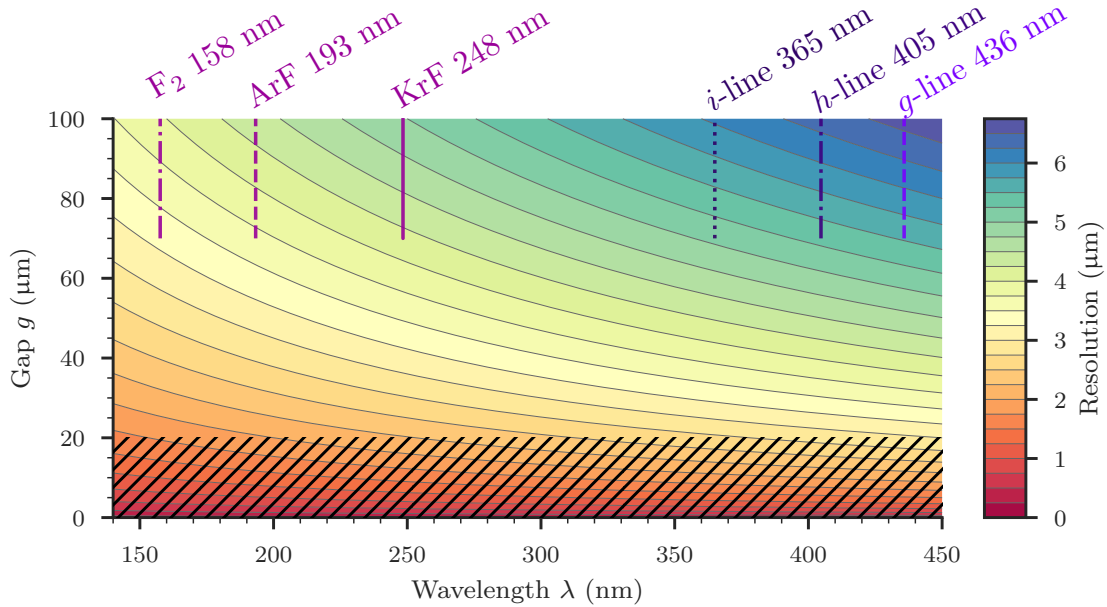


Figure 2.14: Contour plot of the resolution in mask aligner lithography, illustrating Eq. (2.26). In fabrication environments, a gap below $20\ \mu\text{m}$ (hatched area) is not used to prevent contact between mask and resist.

Hence, as a resolution criterion, we may require a minimum contrast when the first orders superpose with the shadow image after propagating across a distance g . The acceptable overlap δ in the image plane is hence

$$\delta = \frac{1}{2}p_{\min} = g \cdot \sin \theta, \quad (2.23)$$

where we used the small angle approximation

$$\sin \theta \approx \tan \theta = \frac{\delta}{g}. \quad (2.24)$$

Applying Eq. (2.19), this yields the resolution in proximity lithography for lines and spaces, that is a grating with a fill factor of 0.5 (as depicted in Fig. 4.15a), that is

$$p_{\min} = k_3 \sqrt{g \cdot \lambda} \quad (2.25)$$

with $k_3 = \sqrt{2}$ [57]. Since k_3 depends in general on the definition of the minimum contrast criterion and on process parameters, similar to k_1 in projection lithography, it is often approximated as $k_3 \sim 1.6 - 2.0$ [28, 34, 45]. When assessing the resolution in optical prints, a practical approach is to discuss the minimum feature size r . In this case, $r \simeq p_{\min}/2$, and assuming $k_3 = 2$ we obtain the crucial relation

$$r \simeq \sqrt{g \cdot \lambda}. \quad (2.26)$$

Figure 2.14 shows the minimum feature size of Eq. (2.26) as a function of illumination wavelength λ and proximity gap g . Important to remember is the square-root law, both in wavelength and gap.

Up to now, in our considerations we have not taken yet into account the finite resist thickness, and hence the above derivation is valid only for a thickness well below g . For

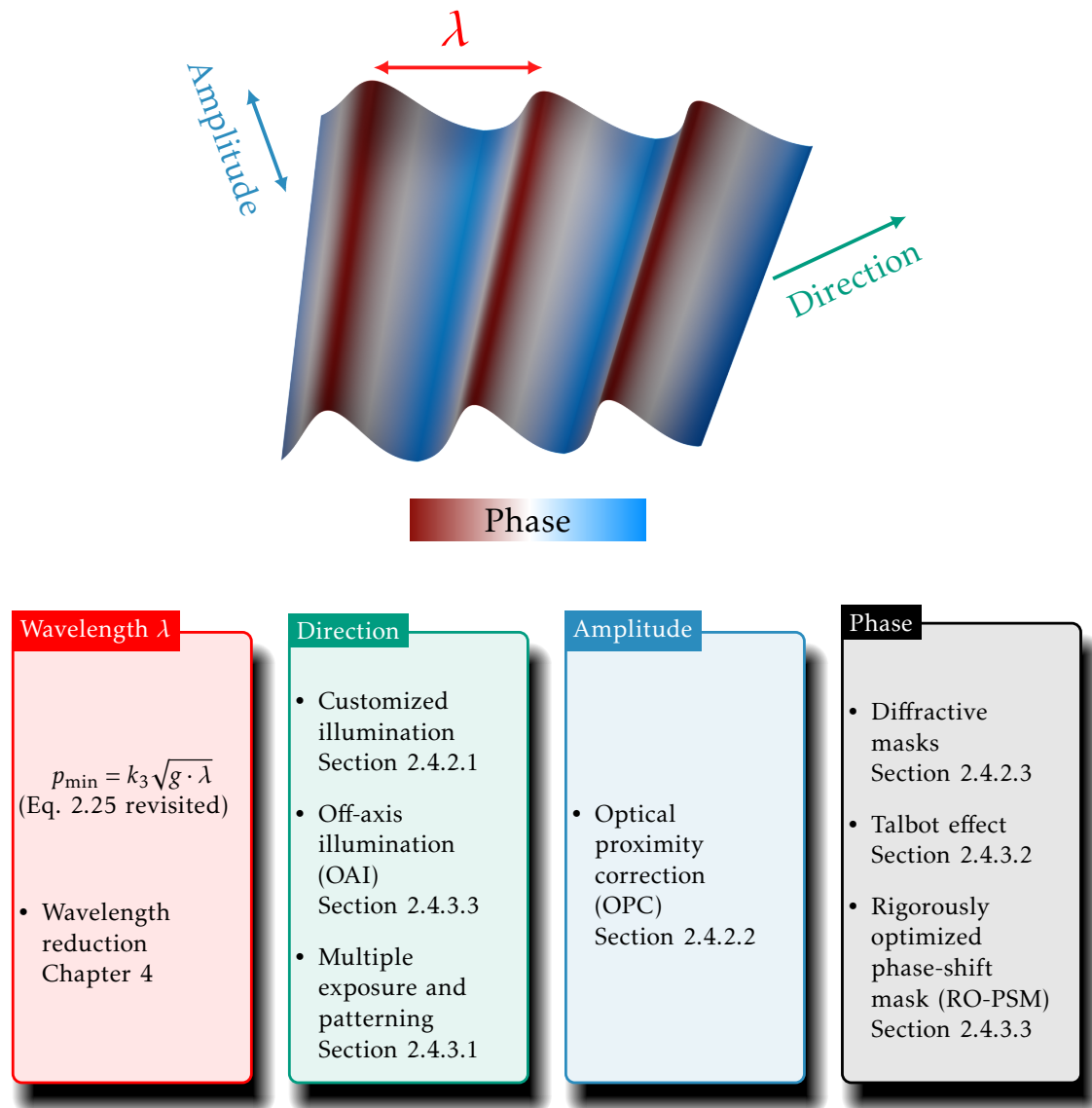


Figure 2.15: Properties of light and RETs [98]. The four different aspects wavelength, direction, amplitude, and phase are addressed in the listed sections or chapters.

completeness and without derivation, we state here the relation for a resist thickness t [97]:

$$p_{\min, \text{res}} = k_3 \sqrt{\left(g + \frac{t}{2}\right) \lambda}. \quad (2.27)$$

Comparing Eq. (2.21) and Eq. (2.25), it is obvious that the resolution enhancement by wavelength reduction is more efficient in projection lithography, as it scales linearly and not only with the square root. However, for projection printing it has the downside of reducing the DOF [see Eq. (2.22)].

Not yet taken into account in this discussion is the resist response, with additional effects as resist bleaching and diffusion, as we discussed already in Section 2.3.2.2.

2.4 Resolution enhancement techniques in optical lithography

Having revisited common knowledge on optical lithography in general and proximity lithography in specific, we review in this section established resolution enhancement

technologies (RETs) commonly used in optical nanofabrication. The idea is to shape the wavefront at the mask level in a way that counteracts the detrimental influence of diffraction on the image formation.

For reasons of clarity and comprehensibility, we divide the existing RETs into four categories, according to the fundamental properties of light waves dictating their propagation⁶: wavelength, direction, amplitude, and phase [98]. These wave properties provide the tools to shape the wavefront. In Fig. 2.15, we state the different methods and the section in which we discuss them. Following Eq. (2.25), apart from the wavelength, the RETs⁷ contribute to k_3 .

We begin with defining vital terms for understanding the computational modeling of lithographic processes. Then, we proceed with introducing RETs, first for non-periodic (arbitrary) nanostructures, and then for spatially periodic nanostructures. Please keep in mind that some concepts are rather general and used for both non-periodic and periodic patterns. Furthermore, the scope of such approaches is broader than only resolution enhancement, for instance when aiming at diminishing the impact of process variations. The most important parameters in mask aligner lithography responsible for process variations are the exposure dose and the proximity gap. The parameter range that attains satisfying results, also with regard to the yield in production, is called the process window [83].

2.4.1 Computational lithographic modeling

For modeling the optics in proximity lithography, we have to consider the stack of materials involved in light propagation: The photomask, the air gap between mask and wafer, one or several layers of photoresist, and the substrate. In addition, the resist might change its optical properties upon exposure, as discussed in Section 2.3.2.2. When simulating the pattern, different levels of complexity can be considered in the simulation [34]:

- The *aerial image* describes the field distribution upon propagation in air, incident on the air/resist interface. It neglects any interaction with the photoresist or any reflections.
- Multiple reflections arising from all the interfaces are considered in the *refracted and reflected image*, solving Maxwell's equations subject to boundary conditions at the interfaces.
- The next level of sophistication is the *latent image*, which describes the effect of the exposure on the resist. To obtain the latent image, one takes the aerial or the reflected image and converts it to the relative PAC concentration $m(\mathbf{r})$ in the resist [compare Section 2.3.2.2 and Eq. (2.13)]. The refractive index of the resist changes as a function of exposure dose, mainly as a result of bleaching or dying (see Section 2.3.2.2 for a detailed discussion).
- The local PAC concentration can be translated into a *dissolution rate image*, describing the dissolution rate as a function of the exposure dose.
- Ultimately, the *resist image* can be calculated, taking into account the latent image and the effect of the developer, resulting in the final resist shape. The process of development starts at the resist surface, and removes resist as it advances deeper into the resist. The local development rate adjusts according to the dissolution rate. Some approaches to describe the developing process are discussed in [28].

⁶The fifth property, polarization, is not discussed here, as we rely on a scalar description of wave propagation.

⁷One has to keep in mind that improving k_3 in Eq. (2.25) regularly increases the complexity of the photomask, which can lead to an increased density of errors in the mask.

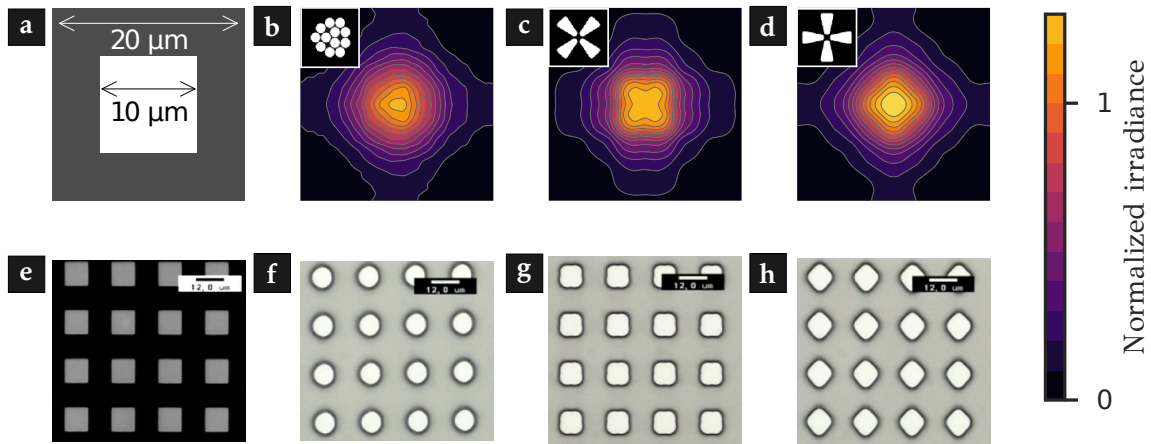


Figure 2.16: Customized illumination using MOEO[®]. Simulation results (top row) are compared to experimental prints (bottom row).

a Design of one unit cell, containing a square opening (white).

b - d Simulated aerial images for a square shape, using the IFP shown in the inset. The proximity gap is 100 μm , and the selected illumination spectrum corresponds to the mercury arc lamp.

e Scanning electron microscope (SEM) micrograph of the binary intensity mask. The colors in this micrograph are inverted to correspond to the schematic in **a**.

f - h SEM images of experimental prints in 1.2 μm thick photoresist. Just by choosing a suitable IFP, the pattern can be adapted to the specific requirements: Using an identical photomask, either circles, squares, or squares rotated by 45° are printed.

SEM images reprinted with permission from [55].

Depending on the application, a different level of sophistication is required. For thin resists, with a thickness of about one absorption length (approximately 1 μm), typically the aerial image is sufficient to accurately estimate the final binary resist shape. For thicker resists, the impact of absorption on the latent image is more severe, and the full resist image is required.

2.4.2 Non-periodic nanostructures

First, we consider RETs for non-periodic nanostructures, i.e., arbitrary patterns which do not adhere to a specific design. Following Fig. 2.13a, the resolution of such a pattern should only depend on how well we can meet the threshold criterion for the pattern under investigation. A necessary assumption is that individual structures are isolated, i.e., they are not influenced by adjacent patterns.

In reality, however, we look for solutions that can be applied to arbitrary structures. We introduce three concepts here, relevant for the research presented in subsequent chapters: (i) customized illumination, that relies on an adjustable angular spectrum, (ii) optical proximity correction, using sub-resolution features to increase pattern fidelity, and (iii) diffractive solutions such as holograms.

2.4.2.1 Customized illumination

MOEO[®], as discussed in Section 2.3.1, allows to shape the illumination angles at will. The combination of pattern shape and illumination configuration can be used to modify the printed structure, especially at large proximity gaps. Coherent areas in the IFP create individual plane waves. Their tilt corresponds to the location within the IFP. These plane waves propagate to the photomask and are modified by the mask pattern. The

superposition of all these plane waves in the wafer plane provides the aerial image [55]. By selectively blocking individual plane waves, the aerial image is subject to modifications.

An impressive example is provided in [55]: Here, squares with a side length of $10\ \mu\text{m}$ are printed using different IFPs. This leads to patterns with shapes reminiscent of circles, squares, and squares rotated by 45° (see Fig. 2.16). The pattern fidelity can hence be increased by tweaking the illumination angles to the pattern, often summarized under the term source-mask optimization (SMO). This requires to connect the illumination source and the pattern, for instance via simulation.

Choosing the correct IFP, i.e., selecting the angles of plane waves illuminating the photomask, can help to increase the process window [83] and can even be combined with optical proximity correction (OPC) methods, which are discussed in the following Section 2.4.2.2 and in Chapter 6.

A special case of customized illumination is off-axis illumination (OAI), which is commonly applied to PSMs used to fabricate periodic structures. We discuss the adaption of OAI to mask aligner lithography in Section 2.4.3.3.

2.4.2.2 Optical proximity correction

OPC summarizes techniques related to the pre-compensation of the mask pattern, to shape the wavefront with the purpose of counteracting the diffraction introduced by the free space propagation over the gap. Numerous image shape distortions can be identified, dealing for instance with the proximity of adjacent features, line-end shortening, and corner rounding in two dimensions (compare Fig. 2.3) [50].

The so-called proximity effect describes the effect of variations in the CD by the environment. Remember the discussion revolving around Fig. 2.13: It is a major difference whether the feature is isolated or an adjacent feature contributes via diffraction to the latent image. Proximity effects are not uniquely found in optical lithography, but rather common in nanofabrication, as emerging for instance in e-beam lithography, in dry and wet etching, and for chemical-mechanical polishing [34].

There are numerous approaches conceivable on how to pre-compensate the mask patterns. For line-end shortening, there are several ways to add assist features, as depicted exemplarily in Fig. 2.17a. Pre-lengthening the structures or adding hammerhead, serif, or assist bar structures allows to sustain the desired length and linewidth. The oldest trick in the book to address corner rounding is the addition of serifs (see Fig. 2.17b), used already by the Romans to enhance the visibility of texts inscribed into stone [99]. Kodak applied serifs to rubyolith masks in 1963, similar to the wedge OPC depicted in Fig. 2.17b [98, 100].

But the underlying question remains: In which way does the pattern have to be pre-compensated, or how does the wavefront have to be shaped? Saleh and coworkers developed the foundations of OPC in the early 1980s for projection lithography [101–103]. Their approach considered the simulation of the imaging system and the resist response, predicting the aerial image in a simple threshold model. The transfer function used for propagation was called *image synthesis*, consisting of a Fast Fourier Transform (FFT), a low-pass filter on the spatial frequencies, and an inverse FFT.

During the development of OPC methods, two main approaches emerged: *model-based* and *rule-based* OPC. The model-based approach follows the idea by Saleh and coworkers. Using transfer functions and resist models to account for the optical system and the resist response, respectively, most of the effects influencing the resist image are taken into account [101, 103]. The forward model-based optimization aims to iteratively improve the mask design by moving the edges of the pattern. As a figure of merit (FOM), one

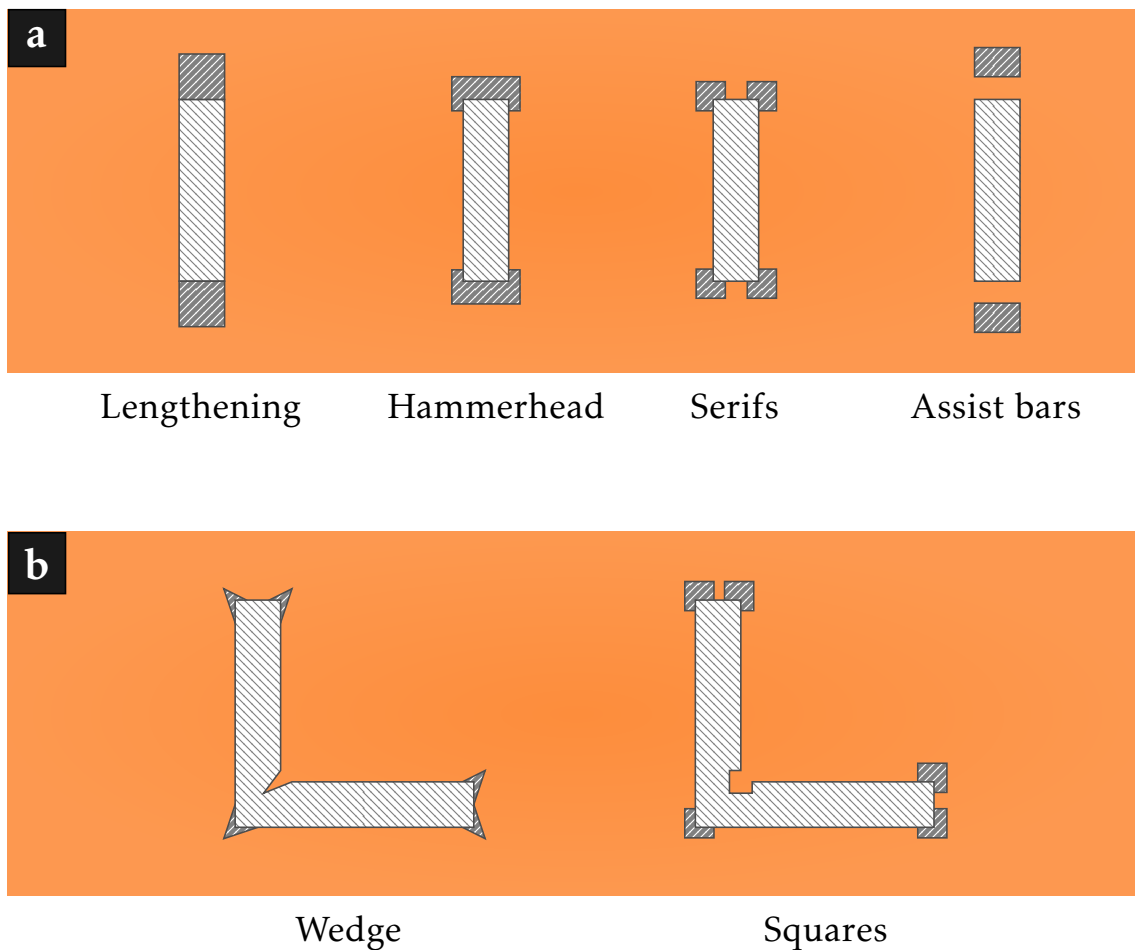


Figure 2.17: OPC approaches to **a** line-end shortening and **b** corner rounding. The opaque chromium mask is shown in orange, the transparent region in hashed white, and the additional transparent OPC structures in hashed gray.

simple approach is to take the difference between desired and achieved resist image. The backward model starts at the desired pattern and uses back-propagation to obtain the mask layout [34, 50, 104].

For rule-based OPC, a set of rules is determined for shapes occurring in the mask design, both one- and two-dimensional. Such - often experimentally obtained - rules are stored in lookup table. Rule-based OPC is not as generally applicable as model-based OPC, and is often restricted to isolated patterns. Commonly, the set of rules is restricted to so-called Manhattan geometries: all shapes are rectangles, and all edges are either in a horizontal or in a vertical orientation [105].

Motzek *et al.* revised OPC for mask aligner lithography, demonstrating simulation [106] and optimization algorithms [107], also in combination with SMO [108, 109]. Weichelt *et al.* extended the concept to PSMs and elbow patterns [56]. Puthankovilakam *et al.* introduced a rule-based correction approach for corner rounding in right angle geometries [110].

It is clear from our discussion in Section 2.3.3 that the minimum feature size cannot improve by applying OPC [45]. However, the positive impact on pattern fidelity and process window has been demonstrated [108, 111]. We present a hybrid approach in Chapter 6, combining both model-based and rule-based OPC for addressing the issue of corner rounding in mask aligner lithography. This is especially interesting for non-

Manhattan geometries.

2.4.2.3 Diffractive solutions

Up to now, we considered only modifying the nature of light in a binary fashion: either completely blocking or completely transmitting the exposure light, and/or introducing a phase shift of π . Naturally, this limits the possibilities to shape the wavefront emerging from the photomask, as the most general case requires complete control over the complex field.

Imagine a photomask that gives an arbitrary control over the wavefront on mask level: It opens the possibility to take the desired pattern on the wafer level and back-propagate the field to the mask, essentially creating a computer-generated hologram (CGH). This requires in general a complex field, spatially varying in amplitude and phase. Such complex transmission patterns require multilevel PSMs combined with a continuous amplitude modulation.

The canonical approach to fabricate multilevel PSMs is the following: Starting from a flat surface, the different phase levels are integrated using a combination of lithography and etch steps. Important aspects here are the overlay accuracy of the succession of fabrication steps and the precision in the etch depth. As a consequence, a quasi-continuous phase progression would require a high number of fabrication steps. Overlay or etch depth errors might occur which result in a degradation of the performance. In practice, for these reasons the number of phase levels in mask aligner lithography is limited to a set of discrete values. We present an alternative approach for continuous phase levels based on optical metasurfaces in Chapter 7.

One approach to obtain the holographic mask design is an iterative Fourier transform algorithm (IFTA), also called the Gerchberg-Saxton algorithm [112], combined with field quantization [113–115] (see Section 7.3). Several groups applied the concept of holographic lithography to mask aligner lithography. Bühling and coworkers resolved a 3 μm lines and spaces pattern at a proximity gap of 50 μm , using four phase and two amplitude levels [116]. Neto *et al.* [117] and Cirino *et al.* [87] demonstrated an improved performance, with diamond like carbon and amorphous hydrogenated carbon thin films for the amplitude modulation. Weichelt *et al.* implemented a photomask with binary control of phase and amplitude, using a chromium layer on a two-level PSM at a proximity gap of 30 μm [56]. They achieved a linewidth of 1.5 μm for non-periodic lines and spaces and 2 μm for an elbow pattern. Further improvement clearly requires more phase and/or amplitude levels, rendering mask fabrication more costly.

The expensive fabrication prevents the use of sophisticated PSMs in modern mask aligner lithography [45]. In Chapter 7, we will introduce a related approach, relying on metasurfaces (MSs) to shape the wavefront on the mask level.

2.4.3 Periodic nanostructures

A variety of optical applications require periodic nanostructures, for instance gratings or metamaterials. Both for design and for fabrication it can be sufficient to consider and optimize one unit cell of the mask pattern, and replicate this unit cell over the entire device size. The following methods apply to at least locally periodic structures.

2.4.3.1 Multiple exposure and patterning

The underlying idea of multiple exposure and patterning is simply to subdivide the entire lithographic process into several steps. Multiple exposure steps on one wafer can be

used either on the same resist or adding a resist layer in between [96]. For the sake of an example, let us assume we want to pattern a periodic grating with a period of $1\ \mu\text{m}$ and a linewidth of $0.5\ \mu\text{m}$. Instead of performing the exposure in one step with a mask with exactly these dimensions, we might use a mask with twice the period, shift the mask after a first exposure laterally by $1\ \mu\text{m}$, and expose once more. The aerial image is the sum of each exposure step. This double exposure relaxes the constraints on the photomask, and allows to adapt the illumination conditions separately. Requirements are a high contrast in the aerial image or a nonlinear resist and a sufficient overlay accuracy between the exposure steps. The former issue can be addressed by applying an additional resist layer for the second exposure, in a litho-freeze-litho-etch process [96].

Multiple patterning, in contrast, is more conservative: In the litho-etch-litho-etch approach, the pattern is transferred to the functional layer (see Fig. 2.1) after each exposure. The obvious advantage is a higher resolution, since subsequent exposure steps do not influence each other, coming at the cost of an increased number of process steps.

A third option is to use an exposure step to create a grating at twice the desired period, and overgrow it with metal. The overgrown volume is etched away, and metal remains solely on both sidewalls of the grating. The resist is stripped, leaving only the sidewalls. Compared to the original pattern, the metal strips have twice the spatial frequency, and can be used for subsequent pattern transfer to the functional layer. Bourgin *et al.* used such self-aligned double patterning to generate features with widths of $90\ \text{nm}$ in proximity lithography with a proximity gap of $10\ \mu\text{m}$ [118, 119].

2.4.3.2 Talbot effect

So far we discussed diffraction as the governing detrimental effect in optical lithography. Under certain conditions, however, the use of diffraction can lead to a substantial improvement in the image transfer of periodic nanostructures. Imagine a plane wave diffracted by a laterally periodic grating in Fresnel regime. The interference between multiple diffraction orders leads to a self-imaging of the grating, first observed in 1836 by H. Talbot [120] and explained in 1881 by Lord Rayleigh [121]. The separation in propagation direction between subsequent self-imaging planes, one Talbot distance z_T , is a function of the lateral grating period and the wavelength of the plane wave. The Talbot field behind a periodic binary intensity mask is depicted in Fig. 2.18a.

Many fields of optics make use of and benefit from the Talbot effect [122, 123]. Worth mentioning are spatial filters in image processing [124–126], a shearing interferometer for probing phase distributions of mirrors and lenses [127], range and depth measurements [128], an array illuminator [129], self-imaging in multi-mode interference devices [130], the plasmon Talbot effect [131], and applications in quantum optics and quantum lithography [132].

J.M. Burch proposed a copying process of gratings in photoresist using the Talbot effect, avoiding contact between the master and the resist [133, 134]. The resist-coated substrate is located in one of the Talbot planes, leading to a self-replication of the (amplitude or phase-shift) structures on the photomask [135–137]. Since all diffraction orders contribute constructively in the Talbot planes, with vanishing phase differences between different orders, a considerable improvement over conventional mask aligner lithography (see Section 2.4.2) is possible. Crucially, such an agreement in the absolute phase is only possible within the validity of the Fresnel approximation. Otherwise, phase errors in large diffraction orders introduce distortions [138].

The depth of focus (DOF) denotes the length scale in propagation direction over which high contrast image transfer is possible. This quantity allows to estimate the required

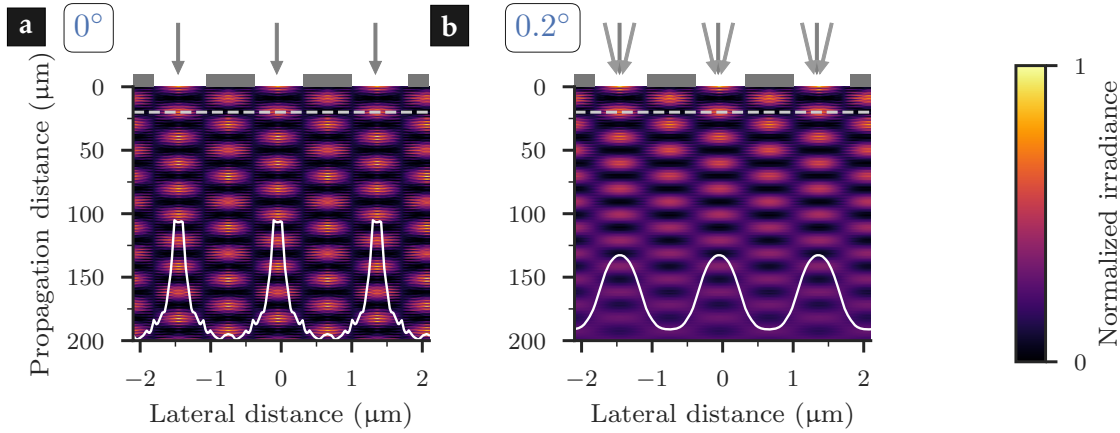


Figure 2.18: Simulation of the aerial image along the propagation direction, illustrating the Talbot effect at 193 nm, for **a** plane wave illumination under normal incidence and **b** illuminated with plane waves under an angular spectrum equally distributed between $\pm 0.2^\circ$.

accuracy for placing the resist-coated wafer in one Talbot plane. We discuss techniques to increase the DOF in optical lithography in Section 2.4.3.3.

Within the realm of Talbot lithography, several extensions have been reported on. Solak *et al.* introduced displacement Talbot lithography (DTL) [139–141]: By varying the gap between mask and wafer during exposure, the Talbot field is integrated over one or several Talbot distances. DTL no longer requires a precise placement exactly in one Talbot plane, but rather mechanical stability and reduced contrast of the integrated aerial image. Combining the vertical movement with lateral translation or rotation, complex patterns can be created from simple mask structures [142]. Further approaches introduce immersion [143], EUV [144], and gray-scale Talbot lithography [145].

In the following, we develop the theory of Talbot lithography in scalar approximation, leading to expressions for the Talbot distance and the DOF valid in the Fresnel regime. While we discuss here the Talbot effect for laterally periodic structures only, the more general condition for self-imaging have been derived by Montgomery [146].

We commence with the complex field distribution $p(\mathbf{r})$ behind the periodic mask features in a plane parametrized by $\mathbf{r} = x\hat{e}_x + y\hat{e}_y$ with Cartesian unit vectors \hat{e}_x and \hat{e}_y . In TEA, the field distribution is given by the product of the incident field and the transmission function of the object, i.e., the amplitude and/or phase-shift mask pattern [9]. The two-dimensional periodic arrangement of unit cells, neglecting boundary effects due to a finite mask size, is parametrized by

$$\mathbf{A}_n = n_1 \mathbf{a}_1 + n_2 \mathbf{a}_2 \quad (2.28)$$

with the basis vectors \mathbf{a}_1 and \mathbf{a}_2 and integers n_1 and n_2 . From the periodicity of the object, $p(\mathbf{r}) = p(\mathbf{r} + \mathbf{A}_n)$, follows the lateral periodicity of the field behind the object in TEA. The set $\{\mathbf{A}_n\}$ spans the space of the object, with pairs $\mathbf{n} = (n_1, n_2)$. Likewise, the reciprocal lattice vectors \mathbf{b}_1 and \mathbf{b}_2 are defined via $\mathbf{a}_i \cdot \mathbf{b}_j = \delta_{ij}$ with Kronecker delta δ_{ij} .

Furthermore, we introduce the reciprocal lattice as

$$\mathbf{B}_n = n_1 \mathbf{b}_1 + n_2 \mathbf{b}_2. \quad (2.29)$$

To analyze the propagation of the field behind a periodic object, it is convenient to consider the two-dimensional Fourier coefficients P_n . Assuming plane wave illumination under

normal incidence, we define the field as

$$p(\mathbf{r}) = \sum_{\mathbf{n}} P_{\mathbf{n}} \exp(2\pi i \mathbf{r} \cdot \mathbf{B}_{\mathbf{n}}). \quad (2.30)$$

For wave propagation at a distance z behind the mask, we require a transfer function $H(|\mathbf{B}_{\mathbf{n}}|, z)$. In the angular spectrum method (ASM) for plane waves, the transfer function is given as [61, 147]

$$H(|\mathbf{B}_{\mathbf{n}}|, z) = \begin{cases} \exp\left(i2\pi \frac{z}{\lambda} \sqrt{1 - (\lambda |\mathbf{B}_{\mathbf{n}}|)^2}\right), & |\mathbf{B}_{\mathbf{n}}| < \frac{1}{\lambda} \\ 0, & |\mathbf{B}_{\mathbf{n}}| \geq \frac{1}{\lambda}. \end{cases} \quad (2.31)$$

Within the ASM, the diffracted field in an arbitrary plane behind the object, under plane wave illumination and an amplitude of unity, is retrieved from [61]

$$u_{\text{diff}}(\mathbf{r}, z) = \iint_{-\infty}^{\infty} d\mathbf{B}_{\mathbf{n}} \tilde{p}(\mathbf{B}_{\mathbf{n}}; z=0) H(|\mathbf{B}_{\mathbf{n}}|, z) \exp(2\pi i \mathbf{r} \cdot \mathbf{B}_{\mathbf{n}}), \quad (2.32)$$

with the Fourier transform of the transmitted field

$$\begin{aligned} \tilde{p}(\mathbf{B}_{\mathbf{n}}; z=0) &= \iint_{-\infty}^{\infty} d\mathbf{r} p(\mathbf{r}) \exp(-2\pi i \mathbf{r} \cdot \mathbf{B}'_{\mathbf{n}}) \\ &= \sum_{\mathbf{n}} P_{\mathbf{n}} \delta(\mathbf{B}_{\mathbf{n}} - \mathbf{B}'_{\mathbf{n}}), \end{aligned} \quad (2.33)$$

using Eq. (2.30). To retrieve the Talbot distance, and hence the condition for self-imaging, let us have a closer look at Eq. (2.32): A reproduction of the original field directly behind the object takes place in a certain plane $z = z_{\text{T}}$, if the phase difference between the zeroth order and all other diffracted orders vanishes, with the result that

$$\exp\left(2\pi i \frac{z_{\text{T}}}{\lambda} - 2\pi i \frac{z_{\text{T}}}{\lambda} \sqrt{1 - (\lambda |\mathbf{B}_{\mathbf{n}}|)^2}\right) \stackrel{!}{=} 1. \quad (2.34)$$

It follows for the Talbot distance

$$z_{\text{T}} = \frac{m \cdot \lambda}{1 - \sqrt{1 - (\lambda |\mathbf{B}_{\mathbf{n}}|)^2}} \quad m \in \mathbb{N} \quad (2.35)$$

with the Talbot order m . Assuming a pattern that is arranged in a quadratic unit cell with a period of Λ along \mathbf{a}_1 and \mathbf{a}_2 , leads to $|\mathbf{B}_{\mathbf{n}}| = 1/\Lambda$. For the fundamental Talbot plane $m = 1$, it follows

$$z_{\text{T}} = \frac{\lambda}{1 - \sqrt{1 - \left(\frac{\lambda}{\Lambda}\right)^2}}, \quad (2.36)$$

a result already derived by Lord Rayleigh along a different way [121]. Equation (2.36) is plotted in Fig. 2.19 as a function of the wavelength and period.

In many applications, the period Λ is much larger than the wavelength, $\Lambda = 1/|\mathbf{b}_{\mathbf{n}}| \gg \lambda$. This allows to approximate Eq. (2.36) using the binomial expansion

$$\sqrt{1 - (\lambda |\mathbf{B}_{\mathbf{n}}|)^2} \simeq 1 - \frac{1}{2} (\lambda |\mathbf{B}_{\mathbf{n}}|)^2, \quad (2.37)$$

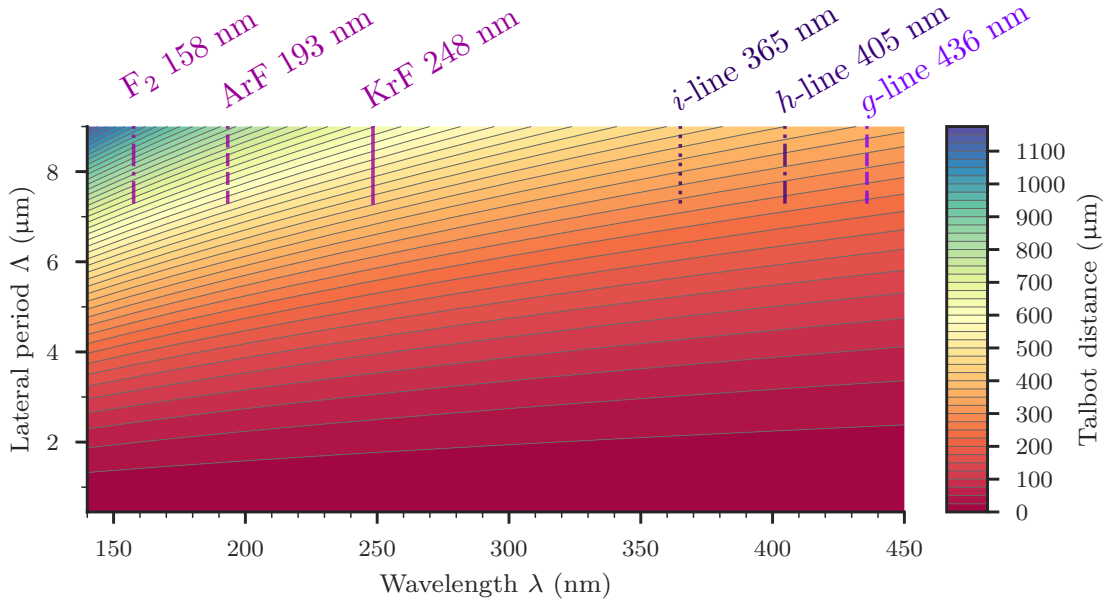


Figure 2.19: Contour plot of the Talbot distance in mask aligner lithography, following Eq. (2.36). It is obvious that for small periods $\Lambda < 2\mu\text{m}$ a proximity gap of tens of μm is required, while for periods above $5\mu\text{m}$ setting the gap is less demanding.

simplifying Eq. (2.36) to

$$z_T \approx 2m \frac{\Lambda^2}{\lambda}. \quad (2.38)$$

To show that this result is equal to the Fresnel approximation, we apply Eq. (2.37) to the transfer function Eq. (2.31) and repeat the calculations of Eqs. (2.32) to (2.35), resulting again in Eq. (2.38). Large errors emerge when applying Eq. (2.38) to periods approaching the wavelength of illumination [148]. For this reason, we restrict the use of Eq. (2.38) to discuss the DOF, and rely on the more accurate expression Eq. (2.36) for all calculations connected with the Talbot effect.

To obtain the DOF in Talbot lithography, we rely on its definition in projection lithography [137, 149, 150]. For a given NA of the optical system, the DOF is [compare Eq. (2.22)]

$$\text{DOF} \approx \pm \frac{\lambda}{2(\text{NA})^2} = \pm \frac{\lambda}{2(n \cdot \sin \theta)^2}. \quad (2.39)$$

The angle θ denotes the maximum half-angle leaving the front lens and n indicates the refractive index of the immersion medium (in our case air, $n \simeq 1$). In proximity lithography, governed by diffraction, no optics exists that limits the half-angle. θ rather corresponds to the maximum diffraction angle. Using the Rayleigh criterion for a single slit, $\sin \theta = \lambda/(n \cdot \Lambda)$, and the DOF reads as

$$\text{DOF} \approx \pm \frac{\lambda}{2(\sin \theta)^2} = \pm \frac{\Lambda^2}{2\lambda}. \quad (2.40)$$

Using Eq. (2.36), we finally obtain

$$\text{DOF} \approx \pm \frac{\Lambda^2}{2\lambda} = \pm \frac{z_T}{4}. \quad (2.41)$$

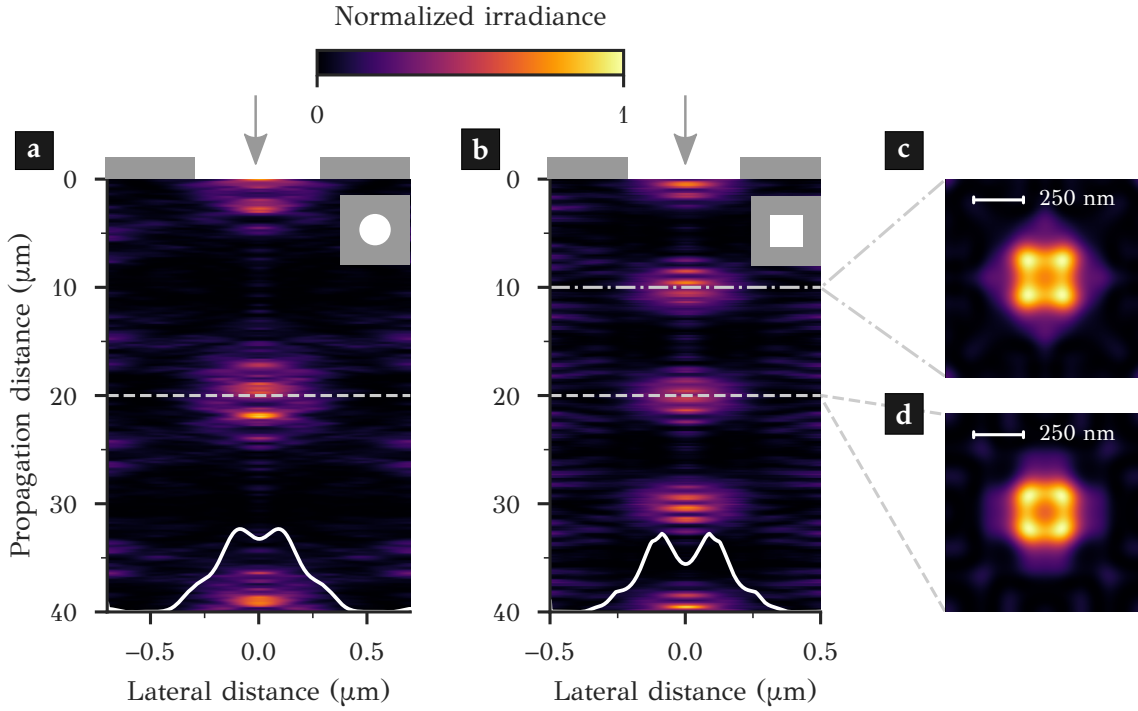


Figure 2.20: Simulation of the aerial image distribution in propagation direction for Talbot structures, for **a** a circular structure in the unit cell for $z_T = 20\mu\text{m}$ and **b** a square-shaped structure for $z_T = 10\mu\text{m}$.

The irradiance distribution for the square structures is depicted in **c** for the first and **d** for the second Talbot plane, at $10\mu\text{m}$ (dash-dotted line in **b**) and $20\mu\text{m}$ (dashed line), respectively. The simulations demonstrate the good replication of the mask structures, at least under normal incidence plane wave illumination.

For completeness, we also give the expression valid for a hexagonal pattern [151]:

$$z_{T,\text{hex}} \approx 3m \frac{a^2}{2\lambda} \quad (2.42)$$

with a the period of the hexagonal array and the basis vectors $\mathbf{a}_1 = \hat{e}_x$ and $\mathbf{a}_2 = (a/2)\hat{e}_x + (\sqrt{3}a/2)\hat{e}_y$. $\hat{e}_{x,y}$ are unit vectors in the rectangular unit cell.

In addition, let us consider the condition for self-imaging in Eq. (2.34) once more. If we allow for a phase shift of π between the zeroth order and the diffracted orders, we end up at half the fundamental Talbot distance. As a consequence, in real space, the pattern is shifted in lateral direction by half the period, $\Lambda/2$, with the image otherwise unaffected. For hexagonal patterns, the intermediate planes are shifted by one period relatively to the mask pattern, and hence the pattern is self-imaged without observable lateral shift.

The story does not end here: In addition, fractional Talbot planes exist at regular fractions of z_T , between planes defined by Eq. (2.35). However, the DOF is strongly reduced compared to regular Talbot planes. Using a metasurface, even arbitrary fractions can be obtained [152]. For practical reasons, we refrain from exploiting the fractional Talbot effect: the low DOF renders wafer placement highly delicate, and the contrast degrades strongly under non-perfect plane wave illumination compared to integer Talbot planes.

The resolution that is achievable in Talbot lithography depends strongly on how well the aforementioned assumptions are met. Plane wave illumination corresponds to a high spatial and temporal coherence of the light source, and leads to features with a high contrast, as shown in Fig. 2.18a.

A reduced spatial coherence diminishes the contrast, as illustrated in Fig. 2.18b for a homogeneous angular spectrum with a maximum half-angle of 0.2° . Different spectral components of the light source lead to Talbot planes located in separate planes. Only a limited number of diffraction orders contribute to the image formation. The propagation over the Talbot distance leads to a 'walk-off' away from the zeroth order.

Errors in the periodicity can be divided into two categories: The absence of (several) elements, and deviations in the period. Since only periodically arranged structures contribute to the self-imaging process, both cases lead to additional background noise in the vicinity of the error [122].

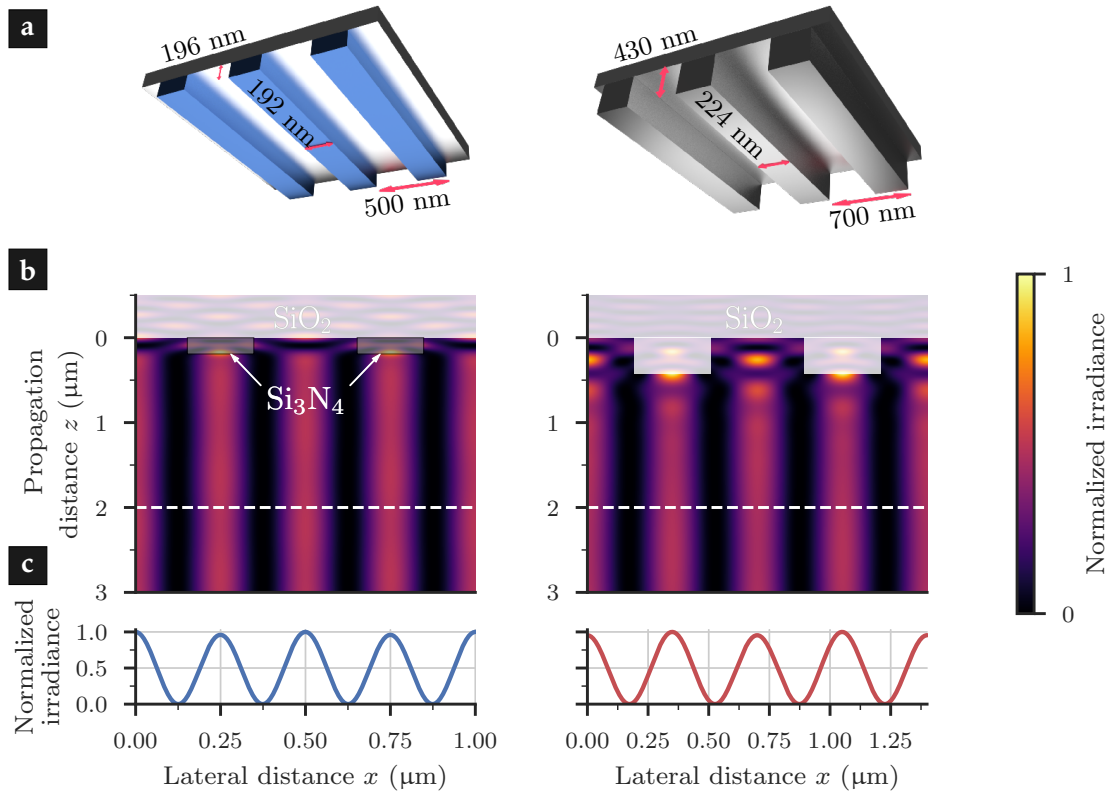


Figure 2.21: Principle of rigorously optimized phase-shift masks (RO-PSMs), for a high-index Si_3N_4 (left) and low-index SiO_2 (right) grating under *i*-line plane wave illumination and normal incidence. The design follows [153, 154].

a Sketch of the rigorously optimized phase-shift mask (RO-PSM), with the crucial dimensions grating period, width, and height annotated. The structure is invariant along the grating direction.

b Fourier modal method (FMM) simulation of light propagation behind the photomask. For high and low index gratings, the high DOF is clearly visible. The free-space propagation is simulated over a distance of $3\ \mu\text{m}$.

c Field intensity along the white dashed line shows the complete suppression of the zeroth order, resulting in a high contrast which can be used for printing.

2.4.3.3 Rigorously optimized phase-shift masks

Having established the principles of PSMs and of the Talbot effect in Sections 2.3.2.1 and 2.4.3.2, respectively, we turn our attention to RO-PSMs. They aim to combine the benefits of both worlds, hence using the high DOF of PSMs and the high resolution of self-imaging [45]. The term *rigorous* reveals already the line of action: One takes the

desired aerial image and extracts the amplitude. The phase distribution is at first arbitrary, and thus can be chosen to maximize the DOF.

By rigorous methods, this complex field distribution is back-propagated to the mask plane. The remaining step, and hence the actual challenge, is to design a suitable PSM or combined amplitude and PSM realizing the back-propagated complex field. The propagation distance is not necessarily a Talbot distance of the periodic structure (compare Section 2.4.3.2). RO-PSMs promise a strong improvement in terms of the contrast in the aerial image as well as the DOF over conventional Talbot and DTL [45]. Rigorous Maxwell solvers are required to calculate and optimize the design periodic in one or two dimensions⁸.

For high-resolution phase-shift lithography, the grating period is typically between one and two wavelengths, corresponding to three propagating diffraction orders in transmission. The interference between the ± 1 st diffraction orders leads to a sinusoidal modulation of the field distribution with a period corresponding to half the grating period, as indicated in Fig. 2.12b. The zeroth order, however, contributes to the field distribution as well, introducing an additional modulation with the period of the photomask [153].

Early work on PSMs used oblique incidence and the interference between the zeroth and the first orders [155–157] to prevent the extra modulation. Such an off-axis illumination (OAI) has later been adapted to projection lithography, both for binary intensity masks and PSMs [158, 159]. In projection lithography, the resolution is fundamentally limited by the spatial frequencies transmitted by the projection optics, as discussed in Section 2.3.3. For the best resolution (smallest period), only the zeroth and \pm first orders are propagating through the optical system, with a cut-off spatial frequency f_{cut} . Under oblique incidence, the illumination angle can be chosen such that the zeroth and the +first orders are symmetric with respect to the optical axis. As a result, the spatial frequencies shift (compare Fig. 2.12b): the +first order away from f_{cut} , while the –first order is cut off. Hence, smaller features (with larger spatial frequencies) can be imaged, until the cut-off is reached [34].

Until now, we were mainly concerned with one-dimensional gratings. When extending the concept to two-dimensional geometries, different illumination schemes are conceivable, for example ring illumination, dipole and quadrupole illumination, and many more. Each scheme will work well for a corresponding pattern, for example vertically oriented features for a horizontal dipole illumination, but worse for horizontally oriented features. For this example, the mask can be split in two, subsequently illuminated with horizontal and vertical dipoles in double-dipole illumination [34].

OAI is widely used in projection lithography, but has the disadvantage that the illumination angles have to be adapted to the structure under consideration, which precludes for instance the printing of patterns with different periods at once. An alternative approach is to consider normal incidence only and design the PSM in a way to cancel the zeroth diffraction order by interference. Hill *et al.* proposed RO-PSMs for the fabrication of fiber Bragg gratings [160], with less than 5% optical power in the zeroth order. Furthermore, Gamet *et al.* suggested to use the mode interplay in binary gratings to achieve zeroth order cancellation [161]. A grating with a period slightly larger than the wavelength can be designed in a way that leaves only the ± 1 st order propagating under normal incidence. RO-PSMs were successfully applied in proximity lithography to the fabrication of binary and blazed gratings, down to a period of 250 nm and a strongly reduced zeroth order [153, 162].

⁸We give a short introduction to one rigorous approach, the FMM, in Section 3.2.

The left column of Fig. 2.21 shows the performance of the high-index grating proposed by Bourgin *et al.*, with an almost invariant field distribution over the proximity gap [153]. This concept has been extended to monolithic SiO₂ RO-PSMs [154, 163], as depicted in the right column of Fig. 2.21.

Using MOEO[®], the illumination angles provide a further degree of freedom to shape the aerial image [164, 165] (see Section 2.4.2.1). The incoherent superposition of a RO-PSM, illuminated by discrete and individual plane waves, can be used to further reduce the period in proximity lithography. Following the Hopkins diffraction model [149], different illumination angles correspond to a lateral shift of the aerial image. By adapting the angular spectrum, this allows to shift the desired pattern by a fraction of the period. We will pick up this concept in Chapter 5 for creating a hexagonal dot pattern, where the period printed on the wafer is only a third of the mask period.

This chapter introduced the basics of optical lithography, with the emphasis on mask aligners. We discussed the optical setup, the limitations imposed by diffraction, and reviewed established methods for achieving an improvement in the printed resolution, focusing on high-volume fabrication in proximity mode. Several concepts, as OPC and the Talbot effect, will be taken up in subsequent chapters. While concentrating here on the main topic of this thesis, optical lithography in mask aligners, we provide a short summary of other nanolithographic techniques in the Appendix B. We continue in the following Chapter 3 with introducing concepts and simulation methods, used for validating and optimizing the approaches for resolution enhancement in mask aligner lithography.

Theoretical and computational tools

Throughout this thesis, we rely on electromagnetic simulations of light propagation to obtain a digital representation of the lithographic setup. An accurate representation of the light distribution is the foundation for resolution enhancement in mask aligner photolithography. Depending on the required degree of accuracy and the complexity of the photomask, simplifying assumptions are possible to keep the computational efforts within acceptable bounds while assuring the necessary predictive power to assess the liability of a specific approach. In this chapter, we introduce the theoretical framework and technical details of each method and discuss the validity in photomask and optical system simulation.

The task at hand is to solve Maxwell's equations numerically on different length scales: The smallest features we want to simulate are photomask patterns with a minimum feature size in the order of one wavelength, the largest features are macroscopic optical elements (for example microlens arrays and diffusers) that are tens of millimeters in diameter. In addition, the required degree of accuracy varies, which allows to introduce approximations that reduce the computational efforts in terms of the required memory and the CPU time.

Throughout this thesis, we apply in essence four different simulation methods to solve the equations governing light propagation. In this chapter we introduce the necessary theoretical background to understand the methods and to elaborate on their limitations. First, we derive the Helmholtz wave equation from Maxwell's equations, and proceed by introducing the four methods in decreasing order of accuracy they provide. The Fourier modal method (FMM) allows for the rigorous simulation of periodic nanostructures. The angular spectrum method (ASM) and the Rayleigh-Sommerfeld diffraction integral enable to calculate the field propagation in a homogeneous medium. Finally, we shortly discuss ray tracing as the canonical method to simulate macroscopic optical systems used for beam shaping.

By no means this selection of optical simulation methods is complete or exclusive. Alternatives include for example finite element methods [166, 167], finite difference methods in time [168, 169] or frequency domain [170], differential methods [171, 172], or integral methods [173]. In addition, we need to mention that the simulation of projection photolithography, which deals with partially coherent imaging optics, requires additional concepts which are beyond the scope of this work [28].

3.1 Introduction to optical simulation methods

We start with the simplest case of monochromatic fields with an angular frequency ω , which is already a good approximation for usual light sources in photolithography (see Section 2.3.1). For time-harmonic electric fields, the field evolution can be written as

$$\mathbf{E}(\mathbf{r}, t) = \tilde{\mathbf{E}}(\mathbf{r}, \omega) e^{-i\omega t}. \quad (3.1)$$

Since the electric field is an observable, corresponding to a Hermitian operator, the relevant physics is contained in the real part of the field. Nevertheless, the introduction of complex fields renders the mathematical treatment more convenient to keep track of the phase evolution in time and space.

For polychromatic light, different frequencies ω contribute to the fields. A Fourier decomposition allows to write the field as the superposition of time-harmonic fields,

$$\mathbf{E}(\mathbf{r}, t) = \int_{-\infty}^{\infty} \tilde{\mathbf{E}}(\mathbf{r}, \omega) e^{-i\omega t} d\omega. \quad (3.2)$$

The Fourier decomposition justifies to consider in the following each frequency component separately, and the general solution is then given by Eq. (3.2).

Light propagation in classical optics is governed by Maxwell's equations. In the frequency domain and for a linear and nonmagnetic medium without external sources, they read as

$$\nabla \cdot [\epsilon(\mathbf{r}, \omega) \tilde{\mathbf{E}}(\mathbf{r}, \omega)] = 0 \quad (3.3)$$

$$\nabla \cdot \tilde{\mathbf{H}}(\mathbf{r}, \omega) = 0 \quad (3.4)$$

$$\nabla \times \tilde{\mathbf{E}}(\mathbf{r}, \omega) = i\omega\mu_0 \tilde{\mathbf{H}}(\mathbf{r}, \omega) \quad (3.5)$$

$$\nabla \times \tilde{\mathbf{H}}(\mathbf{r}, \omega) = -i\omega\epsilon_0 \epsilon(\mathbf{r}, \omega) \tilde{\mathbf{E}}(\mathbf{r}, \omega) \quad (3.6)$$

with the magnetic field $\tilde{\mathbf{H}}(\mathbf{r}, \omega)$, the free space permeability μ_0 and permittivity ϵ_0 , and the relative permittivity $\epsilon(\mathbf{r}, \omega)$. By applying the curl operator from the left to Eq. (3.5) and by using Eq. (3.6) and the vector identity [61]

$$\nabla \times (\nabla \times \cdot) = \nabla (\nabla \cdot \cdot) - \nabla^2 \cdot \quad (3.7)$$

for an isotropic and homogeneous material [$\nabla \cdot \epsilon(\mathbf{r}, \omega) = \nabla \cdot \epsilon(\omega) = 0$], where \cdot is a placeholder for a vector field, we obtain the vector Helmholtz wave equation in frequency domain

$$\nabla^2 \tilde{\mathbf{E}}(\mathbf{r}, \omega) + \frac{\omega^2}{c_0^2} \epsilon(\omega) \tilde{\mathbf{E}}(\mathbf{r}, \omega) = 0 \quad (3.8)$$

with $c_0 = (\epsilon_0 \mu_0)^{-1/2}$ denoting the speed of light in vacuum, with the vacuum permittivity ϵ_0 and the vacuum permeability μ_0 .

Up to now, we considered light propagation in real space made out of a homogeneous material. For the further discussion we also require an expansion into plane waves, by Fourier transforming the spatial coordinates

$$\bar{\mathbf{E}}(\mathbf{k}, \omega) = \int_{-\infty}^{\infty} \tilde{\mathbf{E}}(\mathbf{r}, \omega) e^{i\mathbf{k} \cdot \mathbf{r}} d^3k. \quad (3.9)$$

Indeed, in an homogeneous medium, an arbitrary spatially dependent electric field can always be written as a superposition of plane waves. Plugging this Fourier transformation into Eq. (3.8) leads to

$$\left(-\mathbf{k}^2(\omega) + \frac{\omega^2}{c_0^2} \epsilon(\omega) \right) \bar{\mathbf{E}}(\mathbf{k}, \omega) = 0 \quad (3.10)$$

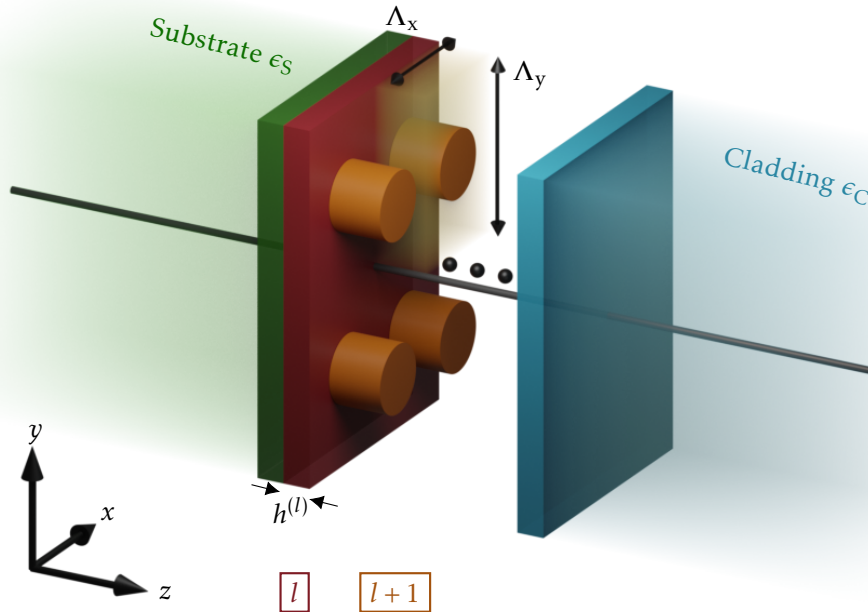


Figure 3.1: Sketch of a periodic structure composed of several layers. Light is incident from the left and propagates in the positive z -direction. The orange volume indicates one unit cell, with a period of Λ_x and Λ_y . Within each layer l , the permittivity distribution $\epsilon^{(l)}(x, y, \omega)$ is required to be invariant in z . Substrate and cladding are assumed to extend into the negative and positive half spaces in z -direction, respectively. Additional layers are implied by black dots.

Adapted from [174].

with the wavevector $\mathbf{k}(\omega)$ and the dispersion relation

$$\mathbf{k}^2(\omega) = k_x^2(\omega) + k_y^2(\omega) + k_z^2(\omega) = \frac{\omega^2}{c_0^2} \epsilon(\omega). \quad (3.11)$$

This dispersion relation is important as it expresses that not every plane wave $\mathbf{E}(\mathbf{r}, t) = \tilde{\mathbf{E}}(\mathbf{k}, \omega) \exp(i[\mathbf{k} \cdot \mathbf{r} - \omega t])$ is a solution to Maxwell's equations but only those for which the wave vector and the frequency obey the dispersion relation. While expansion in plane waves is a useful concept for the homogeneous space, it cannot be directly applied to describe light in structured photonic media. In the next section we deal with such sort of problem while restricting our consideration to periodic media.

3.2 Simulation methods for optical proximity lithography

3.2.1 The Fourier modal method to simulate periodic structures

In this section, we introduce the principles of the Fourier modal method (FMM)⁹ and outline how to calculate the transmission and reflection characteristics of layered periodic structures. In the realm of this thesis, we utilize an implementation of the FMM code that was developed by Dr. T. Paul at the Friedrich-Schiller Universität in Jena/Germany [174]. Thus, in the description of the FMM we mainly follow Ref. [174].

With the help of Fig. 3.1 we introduce some notation used throughout this section. We consider a structure with the lateral periods Λ_x and Λ_y in x - and y -direction, respectively,

⁹In a historic perspective, the FMM was introduced in grating theory by the name of *rigorous coupled-wave analysis* [175, 176]. We use the term *Fourier modal method* throughout this thesis as it captures the crucial idea of Fourier expanding all quantities.

at a single frequency¹⁰ ω . The structure can be made from multiple layers that share the same periodicity. The permittivity distribution

$$\epsilon_l(x, y) = \epsilon_l(x + p_1 \Lambda_x, y + p_2 \Lambda_y) \quad (3.12)$$

with integers p_1 and p_2 is supposed to be known and invariant within one layer l with height $h^{(l)}$ along the propagation direction z (compare Fig. 3.1). The entire layer stack separates two half spaces that are supposed to be made from homogeneous isotropic material. They are called substrate and cladding. The systems is illuminated from the substrate with a linearly polarized plane wave. The purpose is to solve for the electromagnetic field everywhere in space. Outside the periodic media the fields can be expanded into plane waves, just described in the previous section. More care needs to be spend when expanding the field inside the periodic media.

The fundamental idea is to exploit the underlying symmetry of the problem, which allows to expand the fields in each layer l of the structure into a (finite) number of waveguide modes, taking the periodic interface conditions into account. The first step is hence to (numerically or analytically) determine the eigenmodes in each layer as well as in the isotropic substrate and cladding (incident and transmitting region). Each eigenmode is a solution to the wave equation (3.10). In a second step, the unknown amplitudes of the individual modes in each spatial domain are obtained from enforcing the interface conditions among adjacent layers, i.e., the continuity of the tangential field components of $\tilde{\mathbf{E}}$ and $\tilde{\mathbf{H}}$ across the interface. The third and final step is to derive the physical quantities one is interested in, for example the reflectance, the transmittance, or the diffraction efficiencies in specific orders.

First, we consider the isotropic substrate, assumed to be an infinite half space on the illumination side (compare Fig. 3.1). We can write the incident plane wave in the spatial domain as [177]

$$\tilde{\mathbf{E}}_I(\mathbf{r}) = \mathbf{u} \exp(i\mathbf{k}_I \cdot \mathbf{r}) \quad (3.13)$$

with the polarization vector \mathbf{u} , the wavevector $\mathbf{k}_I = \alpha_0 \hat{\mathbf{e}}_x + \beta_0 \hat{\mathbf{e}}_y + r_{00} \hat{\mathbf{e}}_z$, and the unit vectors $\hat{\mathbf{e}}$. The double periodic structure of the problem leads to the emergence of discrete diffraction orders m and n in x - and y -direction. The grating simply provides an additional transverse momentum. Thus, the reflected and transmitted fields in the substrate S and the cladding C, respectively, can be expanded into plane waves

$$\tilde{\mathbf{E}}_R(\mathbf{r}) = \sum_{m,n} \mathbf{R}_{mn} \exp(i\mathbf{k}_{S_{mn}} \cdot \mathbf{r}) \quad (3.14)$$

$$\tilde{\mathbf{E}}_T(\mathbf{r}) = \sum_{m,n} \mathbf{T}_{mn} \exp(i\mathbf{k}_{C_{mn}} \cdot [\mathbf{r} - h_\Sigma \hat{\mathbf{e}}_z]) \quad (3.15)$$

with \mathbf{R}_{mn} and \mathbf{T}_{mn} the vector amplitudes of the diffraction orders in reflection and transmission, and h_Σ the total height of the layer stack. At the moment, the components of \mathbf{R}_{mn} and \mathbf{T}_{mn} are not known. For the individual diffraction orders m and n at a free-space

¹⁰In the following, we suppress ω in the argument of all variables. It is implicitly assumed that we consider a single frequency.

wavelength of λ_0 , the wavevectors read as

$$\mathbf{k}_{Smn} = \alpha_m \hat{\mathbf{e}}_x + \beta_n \hat{\mathbf{e}}_y + \gamma_{Smn} \hat{\mathbf{e}}_z \quad (3.16)$$

$$\mathbf{k}_{Cmn} = \alpha_m \hat{\mathbf{e}}_x + \beta_n \hat{\mathbf{e}}_y + \gamma_{Cmn} \hat{\mathbf{e}}_z \quad (3.17)$$

$$\text{with } \alpha_m = \alpha_0 + m \frac{2\pi}{\Lambda_x}, \quad (3.18)$$

$$\beta_n = \beta_0 + n \frac{2\pi}{\Lambda_y}, \quad (3.19)$$

$$\gamma_{S/Cmn} = \sqrt{\epsilon_{S/C} k_0^2 - \alpha_m^2 - \beta_n^2}, \quad (3.20)$$

$$\text{and } k_0 = \frac{2\pi}{\lambda_0}. \quad (3.21)$$

$\epsilon_{S/C}$ denotes the real-valued permittivity of the substrate and the cladding.

Next, we consider the structure inside the layers. The periodicity in lateral direction, Eq. (3.12), allows to apply the Floquet-Bloch theorem [177, 178],

$$\Psi^{(l)}(x + \Lambda_x, y + \Lambda_y, z) = \exp\left(i\left[\alpha_0 \Lambda_x + \beta_0 \Lambda_y\right]\right) \Psi^{(l)}(x, y, z), \quad (3.22)$$

where $\Psi^{(l)}(\mathbf{r})$ denotes one Cartesian field component in x and y of the electric or magnetic field of one Bloch periodic mode in the layer l . In essence, the Bloch theorem states that the field distribution within l is periodic as well, up to a phase term which contains the Bloch wavevector $\mathbf{k}_B = \alpha_0 \hat{\mathbf{e}}_x + \beta_0 \hat{\mathbf{e}}_y$. As the periodicity is the same for all layers and the lateral wave components are conserved at the interfaces, the Bloch vector \mathbf{k}_B is a conserved quantity through the system. Just as the total field in the homogeneous media is expanded into a series of plane waves, the total field inside the periodic region is expanded into a series of these Bloch modes.

We can now expand the field of each Bloch mode in the layer l in an infinite Fourier series [174]

$$\Psi^{(l)}(x, y, z) = \exp\left(i\gamma^{(l)}z\right) \sum_{m,n} \psi_{mn}^{(l)} \exp\left(i\left[\alpha_m x + \beta_n y\right]\right). \quad (3.23)$$

This equation can also be understood intuitively: As the structure is invariant along z within a layer l , we use the plane wave ansatz for the field evolution along that invariant coordinate. In essence, the mode only accumulates a phase delay upon propagation in z . In the two periodic dimensions, the field amplitude of the Bloch mode is periodic as well so we can expand it into a Fourier series. The Fourier coefficients that expand a given mode are not yet known.

Out of practical relevance, the numerical implementation requires the truncation of the diffraction orders m and n to maximum orders of M and N . This corresponds in total to $(2M + 1)(2N + 1)$ modes (or plane waves in case of the substrate/cladding). Up to now, the modal field coefficients $\psi_{mn}^{(l)}$ for each Bloch mode and the respective propagation constants $\gamma^{(l)}$ are unknown.

Next, we reconsider Maxwell's Eqs. (3.5) and (3.6). This set of six equations for the Cartesian components of $\tilde{\mathbf{E}}$ and $\tilde{\mathbf{H}}$ allows to eliminate \tilde{E}_z and \tilde{H}_z , which leads to four equations containing the fields $\tilde{E}_x, \tilde{E}_y, \tilde{H}_x, \tilde{H}_y$, and their spatial derivatives as well as the permittivity distribution $\epsilon^{(l)}(x, y)$ and its inverse $\left[\epsilon^{(l)}(x, y)\right]^{-1}$. Inserting Eq. (3.23) and the

Fourier expansions¹¹ [177]

$$\epsilon^{(l)}(x, y) = \sum_{q,r} \epsilon_{qr}^{(l)} \exp\left(i2\pi \left[\frac{qx}{\Lambda_x} + \frac{ry}{\Lambda_y} \right]\right) \quad (3.24)$$

$$\left[\epsilon^{(l)}(x, y)\right]^{-1} = \sum_{q,r} \zeta_{qr}^{(l)} \exp\left(i2\pi \left[\frac{qx}{\Lambda_x} + \frac{ry}{\Lambda_y} \right]\right) \quad (3.25)$$

into these four equations leads to a system of algebraic equations for $\psi_{mn}^{(l)}$. An approach to solve the resulting eigenvalue problem is described in the appendix of Ref. [177], which is skipped here for brevity.

The numerical solution results in $S = 2(2M+1)(2N+1)$ eigenmodes $\psi_{mns}^{(l)}$, identified by the index $s = 1, \dots, S$ and the corresponding propagation constants $\gamma_s^{(l)}$. Finally, this allows to express the field distribution in each layer l as the superposition of the eigenmodes [177]

$$\begin{aligned} \tilde{E}_x(x, y, z) = & \sum_{s=1}^S \left[a_s^{(l)} \exp\left(i\gamma_s^{(l)}[z - z^{(l)}]\right) + b_s^{(l)} \exp\left(-i\gamma_s^{(l)}[z - z^{(l)} - h^{(l)}]\right) \right] \\ & \cdot \sum_{m,n} \tilde{E}_{xmn}^{(l)} \exp(i[\alpha_m x + \beta_n y]) \end{aligned} \quad (3.26)$$

and similar expressions for \tilde{E}_y , \tilde{H}_x , and \tilde{H}_y . The missing components \tilde{E}_z and \tilde{H}_z can be obtained from Eqs. (3.5) and (3.6).

We arrive now at the second step, i.e., to obtain the unknown modal amplitudes $a_s^{(l)}$ and $b_s^{(l)}$ as well as the amplitudes from the reflected and transmitted field from the interface conditions. For simplicity, we assume for the moment that we only have one single layer l . At the interface of substrate and the layer, the continuity equation for \tilde{E}_x reads as [177]

$$u_x \delta_{m0} \delta_{n0} + R_{xmn} = \sum_{s=1}^S \left[a_s^{(l)} + b_s^{(l)} \exp\left(i\gamma_s^{(l)} h^{(l)}\right) \right] \tilde{E}_{xmn}^{(l)} \quad (3.27)$$

and similar expressions for \tilde{E}_y , \tilde{H}_x , and \tilde{H}_y as well as similar continuity relations at the interface of the layer to the cladding [177]. For the general case of a multi-layer structure, a scattering matrix (S-matrix) approach can be applied [181], which is explained in detail for example in [174]. Together with the divergence equation (3.3), the resulting linear system can be solved to obtain $a_s^{(l)}$ and $b_s^{(l)}$ as well as the amplitudes of \mathbf{R}_{mn} and \mathbf{T}_{mn} , Eqs. (3.14) and (3.15).

The third and final step is to calculate the quantities of interest. The diffraction efficiencies in reflection, η_{Rmn} , and transmission, η_{Tmn} , of the orders m and n are obtained from the time-averaged Poynting vector in the z -direction as [177]

$$\eta_{Rmn} = \Re\left(\frac{\gamma_{Smn}}{r_{00}}\right) |\mathbf{R}_{mn}|^2 \quad (3.28)$$

$$\eta_{Tmn} = \Re\left(\frac{\gamma_{Cmn}}{r_{00}}\right) |\mathbf{T}_{mn}|^2 \quad (3.29)$$

$$(3.30)$$

with $\gamma_{S/Cmn}$ from Eq. (3.20) and the absolute squared is the sum of the squared x -, y -, and

¹¹The convergence of the Fourier expansions improves by applying so-called *Fourier factorization rules* [179,180].

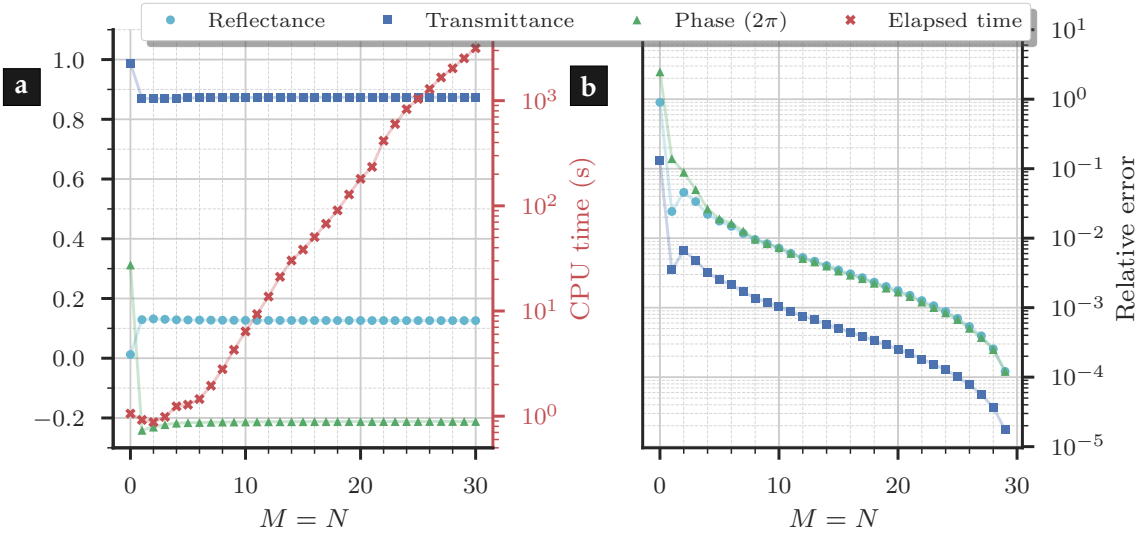


Figure 3.2: Convergence analysis of the FMM. Lines serve as a guide for the eye.

a Some quantities of interest as the reflectance, transmittance, and the phase of the zeroth order are plotted as a function of M . As an example, we select the simulation of a metasurface, as discussed in Section 7.2 [$r = 65$ nm, compare Fig. 7.4]. The CPU time is plotted on a logarithmic scale.

b Relative error $|\Delta x/x|$ as a function of M , relative to the results at $M = 30$.

z -components. The total reflectance R and transmittance T is the sum of all diffraction orders in reflection and transmission,

$$R = \sum_{m,n} \eta_{Rmn} \quad (3.31)$$

$$T = \sum_{m,n} \eta_{Tmn}. \quad (3.32)$$

For periodic structures with an invariant permittivity distribution along z within each layer, the FMM solves Maxwell's equations quite accurately provided that enough orders are taken into account, i.e., M and N are sufficiently large. Figure 3.2 shows a convergence analysis for an example we discuss later in this thesis. The relative error decreases with increasing M , while the CPU time¹² grows exponentially. For $M \geq 10$, the relative error in the phase is below 10^{-2} , which is sufficient for our purposes. All FMM simulations presented throughout this thesis have been conducted with $M = 15$ to simulate the transmission coefficients and $M = 20$ to calculate the field distributions.

¹²Intel® Xeon® CPU E5-2650 v4, Matlab 2018b.

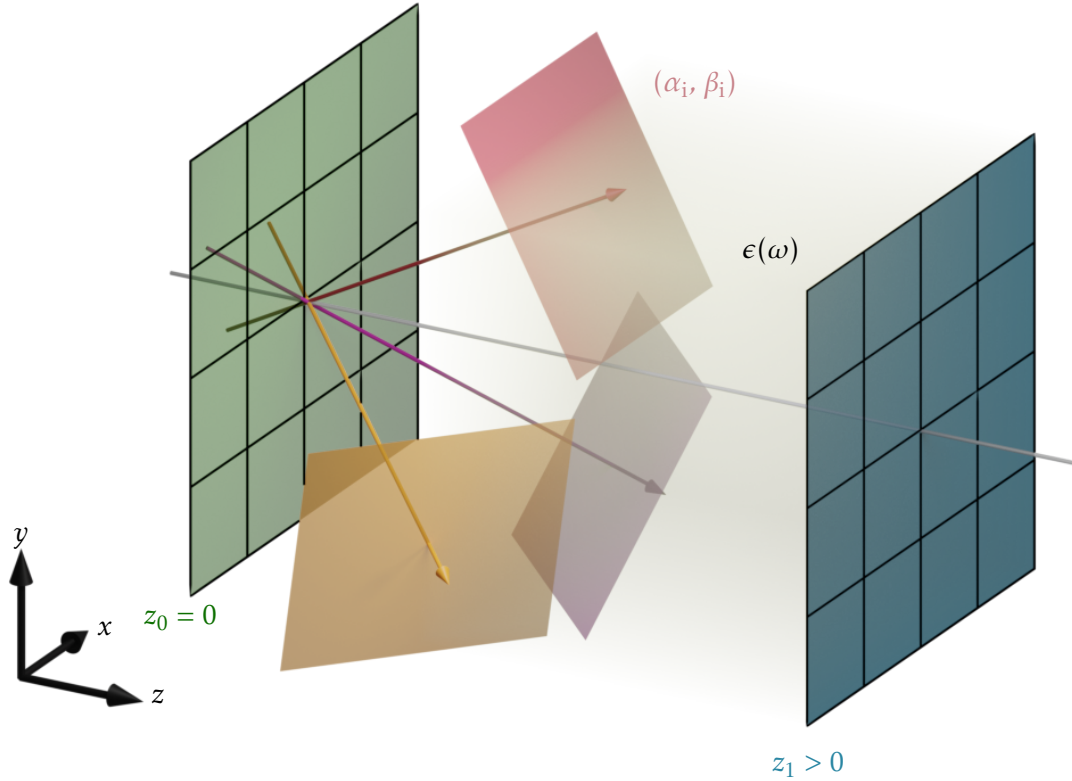


Figure 3.3: Schematic of the ASM. Three sets of spatial frequencies (α_i, β_i) are indicated by colored planes and arrows. By summing up the individual contributions of the plane waves in the plane of interest (blue) the field distribution is calculated for a propagation length of z_1 .

3.2.2 The angular spectrum method to simulate the propagation of arbitrary field distributions

The angular spectrum method (ASM)¹³ is one approach often applied to simulate the propagation of electromagnetic fields in a homogeneous space [182]. The fundamental idea is to take the field distribution in a certain plane¹⁴ (with no loss of generality $z = 0$, left in Fig. 3.3) and to calculate the field distribution in the homogeneous half-space $z > 0$ (z_1 in Fig. 3.3) filled with material of permittivity $\epsilon(\omega)$.

Starting point for the ASM is the vector Helmholtz wave equation (3.8). Each component of the vector $\tilde{\mathbf{E}}(\mathbf{r}, \omega)$ [and $\tilde{\mathbf{H}}(\mathbf{r}, \omega)$] obeys a scalar wave equation, with $\tilde{u}(\mathbf{r}, \omega)$ being a placeholder for any field component [61],

$$\nabla^2 \tilde{u}(\mathbf{r}, \omega) + \frac{\omega^2}{c_0^2} \epsilon(\omega) \tilde{u}(\mathbf{r}, \omega) = 0. \quad (3.33)$$

If we consider homogeneous isotropic linear media, the scalar theory of wave propagation remains exact. It becomes an approximation for inhomogeneous permittivity distributions and/or for coupling between the field components, which we neglect here as we are concerned with free-space propagation only.

Within the realm of Fourier optics and the scalar approximation, the ASM requires in

¹³Also called the *angular spectrum representation* or the *angular spectrum of plane waves* [61].

¹⁴To obtain the field distribution, we use the FMM (discussed in Fig. 3.1) or the TEA (Section 2.3.2). We will not discuss here how to obtain the initial field distribution or how to sample it, but rather assume it as given.

essence three steps, which we introduce here to outline the procedure and discuss afterwards in detail. As before, we mostly drop the frequency argument.

1. We decompose the known (complex) field $\tilde{u}_0(x, y)$ at $z_0 = 0$ into its spectrum of plane waves $A_0(\alpha, \beta)$ that are propagating into different directions in the $z > 0$ half-space. In two dimensions, the corresponding Fourier components or amplitudes of the spatial frequencies $\alpha = k_x$ and $\beta = k_y$ are obtained by applying a two-dimensional spatial Fourier transform.
2. The individual plane waves then propagate to the plane of interest, where they are summed up to obtain the spectrum of plane waves at this location. For an isotropic medium, the propagation of a plane wave is simply the multiplication with a known phase factor.
3. An inverse Fourier transformation from the plane wave domain to the spatial domain leads to the field distribution in the plane at distance z_1 .

In the first step, we obtain the spectrum of plane waves as the Fourier transform of the field $\tilde{u}_0(x, y)$

$$A_0(\alpha, \beta) = (2\pi)^{-2} \iint_{-\infty}^{\infty} \tilde{u}_0(x, y) \exp(-i[\alpha x + \beta y]) dx dy. \quad (3.34)$$

Vice versa, the field in an arbitrary plane at z_1 can be written as

$$\tilde{u}(x, y, z_1) = \iint_{-\infty}^{\infty} A(\alpha, \beta; z_1) \exp(i[\alpha x + \beta y]) d\alpha d\beta, \quad (3.35)$$

showing how the field is expanded into the plane waves.

The second step is now to propagate the spectrum of plane waves to the plane of interest. We have to derive an expression how the spectrum of plane waves $A(\alpha, \beta; z)$ changes with z parametrically. Starting point is the scalar wave equation (3.33) and the dispersion relation (3.11), which reads as [183]

$$\nabla^2 \tilde{u}(\mathbf{r}) + \mathbf{k}^2 \tilde{u}(\mathbf{r}) = 0. \quad (3.36)$$

Now we insert Eq. (3.35) for $\tilde{u}(\mathbf{r})$, drag the integral to the front, and perform the derivatives in x and y [183]. We find that the scalar wave equation is only satisfied if the corresponding expression vanishes for each α and β , leading to

$$\left(\frac{d^2}{dz^2} + \mathbf{k}^2 - \alpha^2 - \beta^2 \right) A(\alpha, \beta; z) = 0. \quad (3.37)$$

A comparison with Eq. (3.11) shows that the expression in the parentheses contains the spatial derivative and the z -component of the wavevector, i.e., the propagation constant $\gamma(\alpha, \beta)$ as a function of the spatial frequencies. Similar to Eq. (3.20), $\gamma^2(\alpha, \beta) < 0$ corresponds to an imaginary wavevector and evanescent waves. On the other hand, $\gamma^2(\alpha, \beta) > 0$ corresponds to a real wavevector and propagating waves. It follows

$$\left(\frac{d^2}{dz^2} + \gamma^2(\alpha, \beta) \right) A(\alpha, \beta; z) = 0. \quad (3.38)$$

A solution for this differential equation is given by [183]

$$A(\alpha, \beta; z) = A_+(\alpha, \beta) \exp[i\gamma(\alpha, \beta)z] + A_-(\alpha, \beta) \exp[-i\gamma(\alpha, \beta)z]. \quad (3.39)$$

To exclude an exponentially growing term for complex $\gamma(\alpha, \beta)$, we set $A_-(\alpha, \beta)$ to zero. In other words, this second term corresponds to waves propagating in negative z -direction

we are not interested in. By inserting $z = 0$ in Eq. (3.39), we retrieve $A_+(\alpha, \beta) = A_0(\alpha, \beta)$, and finally obtain

$$A(\alpha, \beta; z) = A_0(\alpha, \beta) \exp[i\gamma(\alpha, \beta)z] = A_0(\alpha, \beta)H(\alpha, \beta; z), \quad (3.40)$$

$$\text{with } \gamma(\alpha, \beta) = \sqrt{\frac{\omega^2}{c_0^2} \epsilon(\omega) - \alpha^2 - \beta^2} \quad (3.41)$$

and $H(\alpha, \beta; z)$ denoting the optical transfer function.

As we are typically interested in propagating waves that travel over distances of several wavelengths, evanescent components are not contributing, and hence we exclude plane waves with negative $\gamma^2(\alpha, \beta)$.

In a third and final step, the field distribution in the plane at z_1 can be calculated from the spectrum of plane waves as

$$\tilde{u}(x, y, z_1) = \iint_{-\infty}^{\infty} A_0(\alpha, \beta) \exp[i\gamma(\alpha, \beta)z_1] \exp[i(\alpha x + \beta y)] d\alpha d\beta. \quad (3.42)$$

Within the realm of the scalar approximation and neglecting the contributions of evanescent waves, the ASM is exact. In practice, the implemented numerical algorithms for Eqs. (3.34) and (3.42) have a finite accuracy, as they rely on discrete Fourier transforms in the form of Fast Fourier Transforms (FFTs). The field distribution $\tilde{u}_0(\mathbf{r})$ has to be discretized in the spatial domain on a finite grid. The array size of the field and its FFT is equal, and hence the discretization in the spatial domain leads to a finite bin size in the frequency domain and thus the plane wave spectrum. Depending on the required accuracy, the sampling of the plane wave spectrum might not be sufficient.

The pixel size $\delta_{x/y}$ in the spatial domain on a Cartesian grid and the number of pixels $n_{x/y}$ defines the bin size $\zeta_{\alpha/\beta}$ in the frequency domain [61], i.e., the minimum spacing between two spatial frequencies,

$$\zeta_{\alpha/\beta} = \frac{1}{\delta_{x/y} \cdot n_{x/y}}. \quad (3.43)$$

As a consequence, the simulation of the initial field distribution with a finer resolution and/or additional interpolation does not affect the bin size in the frequency domain, since the decrease in $\delta_{x/y}$ is compensated for by the increase in $n_{x/y}$. This means that finer bins in the frequency domain require to introduce a larger field distribution. In practice, one solution is to surround the field in the *signal window* with zeros, a process called *zero padding* [184]. For all results throughout this thesis involving the ASM, we apply zero padding around the quadratic field distributions in each direction, increasing the total field size by a factor of nine. As a side effect, due to the increased area the amount of light being scattered out of the computational domain is reduced.

3.2.3 The Rayleigh-Sommerfeld diffraction integral for the efficient simulation of light propagation

We now want to introduce the numerical solution to the Rayleigh-Sommerfeld diffraction integral, implemented by the commercial software *GenISys LAB* [185] and used to simulate for instance the irradiance distribution in proximity lithography. As we will discuss in the following, this approach is similar to the ASM. Nowadays, powerful computers allow to calculate field distributions without for instance Fresnel or Fraunhofer approximations. In combination with a transfer matrix method (TMM), a stack of materials (photoresist, substrate, coatings, etc.) can be simulated as well.

We reconsider the transfer function $H(\alpha, \beta, z)$ which we defined in Eq. (3.40). The inverse Fourier transform of $H(\alpha, \beta; z)$ provides the impulse response of the system [186],

$$\begin{aligned} h(x, y; z) &= (2\pi)^{-2} \iint_{-\infty}^{\infty} H(\alpha, \beta; z) \exp(i[\alpha x + \beta y]) d\alpha d\beta \\ &= (2\pi)^{-1} \frac{z \exp(ikr)}{r} \left[\frac{1}{r} - ik \right] \end{aligned} \quad (3.44)$$

$$\text{with } k = |\mathbf{k}| \quad \text{and} \quad r = |\mathbf{r}| = \sqrt{x^2 + y^2 + z^2}.$$

The formula of the Rayleigh-Sommerfeld diffraction integral can be written as the convolution of the field $\tilde{u}_0(x, y)$ and the impulse response $h(x, y; z)$ as [186]

$$\begin{aligned} \tilde{u}(x, y, z_1) &= \iint_{\text{Ap}} \tilde{u}_0(\xi, \eta) h(x - \xi, y - \eta; z) d\xi d\eta \\ &= (2\pi)^{-1} \iint_{\text{Ap}} \tilde{u}_0(\xi, \eta) \frac{z \exp(ikr^*)}{r^*} \left[\frac{1}{r^*} - ik \right] d\xi d\eta, \end{aligned} \quad (3.45)$$

$$\text{with } r^* = \sqrt{(x - \xi)^2 + (y - \eta)^2 + z^2},$$

with the integration over the extent of the field distribution \tilde{u} denoted here as the aperture Ap.

The convolution (3.45) can be treated as a Riemann sum to calculate the field $\tilde{u}(x_m, y_n, z)$ at the discrete points (x_m, y_n, z) as [186]

$$\tilde{u}(x_m, y_n, z) = \sum_{j=1}^N \sum_{k=1}^N \tilde{u}_0(\xi_j, \eta_k) h(x_m - \xi_j, y_n - \eta_k, z) \Delta\xi \Delta\eta, \quad (3.46)$$

with the sampling intervals $\Delta\xi$ and $\Delta\eta$ and the field size N in each direction. Equation (3.46) can be reformulated by introducing three two-dimensional FFTs. For the sake of brevity, we skip the corresponding details here and point out the detailed discussion in [186].

Literature suggests that the computational complexity of the Rayleigh-Sommerfeld diffraction integral is comparable to the ASM [186]. The accuracy depends mainly on the size of the sampling intervals. Throughout this thesis, we use $\Delta\xi = \Delta\eta = 50 \text{ nm}$.

Figure 3.4 shows a comparison between the field distribution obtained from the Rayleigh-Sommerfeld diffraction integral in *GenISys LAB* and from the ASM. We obtain a good qualitative agreement, with small differences arising from the sampling and the numerics.

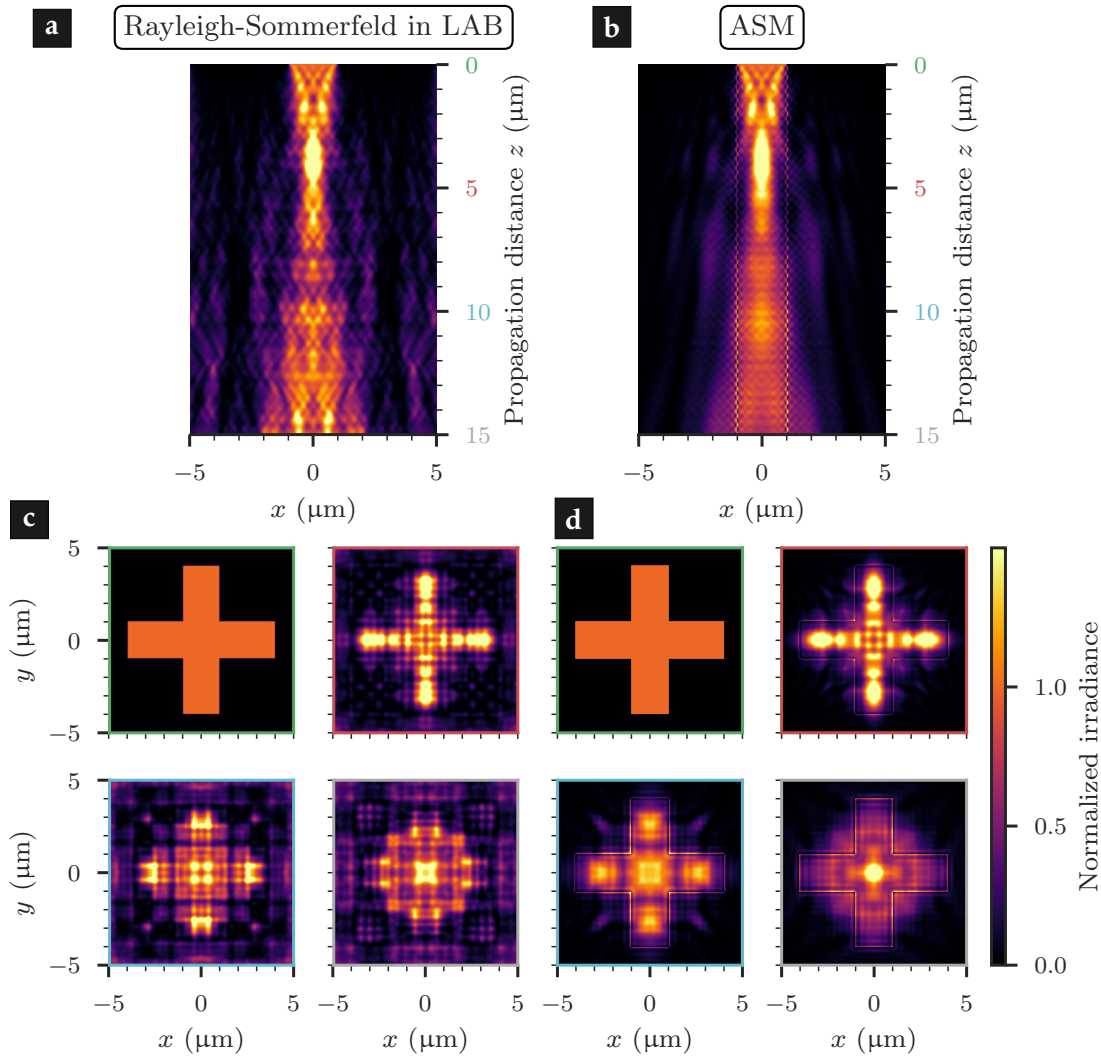


Figure 3.4: Comparison of Rayleigh-Sommerfeld diffraction integral, as implemented in *GenISys LAB*, and the angular spectrum method. We use a cross-shaped test pattern already discussed in Fig. 1.3 with a resolution of 20 nm, but here with plane wave illumination under normal incidence. A good agreement between both methods is observed. **a** and **b** Light propagation along the z -direction. **c** and **d** Irradiance distribution in selected planes, indicated by the color of the frame.

3.2.4 Ray tracing for simulating macroscopic optical setups

For the simulation of macroscopic systems as presented in Chapter 4, we use optical ray tracing¹⁵. This well-established method relies on the geometrical-optical approximation, i.e., the wavelength is assumed to be small compared to the extension of the optical elements [68]. As the name implies, classical ray tracing relies on the reconstruction of optical paths by a large number of individual rays.

It is important to mention that light rays have to be understood rather as a concept and not as an existing physical entity [187]. Hence, we treat light rays in a strictly mathematical sense as geometrical objects with zero lateral extensions. This precludes the integration of diffraction effects in classical ray tracing, while several approaches that combine wave-optical and ray-optical simulations have been demonstrated [68, 188].

The classical ray tracing algorithm comprises a step-by-step propagation of individual

¹⁵The simulations are performed using the commercial ray tracing software *OpticStudio* provided by *Zemax*.

light rays, taking into account the media and interfaces along the propagation path. The general scheme can be outlined in three steps [68]:

1. Propagate the ray over a finite distance in a medium.
2. Calculate the intercept with the next interface at the interface of two media.
3. Compute the new direction of the ray when traversing through the interface. Depending on the optical element, this requires to apply Snell's law of refraction and reflection, grating theory, or Monte-Carlo methods for scattering surfaces.

In sequential mode, the ray tracing algorithm iterates over these steps from the first to the last surface of the system. However, the simulation of illumination systems requires to use a non-sequential ray tracer. This means that the sequence of interfaces is not predefined, but rather calculated in step two at run-time. Non-sequential ray tracing allows to calculate the energy transfer efficiency and the uniformity as well as enables to simulate stray light.

We restrict our considerations to the simulation of a coherent CW laser source presented in Chapter 4. The integration of a rotating diffuser in the light path and the use of a time-continuous laser output creates a large number of independent speckle patterns. In combination with the photoresist acting as an analog integrating sensor, it is sufficient to rely on incoherent ray-tracing simulations [189–191]. However, incoherent simulations prevent us from simulating interference effects due to multiple reflections in the beam path.

Mask aligner lithography using a continuous-wave frequency-quadrupled laser emitting at 193 nm

Practically since the advent of mask aligner lithography, mercury high-pressure lamps are the prevalent light source, offering high power in the UV. In recent years, the implementation of UV LEDs into mask aligner lamp houses opens up new possibilities, but is momentarily limited to wavelengths above ~ 350 nm, ultimately limiting the minimum feature size in proximity lithography. To improve the resolution, novel illumination sources are required, with impact on the photoresist processing.

In this chapter, we demonstrate the integration of a CW laser source emitting at 193 nm in a mask aligner lithographic setup and its performance in soft contact and proximity lithography. We first discuss the source properties, followed by the optical setup to achieve flat-top illumination. Exploiting the high coherence of the source, we demonstrate a further resolution enhancement using a PSM and the Talbot self-imaging effect.

The research presented in this chapter is published in [9, 11, 18–20] and has been conducted in close cooperation with M.Sc. R. Kirner, Suss MicroOptics SA. We developed the optical system and performed the optical prints presented in Section 4.3 together. He performed the simulations of the illumination setup, illustrated in Figs. 4.10b and 4.12b and presented in Figs. 4.11 and 4.19.

4.1 Benefits of continuous-wave laser sources and wavelength reduction for optical lithography

The requirements and performance metrics for light sources in optical lithography are manifold. A division into two categories is reasonable: First, the ability to transfer the desired pattern to the wafer is the foremost metric, ultimately summarized in the resolution. As discussed in Section 2.3, the fundamental properties of light, i.e., wavelength, polarization, angular spectrum, and coherence play the key role for achieving a high quality image transfer. Crucially, a second category revolves around the required infrastructure when using the light source in production environments. What is the price for a light source in acquisition and maintenance? How efficient is the light generation in the UV, wavelength selection, and beam homogenization? What is the total intensity used for lithography, defining the exposure time? Which additional infrastructure is required? We will discuss in the following shortly the performance of light sources emitting in the DUV, showing the benefits of CW laser light sources in optical lithography.

Historically, gas-discharge lamps were the first UV light sources used in photolithography, with broad emission spectra superimposed by peaks corresponding to electronic transitions (compare the discussion in Section 2.3.1 and Table 2.1) [192, 193]. The strong UV emission in the *g*-, *h*-, and *i*-line (436, 405, and 365 nm; see Table 2.1) renders the mercury

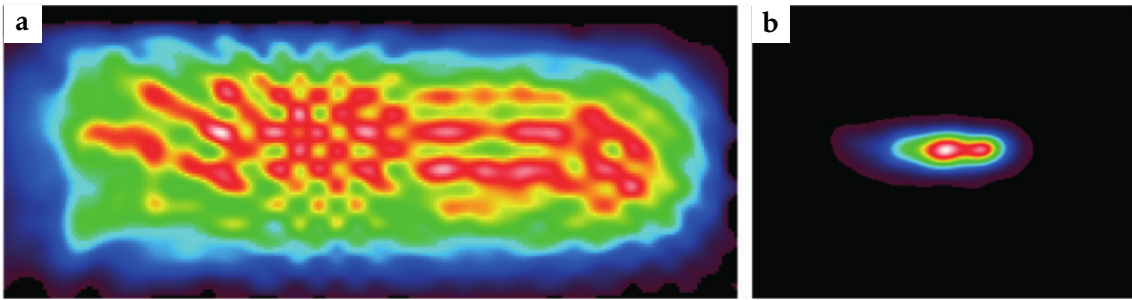


Figure 4.1: Excimer beam profile in the **a** near- and **b** far-field. The multi-mode operation of the source generates a highly non-uniform beam profile. Reprinted with permission from [68].

high-pressure lamp the prevalent light source in mask aligner lithography, still applied in *i*-line steppers to this day.

The advent of excimer¹⁶ lasers [194, 195] enabled a further reduction in the illumination wavelength. The ArF excimer laser, emitting at 193 nm, is nowadays the dominating light source in projection lithography [196–199].

The active media of this pulsed source typically consists of a mixture of noble and halogen gases, which emits coherent radiation under external stimuli such as electric discharges or microwave excitation. It excels in terms of power output (some hundreds of watts [195]), allowing a high throughput in wafer fabrication. In 2010, Partel *et al.* demonstrated the integration of an ArF excimer laser for full-field mask aligner lithography [54], with feature sizes down to 2 μm at a proximity gap of 10 μm .

While being widely adopted in projection lithography, the widespread industrial application of excimers in mask aligners is not reported. The main reasons are the complex and expensive operation, compared to the other comparably simple and low-cost components in mask aligners [11]. High volumes of corrosive gas mixtures and voltages around 40 kV [195] require a well-equipped cleanroom facility and regular maintenance.

In addition, the range of transparent and non-birefringent materials at 193 nm is in practice limited to UV-grade fused silica and crystalline calcium fluoride (CaF_2). The absence of suitable materials renders the correction of chromatic aberrations impossible [34]. The high peak powers during operation influence the beam shaping optics: color centers form, leading to a reduction in transmittance over time [200]. Compaction occurs in fused silica, which changes the refractive index of the material and thus the imaging capabilities [201, 202].

Furthermore, the multi-mode operation of the excimer laser leads to a beam profile that is inhomogeneous and elongated (see Fig. 4.1). The high gain in the active medium of an excimer renders light generation highly efficient, requiring only a few roundtrips in the laser cavity [34]. Hence, the spatial coherence is strongly reduced over conventional lasers. Due to the large étendue, beam shaping requires to block some light especially when requiring small illumination angles, which renders the optical system inefficient (compare Section 2.3.1).

Since only a single material is used for the optics in excimer projection steppers, a narrow linewidth is required in order to avoid chromatic aberrations. Hence, the broadband

¹⁶The term *excimer* refers to an *excited dimer*, a temporarily bound excited state. Using a mixture of noble and halogen gas, the correct term would be *exciplex* (*excited complex*), an expression rarely used in practice. In a strict sense being a misnomer, we use *excimer* throughout this thesis.

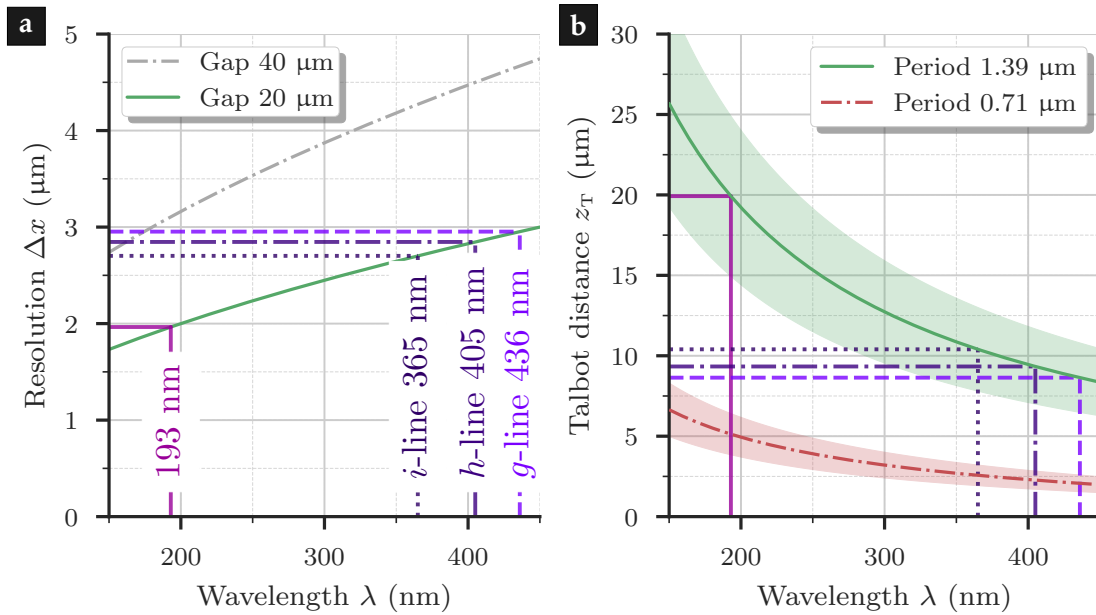


Figure 4.2: Comparison of resolution and Talbot distance with associated depth of focus (DOF) as a function of wavelength. **a** Resolution in proximity lithography according to Eq. (2.25). Tagged are the emission lines of mercury high-pressure arc lamps used for lithography and the presented laser source at proximity gaps of 20 μm and 40 μm . **b** Talbot distance z_T (solid green and dash-dotted red lines) and the corresponding DOF marked in the graph as colored area, following Eq. (2.36) and Eq. (2.41), respectively. The period of 1.39 μm (0.71 μm) corresponds to a Talbot distance of 20 μm (5 μm) at an illumination wavelength of 193 nm.

spectrum of excimer lasers requires subsequent linewidth narrowing, from about 0.45 nm to 0.35 pm (compare Table 2.1 and [203]), for example by using echelle gratings in Littrow configuration [195]. In addition, light might be absorbed by oxygen molecules during free-space propagation in air [204]. Operating in a multi-mode regime, excimer lasers have a low spatial and temporal coherence, as required in optical lithography to prevent interference effects in the optical system, visible in the photoresist (see Section 4.2.2). For further reduction of spatial coherence, typically light mixing rods, optical fibers, and/or rotating mirrors are in use [34]. In addition, the purchasing and regular maintenance of excimer lasers [34] renders their use in mask aligners at least one order of magnitude more expensive than mercury arc lamps.

Here, we present a light source based on a frequency-quadrupled laser diode that emits at 193 nm. The chosen wavelength is compatible to established photoresist technology for the ArF excimer lasers, relying on CARs. The continuous wave (CW) operation, low bandwidth, and low étendue completely mitigate the aforementioned problems associated with excimer lasers. CW illumination leads to a constant power input in time, without heat peaks during the pulse absorption observed for excimer lasers, and strongly reduced material degradation present in lithographic excimer systems. With a native spectral linewidth of ~ 100 kHz [20], our light source even outperforms top-notch narrowed excimer lasers with a linewidth of 2.5 GHz [198]. The low étendue allows for efficient beam shaping, especially for near-plane wave illumination as required for example for Talbot lithography.

The major drawback of our CW light source is the low output power of about 10 mW, compared to a power of 7.5 W demonstrated for mask aligner lithography using an excimer laser [54]. While partly compensated by efficient beamshaping, exposure times become unreasonably large. Thus, we restrict this feasibility study to small exposure fields.

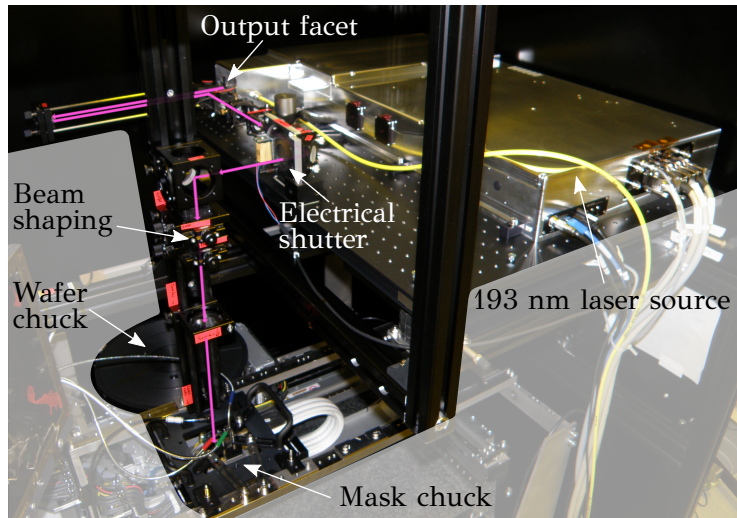


Figure 4.3: Picture of the optical setup. The beam path is marked in pink: From the output of the laser, the light is routed towards the photomask, undergoing beam shaping to achieve a flat-top uniform illumination field in the mask plane. A shutter allows to control the exposure time.

Upscaling to full-wafer printing is possible.

Reducing the wavelength improves the resolution, as already discussed in Section 2.3.3. Figure 4.2a shows the attainable minimum feature size as a function of wavelength, following Eq. (2.26). Compared to the canonical mercury lamp (*g*-, *h*-, and *i*-line), we observe a clear resolution enhancement down to $2\ \mu\text{m}$ at a proximity gap of $20\ \mu\text{m}$.

The benefits of wavelength reduction extend to Talbot lithography, as introduced in Section 2.4.3.2. Figure 4.2b shows the Talbot distance z_T and the corresponding DOF as a shaded area for two periods Λ . Compared to *i*-line illumination at $\lambda_i = 365\ \text{nm}$, the Talbot distance is increased for a fixed periodic pattern. For instance, for a period of $\Lambda \approx 1.4\ \mu\text{m}$ and a wavelength of $\lambda = 193\ \text{nm}$, it follows a Talbot distance and hence a proximity gap of $g = 20\ \mu\text{m}$. This value is about halved for *i*-line illumination to achieve the same period [compare Eq. (2.38)]. Simultaneously, the DOF increases as well, i.e., the process is less sensitive to gap variations.

4.2 Optical setup and laser beam shaping in the deep ultraviolet

In this section, we discuss CW light generation, coherence management, and two approaches for achieving uniform illumination with variable angular spectrum, as required for lithographic prints. Figure 4.3 depicts a photograph of the optical setup.

4.2.1 Frequency-quadrupled 193 nm light source

Figure 4.4 shows a schematic of the frequency-quadrupled CW laser source emitting at 193 nm. The laser operates following the master-oscillator power-amplifier (MOPA) principle: The seed light of the master oscillator is amplified in power, used as an input for the first second-harmonic generation (SHG) stage.

Light generation starts with an extended cavity diode seed laser at 772 nm, featuring a spectral linewidth $< 10\ \text{kHz}$ [205]. After passing a Faraday isolator (FI) to prevent back reflections into the seed laser, a tapered amplifier (TA) enhances the power up to 3 W. In a first SHG bow-tie cavity containing a lithium triborate (LBO) nonlinear crystal, the conversion to an intermediate wavelength of 386 nm and a power of about 1.65 W takes place.

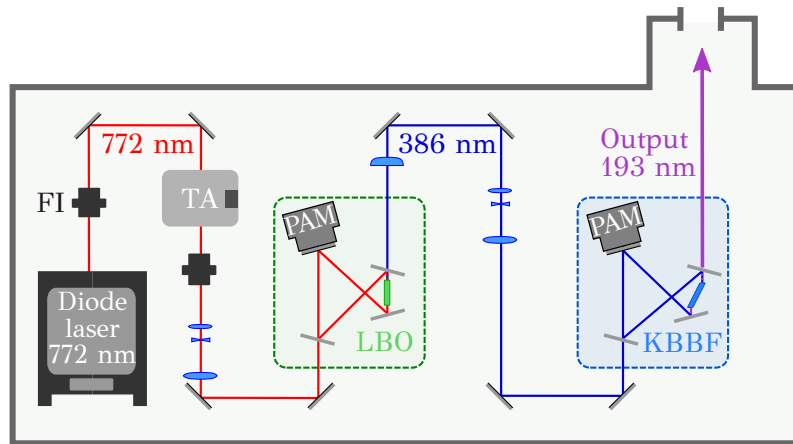


Figure 4.4: Schematic of the 193 nm frequency-quadrupled light source. The output of a diode seed laser emitting at 772 nm (bottom left) passes first a Faraday isolator (FI) to suppress back reflections. After enhancement in a tapered amplifier (TA), the laser beam enters a first second-harmonic generation (SHG) stage, containing a lithium triborate (LBO) nonlinear crystal. Piezoelectric-actuated mirrors (PAMs) controlled by a Pound-Drever-Hall (PDH) feedback routine stabilize the cavity output. The frequency-doubled output at 386 nm is subsequently routed to a SHG bow-tie cavity, containing a potassium fluoro-beryllo-borate (KBBF) crystal which generates the final output at 193 nm. Additional beam shaping elements are indicated in blue. Adapted from [205].

In earlier years, the final upconversion to 193 nm was restricted by the absence of suitable nonlinear materials. The recent availability of high-quality potassium fluoro-beryllo-borate ($\text{KBe}_2(\text{BO}_3)\text{F}_2$, KBBF) bridges this gap [206, 207]. Active feedback controls, relying on fast piezoelectric actuators, adjust the length of both cavities, applying the Pound-Drever-Hall method to stabilize the resonance [208, 209].

For a bare KBBF crystal, the required phase matching for SHG is only attainable at large angles of incidence, along with high Fresnel losses in reflection. To attain the required crystal direction under suitable angles, the KBBF is bonded to CaF_2 prisms, forming a prism-coupled device (PCD) [210], as depicted in Fig. 4.5.

During operation, degradation at the interface between KBBF and the CaF_2 prism limits

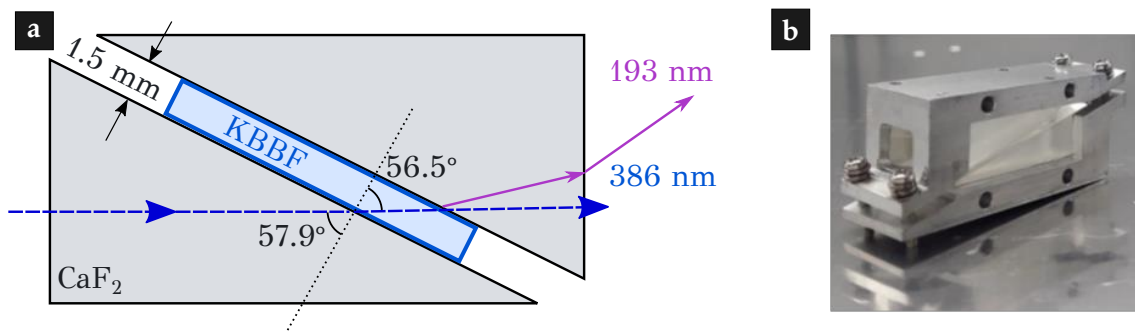


Figure 4.5: Prism coupling of the potassium fluoro-beryllo-borate (KBBF) crystal inside the SHG cavity.

a Sketch of the nonlinear crystal inside two calcium fluoride (CaF_2) prisms, used to attain the required crystal axis for phase matching.

b Photograph of the crystal bonding with mechanical housing. Reprinted with permission from [20].

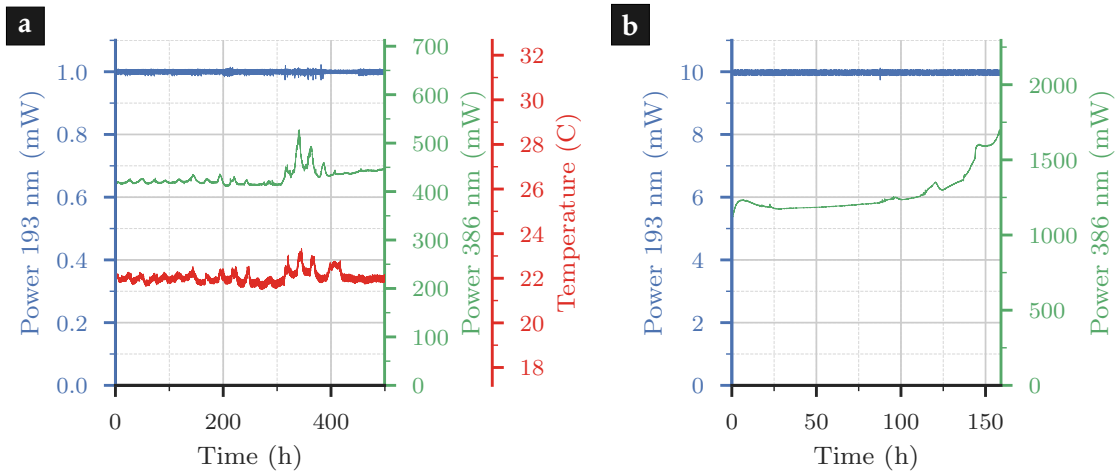


Figure 4.6: Time dependence of the output power to study the laser stability. The stabilized laser output for a power of **a** 1 mW and **b** 10 mW at 193 nm is shown, together with the corresponding output power of the first SHG cavity at 386 nm. In **a**, the fluctuation in the pump power corresponds well to temperature fluctuations in the environment. The laser stability surpasses typical exposure times by several orders of magnitude. Data previously published in [20].

the lifetime of efficient SHG at a selected spot of the crystal. Figure 4.6 demonstrates the longterm stability of the light source at one crystal spot. To stabilize the output power at 193 nm (blue), the power at 386 nm is regulated.

For an output power of 1 mW (Fig. 4.6a), the source is stable for at least 500 h, with only a minor increase of the power at 386 nm. At an increased power of 10 mW (Fig. 4.6b), the degradation accelerates: The power at 386 nm has to be increased with time to keep the output at 193 nm stable for about 150 h. An integrated crystal shifter allows to access several spots on the KBBF crystal, extending the lifetime of the light source to about 10.000 h [20]. An increase in the output power requires improvements regarding the optical bonding of the KBBF crystal [11].

Without additional beam shaping, the laser beam leaving the output facet features an elliptic profile (see Fig. 4.7). The ellipticity arises in the second SHG cavity, where the output direction of the 193 nm beam is slightly tilted with respect to the direction of the pump beam (see [205] for further discussion).

4.2.2 Controlling the spatial coherence

A high spatial coherence, corresponding to small illumination angles in the mask plane, is a crucial prerequisite for interference printing using PSMs and in Talbot lithography (compare Section 2.3). This property is inherent to our light source. However, the spatial and temporal coherence also cause the formation of speckle patterns [211] and interference effects by multiple reflections within the optical system.

Speckle emerge from the interference of waves, which collect different random, but fixed amplitudes and phases while propagating through the optical system. Coherent superposition in the mask plane results in the formation of a random illumination of the photoresist. An example for insufficient speckle reduction is discussed in the context of Fig. 4.20.

To control and mitigate the impact of speckle formation, we use a combination of static and rotating shaped random diffusers. During the exposure, the photoresist integrates over all speckle patterns which are varied by the rotation of the diffuser. The individual patterns

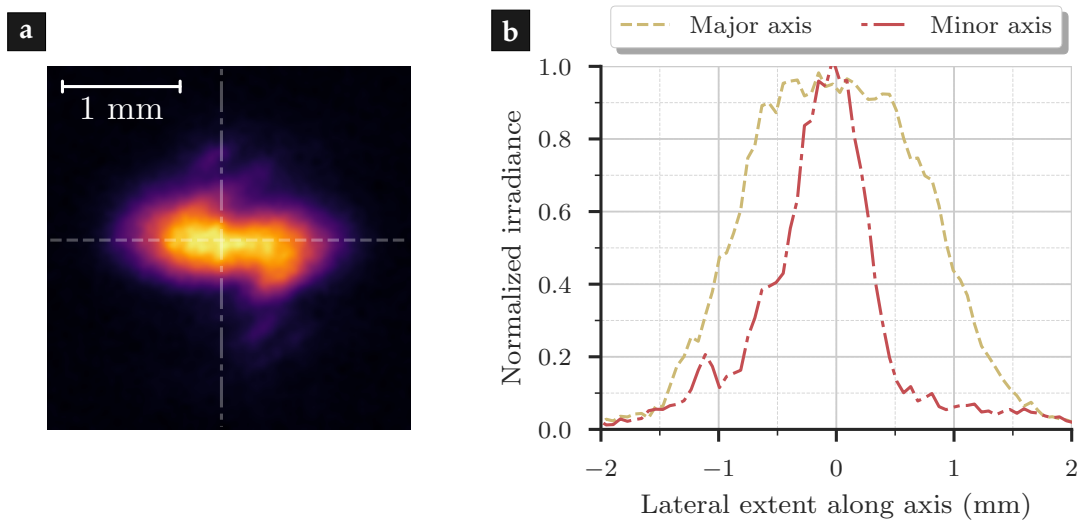


Figure 4.7: Laser beam output at 193 nm, at a distance of 200 mm to the housing.
a Elliptical beam spot. The major and minor axes are marked with a dashed and a dash-dotted line, respectively.
b Cross section along the major and minor axis of the beam profile in **a**, demonstrating the non-uniform beam properties. For being used in lithography, further beam homogenization is indispensable.

depend on the microscopic configuration of diffusers and laser beam. Two speckle patterns are mutually independent if the diffuser rotates more than the lateral speckle size [11]. With a sufficient number of independent speckle patterns, the temporal integration in the resist results in an ensemble average free of visible speckle [75, 212]. Here, the CW operation is of advantage: How well the speckle mitigation works depends mainly on the number of independent patterns during the exposure. Pulsed lasers have a pulse length of tens of nanosecond and below, leading to a practically static diffuser within one pulse. This requires a minimum number of optical pulses with independent patterns during the exposure. In contrast, a CW laser allows a continuous integration, and one complete diffuser rotation ensures efficient speckle mitigation. When m corresponds to the amount of uncorrelated speckle patterns during integration, the contrast of speckle scales with $m^{-1/2}$ [75].

In the beam path behind the rotating diffuser, the micro-optical homogenizer further mitigates of speckle. Interpreting the homogenizer as a mixing element, each sub-aperture is an individual secondary source. By means of a Fourier lens, the light of all sub-apertures is superimposed in the Fourier plane of the homogenizer, effectively reducing the lateral coherence [80].

The diffusers, manufactured by *Suss MicroOptics SA*, consist of a random assembly of microlenses, as visible from the topography shown in Fig. 4.8a obtained by a white light interferometer (WLI). The MLA fabrication ensures that the size of each lens varies, but the curvature of the concave facets is similar. In a first lithographic step, openings in photoresist with varying size are structured. In a second wet-etch step, the facets are etched through this openings. Due to a fixed etch time for all lenses, similar curvatures are obtained for all microlenses. This design allows to shape the directional characteristics of the diffuser, to not loose light scattered into large angles. Goniometric measurements showing the angular distribution for coherent illumination are depicted in Fig. 4.8b for both static and rotating diffusers used throughout this Chapter. Alternatively, CGHs with eccentric rotation have been demonstrated as shaped diffusers in laser illumination for

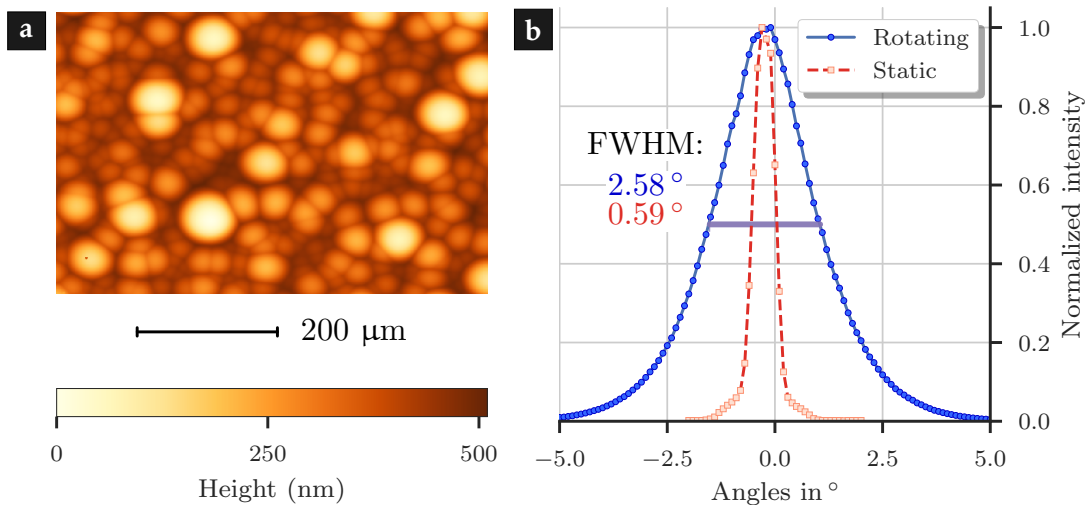


Figure 4.8: Shaped random diffusers.

a White light interferometric microscope image of a shaped random diffuser. The individual microlenses with different aperture sizes, but identical focal lengths are visible.

b Goniometric measurement of rotating and static diffuser, with the full width at half maximum (FWHM) of a Gaussian fit denoted. Please note the defined angular spectrum, with negligible scattering to large angles.

mask aligners [64].

Furthermore, multiple reflections at the various optical elements in the beam path can manifest in the formation of interference fringes in the photoresist. Applying an anti-reflective coating (ARC) to the optical elements, such detrimental reflections can be strongly reduced, with the additional benefit of directing light to the photomask. While in general available for 193 nm [213], in this feasibility study we refrain from applying ARCs to optical components due to a limited availability within the duration of the project.

The impact of interference effects between subsequent optical devices can be discussed by considering the longitudinal coherence length [11]. First, following [214], we estimate the $1/e$ speckle size in longitudinal direction to ≈ 1 mm. Being considerably smaller than the optical path length (OPL) for all optical elements in the beam path, the only remaining length scale relevant for interference effects is the proximity gap between mask and wafer (several 10 μm). The formation of standing waves within the photoresist is discussed in Section 4.3.

4.2.3 Homogenizing the illumination in the mask plane

Uniform irradiance illuminating the photomask, termed a flat-top field distribution, is the main purpose of the beam homogenizer (see Fig. 4.7). In addition, by selectively blocking light in the Fourier plane, the angular spectrum can be shaped. Here, we investigate two concepts concerning their suitability at the wavelength of interest.

As introduced in Section 2.3.1, we implement a micro-optical Köhler integrator in non-imaging and imaging configuration, and compare their properties for operation in the DUV, specifically at 193 nm. Instead of designing dedicated optical elements for this task, we rely on "off-the-shelf" components, typically optimized for wavelengths in the visible regime and without ARC.

4.2.3.1 Non-imaging homogenizer using a diffractive optical element

In a first implementation, we investigate a non-imaging homogenizer with an eight-level DOE as mixing element. The DOE consists of a hexagonal array of Fresnel lenslets, with half axes of 1.9 mm and 2.2 mm. Optimized for a wavelength of 193 nm, the micro-optical mixing element subdivides the incident light to several beamlets (see Fig. 4.9). A Fourier lens superposes the individual beamlets in the homogenization plane, separated by one focal distance.

Figure 4.10a depicts the complete optical setup, including mirrors, an IFP to modify the angular spectrum, an aperture directly behind the field lens to shape the homogenization field, a zeroth order filter, and a relay lens. The use of a relay lens allows more flexibility in laser beam shaping, with access to an intermediate homogenization plane behind the field lens. In reality, the theoretical maximum diffraction efficiency of 95% for an eight-level DOE [215] is reduced by deviations from the optimal step height and other imperfections as scratches. Hence, a strong zeroth order emerges in the Fourier plane, i.e., large parts of the input beam propagates through the DOE without deflection.

We address the resulting reduction in uniformity by introducing a filter to tone down the zeroth order. By placing a small opaque circular aperture ($\varnothing 100 \mu\text{m}$, see Fig. 4.10a) close to the intermediate superposition plane, the peak attributed to the zeroth order is reduced, but not completely blocked. This corresponds to an improvement in the uniformity (compare Fig. 4.11d and Fig. 4.11f). For this setup, following Eq. (2.4) with a focal length of about $f_{\text{DOE}} \approx 39 \text{ mm}$, we estimate the minimal diameter of the hexagonal field in the homogenization plane to $D_{\text{NIH}} \approx 8.8 \text{ mm}$.

For reasons discussed in Section 3.2 in detail, it is sufficient to rely on incoherent non-sequential ray-tracing for simulating our experimental setup in *Zemax OpticStudio*[®]. For modeling the shaped diffuser, we implement a source with a size of 4 mm and random emission angles over 3° , reproducing the goniometric measurements depicted in Fig. 4.8b. The optical simulation setup, depicted in Fig. 4.10b, takes into account the reduction of the focal length in the DUV for all optical elements due to material dispersion.

Mapping the field distribution in the DUV is a complex task, as charge-coupled device (CCD) cameras possess a low sensitivity to DUV light. Additionally, standard CCD devices degrade under UV illumination. In a first iteration, we implement indirect imaging, using a fluorescent dye applied to a polymer film (LUGB 5 from *Luminochem*) as a UV image converter. An optical system images the re-emitted visible light to a CCD camera. This method is limited by the formation of grain on the film and possible non-linearities of the

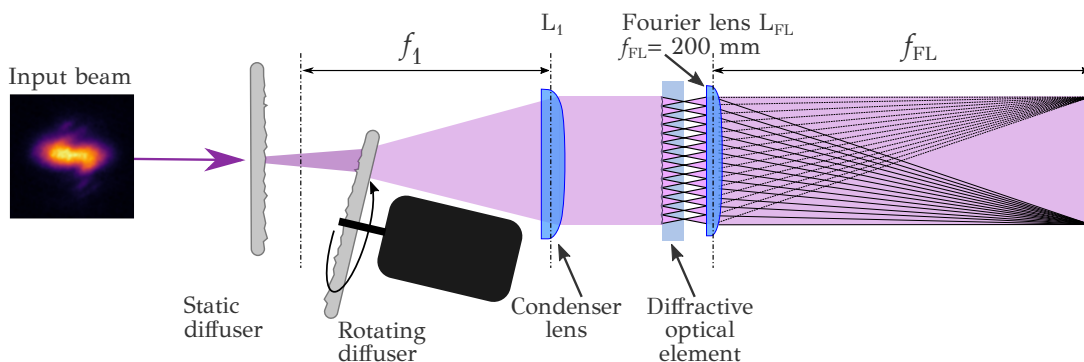


Figure 4.9: Non-imaging homogenizer for illumination at 193 nm. The input beam (left) is homogenized by a condenser lens with focal length f_1 , an eight-level DOE as a mixing element, and a Fourier lens with focal length f_{FL} .

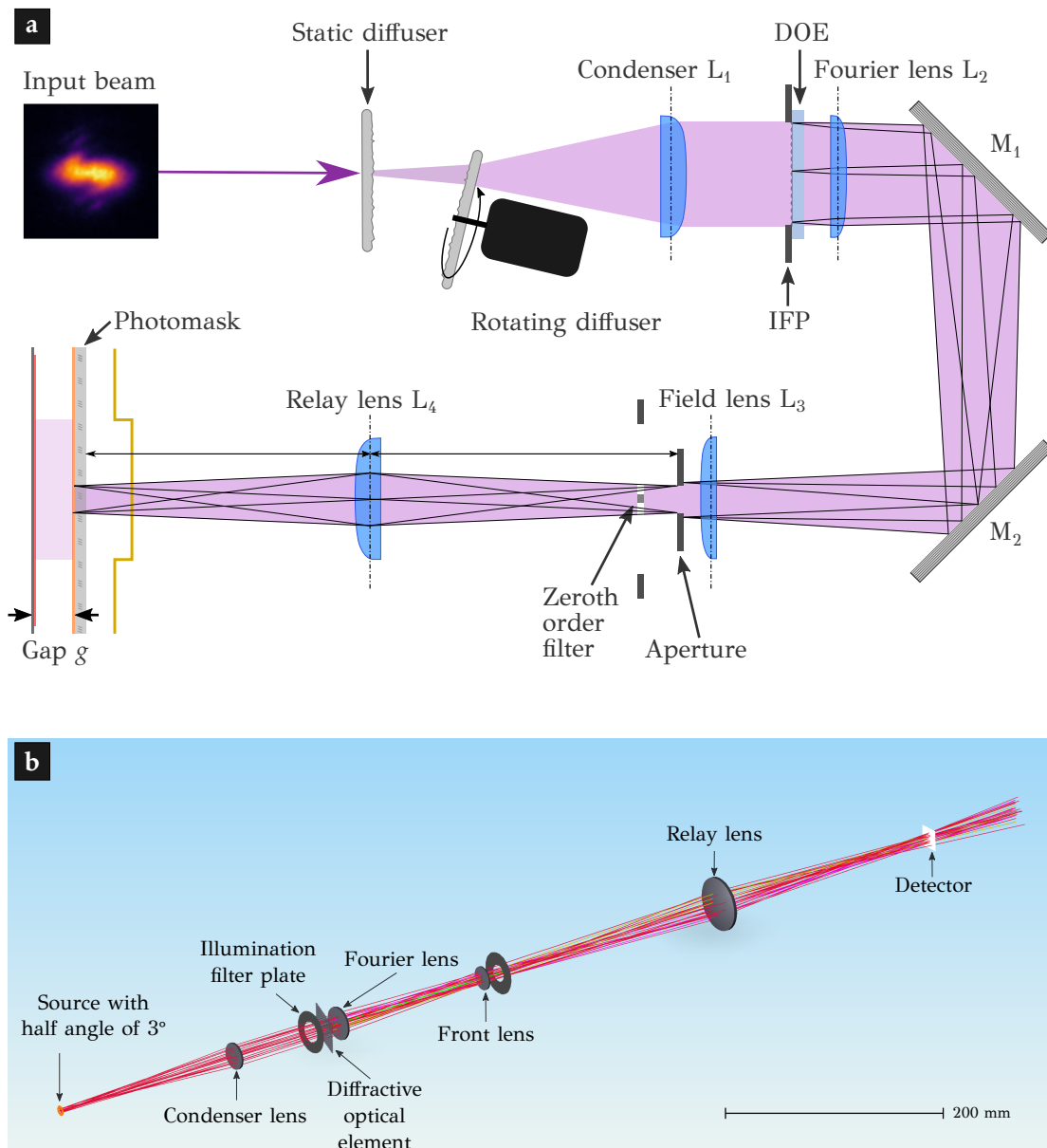


Figure 4.10: Optical setup of the non-imaging homogenizer.

a Sketch of the optical setup, including beam-shaping components made from fused silica. Besides the elements already introduced in Fig. 4.9, an IFP allows to shape the angular spectrum, and a telecentric setup images the homogenized field distribution on the mask plane. A filter for the zeroth order, consisting of an opaque circular aperture, is located near the intermediate image plane. The image of the front lens L_3 is relayed by the imaging lens L_4 to the mask plane. Sketch not to scale.

b Simulation setup for incoherent ray-tracing in *Zemax OpticStudio*[®]. For simplicity, the mirrors are omitted.

dye. We use this measurement system for the data presented in Fig. 4.11b and the insets of Figs. 4.11d and 4.11f.

In an improved approach for field mapping, we scan a DUV-sensitive silicon (Si) photodiode (Hamamatsu S1226-18BQ, with a photosensitivity of 0.13 A/W at 193 nm) in the field plane using a xy -stage with single micron precision and a step size of 300 μm . A laser-cut aperture defines the active area of 300 μm \times 300 μm . Each data point comprises an average over 20 individual measurement, each with an integration time of 10 ms.

Figure 4.11 provides a comparison between simulated and measured field distributions

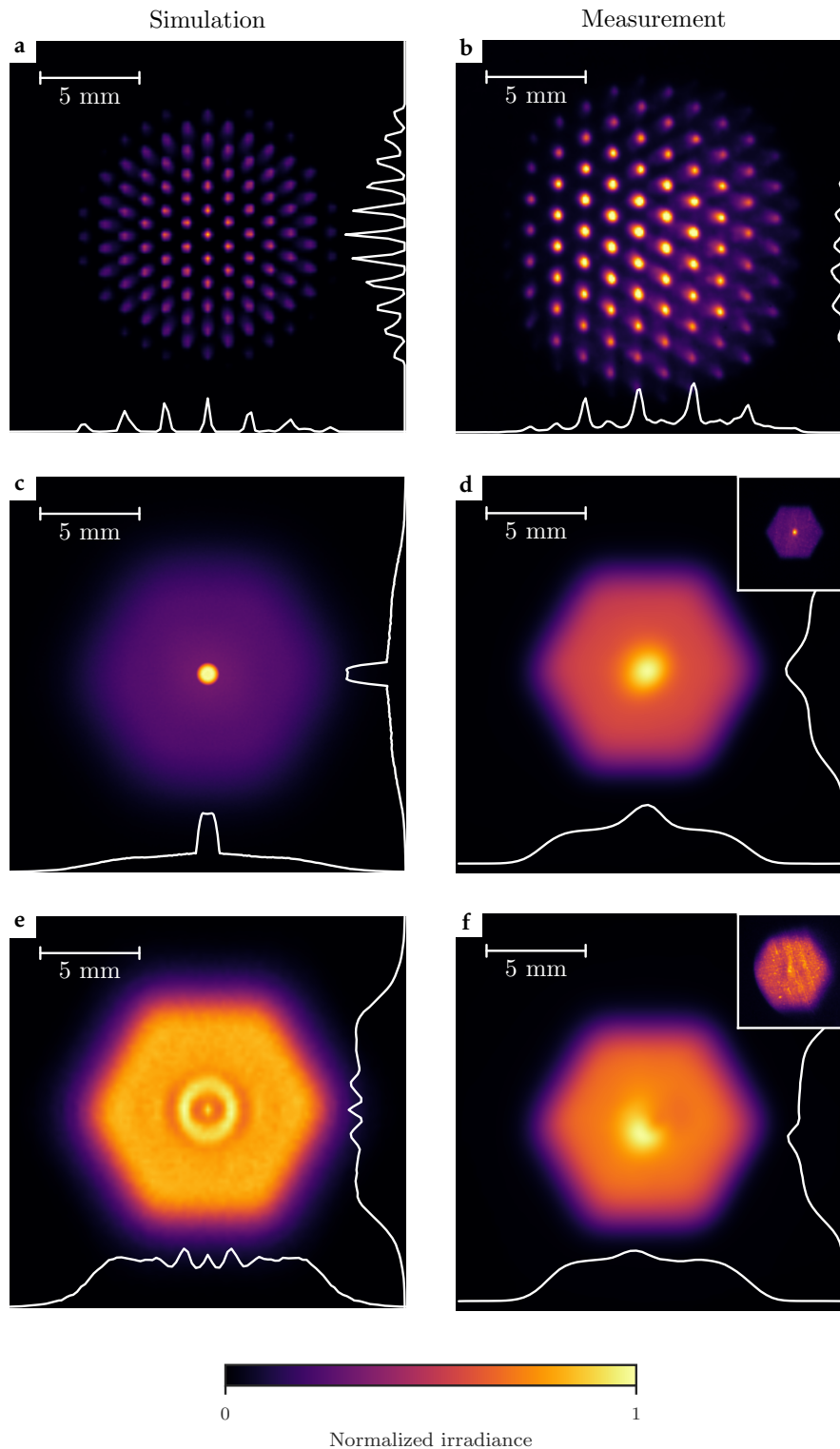


Figure 4.11: Simulated (left column) and measured (right column) irradiance distributions for a non-imaging homogenizer. For imaging, we use a lens with focal length of 150 mm (~ 135 mm at 193 nm). **b** and **f** are imaged with a 200 mm (~ 182 mm at 193 nm) lens, and afterwards scaled by a factor of 1.3. Plots in white show a cross-section of the irradiance along the center of the image. We observe a good agreement between simulation and measurement. Data has previously been published in [11, 19].
a, b Plane conjugated to the DOE. Individual beamlets are clearly visible.
c, d Mask plane without zeroth order filter. The inset shows data retrieved using a fluorescent dye.
e, f Mask plane with zeroth order filter. The inset shows data retrieved using a fluorescent dye.

in a conjugated plane to the DOE [a,b], in the homogenized plane without [c,d], and with the zeroth order filter [e,f]. In general, we observe an excellent agreement between simulated and measured results. A minor disagreement arises from a possible deviation in positioning and a small tilt in the alignment of optical elements. Shaping the angular spectrum is possible by selectively blocking or opening single channels. The individual channels are clearly visible in Figs. 4.11a and 4.11b. We observe a clear improvement in the uniformity of the field distribution in the mask plane, using a zeroth order filter.

Concerning the optical efficiency, defined as the power in the mask plane relative to the laser output power, we reach a value of $\sim 12.5\%$, relying on the setup depicted in Fig. 4.10. A large proportion of the losses emerge from reflections at each optical surface (about 6% per surface at $\lambda = 193\text{ nm}$) and the limited efficiency of the DOE ($> 80\%$). Applying ARCs on the optical elements is possible to enhance the power ending up in the mask plane.

In conclusion, we demonstrate the successful adaption of a non-imaging homogenizer to CW mask aligner lithography at 193 nm. However, especially for near plane wave illumination as required in Talbot lithography, most of the DOE channels have to be blocked, augmenting non-uniformities but also reducing the optical power contained in the beam. In the following section, we discuss an imaging homogenizer that offers the preferred approach for flat-tops with high uniformity.

4.2.3.2 Imaging homogenizer using a microlens array

As discussed in Section 2.3.1, an improvement can be expected from using an imaging homogenizer regarding field uniformity and efficiency. For coherence management, we place a rotating diffuser in the beam path, see Fig. 4.12a. Hence, we build an imaging Köhler integrator using two identical MLAs and a Fourier lens, as depicted in Fig. 4.12a. An additional field lens ensures telecentric illumination over a field of $15\text{ mm} \times 15\text{ mm}$.

Efficient beam homogenization requires a fill factor for the MLAs close to unity. Clearly, arranging spherical microlenses with a circular aperture reduces the fill factor, and square- or hexagonal-shaped spherical lenses would be an asset. However, the fabrication of such lenses with small dimensions is complex and to this day not possible in fused silica. Nevertheless, the same effect is achieved using cylindrical lenses in crossed arrangement (compare the inset of Fig. 4.12b), leading to a flat-top field with a square shape, while greatly reducing the demands on manufacturing. If the working distances are sufficiently large, the MLA in crossed arrangement acts as a single array, since the axial displacement of the principal planes of both cylinder lens arrays is insignificant [80]. Thus, we use uncoated cylindrical lens arrays with a pitch of $300\text{ }\mu\text{m}$, arranged on both sides of a fused silica substrate.

Figure 4.13 shows the irradiance distribution and the angular spectrum of the imaging homogenizer. Compared to Fig. 4.11, a clear improvement in the field uniformity is visible, owing to the greater number of mixing channels, irrespective of the initial beam shape. Also, a lower impact of diffraction effects can be seen especially regarding the zeroth order and blurring around the edges, as predicted by literature [80]. The non-uniformity over the entire field used for lithography is less than 3%, similar to the established MOEO[®] in mask aligner lithography [81]. As a disadvantage, more micro-optical elements are required, rendering the imaging homogenizer more complex and expensive. It is important to note that we chose a small field size for our proof-of-principle investigations, adapted to the mask design. By no means this is a general limitation: Following Eq. (2.5), an extension of the field size is possible by adapting the design parameters of the MLAs and/or the Fourier lens.

Shaping the angular spectrum for an imaging homogenizer requires selectively blocking individual microlens channels, here by introducing an IFP directly in front of the mixing

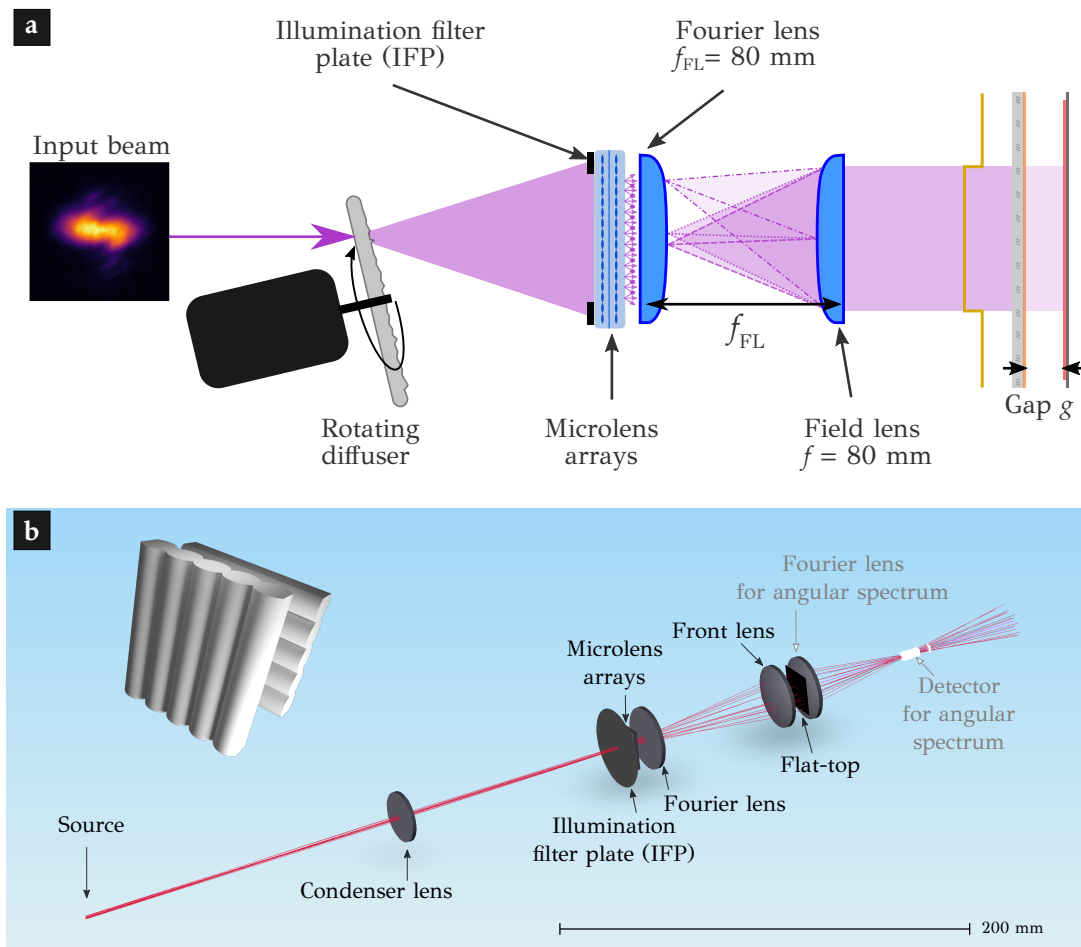


Figure 4.12: Imaging homogenizer for 193 nm.

a The input beam (left) is homogenized in the mask plane (right) by using a MLAs and a subsequent Fourier lens. Following a rotating diffuser, an IFP allows to shape the angular spectrum. The field lens in focal distance to the Fourier lens guarantees telecentricity. Sketch not to scale.

b Simulation setup for incoherent ray-tracing in *Zemax OpticStudio*[®]. An additional Fourier lens in the homogenization plane (flat-top) allows to determine the angular spectrum, illustrating our measurement method. The inset shows the crossed arrangement of cylindrical MLAs.

element. This is understood intuitively, as discussed in Section 2.3.1: The Fourier lens conducts a Fourier transform, i.e. the area illuminated on the MLA is transformed to an angular spectrum in the mask plane. The full angular spectrum of the imaging homogenizer, depicted in Fig. 4.13b, comprises half-angles of up to 2.5° . Two imaging homogenizers can be used in sequence to achieve a uniform angular spectrum: The first homogenizer illuminates the IFP of the second homogenizer uniformly, as exploited by MOEO[®] (see Section 2.3.1). In Section 4.4.1, we discuss near plane wave illumination required for Talbot lithography.

Concluding this section, we discussed two approaches for beam homogenization in CW laser lithography at 193 nm. By means of a rotating diffuser, the impact of a high spatial coherence is mitigated, leading to a high beam uniformity using an imaging homogenizer. In the following section, we report on experimental results of proximity and contact lithography.

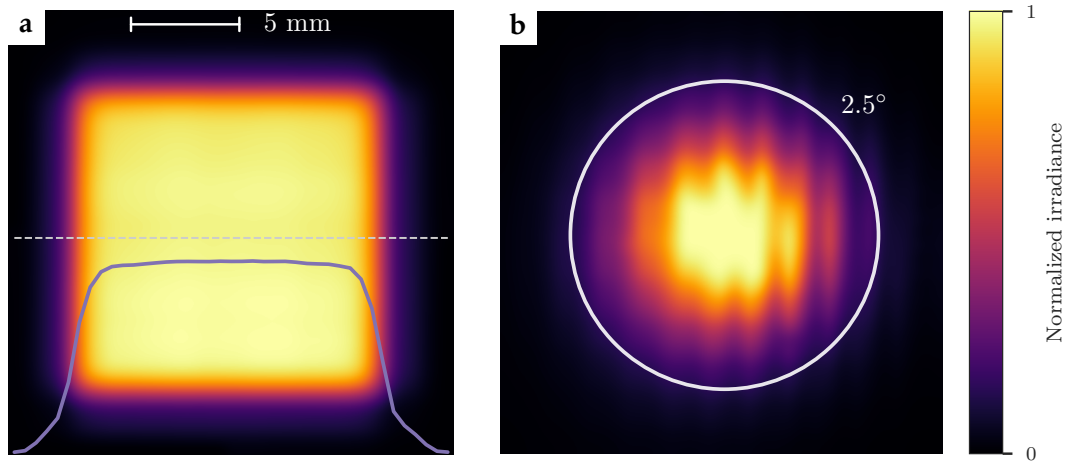


Figure 4.13: Measured **a** irradiance distribution and **b** angular spectrum in the homogenization plane for an imaging homogenizer. In **b**, the white circle indicates half-angles of 2.5° .

4.3 Experimental lithographic results

Having implemented a uniform illumination source, the next step towards experimental verification is the development of a lithographic process. We rely on established material platforms, with a photoresist dedicated to DUV ArF excimer lithography at 193 nm. Concerning the mask aligner setup, we use a mask chuck mounted on a high precision stage (*Etel Sarigan*) and a fixed mask chuck. The exact gap size is controlled at three locations via a spectroscopic reflectometer and a FFT evaluation (*Avantes AvaSpec ThinFilm Bundle*). A typical value for the proximity gap is $20\ \mu\text{m}$.

For the lithographic process, we apply the positive CAR *TOKTARF-P6239ME* with a thickness of 120 nm, measured after a prebake at 110°C for 1 min on top of a Si substrate. Following the exposure, a post-exposure bake again at 110°C for 1 min is performed, and for development we use a puddle process for 1 min in AZ MIF 327[®]. We vary the exposure doses between 10 and $65\ \text{mJ}/\text{cm}^2$.

Multiple interferences, arising from reflection at the interfaces air/resist and resist/Si substrate, cause the formation of standing waves inside the photoresist [93, 94]. The effect has previously been discussed in Section 2.3.2.2, and is shown here in Fig. 4.14a at a wavelength of 193 nm. The reflectance at these interfaces amounts to 6% and 56%, respectively.

To mitigate standing waves in resists, one solution is to apply a bottom anti-reflective coating (BARC), i.e., an additional photoresist layer on top of the substrate. This approach is demonstrated in Fig. 4.14b), featuring a BARC layer (ARC25 developed by *BrewerScience, Inc.*, with a refractive index of $1.84 + 0.46i$ at 193 nm) optimized for the wavelength and materials under consideration. Despite the clear improvement in light uniformity, we don't apply a BARC layer due to its unavailability during our experiment. Literature suggests improvements with regard to sidewall profile smoothness and to the variation of structure sizes when applying a BARC [28].

For demonstrating the capabilities of our lithographic techniques, we use the resist pattern to create a chromium hardmask via lift-off for subsequent inductively coupled plasma (ICP)-RIE of the silicon substrate (*Oxford Plasma Technology Plasmalab 100 ICP180*, HBr with a flow rate of 24 sccm, Cl_2 with 12 sccm, power 150 W).

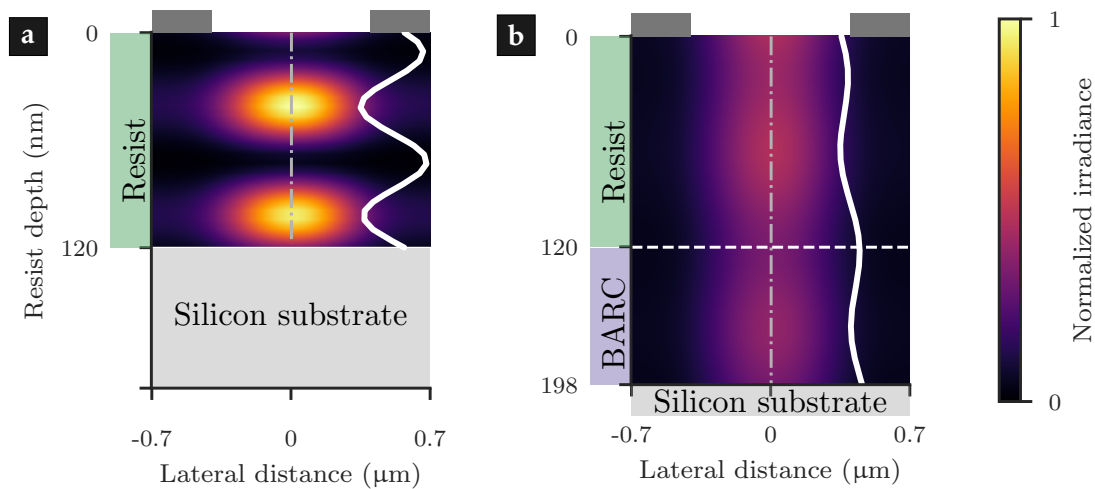


Figure 4.14: Aerial image distribution above a silicon substrate, simulated for $g = 20\ \mu\text{m}$. Both graphs have identical illumination properties, and the colorscale is normalized to the maximum irradiance in the left graph. We show the irradiance distribution along the gray dash-dotted line in white. Graph not to scale.

a The formation of standing waves inside the photoresist leads to hotspots with non-uniform absorption, with detrimental effects on the smoothness and uniformity of patterns in mask aligner lithography.

b The application of a bottom anti-reflective coating (BARC) diminishes the impact of standing waves, and homogenizes the light distribution.

In the following, we describe four approaches to mask aligner lithography: (i) Contact mode, yielding the highest resolution, (ii) canonical binary intensity proximity lithography at various gaps, (iii) diffractive phase-shift photomasks, and (iv) Talbot lithography for periodic patterns with near plane wave illumination.

4.3.1 Binary intensity photomask in contact and proximity lithography

The binary intensity photomasks for our proof-of-principle experiments contain structures to evaluate the resolution, for instance lines and spaces as well as circular and square vias, and are fabricated via e-beam lithography. We use the half-pitch as a CD to assess the resolution, quality, and fidelity of the process. It is paramount to keep in mind that no magnification takes place, i.e., the patterns of the mask are ideally transferred directly to the substrate, without change in the CD.

For the experiments presented in this section, we use the non-imaging homogenizer characterized in Section 4.2.3.1.

4.3.1.1 Contact lithography

SEM images for soft contact results between wafer and the photoresist-coated wafer are depicted in Fig. 4.15. All resolution structures are resolved down to a CD of 375 nm (see Fig. 4.15b), with line-end defects visible for the lines and spaces. The squares and holes are resolved as well, but require a separate optimization of the exposure dose. For contact lithography, the illumination wavelength has only a minor influence on the resolution, and the results presented here are similar to *i*-line illumination.

While the contact mode offers the maximum resolution possible in mask-aligner lithography, it suffers from being limited to wafers without prior topology and a possible damage

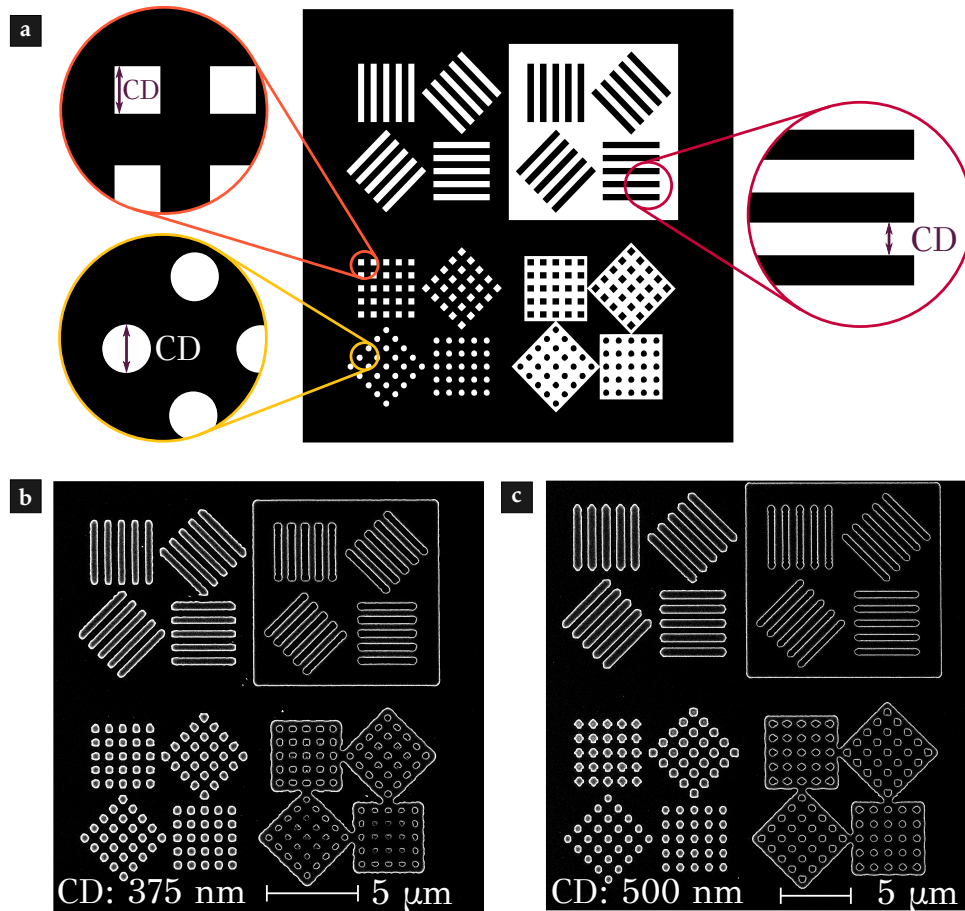


Figure 4.15: Soft contact lithography.

a Mask design of resolution test structures, featuring various CDs varying from 200 nm to 2000 nm. White areas are transparent to illumination, dark areas are chromium coated and opaque (OD of 3).

SEM images of photoresist in soft contact lithography, with a CD of **b** 375 nm and **c** 500 nm. For imaging, a thin gold layer was sputtered atop.

to the mask (see discussion in Section 2.2.1). The formation of defects reduces the reproducibility and the yield, rendering the proximity mode the preferred method for high-volume fabrication.

4.3.1.2 Proximity lithography

In proximity mode, we can resolve features down to a CD of 1750 nm at a proximity gap of $g = 20\ \mu\text{m}$, as shown in Fig. 4.16. For comparison, the typical resolution under *i*-line illumination is about $3\ \mu\text{m}$, as discussed in the context of Eq. (2.26). Line-end variations are more severe than in contact mode (compare Fig. 4.15), and can in principle be addressed by optical proximity correction (OPC) [see Chapter 6]. By adapting the exposure dose, the width of lines and spaces is subject to change, depending on the contrast of the resist and the angular spectrum. The uniformity in the illumination is sufficient to achieve consistent results over the printing field.

Following Eq. (2.25), we observe the expected improvement in the resolution for reducing the proximity gap. Figure 4.17 shows test structures etched in the Si substrate fabricated at a proximity gap of $10\ \mu\text{m}$. As a result, we demonstrate that lithography at 193 nm can be readily combined with existing semiconductor technology.

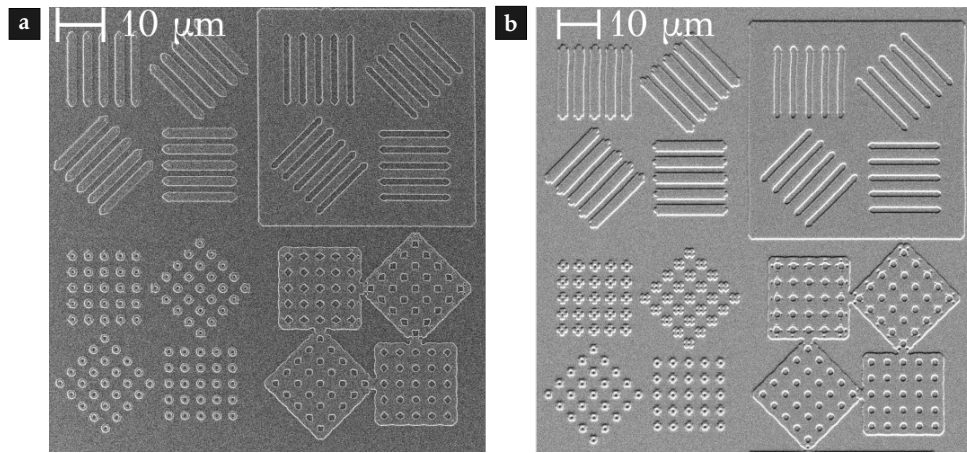


Figure 4.16: SEM micrographs of photoresist patterned in proximity mode, with a gap of 20 μm . CDs of lines and spaces: **a** 1750 nm, **b** 2000 nm.

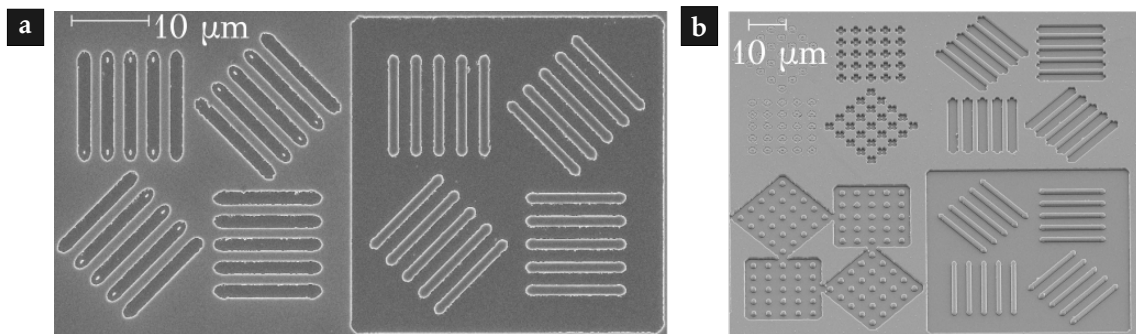


Figure 4.17: SEM micrographs of etched patterns in Si. The proximity gap is 10 μm , and the CD is 1500 nm in **a** and 2000 nm in **b**. The chromium etch mask is not yet removed. The etch depth is 400 nm and 800 nm, respectively.

4.3.2 Diffractive phase-shifting photomask for periodic nanostructures

Exploiting the high coherence of our source, we proceed by investigating a two-level PSM for proximity lithography. To achieve a phase shift of π , following Eq. (2.9) and taking into account the refractive index of quartz glass, the nominal step height is 172.6 nm. The experimentally determined phase shift of the fabricated mask is $\sim 0.986\pi$, measured by the manufacturer. By inserting an IFP as described in Section 4.2.3.1, seven illumination channels are selected, corresponding to the central channel and the inner ring in Fig. 4.11b with illumination half-angles of 0° and 0.57° . Since only seven beamlets contribute to the image formation, the beam is strongly non-uniform. The proximity gap is fixed at 20 μm . We show here two applications for a two-level chromeless PSM.

First, we introduce a one-dimensional grating with a period of 1 μm (see Fig. 4.18a). The grating is reproduced, with visible roughness at the edges. This deviations might arise from non-uniform illumination angles, interfering in the photoresist. Over the plot field, variations in the linewidth arise from non-uniformities in the homogenized beam. We wish to conclude that our light source is appropriate for performing interference lithography, but requires the use of an imaging homogenizer for near plane wave illumination, as discussed in Section 4.4.1 for Talbot lithography.

Second, for applications as metasurfaces [216], photonic crystals (PhCs) used in bio-sensing [217], or microchannel plates in photomultipliers [218], nanohole arrays are of interest. Hence, as a second implementation of a PSM, we demonstrate hole arrays in a

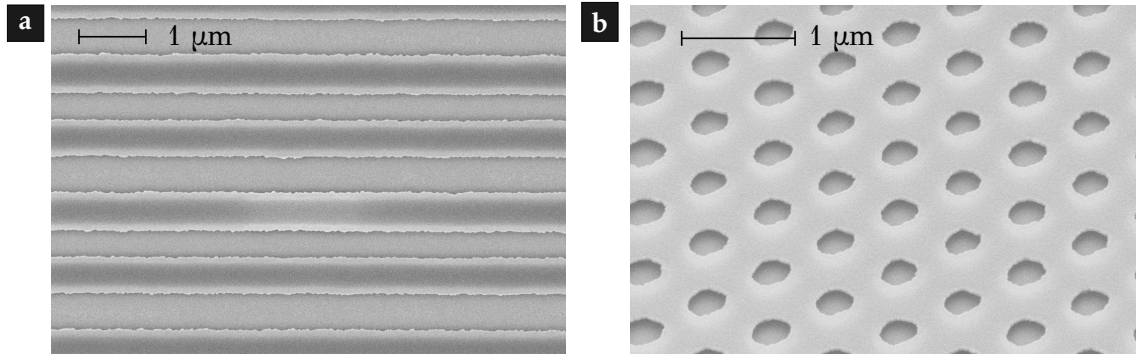


Figure 4.18: SEM images of photoresist patterns structured with PSM at a proximity gap of 20 μm , demonstrating the application of a CW laser emitting at 193 nm to interference lithography.

a 1D grating with a period of 1 μm .

b Holes in a hexagonal array with a center-to-center distance of 650 nm. Imaged under an angle of 35°.

hexagonal unit cell, with a period of about 700 nm (see Fig. 4.18b). The pattern is similar to the dense hole array presented in Chapter 5.

In conclusion, this section introduced the experimental results using a 193 nm CW laser for mask aligner lithography. We demonstrate print results, with efficient speckle mitigation using a rotating diffuser and field homogenization using a non-imaging homogenizer. A strong resolution improvement over canonical *i*-line illumination in proximity lithography is demonstrated for lines and spaces patterns, culminating in resolved features with a CD of 1.75 μm at a proximity gap of 20 μm . Using a PSM, we realize a 1D grating featuring a period of 1 μm and a dense hole array with sub-micron period.

Hence, mask aligner lithography using a CW laser emitting in the DUV shows potential for use in applications requiring a medium resolution. Its cost-effectiveness compared to projection lithography, its parallel operation compared to slow e-beam lithography, and its high yield compared to nanoimprint are beneficial for high-volume fabrication.

By combining the laser source with the Talbot effect, we gain a further resolution enhancement for periodic nanostructures. A simple binary intensity photomask, either blocking or transmitting incident light, is sufficient to print periodic features in high resolution, greatly reducing the complexity of mask fabrication compared to PSMs. Experimental results for Talbot lithography at 193 nm are discussed in the following section.

4.4 Mask aligner Talbot lithography at 193 nm

A laser is the preferential illumination source for Talbot lithography: Its narrow bandwidth prevents spectral blur and avoids additional spectral filtering, and the high brilliance ensures efficient beam shaping for the required near plane wave illumination. As discussed in Section 4.1 in the context of Fig. 4.2b, a reduction in wavelength leads to an increase in Talbot length z_T , also resulting in smaller feature sizes at a fixed proximity gap, compared to *i*-line illumination. Beyond the resolution, likewise the DOF enlarges, augmenting the process window for variations in the proximity gap.

In this section, we first discuss the performance of an imaging homogenizer for near plane wave illumination, proceed by presenting aerial image simulations, and conclude with experimental prints in the first and higher Talbot planes.

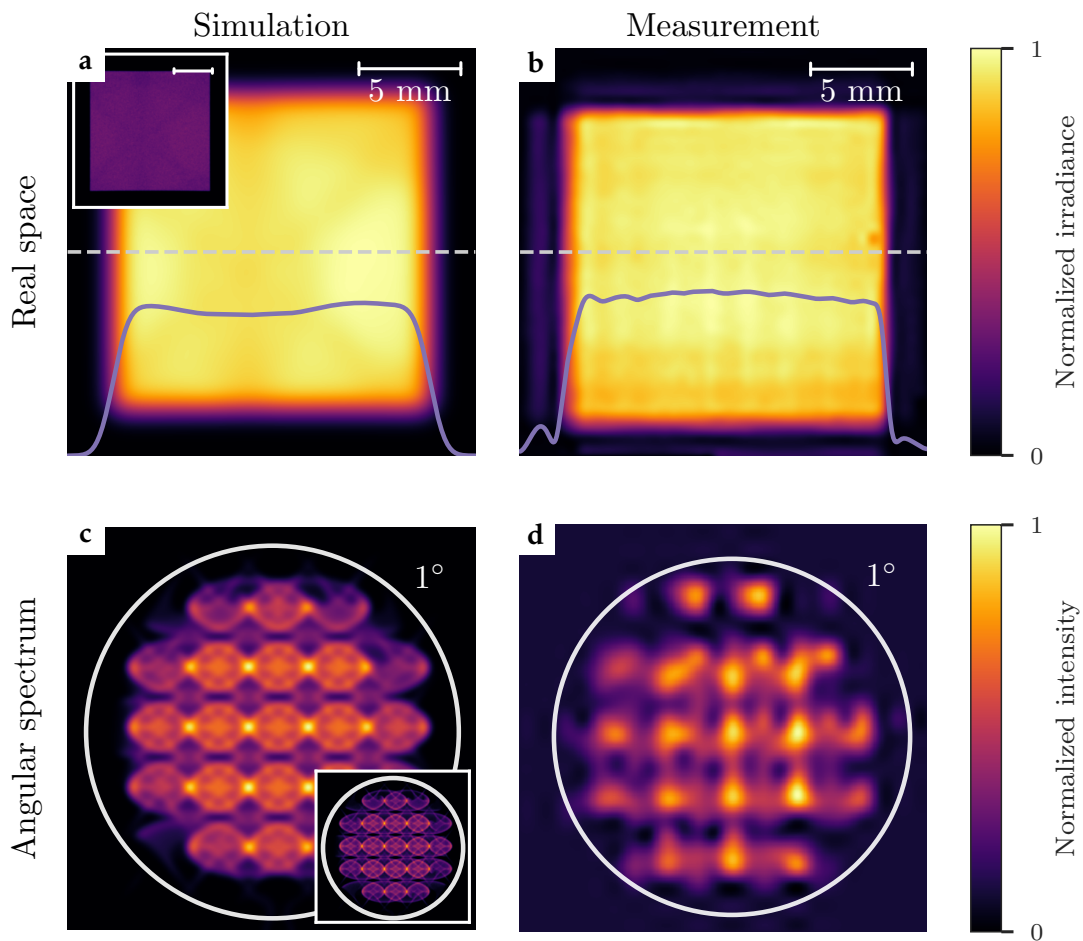


Figure 4.19: Beam profile for near plane wave illumination, according to the schematic in Fig. 4.12a.

a Simulated and **b** measured flat-top irradiance in the mask plane. The insets show the simulated distribution before applying a Gaussian filtering.

c Simulated and **d** measured angular spectrum in the mask plane. The white circle denotes half-angles of 1° .

4.4.1 Near plane wave illumination

For near plane wave illumination (half-angles $< 1^\circ$), only a small area in the center of the imaging homogenizer's MLA is illuminated, corresponding to a small number of channels. We use an iris aperture for selecting the angular spectrum, and use an additional condenser lens to focus the incident light to the aperture area. Due to the reduced pitch of the MLAs compared to the non-imaging homogenizer, more channels contribute in the superposition plane, resulting in an improved field uniformity. For plane wave illumination using imaging homogenizers, the fundamental trade-off emerges between a narrow angular spectrum, achieved with less channels, and a more uniform field by increasing the number of channels. The smaller channel size renders the imaging homogenizer more suited for Talbot lithography.

Figure 4.19 shows the simulation and the experimental results for the flat-top and the angular spectrum in the mask plane. To facilitate a comparison between simulation and measurement, we have to account for the aperture defining the active area of the photodiode. Hence, we apply a Gaussian filter sampling to the simulation results, choosing the standard deviation to be equal to the aperture size (see Section 4.2.3.1). We both simulate

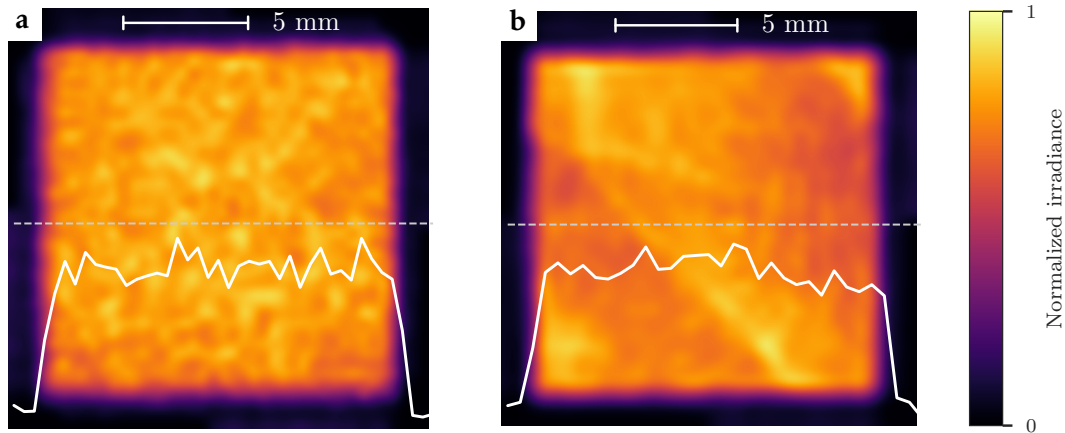


Figure 4.20: Irradiance distribution measured for **a** static and **b** without optical diffuser. The formation of speckle leads to a deterioration of the uniformity.

and measure a uniform flat-top over the print field, with a measured non-uniformity below 3% [9].

By inserting an additional lens located in the mask plane (focal length of ~ 125 mm at 193 nm), we measure the irradiance in the focal plane, corresponding to the angular spectrum (shown in Figs. 4.19c and 4.19d). Individual channels of the MLA are visible, arising from underfilling the NA of the MLA. Both simulation and measurement agree reasonably well, and demonstrate an angular spectrum with half-angles well below 1° . By further reducing the opening area of the IFP and thus the number of channels, a more narrow angular spectrum could be achieved, while sacrificing beam uniformity and total power in the mask plane. Using optical simulations, we show in the following Section 4.4.2 that the demonstrated angular spectrum is sufficient for Talbot lithography.

Again, we rely on a rotating diffuser to mitigate the visibility of speckle. Figure 4.20 justifies the necessity of a diffuser: With either a static or without any diffuser, the non-uniformity rises drastically. The resolution of our measurement setup is not sufficient to resolve individual speckle (compare discussion in Section 4.2.3.1). Next, we investigate the applicability of this near plane wave illumination to Talbot lithography in optical simulations.

4.4.2 Aerial image simulation with near plane wave illumination

By means of optical simulations, we compare the Talbot effect under perfect plane wave illumination and the experimentally determined angular spectrum. As an example, we choose a circular opening with radius of 400 nm in periodic arrangement. We show the field behind the mask in Fig. 4.21. The period of $1.4 \mu\text{m}$ corresponds to a Talbot length $z_T = 20 \mu\text{m}$ at $\lambda = 193$ nm.

As expected, the finite angular spectrum results in a lateral blur of the simulated irradiance, hence diminishing the contrast observed for plane wave illumination. However, the circular shape is reproduced in the Talbot plane (see inset of Fig. 4.21b), which justifies the use of a finite angular spectrum for Talbot lithography. A direct experimental measurement of the field distribution is possible, for example using scanning near-field optical microscope (SNOM) [219] or high-resolution interference microscopy [220, 221] adapted to the DUV. Such experiments are, however, out of scope of this thesis.

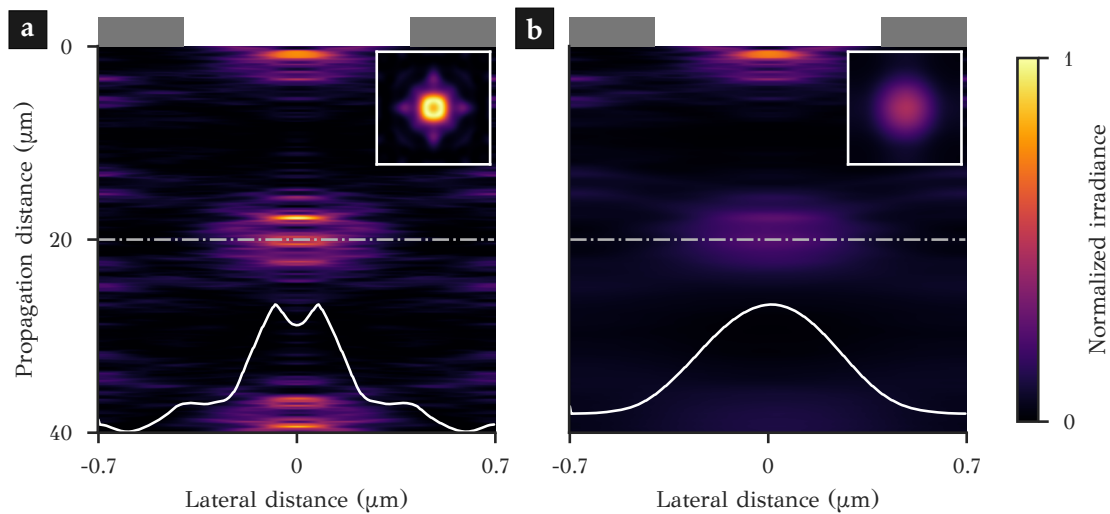


Figure 4.21: Simulated field distribution for Talbot lithography under **a** plane wave and **b** the measured angular spectrum, as shown in Fig. 4.19d. Gray bars indicate the opaque area of the unit cell with a side length of $\Lambda = 1.4 \mu\text{m}$, corresponding to a Talbot length of $z_T = 20 \mu\text{m}$. To ease the comparison, the profile along the dashed line is plotted in white. The circular shape of the feature is transferred to the Talbot plane, though with a lateral blur arising from the finite illumination angles. Graph is not to scale.

4.4.3 Experimental results of Talbot lithography

Self-imaging of periodic mask features using the Talbot effect takes place in several planes, as discussed in detail in Section 2.4.3.2. We restrict our investigations here to a fractional Talbot plane with $m = 1/2$, the fundamental Talbot plane at $m = 1$, and higher Talbot planes featuring $m = 2, 3$, and 4. Our approach aims for a 1:1 replication of the mask feature. Corresponding binary intensity test structures are designed for a quadratic unit cell and a proximity gap of $20 \mu\text{m}$, featuring basic geometric shapes such as squares, circles, and triangles. With periods in the single-digit micron range, such patterns are of interest for the optical lithography of metasurfaces operating in the near- and mid-IR range [216, 222, 223].

4.4.3.1 Fractional Talbot plane

To begin with, we consider the fractional Talbot plane at $m = 1/2$, with a period of $\Lambda_{1/2} = 2.0 \mu\text{m}$ calculated by inverting Eq. (2.35). We use the Talbot effect to expose the positive-tone photoresist, and proceed with a chromium lift-off and RIE. Figure 4.22 shows SEM micrographs of the results for square and triangular features, with the chromium hard mask not yet removed. The insets illustrate the design and dimensions of the mask features and unit cell. We observe a reliable replication, with rounded corners emerging for both shapes under consideration. We attribute corner rounding to higher harmonics that do not propagate and hence do not take part in the image formation [122]. This corresponds to large \mathbf{n} in Eqs. (2.30) and (2.31).

4.4.3.2 Fundamental Talbot plane

In the fundamental Talbot plane ($m = 1$), the period corresponding to a proximity gap of $20 \mu\text{m}$ is $\Lambda_1 = 1.39 \mu\text{m}$. Figure 4.23 shows colorized SEM images of circular structures in the photoresist after development and cylindrical structures after RIE. Again, the desired shape is reproduced with high fidelity, but the cylinders' sidewalls appear slanted. Here,

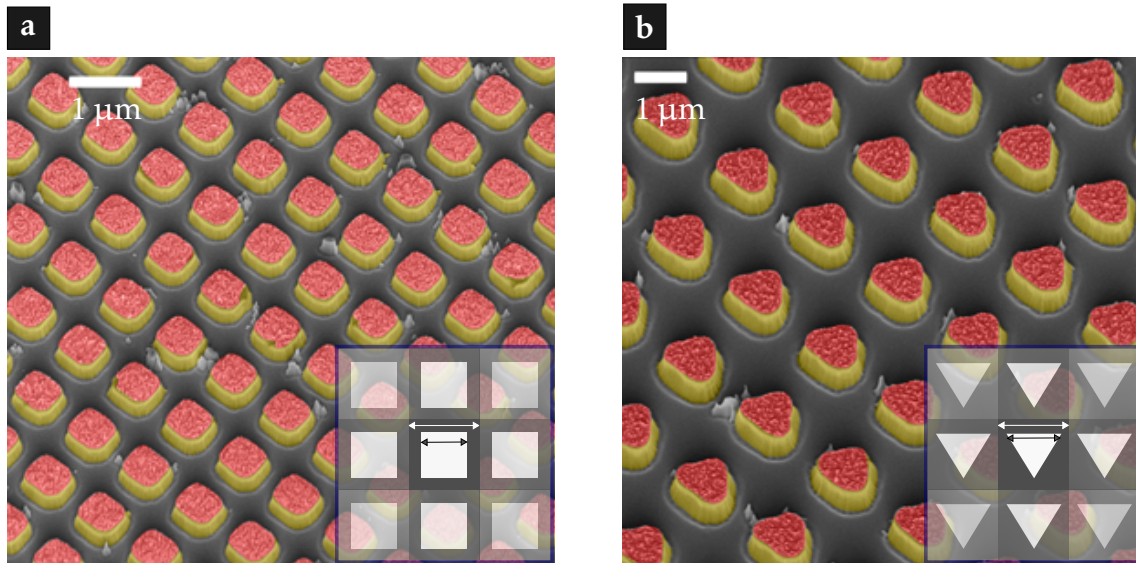


Figure 4.22: Talbot lithography in a fractional Talbot plane. With a unit cell of size $\Lambda_{1/2} = 1.97 \mu\text{m}$ and a proximity gap of $20 \mu\text{m}$, the Talbot order corresponds to $m = 1/2$. These colorized SEM images show the chromium hardmask (dyed in red), patterned by Talbot lithography, and subsequent etching of **a** quadratic and **b** triangular Si structures (dyed in yellow, etch depth $\approx 850 \text{ nm}$). For imaging, the sample is inclined by an angle of 30° . The insets sketch the design of the binary intensity photomask. The transparent areas are depicted in white, while gray areas block the illumination. White arrows denote the size of one unit cell ($\Lambda = 1.97 \mu\text{m}$), and black arrows indicate the side lengths of the squares and triangles of $1.20 \mu\text{m}$.

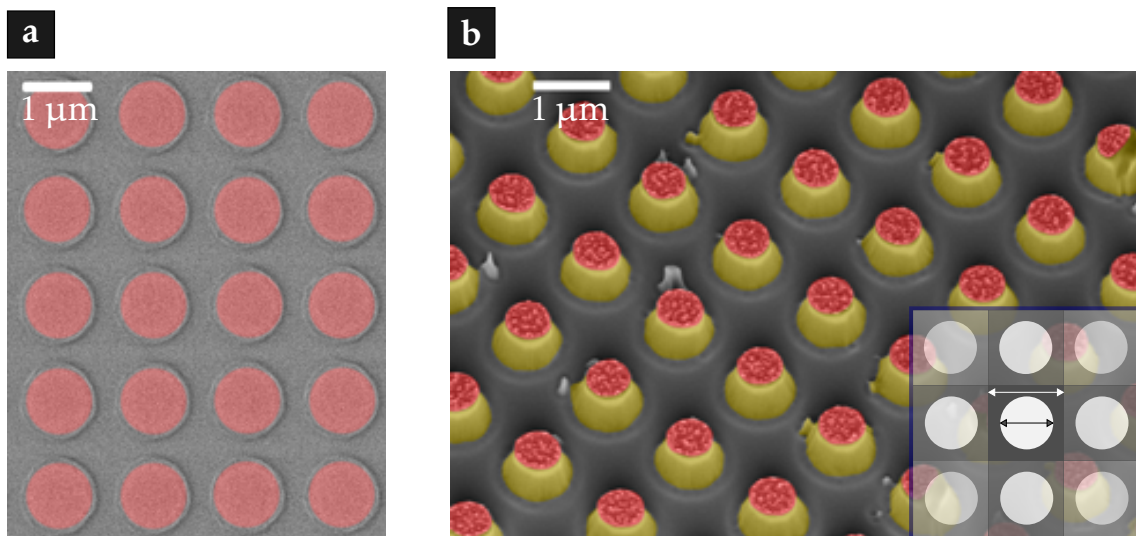


Figure 4.23: Experimental results of Talbot lithography in the first Talbot plane. **a** SEM image of resist openings after development and Cr deposition. After lift-off, the remaining hardmask is used for etching. **b** Si micropillars after etching, with the hardmask (dyed in red) not removed. The inset illustrates the design of the binary intensity photomask. The white arrow denotes the period $\Lambda = 1.4 \mu\text{m}$ of one unit cell and the black arrow indicates the diameter of $0.8 \mu\text{m}$.

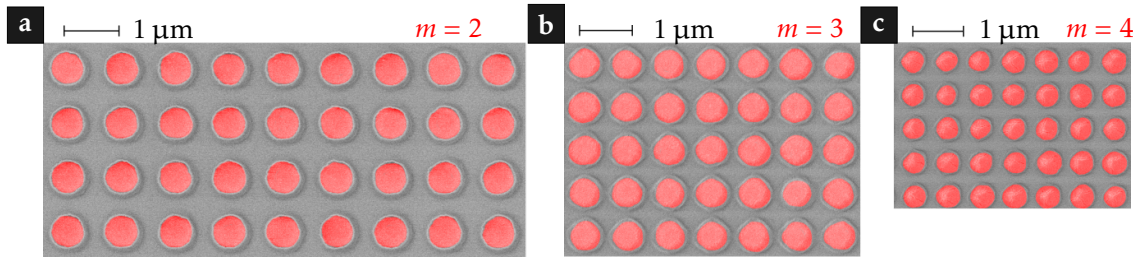


Figure 4.24: Colorized SEM images of the structured photoresist in **a** the second ($\Lambda_2 = 0.99 \mu\text{m}$), **b** the third ($\Lambda_3 = 0.81 \mu\text{m}$), and **c** the fourth Talbot plane ($\Lambda_4 = 0.719 \mu\text{m}$). While conserving the circular shape, the holes in **b** and **c** are not free of photoresist down to the substrate.

for structures with high aspect ratios, deep reactive-ion etching (DRIE) like the Bosch process might be more appropriate. The application at hand for cylindrical structures are polarization-independent metasurfaces [216].

4.4.3.3 Higher Talbot planes

Extending the concept of Talbot lithography at 193 nm, we turn to higher Talbot planes, with $m > 1$ in Eq. (2.38):

$$z_T \simeq 2m \frac{\Lambda^2}{\lambda}. \quad (2.38 \text{ revisited})$$

For a fixed proximity gap equal to z_T , increasing m goes along with a decrease in the period Λ_m , leading to a reduced feature size. For the sake of clarity, let us consider a periodic pattern with a period of 710 nm. Ultimately, using Eq. (2.36), this corresponds to a Talbot length $z_T = 5 \mu\text{m}$. Instead of struggling to set this gap in the experiment, which is difficult due to limited wafer flatness, the original proximity gap can be restored when using the fourth Talbot plane. The only additional complication is the shrinkage of the DOF under non-perfect illumination. Please keep in mind that using a higher Talbot plane for printing requires dedicated mask structures with the actual period, i.e., no dynamic change in the feature size is possible here.

We apply this concept to the second, third, and fourth Talbot plane, corresponding to periods of $\Lambda_2 = 0.99 \mu\text{m}$, $\Lambda_3 = 0.81 \mu\text{m}$, and $\Lambda_4 = 0.719 \mu\text{m}$, respectively. Figure 4.24 shows colorized SEM micrographs of the photoresist, validating the process and demonstrating the excellent quality of the image transfer process. The smallest feature size is hence obtained in the fourth Talbot plane, with a hole diameter of $\simeq 500 \text{ nm}$. While the structures in the second Talbot plane are fully developed to the substrate, in the third and fourth Talbot plane resist remains in the holes after development. Further optimization is needed to enable a lift-off process.

Three reasons are identified for this behavior: First, smaller periods result in high diffraction orders becoming evanescent, not contributing to image formation. Second, the lateral blur due to a finite angular spread in the illumination is more severe at reduced periods and large gaps. Third, the reduced DOF renders the placement of the wafer in the Talbot plane more sensitive to variations.

4.5 Concluding remarks on CW laser lithography at 193 nm

In conclusion, we successfully demonstrated the aptitude of a frequency-quadrupled CW laser source for mask aligner lithography with high resolution. First, we introduced the laser source in the DUV regime and discussed its properties concerning long-term stability and advantages over excimer sources. Coherence management is performed by static and/or rotating shaped random diffusers. We compared the performance of non-imaging and imaging homogenizers, implemented as a DOE and a MLA, respectively.

In proximity mode, we achieve a performance surpassing the canonical *i*-line illumination, arising from the fact that a wavelength reduction diminishes the impact of diffraction, following Eq. (2.25). At a proximity gap of 20 μm , the minimum feature size for lines and spaces is below 2 μm . Under near plane wave illumination, we use the high coherence of the source and perform Talbot lithography, with a minimum period of $\approx 700\text{nm}$ and a minimum feature size of $\approx 500\text{nm}$.

An extension to this proof-of-principle experiment to full wafer size is straightforward, using larger optics and adapting the Fourier lens. However, an upscaling in output power is required to facilitate reasonable exposure times. The strongest potential for improvement lies in the SHG within the KBBF nonlinear crystal, especially with regard to optical bonding. One interesting extension of the setup has been introduced by Weichelt *et al.* [64]. They demonstrate the use of a mirror galvanometer to scan the IFP. Along this way, no light is absorbed, rendering the approach more efficient.

Our DUV laser source can be readily combined with other resolution enhancement techniques, as for example Talbot displacement lithography [140], double patterning [119], off-axis illumination [50], and rigorously optimized PSMs [153], as discussed in the following section.

Rigorously optimized phase-shift mask for creating a dense hexagonal dot pattern

Having investigated the benefits of a reduced wavelength to proximity lithography, we turn now towards optimizing the phase of the illumination while using canonical i-line illumination. In this chapter, we apply the concept of rigorously optimized phase-shift masks (RO-PSMs) to create a dense hexagonal dot pattern, i.e., a periodic pattern in a hexagonal arrangement with sub-micron dimensions. As discussed before, in proximity lithography this usually requires a photomask with feature sizes comparable to the desired pattern to print. To overcome the difficulties and expenses of fabricating such a complex photomask, we apply here the concept of angular RO-PSMs.

We present in this chapter the design and simulation of the RO-PSM, and discuss the experimental results of lithographic prints. Design and fabrication of the RO-PSM has been performed in cooperation with the group of Prof. Uwe Zeitner, Fraunhofer IOF, Jena. Special thanks to Yannick Bourgin and Tina Weichelt from IOF for their help.

Creating a periodic dot pattern in a dense arrangement is an important task for optical lithography, as we discussed in Section 4.4.3. Many important applications especially for dot patterns range from bio-sensors [217], photon multipliers using multichannel plates [218], and microfluidics [224]. The complexity of this task emerges from the high resolution required, with dot sizes in the order of the exposure wavelength, and the required critical dimension uniformity on a wafer scale. Of course, Talbot lithography is an option, but a de-magnification of the mask structure is only possible in the fractional Talbot regime, which suffers from low contrast and limited DOF. Without demagnification, mask fabrication is aggravated. To overcome this problem, we introduce the concept of angular PSMs, which allows to increase the dot density by shaping the angular spectrum.

The underlying idea is easy to grasp: We design the RO-PSM in a way to replicate the dot pattern featuring a large period under plane wave illumination at normal incidence and at a fixed proximity gap. By adding carefully selected plane waves under small angles (see Fig. 5.1), the dot pattern is replicated again, but laterally shifted with respect to normal incidence. In other words, we effectively create sub-lattices which are mutually shifted by adapting the illumination angle.

We use an IFP with three individual openings to obtain the required illumination angles. As discussed in [55], the IFP can be subdivided into small areas which are modeled as an ideal coherent source. However, in good approximation we can assume that each of these coherent areas are mutually incoherent. Each of the openings in the IFP forms a coherent source, but the three sources are incoherent with respect to each other. We follow this model in all simulations presented throughout this chapter.

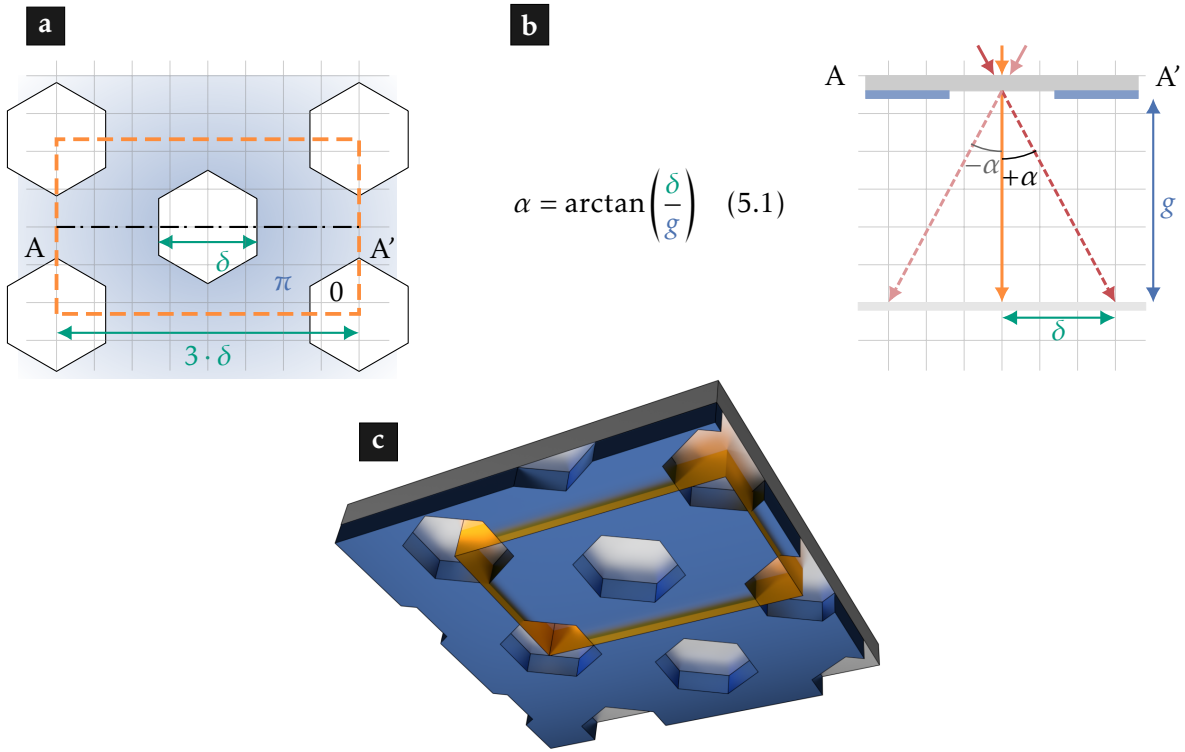


Figure 5.1: Sketch of the RO-PSM design.

a Hexagonal unit cell, with the important dimensions annotated. In the blue area, a phase shift of π is obtained. An individual unit cell is highlighted in orange, with a size of about $2 \mu\text{m}$ by $1 \mu\text{m}$.

b Illustration of the discrete illumination angles. The sketch shows a slice along the propagation from mask to wafer over the proximity gap g along the cut A-A'. The angles α are chosen such that the shift of the pattern δ corresponds to one third of the unit cell's length. Equation (5.1) describes the connection between g and the lateral shift δ , determining α as a low single-digit angle (when measured in degree).

c Rendered image of the hexagonal RO-PSM. The gray structure represents the fused silica substrate, and the blue structure indicates a fused silica layer with a phase shift of π . The orange box denotes one unit cell.

Hence, the incoherent superposition of these individual irradiance distributions leads effectively to a smaller period of the dot pattern. Using three discrete illumination angles, we show a reduction of the printed period to one third of the mask structures. A further objective is to have a wide latitude for setting the proximity gap, as discussed in Section 2.4.3.3, and a high contrast, as discussed in Section 2.3.2.2.

5.1 Mask design and optical setup

The foundation for the design of the RO-PSM is a standard two-level PSM made from fused silica. Figure 5.1a provides a sketch of the hexagonal unit cell. The blue area indicates a π phase shift over the free-space propagation in the hexagonal-shaped white areas. The phase shift arises from a height difference of $d = 384 \text{ nm}$, determined from Eq. (2.9) at *i*-line illumination. Being periodically arranged in a hexagonal pattern, the unit cell is indicated in orange¹⁷.

¹⁷The exact dimensions of the unit cell are not disclosed here, as being part of a customer-related product. At the same time, the dimensions are not of special interest, since the design can be optimized to other geometries as well. We indicate the order of magnitude where applicable.

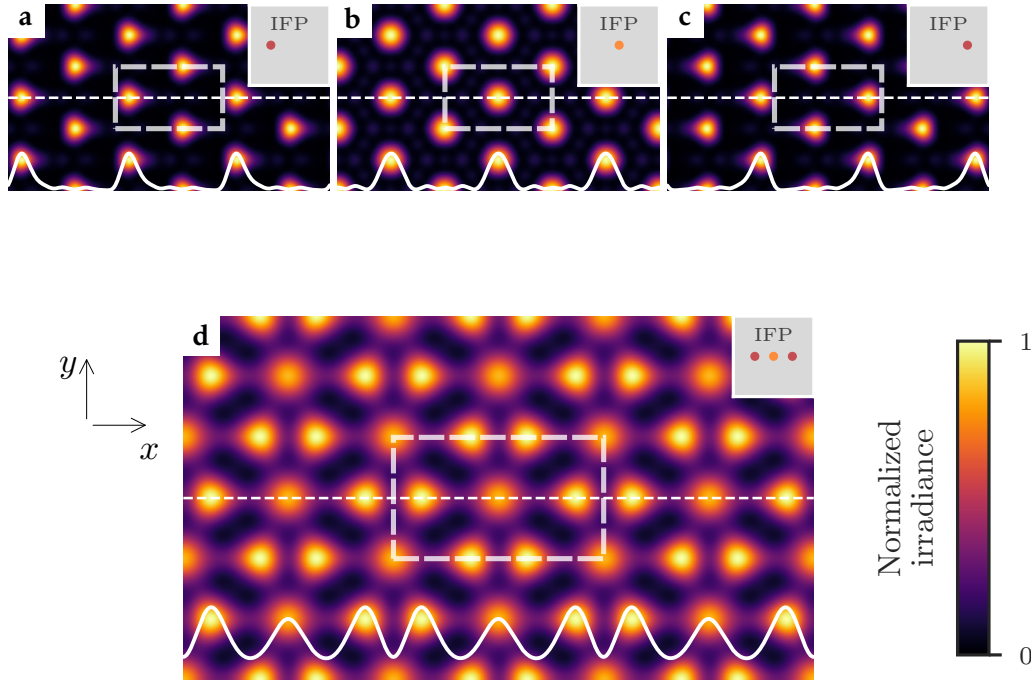


Figure 5.2: Simulation of hexagonal RO-PSM.

The simulated irradiance distributions show an array of 3x3 unit cells for a proximity gap of $g = 22\mu\text{m}$ under discrete plane wave illumination under an angle of **a** $-\alpha$, **b** zero, and **c** $+\alpha$.

d Incoherent superposition of **a**, **b**, and **c**.

We consider unpolarized illumination by averaging over transverse-electric (TE) and transverse-magnetic (TM) illumination [see Eq. (5.2)]. One unit cell is indicated by a white dashed box. The insets show the IFPs to shape the illumination angles. The increased density of dots in **d** is clearly visible.

Figure 5.1b illustrates the derivation of the required illumination angles $\pm\alpha$. Here, we choose the lateral shift δ to be one third of the unit cell size along x . A simple geometric relation, Eq. (5.1), allows to adapt α to the proximity gap g . To obtain the required set of illumination angles in experiment, we employ MOEO[®], as introduced in Section 2.3.1.

5.2 Simulation of rigorously optimized phase-shifting masks

Following Section 2.4.3.3, a rigorous simulation of the mask structure is required to retrieve the aerial image. We use the FMM, as introduced in Section 3.2, to simulate one unit cell with periodic boundaries. The irradiance distributions are retrieved for each plane wave separately, with the plane waves mutually incoherent. This is a crucial aspect and the fundamental difference to the method of three-plane-wave-interference, as discussed for instance in [221].

To take the unpolarized nature of the light source into account, we average over TE and TM polarization p . The total field I_{total} is retrieved from a superposition of the individual irradiance distributions,

$$I_{\text{total}} = \sum_{p=\text{TE, TM}} (I_{x,p} + I_{y,p} + I_{z,p}). \quad (5.2)$$

Figure 5.2 shows the simulated fields for an arrangement of 3 x 3 unit cells at the desired proximity gap of $g = 22\mu\text{m}$. We distinguish three distinct cases, corresponding to illumi-

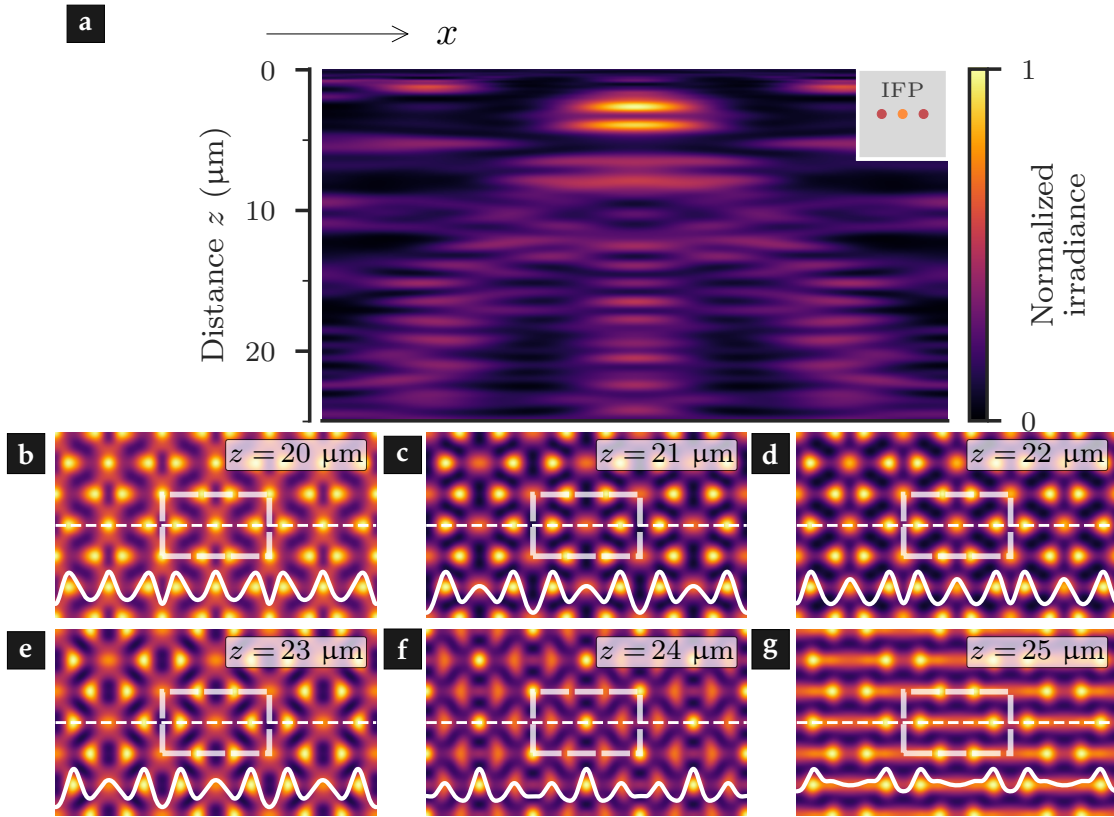


Figure 5.3: Light propagation in the hexagonal RO-PSM.

a Slice of the field irradiance over one unit cell in x -direction and along the gap in z -direction. The three discrete illumination angles are clearly visible, shifting one third of the period when propagating over the gap of 22 μm . Keep in mind that the figure is stretched along x , showing here only one unit cell.

b to g Field irradiance in planes between 20 μm to 25 μm behind the hexagonal RO-PSM. An evaluation of the contrast in different planes is provided in Fig. 5.4a.

nation under $-\alpha$ (Fig. 5.2a), under normal incidence (Fig. 5.2b), and under $+\alpha$ (Fig. 5.2c). The incoherent superposition of these three results is shown in Fig. 5.2d.

Under normal incidence, the periodicity of the mask is reproduced, with the hexagon shape (white areas in Fig. 5.1a) rounded to a dot shape. Illumination under an angle leads to a lateral shift of the irradiance pattern. The transmittance of the RO-PSM is about 89% for all angles under consideration. From simulations of the optical near-field of the mask (not shown here), we can observe a strong transverse redistribution of the wave power in the hexagonal RO-PSM, indicating that the TEA is not sufficient and our rigorous treatment is indeed necessary.

As a measure of quality, we consider the contrast C of the irradiance along the dashed line according to

$$C = \frac{I_{\max} - I_{\min}}{I_{\max} + I_{\min}}. \quad (5.3)$$

From the simulations, we extract a contrast of $C_0 = 0.94$ under normal incidence (higher is better). The hexagonal pattern now shifts in lateral direction under oblique incidence, as shown in Fig. 5.2c. The contrast $C_{\pm\alpha} = 0.84$ is slightly reduced, compared to normal incidence. The superposition of the two patterns, shown in Fig. 5.2d, results in the desired dense dot pattern. The nearest neighbor distance δ corresponds to one third of the mask

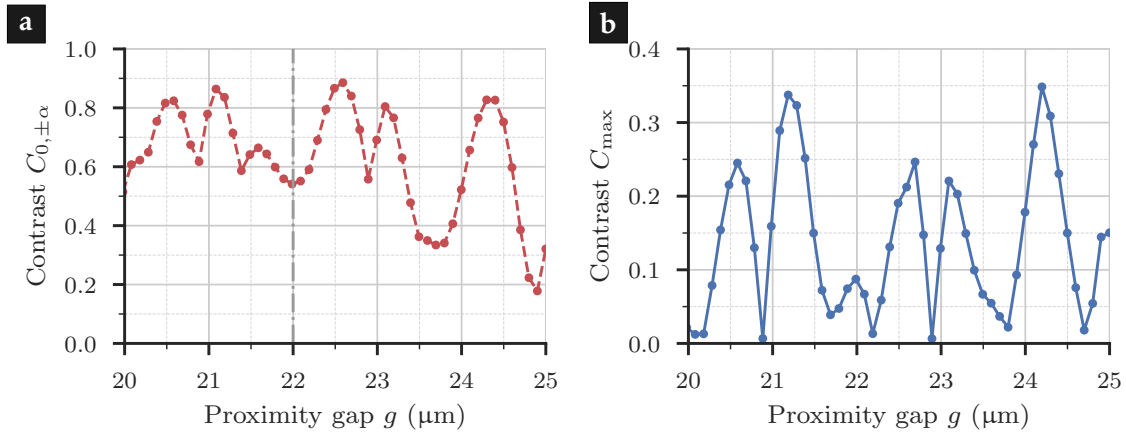


Figure 5.4: Contrast for the hexagonal RO-PSM. The lines serve as a guide for the eye.

a Contrast $C_{0,\pm\alpha}$, following Eq. (5.3) Around the optimized gap of $22\ \mu\text{m}$, the field shows a high contrast.

b Contrast C_{max} , following Eq. (5.4). Here, a lower value is better, as it corresponds to a lower peak-to-peak variation.

period, and the contrast reduces to $C_{0,\pm\alpha} = 0.54$.

Up to now, we considered a proximity gap of $g = 22\ \mu\text{m}$, the distance for which the angles $\pm\alpha$ are designed for. Next, we demonstrate the high DOF of this RO-PSM, which renders the process rather insensitive to gap variations. In Fig. 5.3a, we show the irradiance along the propagation over the gap, in a slice indicated by the dashed line in Fig. 5.2. The three illumination angles are visible, corresponding to the sketch in Fig. 5.1b. Other features in this graph arise from the Talbot effect, with a Talbot length $z_{\text{T,hex}}$ of about $5\ \mu\text{m}$, following Eq. (2.42).

Figures 5.3b to 5.3g show the irradiance for distances between $20\ \mu\text{m}$ to $25\ \mu\text{m}$. From these images, it is obvious that the pattern is well reproduced for variations up to $\pm 2\ \mu\text{m}$, but starts to deviate above $24\ \mu\text{m}$.

For a more quantitative analysis, we consider again the irradiance distribution along a one-dimensional slice (white dashed line) and focus on the contrast. Figure 5.4a shows the contrast $C_{0,\pm\alpha}$ as a function of the gap g (in blue).

The contrast confirms the interpretation of Fig. 5.3, namely, that a pattern transfer of the dense dot array is possible over an extended DOF with a contrast above 0.5 for the overall modulation. The image quality drops significantly above $g = 24\ \mu\text{m}$.

Furthermore, as discussed in Section 2.4.3.3, imperfect zeroth order cancellation contributes to a peak-to-peak variation, as observed in Figs. 5.3b to 5.3g. For evaluation, we define the contrast C_{max} of consecutive maxima, following [153]:

$$C_{\text{max}} = \frac{I_{\text{max}_1} - I_{\text{max}_2}}{I_{\text{max}_1} + I_{\text{max}_2}} \quad (5.4)$$

Figure 5.4b shows the contrast of consecutive maxima as a function of the gap g . Please note that here a value of 0 indicates a vanishing difference between consecutive maxima, and hence is preferred (lower is better). We observe a low C_{max} around the design gap of $22\ \mu\text{m}$, corresponding to the low peak-to-peak variation in Fig. 5.3d. Having established in optical simulations that the hexagonal RO-PSM performs as desired, we focus in the next section on the experimental realization.

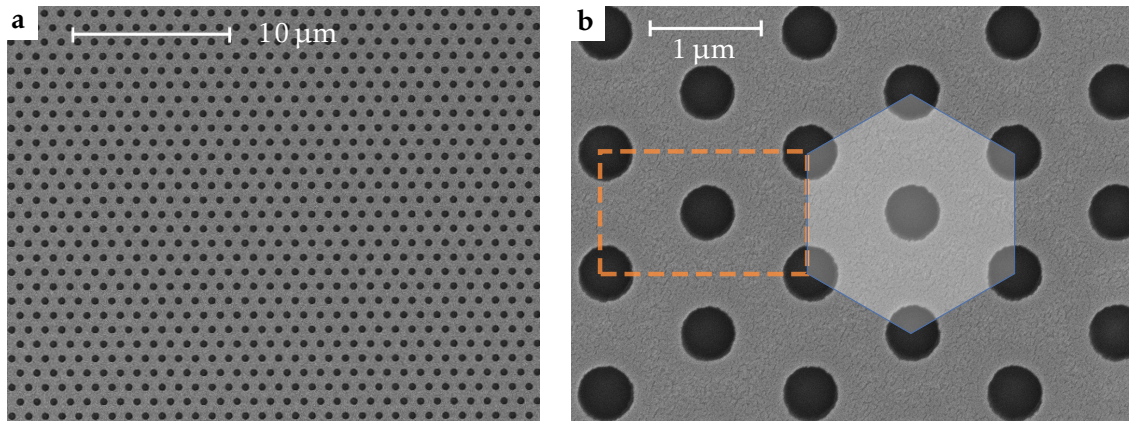


Figure 5.5: SEM images of experimental results for the hexagonal RO-PSM under normal incidence.

a Overview of a larger area and

b detailed view at an exposure dose of 12.5 mJ/cm^2 . The pattern corresponds to the simulation shown in Fig. 5.2b. The brighter area is sputtered gold required for SEM imaging on top of the photoresist, with the dark holes removed photoresist. For better orientation, we provide the unit cell (in orange) and the hexagon of holes (in blue and white).

5.3 Experimental results

For experimental verification, the fabricated hexagonal RO-PSM contains repeated arrangements of the unit cell (see Fig. 5.1a), spatially extended over a pattern area several square centimeters. For mask and wafer alignment, the prototype mask aligner described in Section 4.3 is used. Concerning the optical setup, we use a standard SUSS lamp house (MA150, 1 kW), with MOEO[®] for beam shaping. An additional *i*-line filter ensures monochromatic illumination.

The three illumination angles are selected simultaneously using one IFP situated in the Fourier plane, with the optical setup similar to Fig. 2.9. We use a laser-cut aluminium IFP with three circular openings, as schematically depicted in the insets of Fig. 5.2. The holes in the IFP are around 2 mm in diameter, with a hole-to-hole distance of 10 mm.

Considering the photoresist chemistry, we use AZ[®] 1512, diluted 1:1 to achieve a thickness of about 750 nm on Si substrates. Typical exposure doses are around 15 mJ/cm^2 . After exposure, the wafer is developed in AZ[®] 400K (diluted 1:4 with deionized water) for 3 min.

First, we perform experimental prints under normal incidence only, corresponding to the simulation shown in Fig. 5.2b. As presented in Fig. 5.5, the hexagonal dot array is reproduced, with the individual elements featuring a circular shape. The dot array is reproduced over the entire pattern area, with a low number of defects. Figure 5.5a shows an overview of a larger section, confirming the excellent shape uniformity. Ultimately, the uniformity is limited by gradients in the design parameters for the mask fabrication, resulting in geometry and phase errors, and the flatness of mask and wafer, introducing local gap variations.

Using all three angles 0° and $\pm\alpha$ for illumination, we obtain the prints shown in Fig. 5.6. To perform these exposures, we only require to change the IFP, as discussed in the previous section. Again an excellent agreement between the rigorous simulation and the experimental prints is observed (compare Figs. 5.2d and 5.3). For the target gap of $22 \mu\text{m}$, as shown in Fig. 5.6a, the shapes are again almost circular, with a slight distortion also

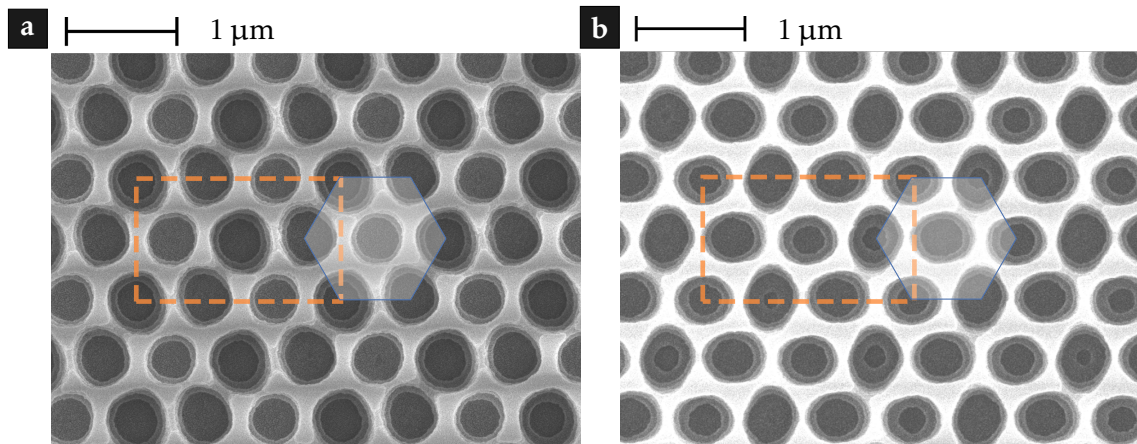


Figure 5.6: SEM images of experimental results for the hexagonal RO-PSM illuminated by three plane waves, at a gap of **a** 22 μm and **b** 20 μm . As in Fig. 5.5, the brighter area is sputtered gold required for SEM imaging on top of the photoresist, with the dark holes removed photoresist. For better orientation, we provide the unit cell (in orange) and the dense hexagonal arrangement of holes (in blue and white). The minimum feature size is around 400 nm. The exposure dose amounts to 10 mJ/cm^2 .

visible in the simulation Fig. 5.2d. In addition, the hole size is subject to variations, but can be adapted by slightly modifying the IFP: A larger opening allows to get more light exposing the corresponding sub-lattice, which according to the threshold model leads to larger feature sizes (compare Fig. 2.13a).

Up to now, we assumed perfect plane wave illumination. In essence, the finite size of the openings in the IFP leads to a blurred angular spectrum, which can be modeled by a wave packet of plane waves, centered around the design angles. From the IFP design, we can estimate the variation in the angular spectrum to be about $\alpha/10$. In addition, the finite spectrum for *i*-line illumination introduces a chromatic spread.

The fundamental tradeoff for using the proposed RO-PSM in large-scale fabrication concerns the angular spread and the power used for exposure: Shrinking the IFP feature size sharpens the angular spectrum, but less light is transmitted and hence the exposure time increases. One option to increase the exposure power without sacrificing performance is to focus light in the MOEO[®] setup on the discrete IFP openings, as discussed in the context of Section 4.4.1. Otherwise, only a fractional amount of the available power of the light source is used for actually doing lithography.

An interesting alternative to the canonical mercury lamp would be the use of laser sources for this task. Since a coherent superposition is neither necessary nor desired, three individual laser sources can be arranged to create the desired angular spectrum. When only a single laser shall be used, the use of a galvanometric mirror allows to dynamically adapt the angular spectrum, as demonstrated by Weichelt *et al.* [64].

Figure 5.6b shows the printed pattern for a gap of 20 μm , i.e., with a variation of 2 μm with respect to the optimization objective. Again, the pattern is reproduced with high fidelity, but the distortions strengthen, manifesting in slightly elliptical shapes.

The visible sub-structure inside the holes arises from the formation of standing waves, as better visible in the resist cross-section provided in Fig. 5.7. As discussed in Section 2.3.2.2, the standing waves form due to interference between incident and reflected light. The solution to diminish the formation of standing waves is to apply a BARC or use a substrate with reduced reflectance.

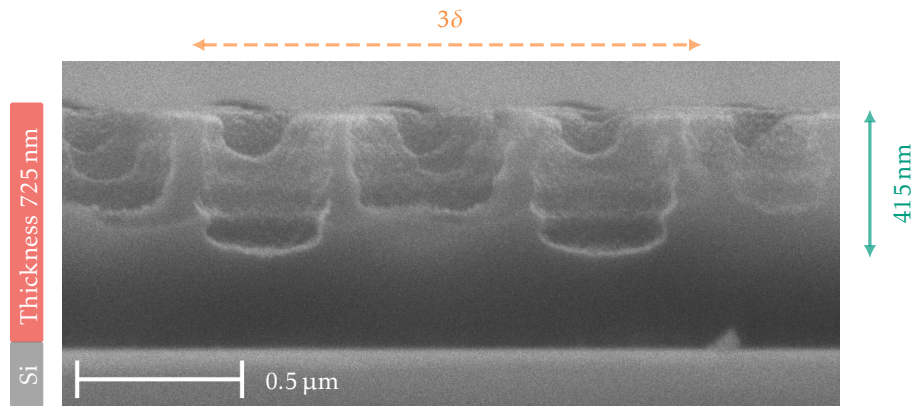


Figure 5.7: SEM micrograph of the resist cross-section. The Si wafer is deliberately broken along one crystal axis to facilitate imaging of the photoresist. We observe that the resist is not fully developed and the formation of standing waves leads to jagged resist sidewalls.

In addition, we discover that the resist is not developed down to the substrate, but rather about half the distance. This arises from the rather high absorption coefficient of the photoresist in use for *i*-line illumination, compared to other high-resolution photoresists. Increasing the exposure dose would mostly enlarge and eventually merge the structures. To resolve this issue, a thinner and/or an alternative resist with a lower absorption coefficient (e.g. AZ[®] 9260, [92]) can be used, to further enable RIE and lift-off processes.

In this chapter, we demonstrated a RO-PSM to create a dense hexagonal dot array by means of proximity lithography. Relying on a rigorous simulation method and a binary level PSM, we discussed the mask design and the aerial image after propagation over the proximity gap. By incoherent superposition of three plane waves, the pattern density is further increased. This reduces the requirements on mask fabrication and enables high-resolution proximity lithography at a high contrast > 0.5 . The process is designed to be insensitive against gap variations, which has been experimentally confirmed. Further optimization on the experimental side concerns the pattern transfer to the underlying substrate.

In the following Chapter 6 we leave the path of modifying the phase of light and turn towards amplitude photomasks to correct for image distortions as corner rounding.

Rule-based corner correction of non-Manhattan structures

Modifying light propagation by intensity modulation at the mask level is appealing: The modification is once encoded directly when fabricating the photomask. A mask aligner without further changes to the optical setup is continued to be used for printing using such photomasks. Adapting the photomask design offers a plethora of parameters that can be optimized, in practice only restricted by the finite resolution of the photomask fabrication. Within this large parameter space, a question arises concerning how to efficiently find photomask designs suited to increase the pattern fidelity. In literature, this task is commonly summarized by the term 'optical proximity correction' (compare Section 2.4.2.2).

In this chapter, we discuss two approaches for rule-based corner correction using binary intensity photomasks based on a rigorous simulation of light propagation. We discuss the design, the simulation, the optimization routine, and the sensitivity of the approach to process variations. Furthermore, we verify the results obtained from simulation in experimental prints. Parts of the research presented in this chapter have previously been published in [1].

For IC applications, the vast majority of photomask designs rely solely on so-called Manhattan geometries. Such designs consist of rectangular shapes in vertical or horizontal orientation only, just as the grid layout of streets in Manhattan. Recent advancements in the field of micro-optics require now to extend the technique to non-Manhattan layouts as well, hence relaxing the design constraints, but at the same time rendering the design of optical proximity correction structures more complex. The goal of this chapter is to extend the applicability of mask aligner photolithography to future challenges arising in optical fabrication.

6.1 Incentives and limitations of optical proximity correction in mask aligner photolithography applied to non-Manhattan geometries

As discussed in Section 2.4.2.2, optical proximity correction (OPC) deals with the pre-compensation of image shape distortions, with corner rounding and line-end shortening as the most prominent consequences. Here, we investigate a rule-based computational corner correction, with the goal to find simple geometric rules for OPC. Once such rules are obtained and verified, they can be applied to an arbitrary photomask design. Here, we impose the following prerequisites and assumptions to our method:

1. There is an efficient way to retrieve the shape of the features that are printed, either in simulation and/or in experiment. This includes to calculate the resist image, as discussed in Section 2.4.1.

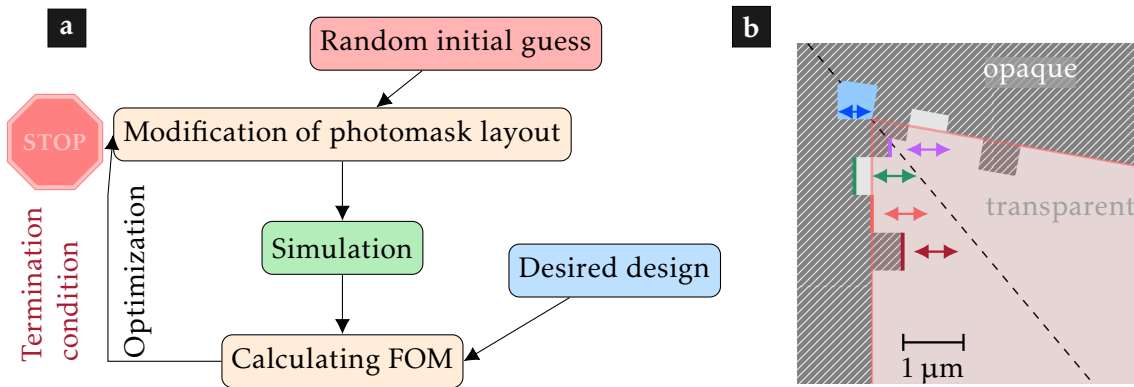


Figure 6.1: Optimization routine and serif bar design.

a Schematic diagram of the optimization routine. Based on a random initial guess, the photomask layout is modified. We simulate the aerial image distribution and retrieve a figure of merit (FOM), as described in Section 6.2.3. Using a particle swarm optimization (PSO) algorithm, the photomask layout is iteratively modified, with the goal to improve the FOM. The results are parameters specific to the inner angle under consideration.

b Illustration of the optimized correction structures around a corner, here exemplarily shown for an inner angle of 80° . Degrees of freedom during the optimization are the size of the corner serif (blue), the position, and the width of the four bars (red to magenta). The read area indicates the desired resist image. For all non-Manhattan geometries under consideration here, we make use of the underlying mirror symmetry along the bisectrix (black dashed line).

2. The distance of the correction structures to adjacent structures is sufficiently large, i.e., the mutual influence can be neglected. We investigate in Section 6.4.3 how close adjacent structures can approach a corner of interest until such a mutual influence is noticeable.
3. The correction structures comply with the requirements for full-field photomask fabrication using direct laser writing or e-beam lithography, especially with regard to minimum feature size and photomask registration.

In addition, for a tangible example, we choose a specific mask aligner setup:

4. For the exposure optics, we adapt the parameters of a standard mask aligner setup, including MOEO[®] and the HR-A IFP (compare Section 2.3.1). To achieve a high resolution in the experimental prints, we use an *i*-line filter, with an exposure spectrum centered at 365 nm and with a FWHM of 5 nm. However, the procedure can be applied to arbitrary spectra with ease.
5. Concerning the proximity gap, we select $g = 30\mu\text{m}$ as a typical gap used in proximity photolithography. While all optimizations are performed for this gap, we investigate the process sensitivity to gap variations as well. Please note that in general arbitrary gaps can be selected.

Up to now, most approaches to OPC in mask aligner photolithography cover Manhattan geometries only (see Section 2.4.2.2 for a review). Here, we describe two OPC approaches for non-Manhattan designs, by way of example for convex corners with an inner angle in the range of 45° to 130° , in 5° increment. This is a rather arbitrary choice but at one point we have to get definite. It has to be stressed that the OPC rules can be adapted to any other specific layout as well. The goal is to approach a digital twin of the lithographic process [58], which allows to assess the performance and the limitations imposed by this

method. It also allows to troubleshoot in case of emerging process errors and quality issues.

In the following sections we describe the design, simulation, evaluation, and optimization routines we apply to improve the pattern fidelity. Two approaches for the corner correction structures, called serif bar design and pixel-flip design, are introduced. We schematically illustrate all the ideas and concepts for an inner angle of $\alpha = 80^\circ$, but it is important to note that this value is chosen just for the sake of illustration. The concepts apply to all other angles under consideration in an analogous manner and indeed results thereof are presented at a later stage.

6.2 Optical proximity correction using the serif bar design

The serif bar design consists of simple geometries surrounding the corner of interest, which are subject to modifications of shape and size. The goal is to find a configuration that improves the shape contour of the printed feature, in comparison to the desired shape. The course of action is depicted in Fig. 6.1a: We start from a correction design, i.e., geometrical shapes that are added to or removed from the design. Next, we simulate the resist contour of the correction design and evaluate the resulting aerial image following a threshold resist model.

By comparison to the desired shape, we retrieve a figure of merit (FOM) that quantifies the mismatch between desired and actual shape. Using this FOM as a cost function, the optimization routine searches for an improved congruence. The following subsections introduce the individual steps of the analysis as detailed in Fig. 6.1a for the serif bar design. Except for the optimization routine, the principles apply in an analogous manner to the pixel-flip design we introduce in Section 6.3.

6.2.1 Layout of serif bar correction structures

Figure 6.1b depicts a schematic of the serif bar OPC design for a 80° corner. The binary intensity photomask either completely transmits or completely blocks the exposure light. The red area illustrates the desired shape of the resist contour after printing. To bring the simulated and the desired contour in congruence, the degrees of freedom subject to modifications are the size of the corner serif (shown in blue) and the size and width of four bars (red, orange, green, and magenta). All bars are designed to have the same width. To comply with typical limitations in photomask manufacturing, we set the lower width for the bars to be $0.6 \mu\text{m}$. The serif correction is turned off for inner angles $\alpha \geq 105^\circ$, since less correction is necessary for obtuse angles. To simplify the optimization problem, we exploit the symmetry of the corners by mirroring the corner design along the bisectrix (dashed black line).

As corner rounding is a severe issue in mask aligner photolithography (see the discussion in Section 2.4.2.2), the serif allows to use additional light to expose the corner, effectively pushing the resist contour into the corner. At the same time, the irradiance distribution is disturbed by the serif. It is the task of the bars to compensate for such distortions and to homogenize the irradiance distribution.

6.2.2 Aerial image and resist simulation

In this layout, we have now six parameters to optimize. The forward optimization requires to perform a large number of simulations, and we need an efficient and fast simulation approach. As described in Section 3.2 in detail, we use *GenISys LAB* [106, 225, 226] for calculating the Rayleigh-Sommerfeld diffraction integral in TEA for the binary intensity photomask, taking into account the angular spectrum of the exposure light.

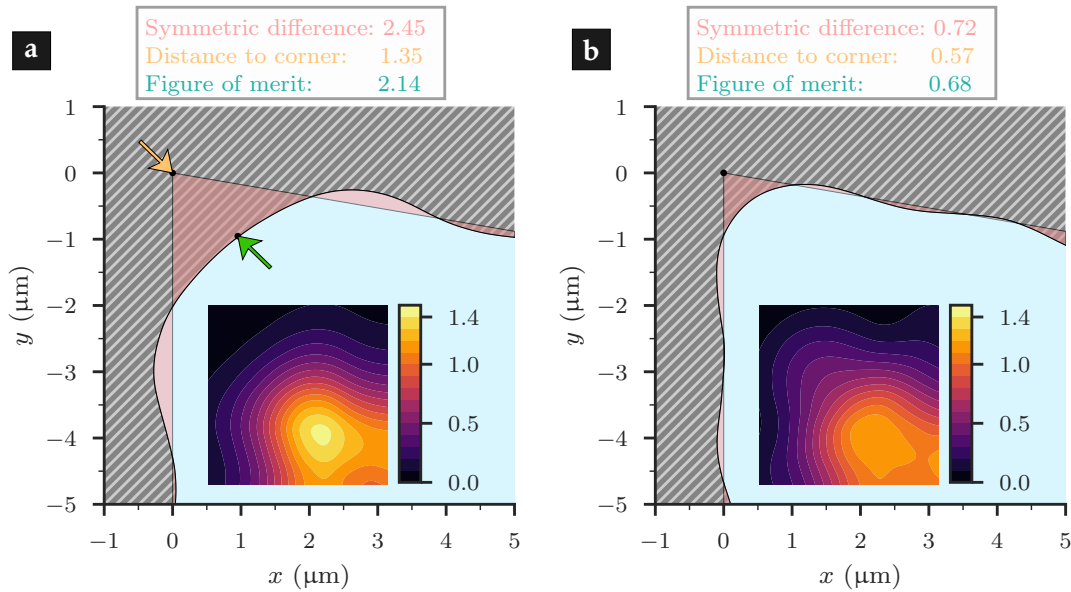


Figure 6.2: Simulated resist contour for **a** an uncorrected and **b** an optimized corner. We use a threshold resist model, with a threshold value of $t = 0.30$. The background, hatched in gray, indicates resist remaining after development. The FOM is calculated from the symmetric difference in the area (indicated in red) and the distance of the corner to the simulated resist contour (arrows in yellow and green). The data in the gray box quantifies both contributions and the FOM, following Eq. (6.1). A lower FOM indicates a better agreement between the desired and the simulated resist contour. The slight asymmetry with respect to the bisectrix arises from the finite resolution of the numeric simulation. The photomask layout for **b** is shown in Fig. 6.1b.

The insets show the normalized irradiance of the aerial image, indicating the emergence of a hotspot (> 1) in the uncorrected corner. For the corrected corner, the formation of a hotspot is suppressed.

The simulated aerial image of the exposure light (at a proximity gap of $30\ \mu\text{m}$) is then normalized to the incident irradiance and evaluated as iso-irradiance contours. As discussed in Section 2.4.1, for thin photoresists we can apply in good approximation a simple threshold model, as introduced in Fig. 2.13a. This means, if the irradiance exceeds the chosen threshold value t , a positive photoresist dissolves in the development step. Below this threshold, the resist is assumed to be unaffected. Throughout this chapter, we assume a threshold value of $t = 0.30$. We obtain this value by comparing the width of typical patterns subject to OPC in the original design and in the simulation for varying thresholds.

Already implemented in an algorithm, but skipped here for brevity, is the extension to sophisticated resist models. As implemented in *GenISys LAB*, the Mack model can be employed [227].

6.2.3 Figure of merit and optimization

As an input for the optimization, we require a method to assess the quality and results of the OPC approach. We introduce a figure of merit (FOM), evaluated close to the corner in an area $100\ \mu\text{m}^2$ in size. To define the FOM, we consider two contributions:

- The shape similarity between the simulated and the desired design is evaluated as the symmetric difference d_{diff} . This geometric operation can be best understood in terms of logical operators, namely as the XOR operation. It describes the geometrical area that is either in the simulated resist area or in the desired design, but not in

both. Figure 6.2 shows this contribution in red color. Obviously, it is the goal of the optimization to minimize the symmetric difference. To obtain a dimensionless quantity, we evaluate d_{diff} in units of μm^2 .

- The minimum distance d_{min} between the corner (yellow arrow in Fig. 6.2a) and the closest point on the resist contour (green arrow). Adding such a contribution provides an incentive to push the resist contour towards the corner. To obtain a dimensionless scalar, we take d_{min} in units of μm .

In the scalar FOM, both contributions are combined as the weighted average

$$\text{FOM} = w_{\text{diff}} \cdot d_{\text{diff}} + w_{\text{min}} \cdot d_{\text{min}}, \quad (6.1)$$

with the weighting factors w . We obtain fast convergence with $w_{\text{diff}} = 0.71$ and $w_{\text{min}} = 1 - w_{\text{diff}} = 0.29$, but different parameters can be used as well. A lower FOM corresponds to a better agreement between the simulated and the desired design.

Regarding the optimization, we employ a particle swarm optimization routine (*PySwarms* in Python 3.6 [228]) to reach a local minimum in the parameter space. Two things are worth emphasizing: First, the optimization has to be performed for each inner angle α separately. But of course the existing solution for a different angle can be taken as an input for the initial guess. Second, we are not necessarily interested to reach a global minimum in the optimization, but rather a significant improvement in the FOM with a finite number of optimization steps.

Figure 6.2b depicts the simulated resist contour after optimization (200 steps), which indicates a strong improvement over the unoptimized corner shown in Fig. 6.2a.

6.2.4 Optimization results

6.2.4.1 Pattern quality

Figure 6.3 illustrates the simulated performance of unoptimized and optimized corners as a function of α . First, the FOM of the uncorrected angles decreases monotonically with

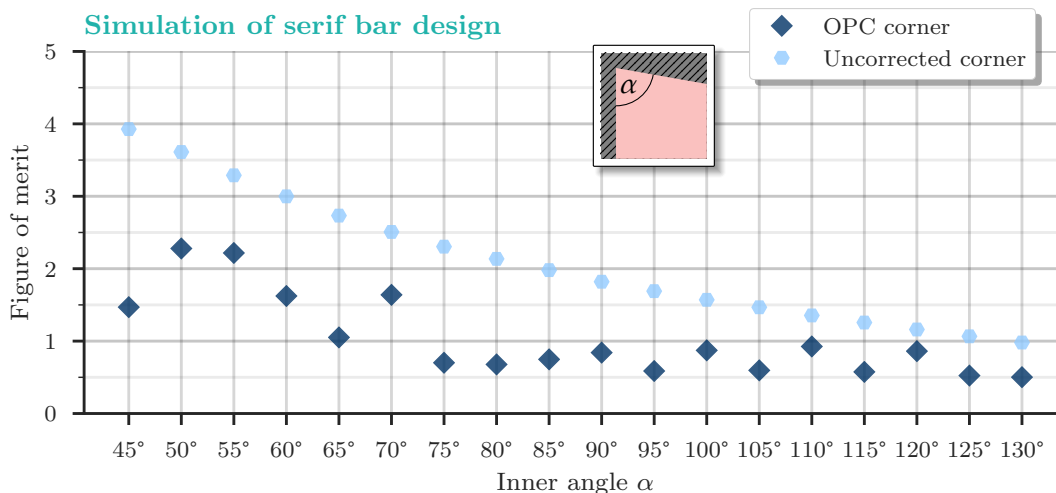


Figure 6.3: Results of OPC optimization for the serif bar design. We apply a threshold resist model using $t = 0.30$. Dark blue diamonds indicate the FOM for the OPC corrected corners. For comparison, the results for uncorrected corners are depicted by blue hexagons. By applying OPC to non-Manhattan geometries, the simulation indicates an improvement for all inner angles. The largest improvement is expected for $\alpha \approx 45^\circ$ and around 90° .

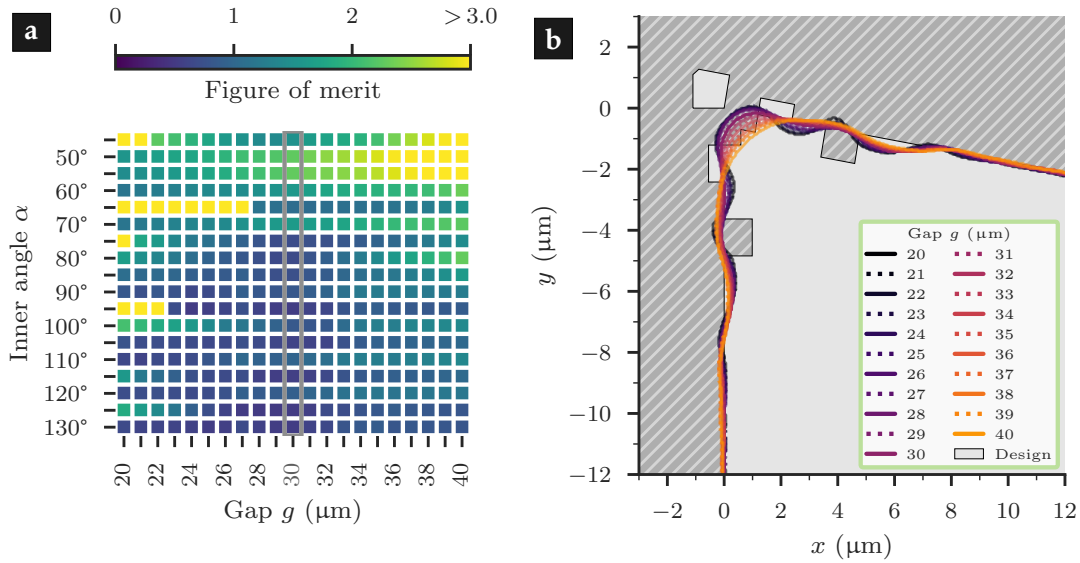


Figure 6.4: Sensitivity of the lithographic process to gap variations.

a Plot of the FOM as a function of the proximity gap g . The nominal gap of $g = 30 \mu\text{m}$ used for the optimization is indicated by a gray box (corresponding to the data presented in Fig. 6.3). We observe a strong sensitivity to gap variations at the lower range of inner angles under consideration.

b Resist contours as a function of the gap, here by way of example shown for $\alpha = 80^\circ$.

increasing α . Furthermore, we observe an improvement in the FOM for all α by applying the OPC, although the magnitude of the improvement varies strongly with α . For $\alpha \geq 75^\circ$, the FOM is below 1. At lower angles, the FOM increases, and hence the serif bar design is inappropriate for such geometries.

For all simulations demonstrated up to now we assumed perfect conditions. However, during experimental prints, in particular two parameters are subject to variations, i.e., the proximity gap and the exposure dose. In simulations, we can assess the sensitivity of the process to such variations, as presented in the following sections.

6.2.4.2 Gap variations

Figure 6.4a shows the FOM for variations of the gap around $g = 30 \mu\text{m}$ as a function of g and α . A high sensitivity to gap variations is observed for small angles, while the method can be considered robust for angles above 80° . Even for gap variations of up to $10 \mu\text{m}$, the simulations indicate an improvement of the optimized corners in comparison to uncorrected ones.

Figure 6.4b depicts the resist contours for an 80° corner at all simulated gaps. It becomes apparent that gap variations lead to ripples in the resist contour, corresponding to the position of the correction bars.

6.2.4.3 Dose variations

In a similar manner we investigate the sensitivity to dose variations, as depicted in Fig. 6.5. While the threshold remains at $t = 0.30$, the relative exposure dose is varied between 0.8 and 1.2. Similar to the gap variations investigated before, the process is quite insensitive for angles above 75° (Fig. 6.5a). A small improvement of the FOM is observed for smaller relative exposures doses about 0.94. A variation in the exposure dose leads to a shift of the shape contour (see Fig. 6.5b), slightly shrinking or enlarging the printed structures.

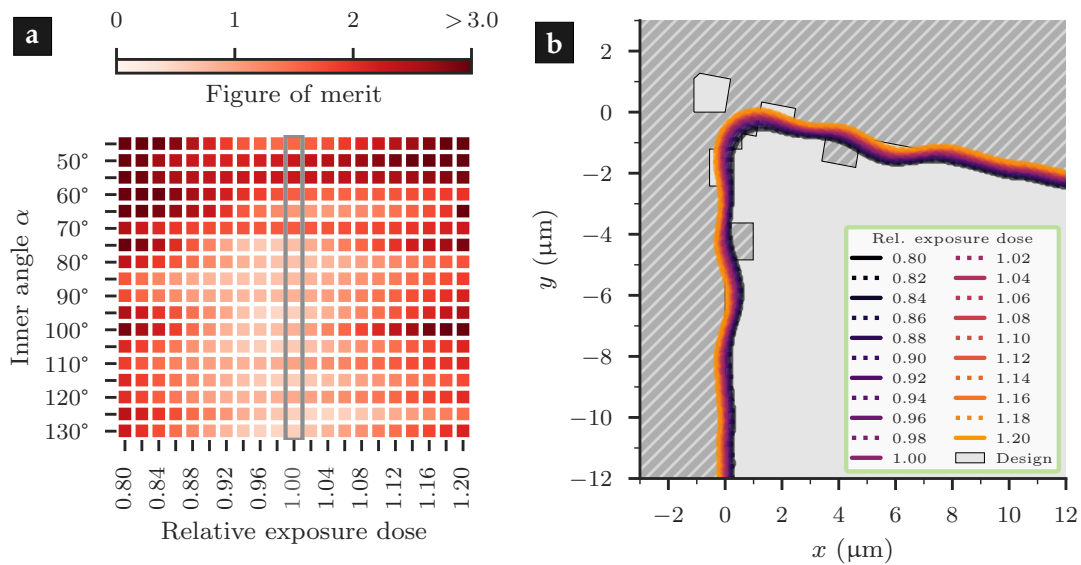


Figure 6.5: Sensitivity of the lithographic process to dose variations.

a Plot of the FOM as a function of the relative exposure dose. The nominal exposure dose of 1 used in all optimizations is indicated by a gray box. The plot indicates a slight improvement for a reduced dose for $\alpha \geq 75^\circ$.

b Corresponding resist contours for $\alpha = 80^\circ$.

6.2.5 Retrieving the process window

Of relevance for experimental fabrication is the combination of both sensitivities, i.e., the set of process parameters that enable manufacturing within given specifications [83]. Here, we investigate and present the results for the process window of an 80° corner, but an extension to the other angles is of course possible. To derive the process window from simulations, we plot the FOM as a function of gap and relative exposure dose in

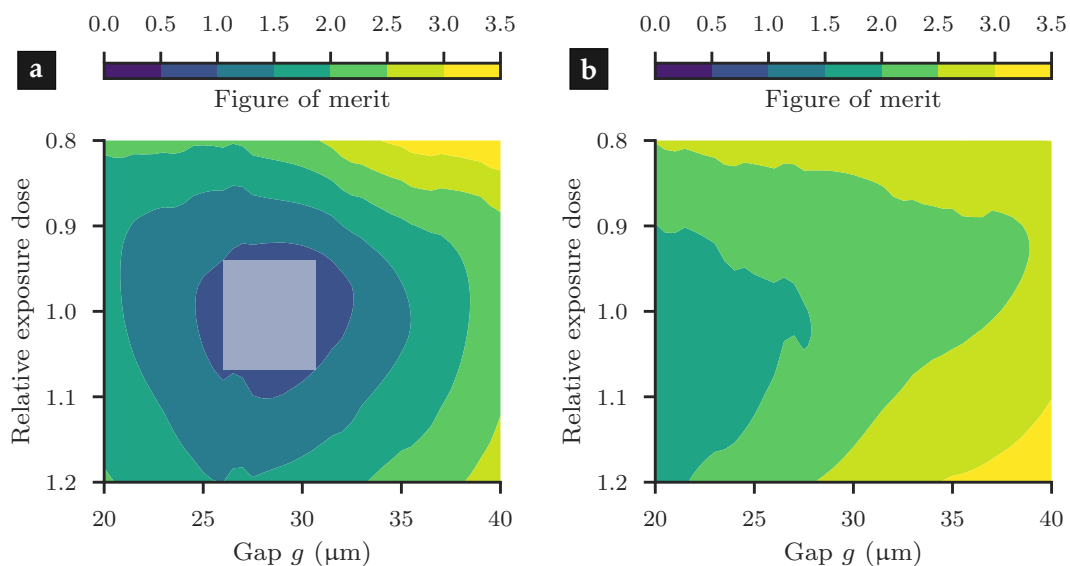


Figure 6.6: Contour plot illustrating the FOM for an 80° corner **a** with OPC correction and **b** without OPC, as a function of relative exposure dose and proximity gap. Depending on the FOM specifications for a given process, the process window can be derived as the maximum variation in dose and gap. The white rectangle in **a** indicates the process window for $\text{FOM} \leq 1.0$.

Fig. 6.6, together with contour lines for different FOM values. The white rectangle in Fig. 6.6a illustrates the OPC process window assuming the condition $FOM \leq 1.0$. We observe the tendency of an improved performance for smaller proximity gaps below $30 \mu\text{m}$, which implies that smaller gaps should be favored if the gap cannot be set exactly. The uncorrected corner, shown in Fig. 6.6b, does not reach a FOM below 1 and scales with g following Eq. (2.26).

6.3 Optical proximity correction with the pixel-flip design

Inspired by computational inverse design approaches applied to solar cells [229] and Bloch surface wave geometries [5], we follow a second approach for non-Manhattan OPC in mask aligner photolithography by implementing a pixel-flip algorithm. Similar approaches have been pursued in the field of projection lithography [230–233]. The advantage of pixel-based OPC concerns the photomask fabrication, as the pixel size can be adapted to the dimensions feasible for photomask writing. For example, in e-beam lithography with variable shape beam technology, the pixel approach requires only a square pixel as the fundamental geometrical shape for photomask writing.

The basic idea of our pixel-based OPC approach is sketched in Fig. 6.7: The area of interest on the photomask is subdivided into pixels, and each of those pixels is subject to modification. The pixels are oriented along the left edge of the pattern. Here, the initial

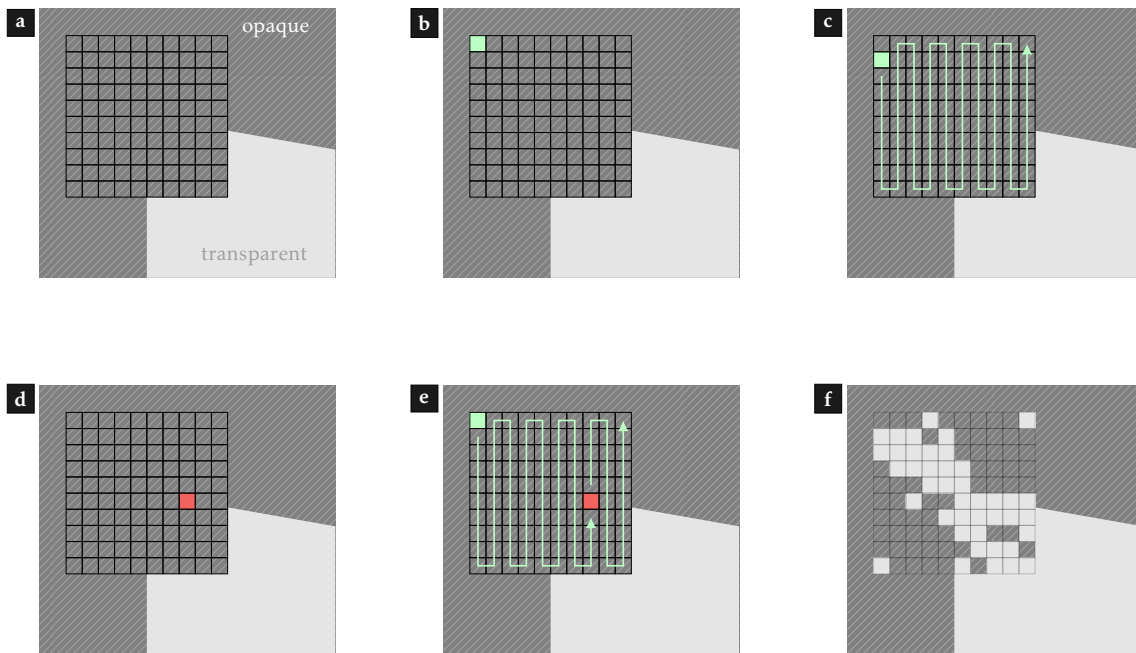


Figure 6.7: Schematic of the pixel flip algorithm.

a Starting point is an empty grid blocking the exposure light, where the side length of each square is $0.6 \mu\text{m}$.

b The first pixel (green) is momentarily flipped, transmitting light.

c Iteratively, all pixels are flipped, the photomask layout is simulated, and the FOM is calculated.

d At the end of the iteration, the pixel with the strongest improvement (lowest FOM) is permanently flipped (illustrated in red).

e During the next iteration, all remaining pixels are flipped. Again, the objective is to find the strongest improvement, under condition of all previously flipped pixels.

f The optimization stops when flipping all remaining pixels leads to no further improvement, taking into account not-optimal sub-trees.

design consists of the corner we want to optimize, with a square grid centered at the corner being deliberately cut out. This grid consists of 10×10 pixels with a side length of $0.6 \mu\text{m}$ per pixel. The grid size is chosen as a compromise between the size of the correction structures and the optimization time.

At the beginning of the optimization routine, all pixels are opaque (Fig. 6.7a). One after the other, the pixels are 'flipped' (Fig. 6.7b), i.e., they are turned transparent to the exposure light. Likewise as explained in Sections 6.2.2 and 6.2.3, the FOM is calculated from the simulation of the aerial image (Fig. 6.7c). After simulating all pixels, the pixel with the strongest improvement will be flipped permanently (red pixel in Fig. 6.7d).

The meander pattern starts all over again (Fig. 6.7e), with the already flipped pixel being unaffected. If no further improvement is obtained after flipping all remaining pixels, the algorithm starts a subtree optimization [5]. The idea is here to avoid being stuck in a local minimum. The algorithm reverts the last optimization step and flips the second-best pixel (instead of the best), and proceeds with the routine. For the results presented in this chapter, we use a subtree search depth of 3. That means the optimization does not search deeper than three non-optimal pixel-flips.

6.3.1 Optimization results

The optimization result for the 80° corner is illustrated in Fig. 6.7f. On the first glance we notice the missing symmetry with respect to the bisectrix (which we enforced for the serif bar design) due to the discretization in the simulation step. However, we notice a certain resemblance to the serif bar design, shown in Fig. 6.1b, especially the emergence of a serif-like corner element.

Figure 6.8 shows the FOM for the pixel-flip design, once more shown as a function of α . Here, we obtain a FOM below 1 for all angles under consideration. This is a strong improvement compared to the results of the serif bar design, as presented in Fig. 6.3. Two reasons lead to this improvement: First, the extended parameter space offers more

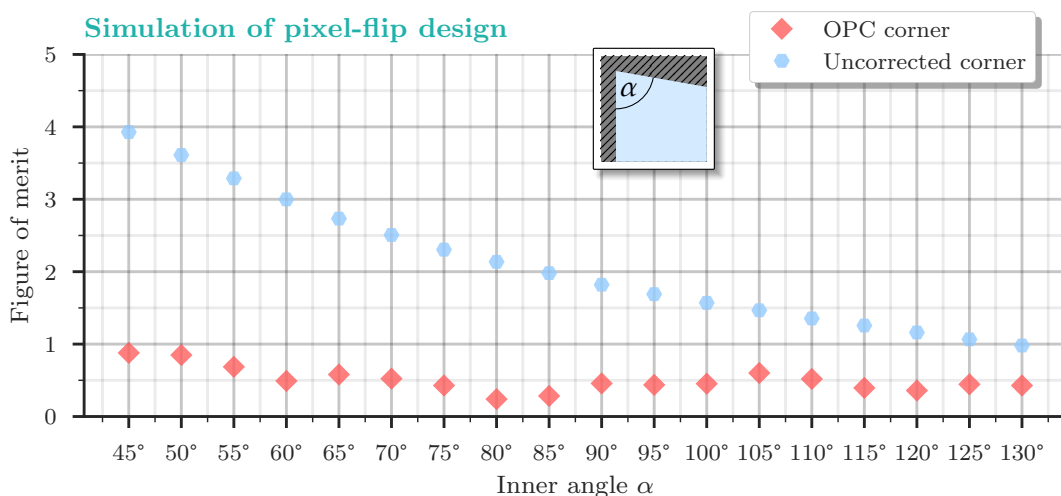


Figure 6.8: Results of OPC optimization for the pixel-flip design. We apply a threshold resist model using $t = 0.30$. Red diamonds indicate the FOM for the OPC corrected corners. For comparison, the results for uncorrected corners are depicted by blue hexagons (same data as presented in Fig. 6.3). The predicted improvement is bigger compared to the serif bar design, as the pixel-flip design provides more degrees of freedom to shape the aerial image.

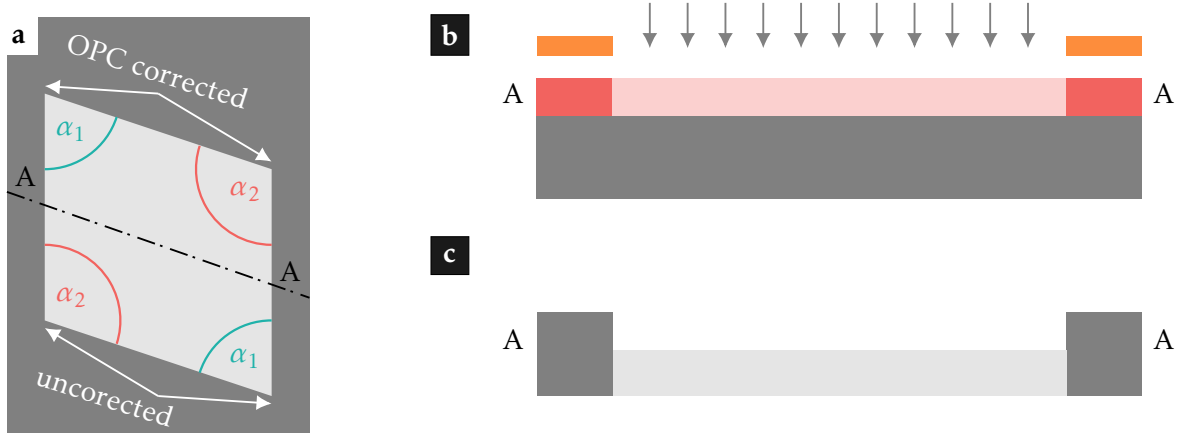


Figure 6.9: Schematic on the interpretation of the experimental results.

a Example of how a printed test structure looks like under an SEM, with inner angles $\alpha_1 \leq 90^\circ$ and $\alpha_2 \geq 90^\circ$. The top corners are OPC corrected. The bottom corners are uncorrected and allow for a direct comparison.

b Diagram of the experimental process, illustrated along the cut line A–A. First, the positive photoresist (red) is exposed (light red) through the photomask (orange). The exposed volume is dissolved in the development step (not shown).

c The resulting resist etch mask is subject to RIE, removing material in the exposed areas. As indicated in the graph, the etched regions appear brighter in the SEM images. Furthermore, the edge effect in electron microscopy enhances the contrast around the contour of the structures.

possibilities to reach a low FOM. Second, the subtree optimization routine prevents getting trapped in local minima.

6.4 Evaluation and characterization of experimental results

For evaluating the performance of the optimized OPC corners in experiments, we designed dedicated test structures, depicted in Fig. 6.9a. The rhombus shape allows to combine two corner angles, α_1 and $\alpha_2 = 180^\circ - \alpha_1$, in the same structure, and to compare the corrected (top) and uncorrected corners (bottom) in vicinity to each other. Hence, a direct comparison is made possible, with minimized variation in the experimental conditions (such as proximity gap and exposure dose). With a side length of $\geq 50 \mu\text{m}$, the corners are sufficiently far apart to not influence each other.

6.4.1 Experimental setup

The test structures for all corner angles between 45° and 130° are arranged in the photomask design. The binary intensity photomask is fabricated by a commercial supplier. The nominal photomask specifications indicate a critical dimension of 200 nm on a writing grid with a resolution of 1 nm. For the test exposures, we use our prototype mask aligner setup, with the light source described in Section 5.3 and the high precision stage introduced in Section 4.3. The angular and the optical spectra of the exposure light were discussed in Section 6.1. To level substrate and photomask, we use the AVANTES AvaSpec ThinFilm bundle, featuring three individual spectroscopic channels for gap metrology.

The experimental prints were performed using AZ[®] 1512 positive photoresist on a Si wafer, with a measured thickness of $1.2 \mu\text{m}$ (see Fig. 6.9b). We don't apply a BARC to enable dry etching into the substrate. All results presented within this section have been obtained using an exposure dose of $250 \text{ mJ}/\text{cm}^2$ under *i*-line exposure. Resist development

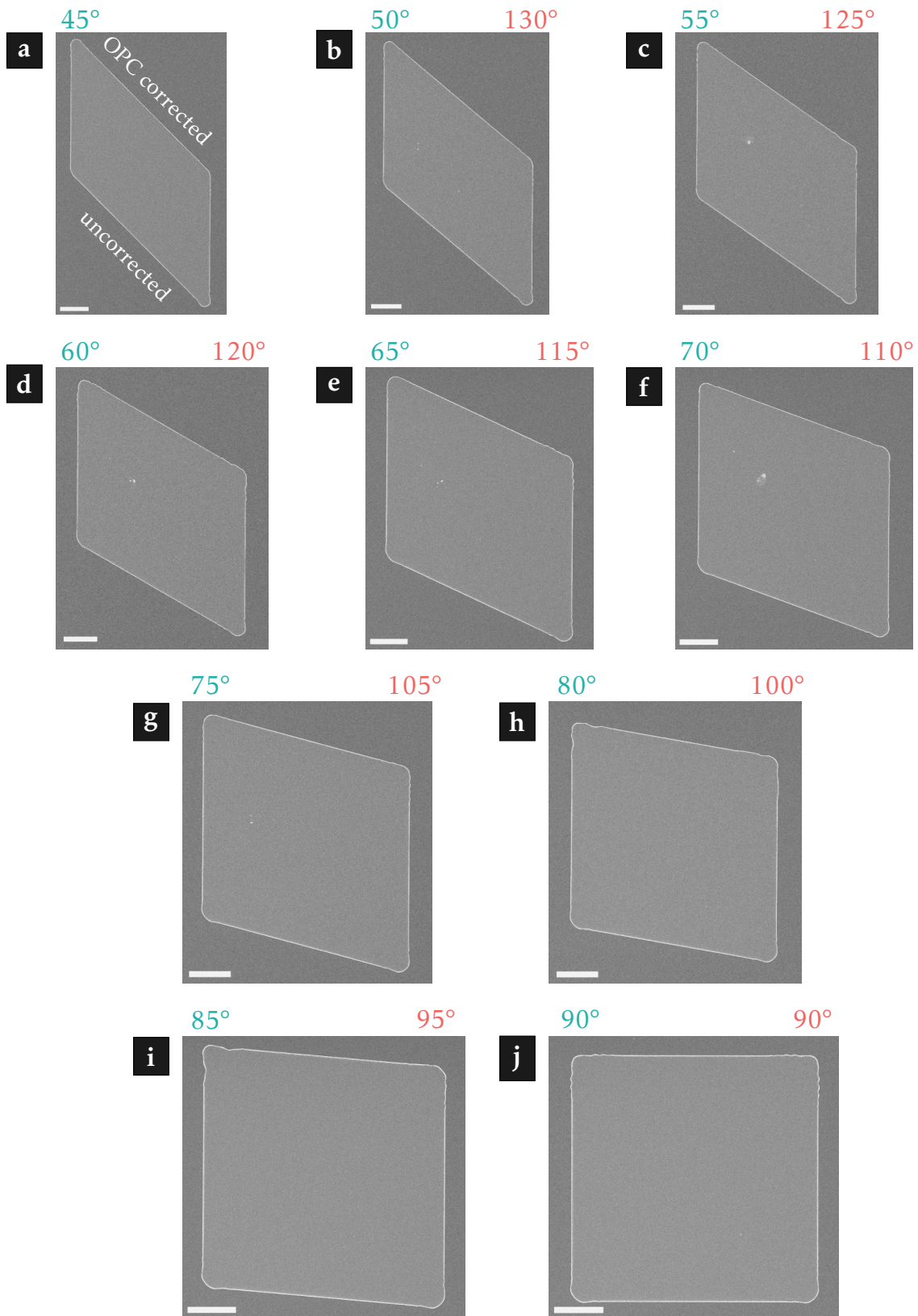


Figure 6.10: Experimental results on corner optimization for the serif bar design. The SEM images show the test structures etched into the Si substrate. As explained in Fig. 6.9, the top corners are OPC corrected, while the bottom corners are uncorrected to facilitate a direct comparison. The inner angles range from a 45° to j 90°. All scale bars are 10 μm in length.

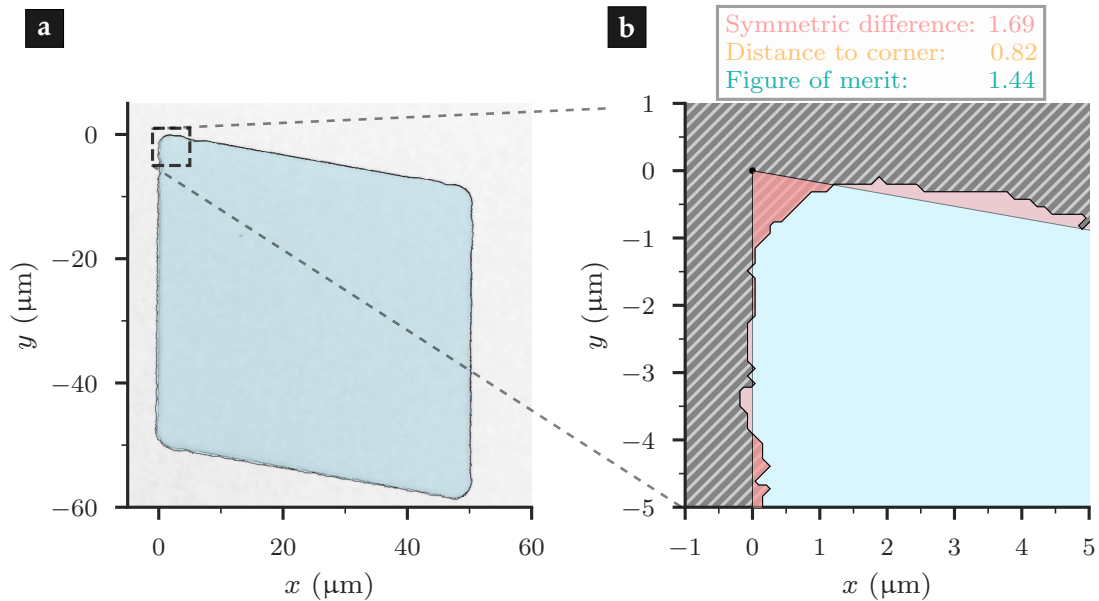


Figure 6.11: Evaluated shape contour for an inner angle of 80° , as retrieved from the SEM image shown in Fig. 6.10h by applying clustering-based image evaluation.

a The blue area is enclosed by the shape contour, which is used to determine the FOM.

b Magnified view of the top left corner, overlaid by the symmetric difference. In comparison to Fig. 6.2b, the FOM is diminished, arising from an increased symmetric difference. The SEM resolution (here a pixel size of 83.8 nm) limits the precision of the evaluation.

is performed using AZ[®] 400 (diluted 1:4 with deionized water). We evaluate the dry etched test structures (OXFORD Plasmalab 100 ICP 180, Cl₂ and HBr plasma) after resist removal in an SEM (ZEISS Supra 55 VP, compare Fig. 6.9c).

6.4.2 Evaluation of serif bar design

Figure 6.10 depicts images of the test structures, sorted by inner angle α . By comparing the corrected to the uncorrected corners, we observe qualitatively an improvement by

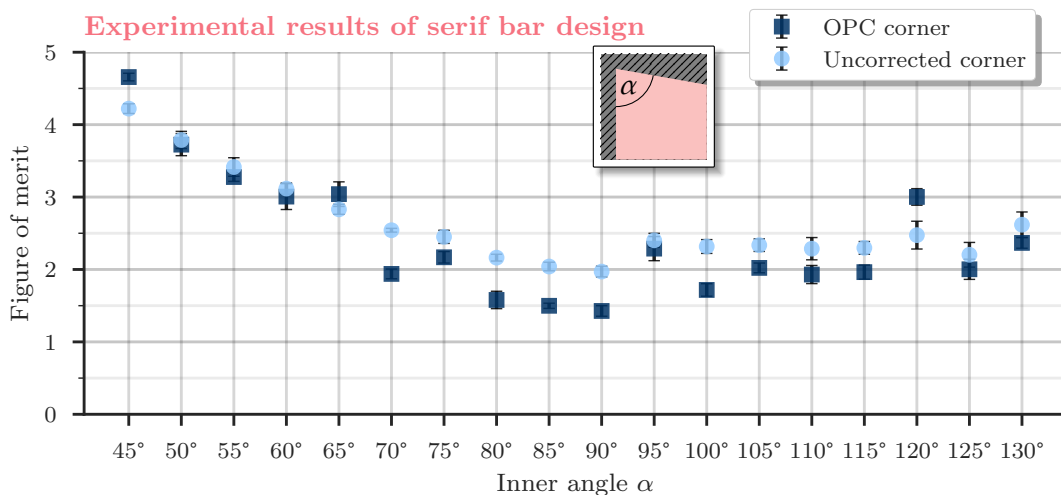


Figure 6.12: Using cluster-based image evaluation of the test structures, we retrieve the FOM. The markers indicate the mean value of six independent structures, while the error bar denotes the standard deviation. By applying OPC, we note an improvement for α between 70° and 115° .

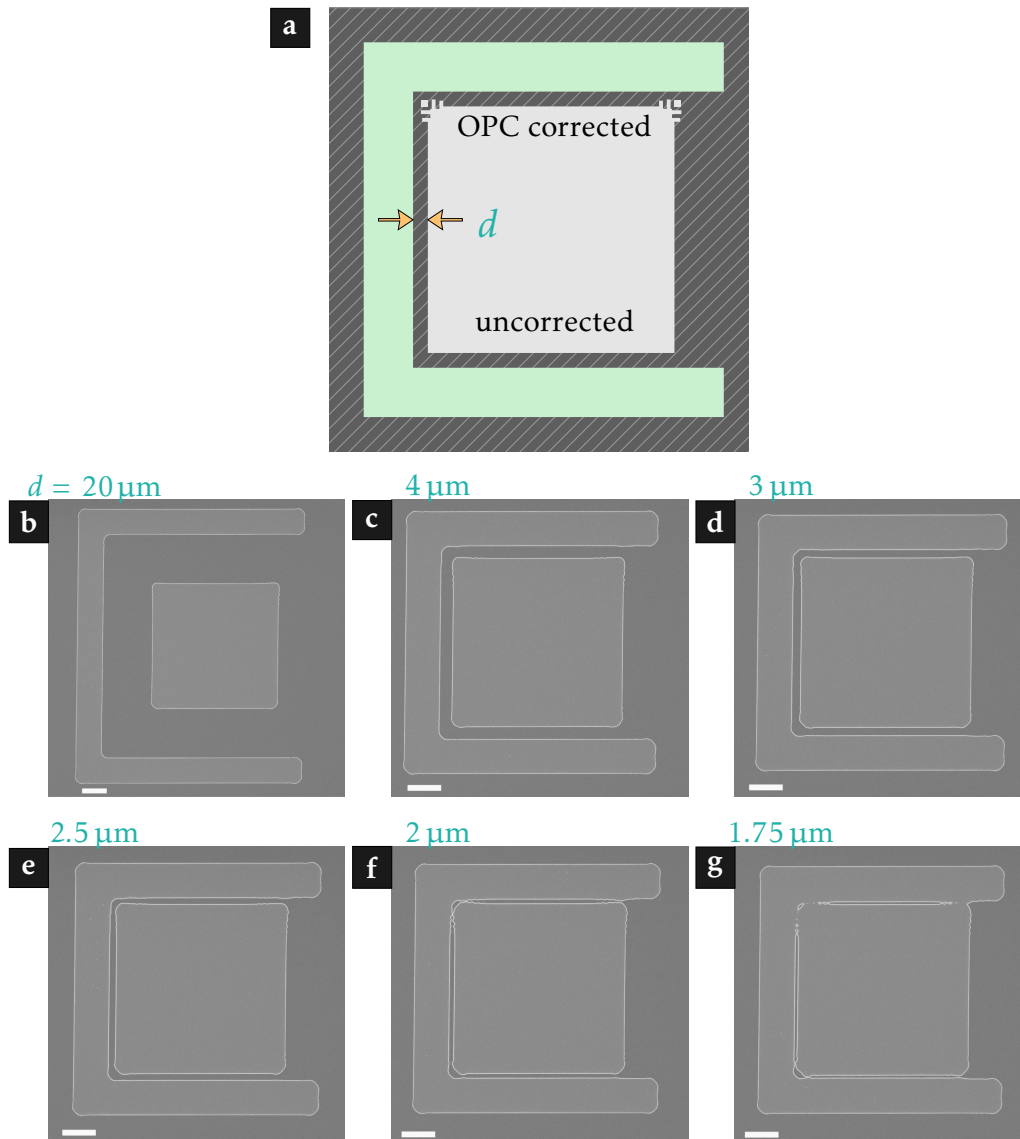


Figure 6.13: Iso-dense bias in OPC.

a Schematic illustration of test structures dedicated to investigate the iso-dense print bias. The distance d of the corrected and the uncorrected corners to the adjacent structure (shown in green) is varied.

b – g SEM images of fabricated test structures. d is varied from $20\ \mu\text{m}$ to $1.75\ \mu\text{m}$. For $d \approx 2.5\ \mu\text{m}$ and below, the surrounding introduces distortions to the OPC corrected corners. Coalescence emerges at $d = 1.75\ \mu\text{m}$. In contrast, the uncorrected corners show only a weak dependence on the surroundings, here even below the resolution limit of $r \approx 3.3\ \mu\text{m}$, Eq. (2.26).

All scale bars correspond to a length of $10\ \mu\text{m}$.

applying the OPC. Arguably this is best visible for the 90° corner (Fig. 6.10j). Here, the corner rounding is clearly visible for the uncorrected corners, but is significantly reduced in our OPC implementation. Furthermore, we also observe an improvement when we compare our results to previously reported OPC approaches reported on in [55,110]. Small ripples arise in the contour around the corner (for example shown in Figs. 6.10a and 6.10j; see also the discussion in Section 6.2.4.2). They are a consequence of the discreteness of the correction bars, i.e., they can be diminished by increasing the number of bars and reducing their width.

Next, we systematically evaluate the SEM images in a quantitative manner. First step is to retrieve the shape contour using clustering-based image evaluation, also called Otsu's method [234]. We use the computer vision package `OPENCV` with a Python interface. Figure 6.11a shows the contour of 80° and 100° corners after image evaluation of Fig. 6.10h. The structure is centered with respect to the contour, while no additional image manipulation is required.

In a second step, we apply the same procedure as introduced in Section 6.2.3 to retrieve the FOM. This is illustrated for the 80° corner in Fig. 6.11b. Performing this evaluation for six individual test structures per inner angle, both for corrected and uncorrected corners, results in the data presented in Fig. 6.12. The first thing to notice is that the FOM of the uncorrected corners follows the general trend predicted by the simulations (compare Fig. 6.3), and saturates for $\alpha \geq 95^\circ$. Especially for $\alpha \geq 70^\circ$ we observe a considerable improvement by applying the OPC over the uncorrected corners.

Compared to the results expected from optimization, the agreement is rather poor, with the best FOM obtained for the right-angled corner. The difference between expected and measured performance can be attributed to inaccuracies in the resist modeling and in the SEM evaluation, exposure dose as well as gap variations, reflections at the Si substrate, and imperfections in photomask fabrication. An improved performance can be expected especially when the resist development is taken into account during optimization. Nevertheless, applying the serif bar design leads to an improvement in the pattern fidelity and corner sharpness in non-Manhattan geometries, with minor overhead in photomask fabrication. In the presented configuration, our rule-based approach guarantees that the optimization has to be performed only once for a given proximity gap.

6.4.3 Iso-dense print bias and the influence of adjacent structures

One question that we raised in Section 6.1 remains: How close can adjacent structures be located without influencing the OPC corrected corners? Obviously, the approach breaks down when this structure overlaps with the OPC layout, distorting the optimized solution. Even more, a photomask opening close to the OPC corner increases the irradiance. What we observe is termed the iso-dense print bias in literature: the aerial image of features looks differently, depending on whether they are in an isolated or in a dense arrangement [28].

Figure 6.13a shows our approach to assess the iso-dense print bias experimentally for a 90° corner. The gray structure contains the OPC corrected corners (top) and uncorrected corners (bottom), which is surrounded by an additional photomask opening (shown in green). We vary the distance d between the additional opening and the test structure to estimate the mutual influence. Figures 6.13b to 6.13g show SEM images for d between $20\ \mu\text{m}$ and $1.75\ \mu\text{m}$. For $d = 4\ \mu\text{m}$, no influence is visible, while at $3\ \mu\text{m}$ the tip of the corner is slightly rounded. At $d = 2\ \mu\text{m}$ the structures start to coalesce. In contrast, the uncorrected corners remain mainly unaltered down to $d = 2\ \mu\text{m}$. All in all, for the given experimental setup and design of correction structures, we estimate that our proposed method works down to $d \approx 3\ \mu\text{m}$ reasonably well. This range can be extended by designing correction structures with a reduced additional footprint.

6.4.4 Evaluation of the pixel-flip design

Figure 6.14 shows SEM images of test structures of the pixel-flip design. The experimental conditions are identical to the test structures in Section 6.4.2, except that the exposure dose has been slightly reduced to $230\ \text{mJ}/\text{cm}^2$ for the best results. Compared to the serif bar design, the corners are more rounded, which also results in an increased FOM (shown in Fig. 6.15). Well visible in Fig. 6.14j is the shrinkage of the printed area around the corner, compared to the contour of the uncorrected corner (as depicted in Fig. 6.10j).

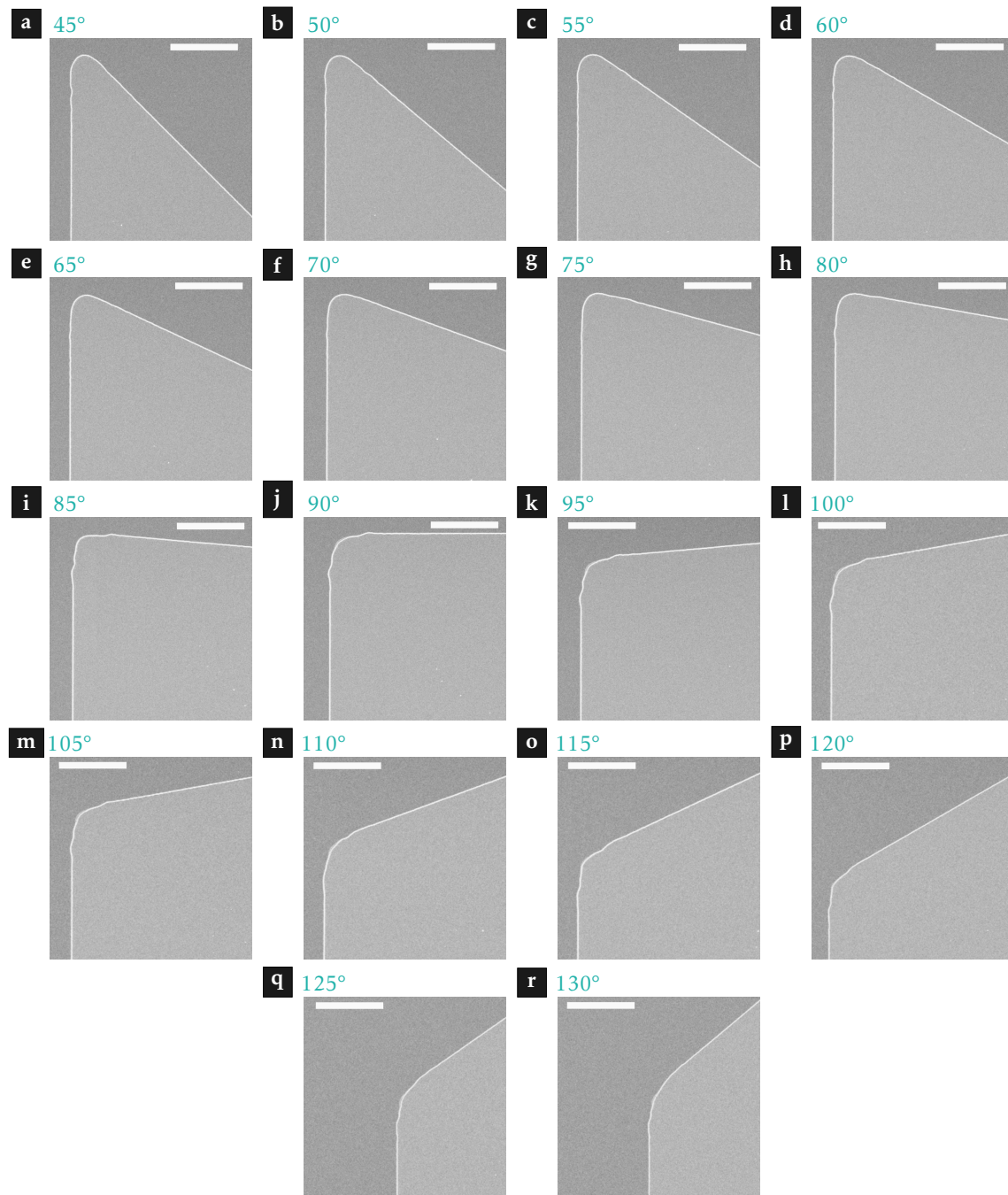


Figure 6.14: Experimental results on corner optimization for the pixel-flip design, with angles a 45° to r 130°. The white scale bars are 10 μm in length.

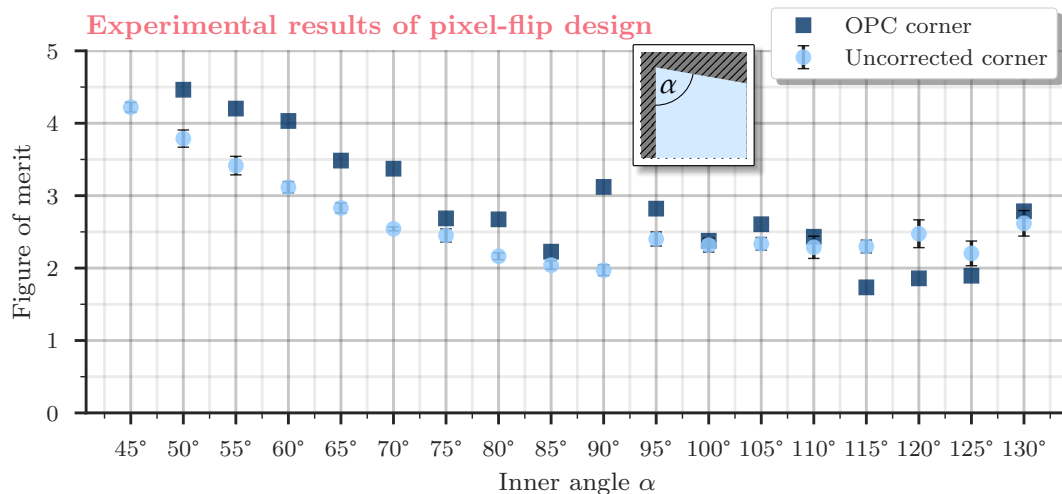


Figure 6.15: FOM of the test structures for pixel-flip design. Here, we only evaluate a single print, and hence the error bars are omitted. Compared to the optimization results with a FOM below 1 for all α , the experimental results are strongly deteriorated. For $\alpha = 45^\circ$, the FOM is about 8.3 and hence not shown in the graph. As a reference, we show the FOM for the uncorrected corners (blue circles), with the same data as already presented in Fig. 6.12.

In the current configuration, the pixel-flip design seems inferior with regard to the serif bar design, despite the superior optimization results (shown in Fig. 6.8). We attribute this disagreement to an increased sensitivity to gap and exposure dose variations (not shown here), and a stronger influence of the resist development process. Further investigations are necessary to exploit the full potential of the pixel-flip design.

6.5 Concluding remarks on optical proximity correction in mask aligner photolithography

In this chapter, we described two methods to increase the pattern fidelity in mask aligner photolithography, deriving a rule-based OPC method for non-Manhattan geometries. This approach relies on correction elements added to the photomask design, with minimal overhead to photomask fabrication. The lower size limit of the correction structures is fixed to $0.6 \mu\text{m}$, in compliance with established wafer-level fabrication. Apart from the photomask, no additional modifications to the optical setup are necessary, and we use our prototype mask aligner with *i*-line illumination at a proximity gap of $30 \mu\text{m}$.

We introduced two kind of correction structures to provide a glimpse on the capabilities offered by this technique. The ultimate goal is to mitigate distortions in the image shape and to increase the pattern fidelity. In a more general sense, we investigated to which extend OPC is useful in modern lithographic applications: While OPC is a well-established technique in projection photolithography, it is rarely applied to mask aligner lithography. In this proof-of-principle work, we showed that rule-based OPC can be adapted to mask aligners as well, being useful especially for non-Manhattan geometries.

OPC relies heavily on the simulation of the lithographic processes. Our approach relies on a scalar FOM quantifying the shape similarity between the simulated and the desired pattern. This measure allows to investigate the sensitivity of the process to variations in the proximity gap and the exposure dose.

We observe experimentally for the serif bar design a slight improvement of pattern fidelity, especially for corner angles between 70° and 115° , which appears to be quite insensitive

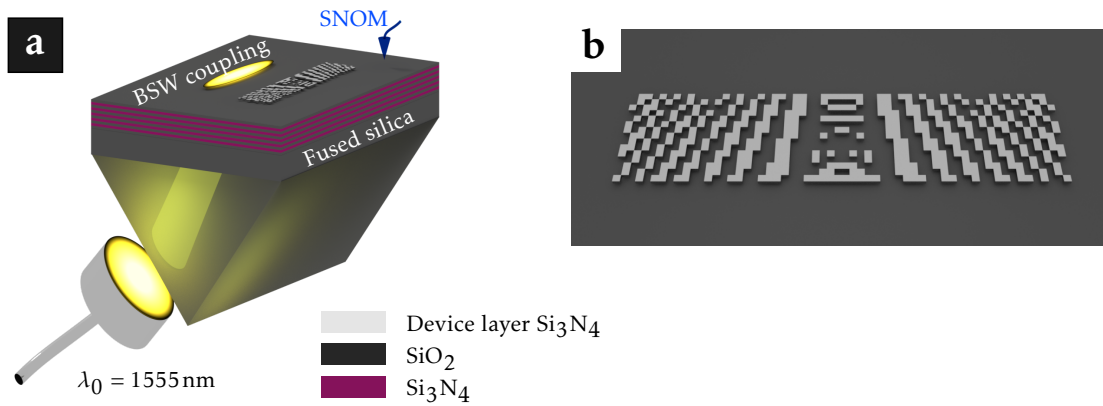


Figure 6.16: Sketch of experimental setup to focus Bloch surface waves (BSWs).

a A 1D photonic crystal (PhC) crystal (alternating black and violet layers) supports BSWs at the interface of the top layer and the air environment. By frustrated total internal reflection, BSWs are excited in Kretschmann coupling configuration at a free space wavelength of $\lambda_0 = 1555\text{ nm}$ in TE polarization $100\ \mu\text{m}$ away from the device (light gray) on top of the BSW platform. A scanning near-field optical microscope (SNOM) with an aperture size of $200\ \text{nm}$ images the intensity distribution about $40\ \text{nm}$ over the surface.

b Illustration of a device that focuses BSWs $5\ \mu\text{m}$ atop the element. The total device size is $40\ \mu\text{m}$ by $10\ \mu\text{m}$, divided into pixels with a side length of $0.67\ \mu\text{m}$. The light gray structure is made from Si_3N_4 atop of the $\text{SiO}_2/\text{Si}_3\text{N}_4$ multilayer, and provides an index contrast of $\Delta n \approx 0.1$.

to gap and dose variations. The pixel-flip based approach promises a better performance in simulations, but requires additional work to bring simulations and experimental prints in agreement.

This section precludes the topic on RETs based on intensity modification. Nevertheless, there would be a lot more to discuss though: A more holistic approach requires to include both source-mask optimization and sophisticated resist development models. Regarding the pixel-flip design, the dependence of the FOM on the pixel size allows to determine the fundamental resolution of this technique. An extension to more complex patterns should go hand in hand with the development of dedicated optimization routines, as for example with neural networks, which is beyond the scope of our discussion here.

At the end of this chapter, we describe the application of a very similar pixel-flip algorithm to a different optical system, i.e., the shaping of surface waves at the interface of a photonic crystal (PhC) and air.

6.6 Application of pixel-flip algorithm to inverse design in Bloch surface wave devices

The pixel-flip algorithm introduced in Section 6.3 was motivated by work we performed in the field of beam shaping applied to surface waves, previously published in [5]. Here, we summarize the most important concepts and results. For more details and additional results, we refer to the corresponding publication and its Supplementary Information. In this work the optimization of the structures and simulations in 2D were made by MSc. Y. Augenstein, at that time a master student in our group, and the experimental characterization has been performed by Dr. B. V. Lahijani and Dr. M.-S. Kim from the École Polytechnique Fédérale in Lausanne. It has been my contribution to perform 3D simulations and to fabricate the samples.

A multitude of optical sensing techniques requires the confinement of light on small length scales [235]. In addition, a strong interaction of light with the material under investigation

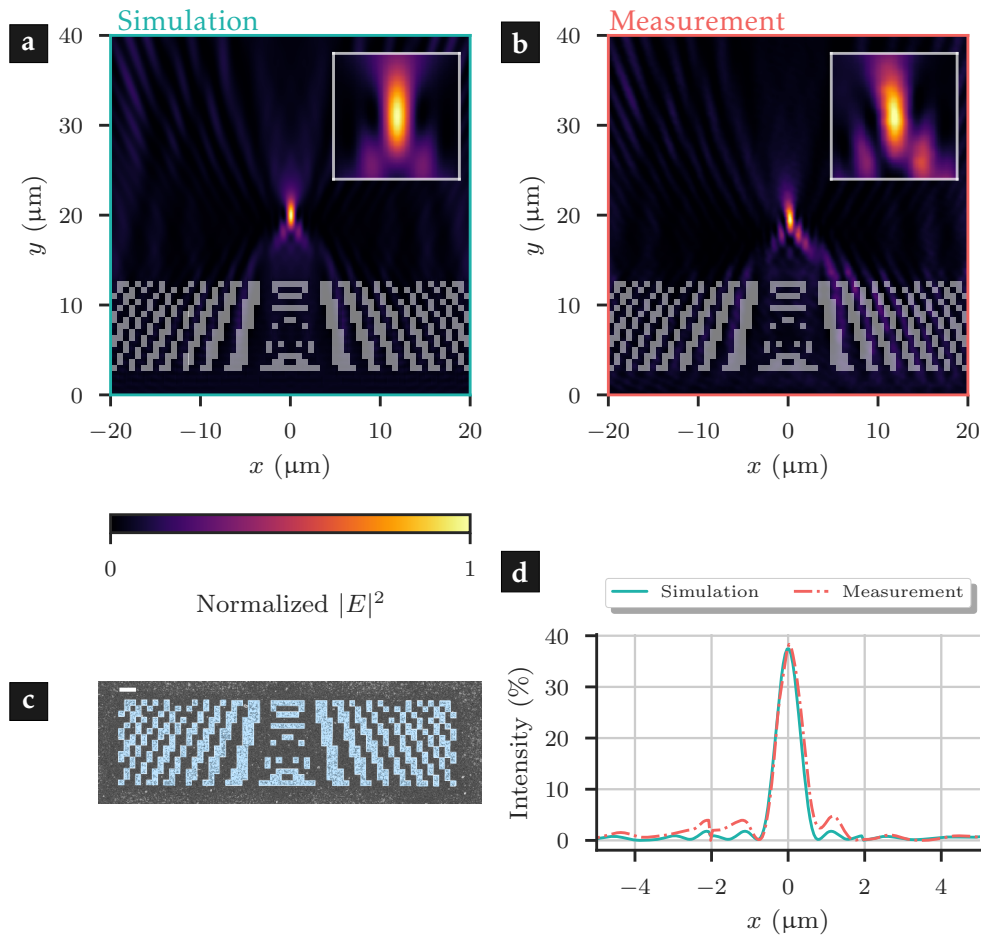


Figure 6.17: Focusing BSWs 5 μm behind the device. Data previously published in [5]. **a** Simulated and **b** measured intensity distributions. The insets provide a magnified view around the focus, in **b** with a high-resolution SNOM scan. **c** SEM image of a fabricated device. The black and white grains in the image emerge from the conductive layer applied to avoid charging during imaging, which is removed prior to measurements. The white scale bar in the upper left corner indicates a length of 2 μm . **d** Comparison of simulated and measured intensity distributions through the focus. We retrieve a FWHM of $0.495 \lambda_{\text{BSW}}$ in simulation and $0.529 \lambda_{\text{BSW}}$ in measurements. The peak intensities are 37.41 % and 38.32 %, respectively.

is desirable [236]. One interesting option is to confine the electromagnetic wave at the interface between two media. The solutions to Maxwell's equations lead to propagating surface waves, in a way that they travel along the interface and decay exponentially in both adjacent media [237]. The complete characteristics of the surface wave comprises a dispersion relation that describes the wave propagation and a field profile inside the media.

Showing deeply sub-wavelength wave confinement and strong interaction, propagating surface plasmon polaritons (SPPs) arising at the interface between a metal and a dielectric medium [238] are the prime example for surface waves used in optical sensing schemes [239, 240]. Here, the energy of the excitation is shared between the oscillations in the charge density of conduction electrons in the metal layer and the electromagnetic field in the dielectric medium. The main disadvantages of SPPs are connected to the large dissipative losses in the metal, limiting the Q-factor of the surface plasmon resonance

as well as the propagation length [241]. Typical propagation lengths of SPPs are tens of micron in the visible regime and below one millimeter at telecom wavelengths [242]. This limits their use in optical sensing.

For this reason, the notion of surface waves based on all-dielectric constituents is of particular beauty. One class of such devices relies on Bloch surface waves (BSWs), which exist on the interface between a dielectric (in our case air) and a one-dimensional PhC (consisting of an alternating succession of high- and low-permittivity layers), as illustrated in Fig. 6.16a [243]. At frequencies inside the photonic band gap of the PhC, the evanescent fields decay exponentially in both half spaces. In many material platforms, the absorption in the dielectrics can be neglected, and the propagation length is fundamentally only limited by the number of layers the PhC is made of. Propagation lengths of several millimeters [244] and the application of BSWs to biosensing have been demonstrated [245, 246].

To further enhance the interaction with the sensing medium, for example contained in microfluidic channels [247, 248], beam shaping and focusing of the BSWs is a desirable feature. For this purpose, a device layer atop the PhC is deposited. A spatially structured device layer locally changes the dispersion relation and hence the effective refractive index that the BSWs experience. However, the performance is hindered by the limited effective refractive index contrast of $\Delta n \approx 0.1$ between the presence or absence of the device layer [249]. Isosceles triangles have emerged as a suitable candidate to boost the focusing behavior at visible and near-infrared wavelengths [250]. Still, the performance suffers from a broad focus far from the diffraction limit and a low intensity in the focus.

Inverse photonic design gives an opportunity to overcome these limitations. In analogy to the optimization routine already introduced and discussed in Section 6.3 [5, 229], the device domain is subdivided into individual pixels. Figure 6.16b illustrates the result of such an optimization, with the objective to focus light $5 \mu\text{m}$ behind the device. As a FOM, we take the simulated intensity in the anticipated focal region, and the optimization problem can be written as [5]

$$\max_{\epsilon(\mathbf{r})} \text{FOM}_{\text{BSW}} = \max_{\epsilon(\mathbf{r})} \int_{a_z}^{b_z} \int_{a_x}^{b_x} \left[|E_x(x, z)|^2 + |E_z(x, z)|^2 \right] dx dz \quad (6.2)$$

with the material distribution $\epsilon(\mathbf{r})$ in the device domain and $[a, b]$ defining the focal region considered during optimization. Please note that the optimization here seeks to maximize the FOM (in contrast to Section 6.3, where we aimed to minimize the FOM).

The BSW platform relies on an established design adapted to $\lambda_0 = 1555 \text{ nm}$ and TE polarization, with multilayers made of SiO_2 (thickness 450 nm) and Si_3N_4 (260 nm). The thickness of the Si_3N_4 device layer is 70 nm (compare Fig. 6.16a). The optimization result shown in Fig. 6.16b corresponds to a pixel size of $0.67 \mu\text{m}$.

For the experimental realization, we utilize a scanning near-field optical microscope (SNOM) to measure the electromagnetic near-field close to the surface. To manufacture the spatial distribution in the device layer sketched in Fig. 6.16, the following fabrication procedure is applied. We start from depositing the PhC multilayers on a SiO_2 wafer using plasma-enhanced chemical vapor deposition. To structure the device layer, we employ e-beam lithography (JEOL JBX-5500FS 50 kV e-beam writer) on a negative photoresist (ma-N 2403) and a conductive polymer (Espacer). The polymer is removed in deionized water after exposure, and the resist is developed (MF-319). Finally, the device layer is etched using a CHF_3 and O_2 plasma, and the resist is removed in a pure oxygen plasma.

Figures 6.17a and 6.17b show the simulated and measured field intensities $|E_x(x, z)|^2 + |E_z(x, z)|^2$ around the device. We observe an outstanding agreement between simulation and experiment, with the bright focal area $5 \mu\text{m}$ behind the device clearly visible. Figure 6.17c shows an SEM image of the fabricated device. The large pixel size enables a high pattern fidelity. Finally, in Fig. 6.17d, we compare the intensities in the focal region. Again, an excellent agreement is obtained, with a FWHM of $.495 \lambda_{\text{BSW}}$ in simulation and $0.529 \lambda_{\text{BSW}}$ in measurements indicating a diffraction-limited performance. This clearly outperforms previous approaches of focusing elements adapted to the BSW platform. This statement holds true as well considering the collected intensity, reaching close to 40% both in simulation and experiment.

The design obtained from the computational optimization approach resembles an arrangement of waveguides that collect the waves over the device width and funnel the light into the focal region. Constructive interference is achieved via proper phase accumulation in the side wings.

In conclusion, this work shows how a computational approach to electromagnetic field propagation can be harnessed to design integrated optical circuitries with limited effective refractive index contrast. As an example, we show here the focusing of BSWs to a sub-wavelength domain, using a pixel-flip algorithm. Our approach is not limited to focusing only, but is rather adaptable to the requirements of the application in mind.

Proximity lithography based on optical metasurfaces

In this section, we introduce and discuss an approach to extend the capabilities of beam shaping and wavefront control at the photomask level. In recent years, optical metasurfaces emerged as a new line of research, promising compact optical components with unprecedented opportunities to shape wavefronts in amplitude, phase, polarization, and direction. Such rationally designed planar optical components consist of two-dimensional arrays of scatterers, with a unit cell size typically smaller than the wavelength. However, the diffractive nature manifests itself in strong chromatic aberrations, similar to conventional DOEs, which currently limits the applicability of metastructures in broadband optical imaging.

In this chapter, we demonstrate that optical metasurfaces operating in the UV represent an ideal building block for proximity lithography, as the operation at a fixed frequency avoids chromatic aberrations. We show that full 2π phase coverage at near-unity transmittance is feasible. First, we introduce suitable material platforms and layouts, and then discuss a modus operandi to retrieve metasurface designs for printing arbitrary patterns. In the Appendix C, we discuss the necessary steps for an experimental realization.

Metamaterials are artificial structures assembled from rationally designed building blocks, often aiming to extend the capabilities of their bulk counterparts [251]. In a sense, besides the intrinsic bulk properties, the design of the metamaterial define its physical properties. This is in contrast to the bulk materials, whose properties are simply defined by the actual material. Closely related is the notion of effective constitutive parameters, i.e., to homogenize the complex structure and to replace it with a homogeneous material that has effective properties such that the homogeneous material offers the same optical response as the actual metamaterial [251–253]. Originally, the field of metamaterials aimed to implement negative-index materials [254, 255], with the combination of electric and magnetic responses leading to simultaneously negative¹⁸ effective permittivity ϵ and permeability μ . Nowadays, the concepts of metamaterials are adapted to farther-reaching applications in physics, from tailoring the propagation of electromagnetic waves [256–261] to sound waves in acoustics [262–264] and material properties in mechanics [265, 266]. All lines of research benefit from the recent advances in fabrication techniques (compare Appendix B) and optimization approaches of metamaterial designs using computers¹⁹.

¹⁸Negative index metamaterials at optical frequencies are commonly realized with less restrictive conditions on permittivity and permeability, as it is difficult to obtain magnetic activity at such frequencies. For example, to focus electric fields, it is sufficient to have an effective material with $\epsilon = -1$ at arbitrary μ [256].

¹⁹Anisotropic metamaterials can be used to create so-called *hyperlenses* [267]. Such metamaterials overcome the diffraction limit inherent to conventional lenses by converting evanescent components of the wave to propagating waves. Sun and co-workers used a cylindrical hyperlens constructed from alternating Ag/Ti₃O₅ layers to demagnify the mask pattern [268, 269].

7.1 Introduction to optical metasurfaces

Within this broad area of metamaterials, here we investigate nanoscatterers arranged in periodic two-dimensional arrays, commonly called *metasurfaces* [270–273]. This subclass of metamaterials consists of one or few layers of functional planar structures, and is hence compatible with large-volume fabrication methods [272]. The optical metasurfaces commonly consist of individual building blocks or *metaatoms* located in a unit cell with sub-wavelength size. Despite the small layer thickness, a strong interaction between an incident electromagnetic wave and the metasurface can be achieved. The distinct and crucial feature of metasurfaces is the capability to introduce spatial variations in the wavefront emerging in transmission or reflection by spatially varying geometries.

7.1.1 The physics of optical metasurfaces

In this section, we want to provide a brief overview of state-of-the-art optical metasurfaces. As it is a vivid topic with the contributions of many research groups, we can only scratch the surface of a broader research field; for more in-depth information, we advert to a list of reviews, aiming at various aspects of optical metasurfaces [271–283].

It is the unique properties of planar metamaterials that attracted increasing interest in recent years: They allow to introduce abrupt modifications of the properties of light (compare Fig. 2.15) on length scales of about one free-space wavelength. This is the crucial difference to conventional optical devices, where the change in polarization, amplitude, phase, or direction emerges from propagation through layers typically much thicker than the wavelength. Two distinct advantages of metasurfaces are the elimination of undesired diffraction orders and the possibility to alter the magnetic field components as well, enabling impedance-engineering to minimize reflection losses [271].

The applications of optical metasurfaces are diverse; they often aim to mimic or replace existing bulk optical elements. Hence, the applications are manifold: From metalenses [284] for imaging over polarization control [285, 286] to holography [287, 288]. Before we address the operation mechanisms in detail, we discuss material classes used in optical metasurfaces.

- **Plasmonic metasurfaces** are built from small metallic nanoscatterers whose optical response is dominated by localized plasmonic resonances of the individual metaatoms [289]. The displacement of the conduction electrons around the equilibrium position generates both a polarization and a restoring force. Upon excitation by an external field, the conduction electrons perform a collective motion. This response can be approximated by a Lorentz oscillator. Depending on the spectral location of the Lorentz peak with respect to the operating frequency, a strong phase shift is induced.

The main disadvantage of plasmonic metasurfaces is the presence of Joule losses inherent to the material that lead to absorption losses, often limiting the transmission efficiencies to below 10%. An encouraging approach based on multipole engineering demonstrated recently an efficiency above 40% [290].

- **All-dielectric metasurfaces** are made from high-permittivity dielectric materials, with low inherent absorption losses. The notion of dielectric resonators is already 80 years old [291], and has gained increasing attention over the last two decades. Depending on material properties and the shape of the nanoscatterer, such resonators support magnetic and electric *Mie*-like resonances [272]. The lowest order resonance for spherical building blocks is typically the magnetic dipole mode, arising from circular displacement currents [292]. The resonances are engineered varying the geometrical parameters, for example the aspect ratio for nanocylinders.

- **Hybrid metal-dielectric metasurfaces** aim to combine the best of both worlds [275]: High Purcell factors and highly directive emission at near-unity efficiencies have been demonstrated for hybrid nanoantennas [293, 294].

Which physical mechanism is responsible for the modification of optical waves on a sub-wavelength scale? In general, three categories can be distinguished:

- **Huygens' metasurfaces** are based on the interference of incident light with induced electric and magnetic dipole radiation, which strongly affects the directional characteristics of scattering. If the dispersion in the electric and the magnetic dipole moment is equal in magnitude and phase, the interference leads to a complete cancellation of backward scattered light over a broad spectrum and every light is scattered in the forward direction. This promises high efficiency metasurfaces. Dielectric metasurfaces with a suitable design show such characteristics. As a consequence, the transmittance is close to unity, and the phase varies by 2π over the resonances²⁰ [275]. Polarization-insensitive holographic projections have been demonstrated [222, 296]. Also, as most metasurfaces are operated at a fixed frequency, the phase of the transmitted signal can be controlled by changing the periodicity. This is the key to implement any holographic picture.
- **Waveguide-confinement metasurfaces** rely on the non-resonant propagation delay in high-permittivity dielectric nanostructures [297–299], and have already been discussed within the framework of high contrast optical gratings over 20 years ago [176, 299–302]. Multi-mode propagation inside the scatterers dominates the optical response. With a height in the order of one wavelength, the phase difference can reach values of up to 2π . In principle, the phase difference is fundamentally only limited by the height-to-width ratios that can be fabricated. Here, high permittivities enhance the effect and hence allow to reduce the height.

To tune the phase, geometrical parameters as the radius of nanocylinders can be varied, which corresponds to a waveguide with a varying effective refractive index. The high permittivity guarantees that the fields are mainly concentrated inside the waveguide, and hence coupling to an adjacent nanoscatterer that would act as an adjacent waveguide is low. A low coupling enables to simulate the transmission characteristics in a global design approach for a perfectly periodic arrangement, with negligible changes for non-periodic designs where the adjacent nanoscatterers actually vary in size²¹.

- **Geometric or Pancharatnam-Berry phase metasurfaces** [307, 308] are based on the change in polarization by suitably rotated anisotropic scatterers. The main difference to the waveguide-confinement metasurfaces is the mechanism responsible for the phase shift: Here, all metaatoms have the same geometrical shape, and the orientation (mostly the rotation) of the individual metaatoms defines the phase. This structural birefringence is hence independent of the wavelength, and is thus frequently used to realize broadband metasurfaces.

The mechanism is presumably best understood within the framework of Jones calculus. For an anisotropic scatterer with scattering coefficients t_o and t_e in transmission along the two principal axes, the Jones matrix in a linear base reads as [272, 309, 310]

$$\hat{M} = \hat{R}(\alpha) \begin{pmatrix} t_o & 0 \\ 0 & t_e \end{pmatrix} \hat{R}(-\alpha) \quad (7.1)$$

²⁰If only an electric resonance contributes to the optical response, as it is the case for symmetric plasmonic particles [295], the maximum phase variation is π .

²¹There are some approaches to correct for the nearest-neighbor coupling in the design, see [303–306].

with $\hat{R}(\alpha)$ indicating a rotation by an angle of α ,

$$\hat{R}(\alpha) = \begin{pmatrix} \cos \alpha & \sin \alpha \\ -\sin \alpha & \cos \alpha \end{pmatrix}. \quad (7.2)$$

If we now consider the illumination of a Pancharatnam-Berry phase metasurface with light that is left or right circularly polarized, $\mathbf{E}_i^{L/R}$, the transmitted field $\mathbf{E}_t^{L/R}$ is given as [272]

$$\mathbf{E}_t^{L/R} = \hat{M} \mathbf{E}_i^{L/R} \quad (7.3)$$

$$= \frac{t_o + t_e}{2} \mathbf{E}_i^{L/R} + \frac{t_o - t_e}{2} \exp(mi 2\alpha) \mathbf{E}_i^{R/L} \quad (7.4)$$

with $m = 1$ for left and $m = -1$ for right circularly polarized light. The first summand is the contribution of light scattered in the same polarization. More important is the second summand, which describes the contribution of the *cross-polarized light*. If this second component is selected (in experiments in transmission using a quarter-wave plate and a polarizer), the entire 2π can be assessed by rotating the anisotropic scatter by up to $\alpha_{\max} = \pi$.

7.1.2 Wavefront shaping

We want to discuss how the wavefront can be shaped behind a metasurface, assuming plane wave illumination. This requires to derive the optical characteristics of individual metaatoms arranged in a periodic array. As it turns out, for our purposes it is beneficial to translate the effective material parameters (permittivities and permeabilities) to the language of diffractive optics. Hence, we characterize the individual metaatoms in terms of the phase difference $\Delta\phi$ (compared to free-space propagation) and the amplitude of the transmitted wave (similar to phase-shift masks (PSMs), compare Section 2.3.2.1).

This is a valid approach, as the sub-wavelength size of the unit cells ensures that the reciprocal lattice vectors are larger than the wavenumber k_0 in vacuum. Hence, all diffraction orders – except for the zeroth order – are evanescent outside the metasurface. Thus, we are able to directly apply well-established concepts of photomask design to optical metasurfaces.

Let us consider an example to showcase the operating principle of wavefront manipulation using optical metasurfaces. We consider a metasurface at the interface between two media, and arrange the nanoscatterers in a way that $\Delta\phi$ forms a phase gradient $\frac{d(\Delta\phi)}{dx}$ along x . Fermat's principle of stationary phases allows to derive the *generalized law of refraction* as [312–314]

$$k_{t,x} - k_{i,x} = k_0 (n_t \sin \theta_t - n_i \sin \theta_i) = \frac{d(\Delta\phi)}{dx} \quad (7.5)$$

and similar expressions in reflection and for an additional phase gradient in y -direction [313]. The angles and refractive indices are defined in Fig. 7.1a. $\mathbf{k}_{t/i}$ are the transverse wavevectors and $k_0 = 2\pi/\lambda_0$. Hence, by introducing a spatially varying phase difference, the direction of a transmitted wavefront can be tuned, independent of but in addition to the angle of incidence. For the trivial case of $\frac{d(\Delta\phi)}{dx} = 0$ (no metasurface), the expressions reproduce Snell's law.

To put it in other words, the metasurface adds an effective wavevector $k_{\text{eff}} = \frac{d(\Delta\phi)}{dx}$ to the transverse wave components, which are conserved over the interface for isotropic media. This anomalous refraction is the starting point for more complex wave manipulation, as we will discuss in the following sections.

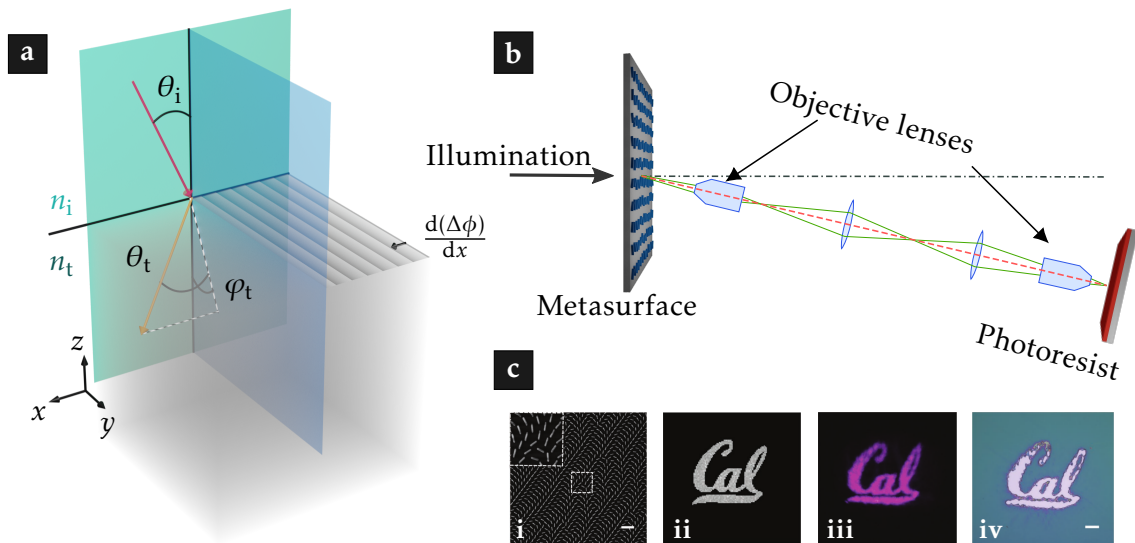


Figure 7.1: Beamshaping and projection lithography using optical metasurfaces. **a** Generalized law of refraction. A phase-gradient metasurface at an interface between two media with refractive indices n_i and n_t leads to anomalous refraction (here shown in transmission only). $\varphi_t = 0$ in the absence of a phase gradient in the y -direction. **b** Optical setup for off-axis metasurface projection lithography. The illumination consists of circularly polarized light at $\lambda = 380$ nm. The optical system behind the metasurface images the field to the photoresist, with a demagnification factor of 20. Adapted from [311]. **c** From left to right: **i** SEM image of fabricated metasurface. Scale bar indicates 500 nm. **ii** Holographic test pattern. **iii** Measured field distribution in an intermediate focal plane (between the two lenses in **b**). **iv** Exposed photoresist. Scale bar is 10 μ m in length. Reprinted from [311] with permission.

7.1.3 Advantages of all-dielectric metasurfaces in proximity lithography

We aim to replace traditional PSMs relying on the phase difference a wave picks up when traversing through a bulk material (see Fig. 2.10) by flat optics, i.e., designer optical metasurfaces. To the best of our knowledge, the first experimental application of metasurfaces in optical projection lithography is reported on in Ref. [311]: Deng and co-workers used Si nanorods as building blocks for a Pancharatnam-Berry phase metasurface with 32 phase levels. As shown in Fig. 7.1b, they used an inverse Keplerian telescope to demagnify the transmitted wavefronts to the photoresist layer, with a demagnification factor of 20. The off-axis configuration ensures that transmitted light that is not diffracted does not expose the photoresist. Figure 7.1c shows the excellent reproduction of the test pattern in the photoresist.

As mask aligner lithography involves full field prints at a small separation between photomask and resist-coated substrate, the use of imaging optics as used in this prior literature, therefore, is not possible. Figure 7.2 illustrates how a metasurface might be used to modify the wavefronts in proximity lithography. The lithographic pattern we like to print is encoded in the arrangement of dielectric metaatoms on a fused-silica substrate. The field behind the metasurface is the multiplication of the incident field (for instance a plane wave) with the complex transmission coefficient of the metaatom in a periodic array. To guarantee polarization-independent operation, we rely on centrosymmetric scatterers²² [298]. All nanocylinders have the same height that is in the order of the exposure wavelength. However, they vary in radius (indicated by different shades of blue and green in Fig. 7.2b) within the 2D array, which modulates the phase difference.

²²An interesting alternative based on anisotropic nanostructures is discussed in [315].

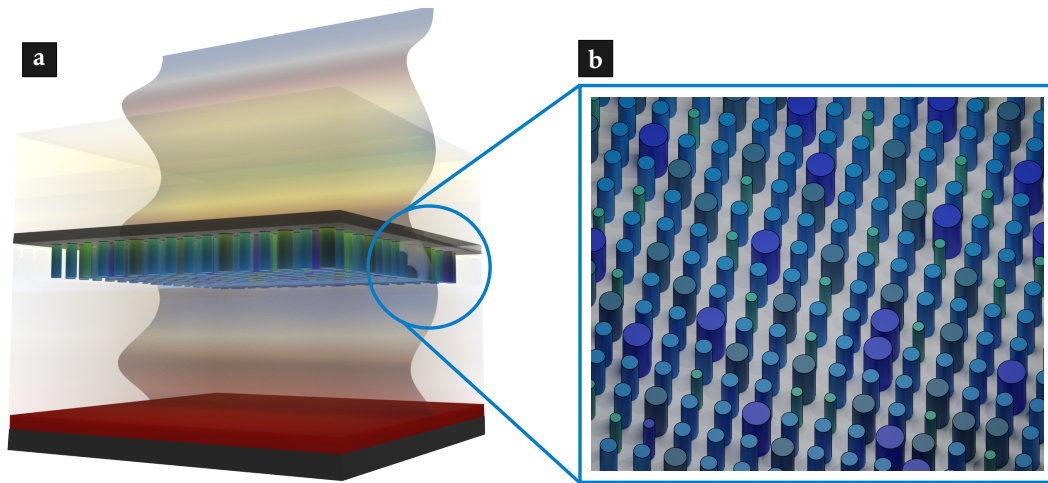


Figure 7.2: Schematic illustration of a metasurface used in proximity lithography.
a Analogue to a multilevel PSM, the metasurface locally modifies the phase of the transmitted wavefront. The superposition of the wavefronts in the photoresist performs the exposure. The illustration is not to scale.
b An array of nanocylinders forms a polarization-insensitive metasurface. Each individual nanocylinder, indicated by different shades of blue and green, corresponds to a specific complex transmission coefficient characteristic for this unit cell. The arrangement of the nanocylinders is determined from a CGH and contains the structural information of the mask structures.

Several advantages of such a metasurface photomask over conventional masks can be identified. The most striking advantage is the implementation of a quasi-continuous range of phase differences (i.e., transmission coefficients with amplitude close to 1 and full 2π phase coverage) in a single fabrication cycle. Conventional multi-level DOEs are fabricated in sequence, i.e., alternating lithographic and etching steps. The step-to-step alignment and the etch depth accuracy limits the applicability of this procedure and increases the fabrication costs. As a consequence, mostly binary PSMs that can encode only two different phase values are applied in photolithography.

In contrast, the nanocylinders with varying radii can be fabricated in a single process, with the number of phase steps only limited by the inherent resolution and the registration accuracy of the underlying fabrication process (see Appendix C). As we show in the following section, metasurfaces in the UV can be designed in a way that they show near-unity transmittance, enabling highly efficient lithographic prints. The sub-wavelength size of the individual unit cells renders the concept robust to fabrication errors, as the information is redundantly stored across the photomask.

Furthermore, we introduce a hybrid metasurface design that combines planar layers of a plasmonic absorber and a dielectric nanocylinder. Such a hybrid platform allows the complete control over the transmission coefficients in the entire complex plane, greatly increasing the opportunities of metasurface proximity lithography.

7.2 Layout of metasurface building blocks with complex transmission coefficients and 2π phase coverage working in the deep ultraviolet

First, we stipulate a list of necessary requirements on optical metasurfaces for efficient proximity lithography. We demand

1. a single-layer metasurface working in the UV, to comply with standard photoresists and UV light sources (compare Section 2.3.1),

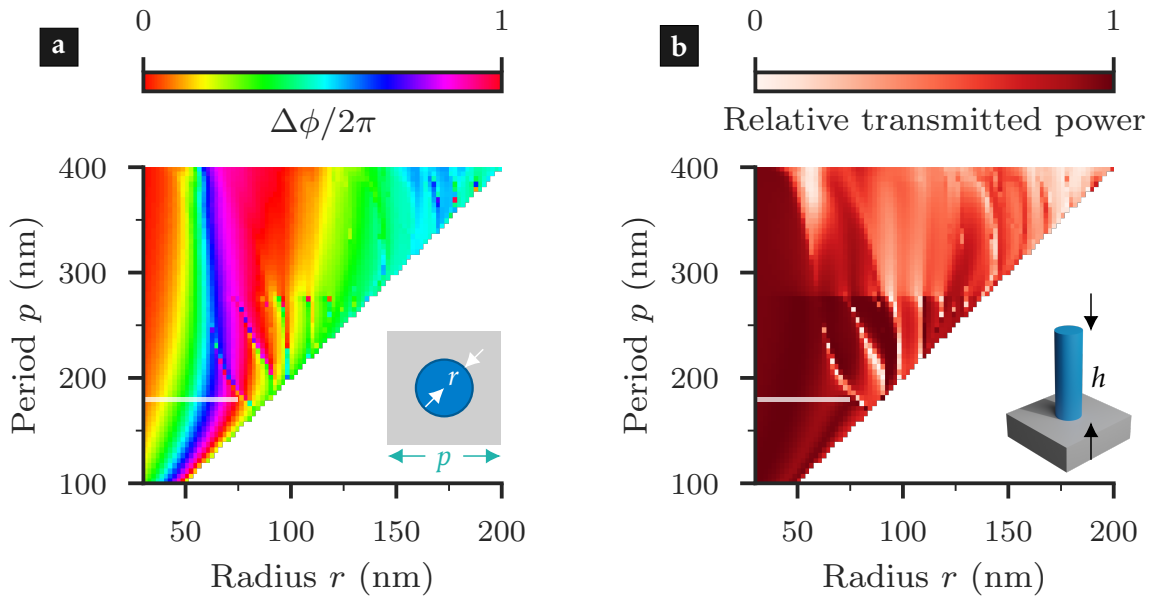


Figure 7.3: Complex transmission coefficient of a TiO_2 metasurface at $\lambda_0 = 405\text{ nm}$, decomposed in **a** the phase difference $\Delta\phi$ and **b** the transmitted power. We simulate different radii r and periods p of TiO_2 nanocylinders in a quadratic unit cell on a SiO_2 substrate. The height of the nanocylinders is fixed at $h = 400\text{ nm}$. The insets illustrate the geometry, in **a** with a top view and **b** a rendered three-dimensional image of one unit cell.

To avoid that the nanocylinders touch each other, we impose $2r \leq p$; as a fabrication constraint, we impose $r \geq 30\text{ nm}$ to allow for the fabrication of the metasurface with conventional e-beam lithography. The white lines denote a period of $p = 180\text{ nm}$ with full 2π phase coverage at near-unity transmission for $30\text{ nm} \leq r \leq 75\text{ nm}$.

2. a lossless material platform with near-unity transmittance to maximize the power throughput and reduce thermal effects due to heating,
3. full 2π phase coverage at a single wavelength in transmission,
4. a high permittivity to achieve reasonable height-to-width ratios,
5. a polarization-independent operation to avoid the implementation of additional polarizers reducing the efficiency,
6. a low sensitivity to variations in the illumination angle, and
7. no additional optical elements between the metasurface and the wafer (free-space propagation).

The first two items require a material with negligible absorption at the wavelength of choice. We select $\lambda_0 = 405\text{ nm}$ for three reasons: (i) This wavelength is close to the h -line of high-pressure mercury lamps (compare Table 2.1), (ii) compact high power solid-state laser sources are available as well²³, and (iii) suitable high-permittivity dielectrics have been identified and demonstrated [297, 301, 315–324].

Two materials of particular interest are amorphous titanium dioxide, TiO_2 , and gallium nitride, GaN , with permittivities of $\epsilon_{\text{TiO}_2} = 6.92$ [316] and $\epsilon_{\text{GaN}} = 6.50$ [325] at λ_0 , respectively. Both materials can be grown by atomic layer deposition (ALD) on fused silica substrates (see also Appendix C). At lower wavelengths of about 387.4 nm and 364.6 nm , respectively, the onset of interband transitions strongly increases the material absorption [311]. In the following, we discuss TiO_2 metasurfaces, as fabrication procedures with

²³For example *iBeam smart* from TOPTICA PHOTONICS.

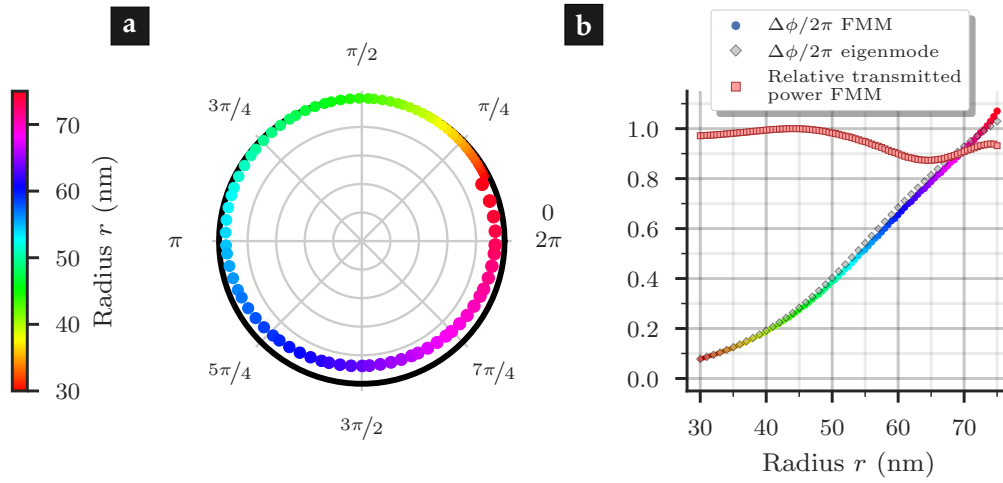


Figure 7.4: Design of a TiO_2 metasurface for UV proximity lithography, with $p = 180$ nm and $h = 400$ nm. The data presented here corresponds to the white line indicated in Fig. 7.3.

a Polar plot of the transmission coefficients in the complex plane. The size and the color of the markers indicate the radius of the nanocylinder. The bold black ring indicates an amplitude of unity.

b The same data, decomposed into transmitted power and phase difference $\Delta\phi$. In addition, gray diamonds indicate the phase difference obtained from two-dimensional waveguide simulations.

height-width ratios and low sidewall roughness have been demonstrated [297, 316]. Due to the similarity of the permittivities, the simulation results for GaN are comparable.

Here, we use a metasurface design relying on waveguide-confinement (see Section 7.1.1). The non-resonant character of light manipulation ensures a low dependence on the angle of incidence, in contrast to Huygens' metasurfaces. The close proximity of metasurface and photoresist results in insufficient space for additional optical elements to filter out the co-polarized light in Pancharatnam-Berry phase metasurfaces.

We consider here TiO_2 nanocylinders arranged on a quadratic two-dimensional grid, as illustrated in Fig. 7.2 and initially proposed in [297]. Here, we use a height of $h = 400$ nm, and the phase is controlled by changing the radii of the nanocylinders.

To simulate a perfectly periodic arrangement of unit cells, each one containing a single nanocylinder, we apply the Fourier modal method (FMM), as introduced in Section 3.2.1 ($M = N = 15$). For the graph shown in Fig. 7.3, we systematically vary the period p as well as the radii r and retrieve both the phase difference $\Delta\phi$ (Fig. 7.3a) and the transmitted power (Fig. 7.3b). We observe a 2π phase coverage when varying the radii from 30 nm to about 90 nm, only weakly depending on the period. However, the transmitted power depends strongly on p : For $p > \frac{\lambda_0}{\sqrt{2}}$, the (1,1)-diffraction order is no longer evanescent and reduces the transmitted power in the zeroth diffraction order considerably. In addition, several Mie-like resonances of isolated nanocylinders influence the transmitted power as well. By selecting $p = 180$ nm and $30 \text{ nm} \leq r \leq 75 \text{ nm}$, we obtain full 2π coverage at near-unity transmittance. Hence, the minimum distance between the surfaces of the nanocylinders is 30 nm.

We analyze this configuration in Fig. 7.4 in more detail. Figure 7.4a shows the transmission coefficients in the complex plane, and in Fig. 7.4b the same data is presented decomposed into transmitted power and phase. We observe near-unity transmittance and a nearly linear dependence of the phase difference on the radii. In addition, we plot in Fig. 7.4b

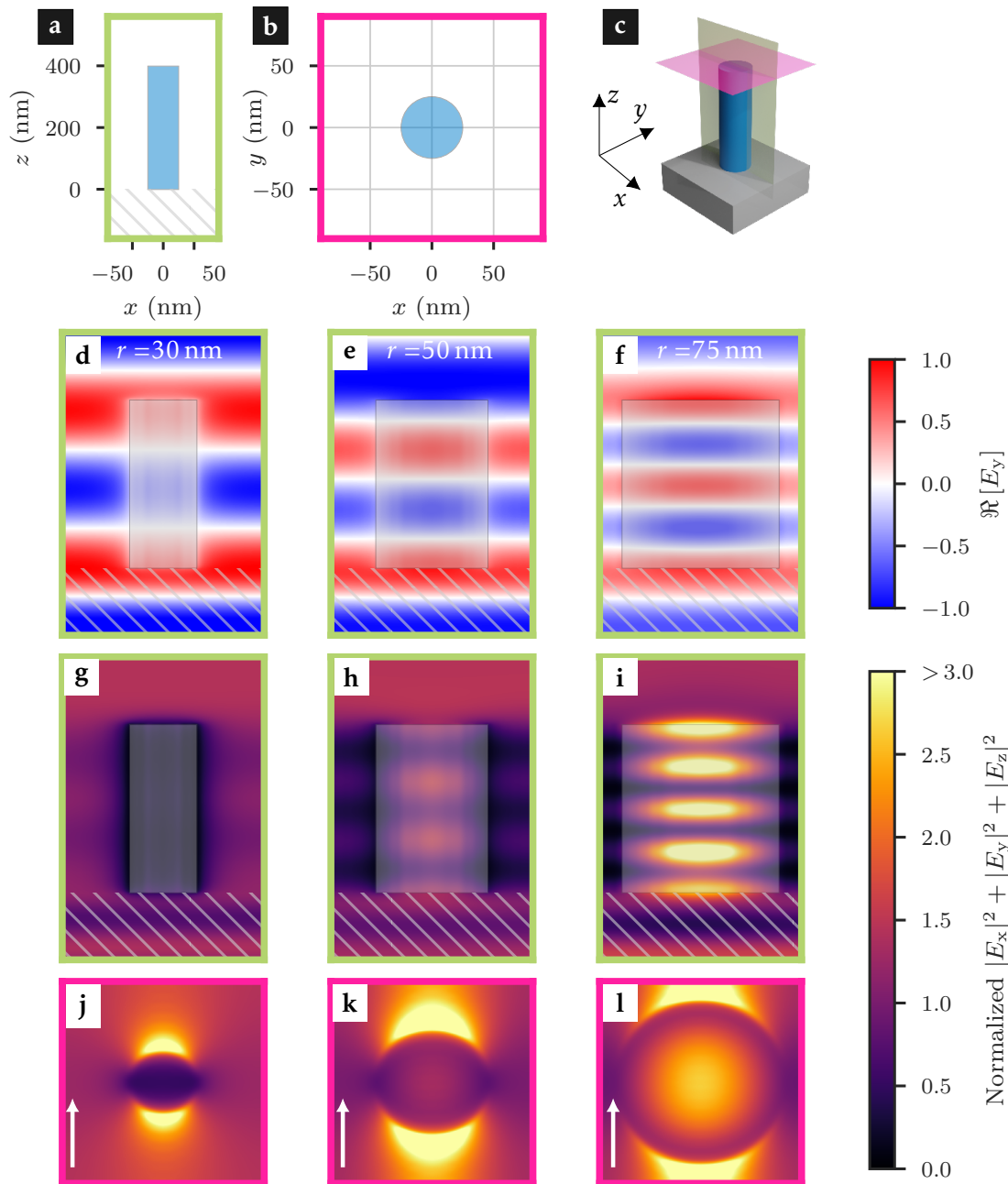


Figure 7.5: Field distribution in and around the nanocylinders, as obtained using the FMM. The hatched area visualizes the substrate, the illumination is from the bottom and polarized in y -direction. The aspect ratio is not to scale, and the intensities are normalized to the incident field.

a – c Sketch of the geometry. **a** Plane through the middle of the nanocylinders (green box). **b** Plane just above the nanocylinders (pink box). **c** 3D sketch with the annotated axes.

d – f Real part of the y -component of the electric field for $r = 30$ nm, 50 nm, and 75 nm. The graphs illustrate the phase differences light picks up when propagating along the nanocylinders. A 2π phase difference in the field above the cylinder emerges when the radius is changed between $r = 30$ nm and 75 nm, once more illustrating the complete phase coverage of this particular metasurface design.

g – i Field intensity $|E_x|^2 + |E_y|^2 + |E_z|^2$ in a cut through the middle of the nanocylinders. The gray rectangle indicates the device dimensions. The field is mainly located inside the high-permittivity dielectric, and for large radii a strong field enhancement emerges.

j – l Field intensity in a plane parallel to the substrate just above the nanocylinders. The white arrows denote the direction of polarization.

$\Delta\phi$ as obtained from two-dimensional waveguide simulations, according to

$$\Delta\phi = k_0 [n_{\text{eff}}(r) - 1] h \quad (7.6)$$

with $k_0 = 2\pi/\lambda_0$. The effective refractive index $n_{\text{eff}}(r)$ is obtained from a two-dimensional finite element solver (*Comsol Multiphysics 5.4*) with periodic boundary conditions. We observe an excellent agreement between both approaches, with a maximum difference of 0.08π . As discussed in Section 7.1.1, the nanocylinders act as individual mono-mode waveguides [297, 302, 326, 327], truncated to a height of h .

In other words, according to Eq. (7.6) we can select h in a way that the full 2π phase shift is covered. A height of 400 nm is a reasonable choice for TiO_2 nanocylinders at the wavelength of interest. Figure 7.5 shows the field distributions inside and on top of the nanocylinders for three selected radii, simulated using the FMM. In Fig. 7.5d–f, the phase shift as a function of cylinder radius is demonstrated, again illustrating the full 2π coverage. Figure 7.5g–i shows that the electric field is mainly concentrated inside the high-permittivity nanocylinders, in accordance with the variational principle [328].

Here, the metasurface is supposed to be operated under normal incidence only. As discussed in Sections 2.3.1 and 4.4.1 in detail, this can be implemented using for example an imaging homogenizer, although a finite angular spectrum can emerge. Figure 7.6 shows that the performance of the metasurface is insensitive to small variations in the illumination half angle θ . The transmitted power in the zeroth order starts to drop for $\theta > 6^\circ$, and a resonance appears for $\theta > 8^\circ$ and larger radii. However, for $\theta \leq 2^\circ$, no considerable effect is observed.

Up to this point, we merely considered phase-only metasurfaces. However, for DOEs and holograms with increased accuracy and lower noise, complex amplitude transmission coefficients are desirable [281]. For this purpose, we design a hybrid metasurface that combines plasmonic and dielectric nanostructures. The main idea is based on a division of

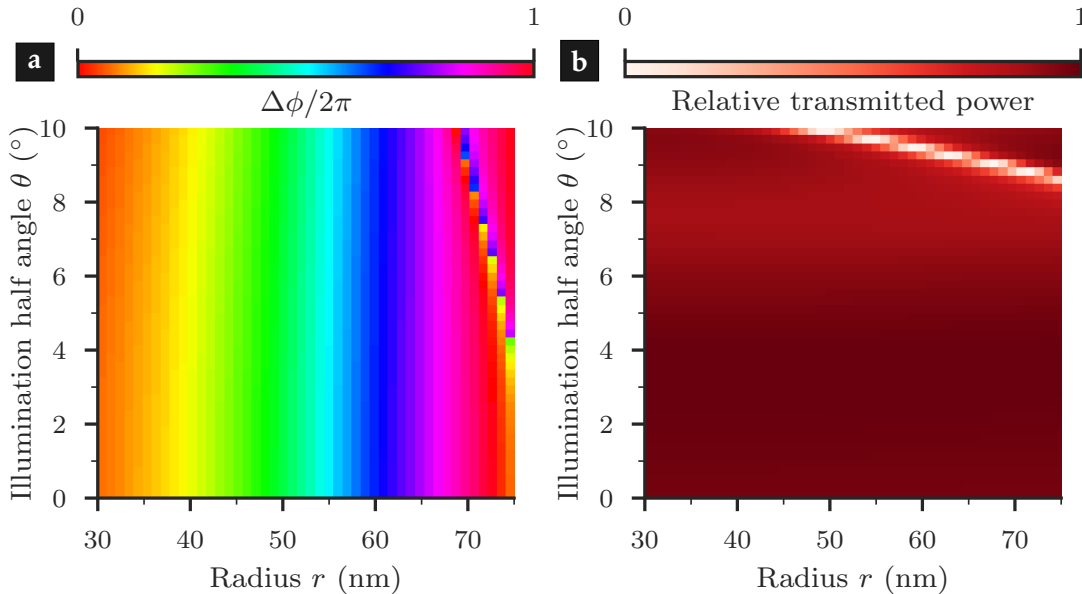


Figure 7.6: Performance of the metasurface as a function of the angle of incidence θ , equal to the illumination half angle in proximity lithography (compare Fig. 7.1a), and the nanocylinder radius r .

a Phase difference and **b** relative transmitted power. We observe that up to $\theta \approx 8^\circ$ and $r \approx 70$ nm the metasurface still operates as desired, with phase difference and transmitted power close to the values obtained at normal incidence.

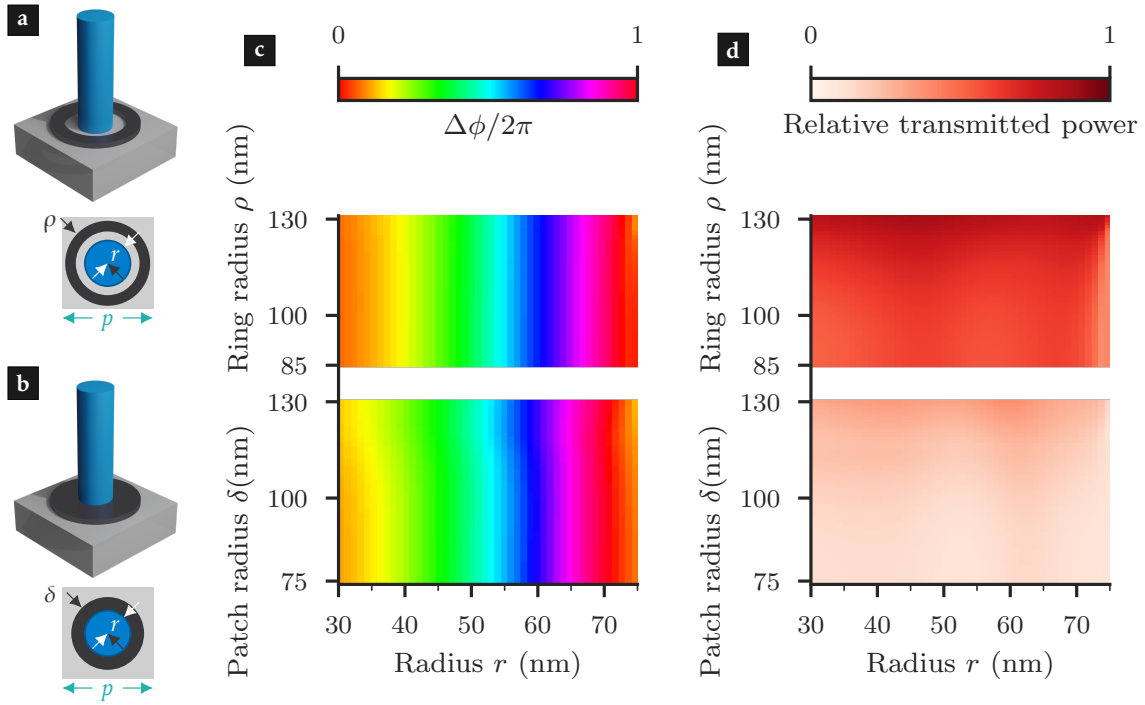


Figure 7.7: Metasurface design for complete control over the complex transmission coefficients. As before, $h = 400$ nm and $p = 180$ nm. In contrast to the design shown in Fig. 7.3, a thin absorber layer (Cr, thickness $t_{\text{abs}} = 20$ nm) is added in two different configurations: **a** Ring design for low absorption and **b** patch design for high absorption. In the patch design, the nanocylinder are located on top of the absorber layer. For radii greater than $p/2 = 90$ nm, the parts of the absorber layer exceeding the size of the unit cell are cut off. **c** Phase difference $\Delta\phi$ and **d** relative transmitted power as a function of nanocylinder radius r and patch radius δ /outer ring radius ρ . The inner ring radius is fixed at 75 nm. The phase difference is mainly unaffected by the absorber structure.

labor: A thin plasmonic absorber layer allows to modify the amplitude, and the dielectric nanocylinders enable phase modifications, as discussed before.

For ideally complete control over the transmission coefficients in the complex plane, we introduce an absorber/reflector design based on two configurations, as shown in Figs. 7.7a and 7.7b. In the following, we denote the plasmonic structure solely as absorber, while also considerable reflection is involved, which causes no problems in mask aligner lithography.

The absorber consists of a chromium layer with a thickness of 20 nm. Just as for the nanocylinders, all absorber structures can be fabricated in a single process (see Appendix C for details). For a high relative transmitted power, $> 60\%$ of the incident power, we introduce a ring surrounding the nanocylinder, as presented in Fig. 7.7a, with varying outer ring radius ρ . For a further reduction of the power, we use a patch underneath the nanocylinder, as shown in Fig. 7.7b, with varying patch radius δ .

The FMM simulations of the design reveal that the phase difference is insensitive to the absorber layer and depends only on the radius r of the nanocylinders (see Fig. 7.7c). In contrast, the relative transmitted power depends only weakly on r (see Fig. 7.7d). Selecting seven absorber configurations, each with 23 different nanocylinder radii, allows to cover a large part of the complex plane, as shown in Fig. 7.8.

The polar plots of Figs. 7.4a and 7.8a illustrate the quasi-continuous distribution of transmission coefficients. We store these values in a look-up table as fundamental building blocks of the metasurface, and discuss in the following section how to design a metasurface that prints an (arbitrary) test pattern.

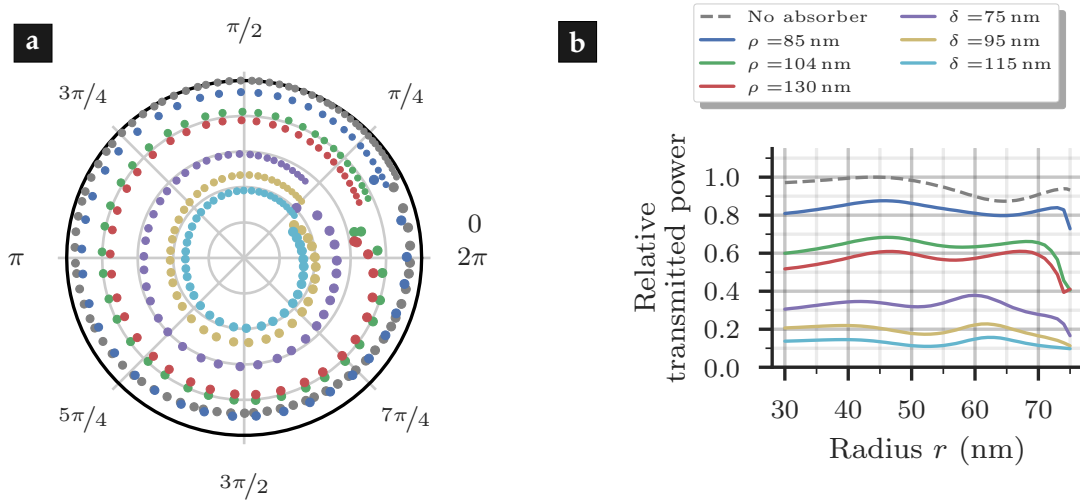


Figure 7.8: Parameter study for complete control over the complex transmission coefficients. The plot shows the data of Fig. 7.7 for six selected absorber configurations and the design without absorber (gray circles and dashed line).

a Polar plot of the transmission coefficient in the complex plane. Except for small amplitudes, the complete complex plane is covered.

b Relative transmitted power as a function of nanocylinder radii r . We observe that the transmitted power follows a weak dependence on the radii, except for $r > 70$ nm.

7.3 Designing lithographic metasurfaces with an iterative soft-quantized propagation algorithm

Equipped with a building set of complex transmission coefficients as a look-up table, connecting the geometry to the optical performance, we need to retrieve suitable photomask layouts. Evidently, we can apply optical metasurfaces directly to replace conventional PSMs, as for instance the RO-PSMs presented in Chapter 5. Instead, we want to follow a different path here, i.e., adapting CGHs to proximity lithography²⁴. This method allows for printing arbitrary patterns, and has been adapted to mask aligner lithography by Weichelt *et al.* using conventional PSMs [56].

The basic principle is to encode the desired pattern in a phase-amplitude or phase-only metasurface, with the goal to modify the wavefront transmitted by the metasurface. Then, the coherent superposition in the image plane (where the substrate with the photoresist is positioned) results in the desired pattern distribution.

The task at hand is to solve the inverse problem: Starting from the desired intensity distribution in the image plane, how can a corresponding diffractive element or CGH be designed? If we had the complete complex plane of transmission coefficients at our disposal, the solution would be quite simple: we would perform the backpropagation of the image field to the hologram, and translate the corresponding distribution of complex transmission coefficients to the parameters defining the metasurface.

However, as presented in Section 7.2, depending on the fabrication resolution only a subset of coefficients covering the complex plane can be used. Since the invention of the CGH by Lohmann and colleagues in the 1960s [331, 332], a large variety of approaches emerged to overcome this restriction [112, 333–337]. Some of these methods are based on a Fourier transformation for wave propagation, and hence are limited to the far-field.

²⁴We refrain from using the term *holographic lithography*, as it is commonly used in the context of mask-less interference lithography [329, 330]. However, we still use the term *hologram* for the photomask design.

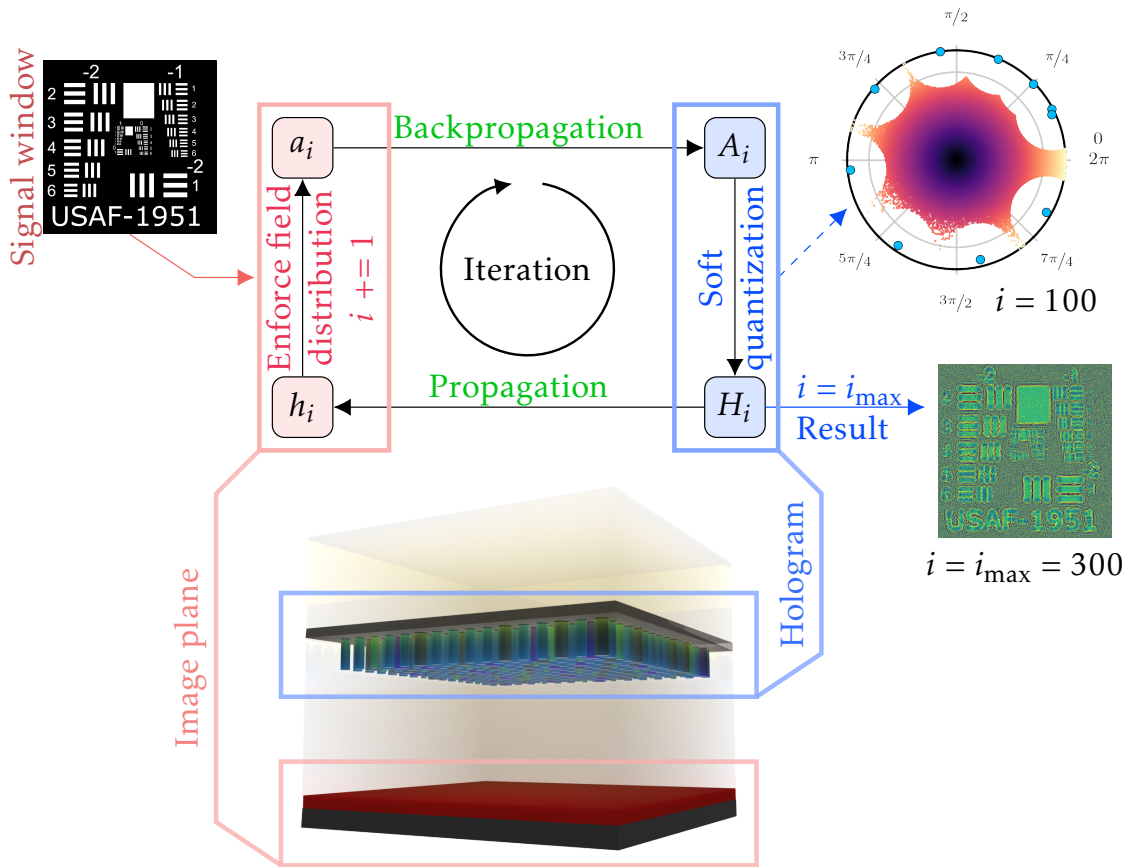


Figure 7.9: Iterative propagation algorithm to retrieve the mask configuration, given a subset of complex transmission coefficients. The goal is to obtain the distribution of metasurface elements in the hologram plane (blue box) that projects the desired image (signal window, top left) to the image plane (red box). For the propagation of the field distribution, we apply the ASM. Soft quantization iteratively restricts the transmission of each pixel to the subset of predefined coefficients (blue circles in top right graph, shown here after completing one third of all iteration steps). The result is a hologram (right), here restricted to ten complex transmission coefficients corresponding to ten nanocylinder radii.

Here, we introduce an implementation of an iterative propagation procedure, adapted from the original Gerchberg-Saxton algorithm²⁵ [112], and adapt the implementation of Walther *et al.* reported on in the Supplementary Material of Ref. [115]. Initially, we constrain the set of transmission coefficients to a finite number (see Section 7.2), here $n_\phi = 10$.

The underlying idea is now to make use of the remaining degrees of freedom²⁶, i.e., the phase distribution in the image plane [338] to find a solution. As we are only interested in the absolute field irradiance, the phase distribution in the image plane is arbitrary and indeed a degree of freedom. As an input, we impose the desired irradiance distribution in the image plane. Iteratively, the constraints are applied, and the algorithm converges to a solution only consisting of the discrete set of transmission coefficients.

²⁵The Gerchberg-Saxton algorithm is known by many names; Ping-pong algorithm, methods of generalized projection, and iterative Fourier transform algorithm are only three terms often used in literature.

²⁶Other degrees of freedom could be used as well, for instance by separating the image into a signal window and the remaining area, where an arbitrary field is allowed. However, in proximity lithography, we often desire a 1:1 mapping of hologram and image, and the signal window covers the entire image.

The deterministic procedure to obtain the CGH comprises four steps that we want to introduce with the help of Fig. 7.9. The algorithm starts in the image plane by imposing the desired irradiance distribution of the lithographic pattern on an array of pixels. For our example here we use the 1951 USAF resolution test chart (left upper graph in Fig. 7.9, not to scale). Initially, the phase ϕ in the image plane is set to zero.

1. The field is subsequently backpropagated to the hologram plane. If the absolute amplitude of a pixel exceeds unity, it is shifted back to the unit circle of the complex plane to exclude gain during the propagation.
2. The soft quantization applies the constraints on the hologram, with regard to the look-up table of allowed transmission coefficients (see Section 7.2).
3. Forward propagation from the hologram to the image plane.
4. The desired irradiance distribution is enforced on the amplitude of the field, while keeping the phase distribution as obtained from the field propagation.

These four steps are iteratively repeated, and the algorithm is stopped after a fixed number of iteration steps (here $i_{\max} = 300$).

The algorithm now involves two important concepts we want to discuss in more detail. First, the repeated simulation of light propagation requires a suitable algorithm. The typical separation between hologram and image plane in mask aligner lithography amounts to about $g \simeq 30 \mu\text{m}$ (compare the discussion in Section 2.2.1). For the sake of our example, we consider a quadratic metasurface with a side length of $s = 180 \mu\text{m}$ (10^3 by 10^3 unit cells) at a wavelength of $\lambda_0 = 405 \text{ nm}$. From the Fresnel number N_F [339],

$$N_F = \frac{s^2}{4\lambda g} \simeq 667 \gg 1, \quad (7.7)$$

it follows that simulating wave propagation requires a rigorous method, and the Fresnel approximation ($N_F \sim 1$) is not valid. Hence, we use the angular spectrum method (ASM), as introduced in Section 3.2.2, assuming plane wave illumination. Please note that an extension to a finite angular spectrum is possible, as the individual building blocks operate just as well under oblique illumination (compare Fig. 7.6). However, modifications to the iterative algorithm are required, which are beyond the scope of our discussion here.

Second, we apply a soft quantization [115, 340] to impose the constraints on the transmission coefficients. The concept is depicted in the upper right graph of Fig. 7.9. Blue dots indicate the look-up table of $n_\phi = 10$ constrained coefficients. In each step, we calculate the distance between the transmission coefficient of each pixel (indicated by individual small dots, with colors yellow to black) to the closest blue dot. If this distance is below a certain threshold $d_{\text{th}}(i)$, the transmission coefficient is replaced by the corresponding constraint coefficient. We linearly increase $d_{\text{th}}(i)$ as a function of the number of iterations i , in a way that at $i = i_{\max}$ all pixels are being replaced [115].

Figure 7.10a shows the resulting hologram. The initial intensity distribution of the test pattern is still visible, with strong phase gradients emerging at the edges (see inset). To quantitatively assess the performance of the algorithm, we define the SNR in analogy to image processing as [341]

$$\text{SNR}_{\text{dB}} = 10 \log_{10} \left(\frac{\mu_S}{\sigma_N} \right), \quad (7.8)$$

with μ_S the mean of the signal power (white regions in the test pattern, Fig. 7.9) and σ_N the standard deviation of the background noise (black regions). Figure 7.10b presents the evolution of the SNR as a function of the number of iterations, together with the linearly

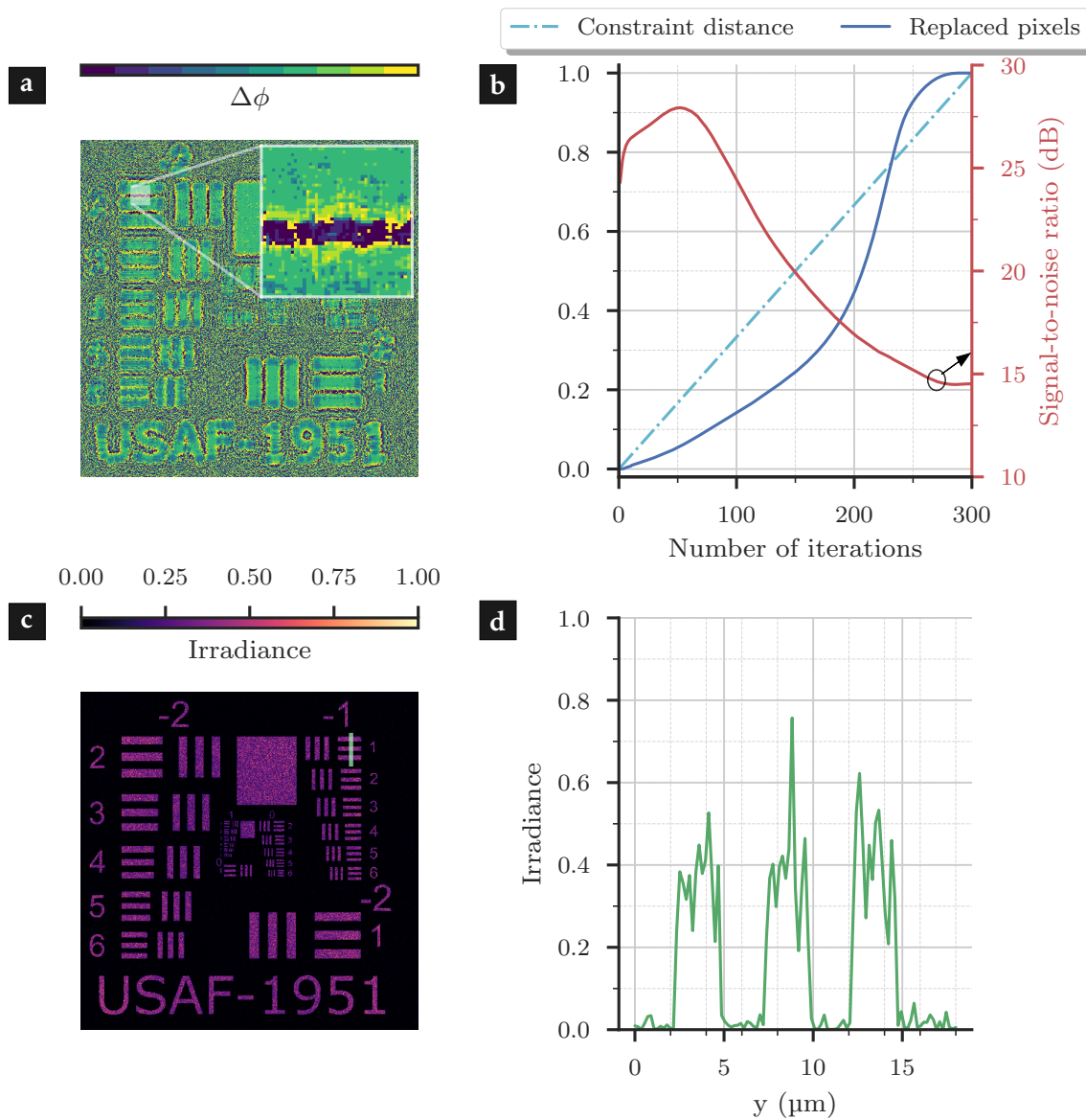


Figure 7.10: Example of iterative propagation algorithm results, assuming ten complex transmission coefficients for the metasurface for $30 \text{ nm} \leq r \leq 75 \text{ nm}$ and 5 nm increment. **a** Phase distribution of the resulting hologram. Colors indicate the ten different phase values, as obtained from the soft quantization (see top left graph of Fig. 7.9). The pixel size is equal to the period, 180 nm in our example. The total extent of the hologram is 10^3 by 10^3 pixels.

b The soft quantization restricts the possible transmission of the pixels to the predefined subset in an iterative procedure. The constraint distance d_{con} increases linearly as a function of the number of iterations, and the number of pixels replaced by the soft quantization rises. Restricting to a subset of transmission coefficients reduces the signal-to-noise ratio (SNR).

c Simulated irradiance distribution in the image plane for the hologram shown in Fig. 7.10a. The side length of the image is $180 \mu\text{m}$.

d Normalized irradiance distribution along the green line in **c**. We observe strong fluctuations both in the signal and the noise background.

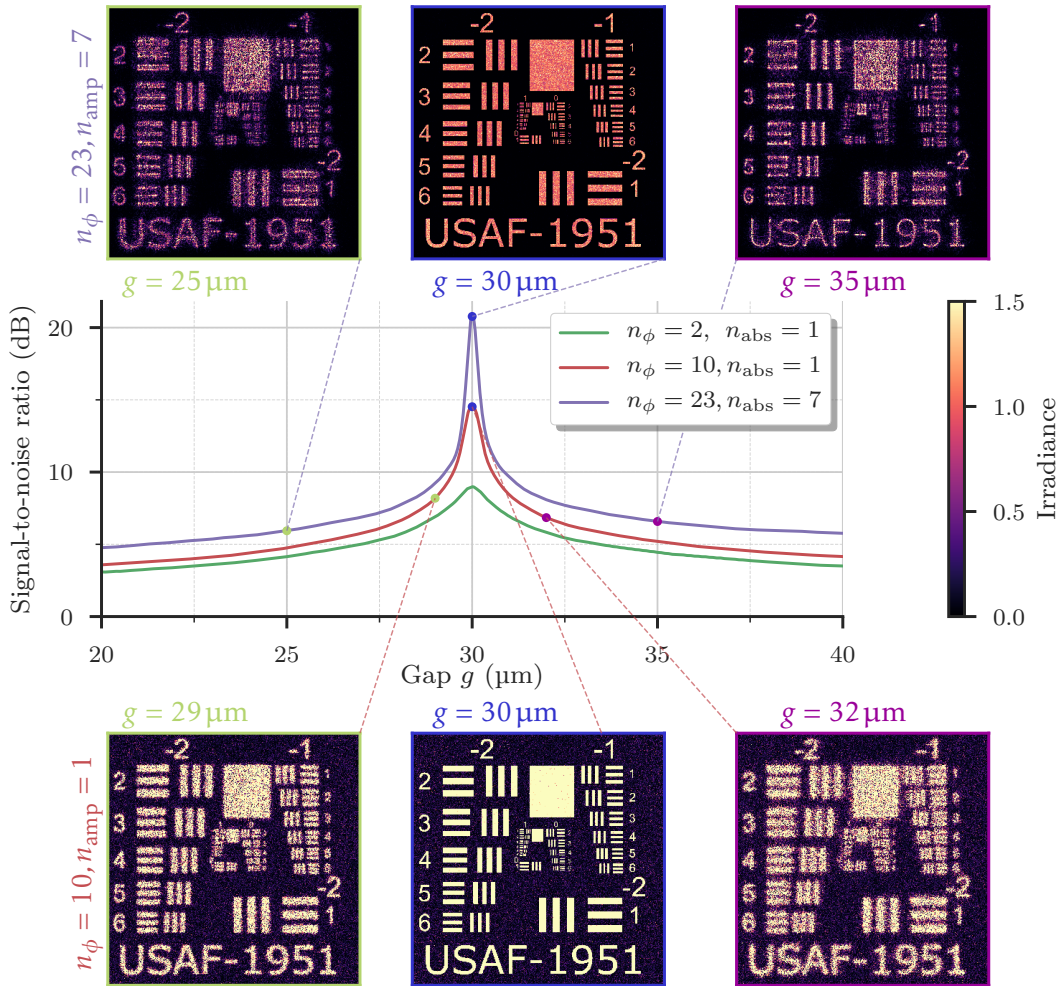


Figure 7.11: SNR for the simulated test pattern at varying proximity gaps g and three different subsets of transmission coefficients. For illustration, we chose a binary PSM (number of phase levels $n = 2$), the subset used for Fig. 7.10 ($n = 10$), and with additional amplitude modulation ($n = 23$, number of absorber configurations $n_{\text{abs}} = 7$). The mask patterns are optimized for $g = 30 \mu\text{m}$. The simulated test patterns for the amplitude modulation and the ten phase-only configurations are shown in the top and bottom row, respectively.

increasing d_{th} and the normalized number of replaced pixels. Initially, the SNR increases, as the iterative procedure improves the quality of the hologram. As the constraint distance grows, more pixels are replaced, and the SNR drops.

Figure 7.10c shows the resulting irradiance distribution, which closely resembles the initial test pattern, with a SNR of about 14.5 dB. However, the resulting signal shows significant fluctuations, as visible in the cross-cut in Fig. 7.10d. As discussed in [114], for a phase-only hologram ($n_{\phi} = 10$) the phase freedom is not sufficient to obtain a flat-top intensity distribution.

Apart from the SNR, the efficiency of the hologram is a quantity of interest. Here, we differentiate between the transmission efficiency, that is how much power of the incident wave contributes to the formation of the image, and the signal efficiency, which describes the power ending up in the desired area of the image. For the presented example the transmission efficiency is with 93.8% close to unity – almost all light transmitted by the metasurface contributes to the image formation. The deviation from unity mainly arises

as a consequence of the dip in the transmitted power for radii around $r = 60\text{ nm}$ (compare Fig. 7.4b). Due to the considerable background noise, the signal efficiency is 81.9% and thus clearly reduced compared to the transmission efficiency.

A third efficiency of interest is the diffraction efficiency, i.e., which amount of the incident power is scattered. Light that does not interact with the metasurface will contribute to a constant background and hence reduces the contrast of the printed pattern. The diffraction efficiency depends strongly on the quality of the fabrication process (compare Appendix C and Table 1 in [342]). Important parameters are the sidewall roughness

One solution to reduce the strong irradiance fluctuations is to add amplitude modulation to the hologram, as we introduced in Section 7.2 with the hybrid plasmonic/dielectric metasurface. In Fig. 7.11 we present the SNR as a function of the gap g for three different configurations:

- Ten transmission coefficients with a transmittance near unity, as used in the above example,
- the hybrid metasurface with 23 transmission coefficients for each out of seven absorber configurations,
- and a binary PSM as a reference.

Here, we optimize the hologram for a $g = 30\text{ }\mu\text{m}$, and calculate the field distributions in planes between $20\text{ }\mu\text{m}$ and $40\text{ }\mu\text{m}$.

We observe a strong improvement of the SNR for the hybrid metasurface of up to 20.8 dB, while the transmission efficiency drops to 21.2%. The signal efficiency is 20.5%, which again expresses the strongly reduced noise background. Gap variations lead in all configurations to a strong deterioration in the SNR. While for $n_\phi = 10$ gap variations of more than $1\text{ }\mu\text{m}$ lead already to a strong image blur (bottom row in Fig. 7.11), the hybrid metasurface preserves the edge locations for even larger variations (top row in Fig. 7.11). In comparison, the binary PSM leads to a degraded performance, with a maximum SNR of 9.0 dB.

7.4 Concluding remarks on proximity lithography using optical metasurfaces

Metasurfaces are planar metamaterials that allow an unprecedented control over the propagation of wavefronts, in polarization, scattering amplitude, phase, and direction. Optical lithography and metasurfaces are an ideal combination, for several reasons: Photolithography is typically a monochromatic technique, and chromatic aberrations often limiting the application of metasurfaces in modern broadband optics are avoided. In addition, a photomask in mask aligner lithography is used for large-volume manufacturing, and in proximity mode the operational lifetime of the photomask is not limited by wear. Hence, the higher costs of fabricating an optical metasurfaces with sub-wavelength dimensions over conventional photomasks can be justified by the possible gain in resolution and yield.

In this section, we presented a novel approach to proximity lithography based on dielectric and hybrid plasmonic/dielectric metasurfaces. In combination with an iterative propagation algorithm, arbitrary patterns can be printed with high fidelity. We investigated the signal-to-noise ratio of a test pattern, and demonstrated that holographic printing is rather insensitive to gap variations.

Approaches to large-area metasurface fabrication have been presented [343, 344]. With an arbitrary control over the transmission coefficients in the complex plane, proximity lithography with metasurface masks allows a high pattern quality at a high contrast.

Alternative approaches might require to investigate novel materials [278], active tuning of metasurfaces to correct imperfections in the fabrication process [345–347], disorder-engineered metasurfaces [348], holographic multiplexing [349–352], or light-emitting metasurfaces [353]. As usual, such principles are often first demonstrated for infrared wavelengths; they have to be adapted to the UV regime to become useful for optical lithography.

Conclusion and outlook

The presented work establishes diverse resolution enhancement technologies applied to mask aligner photolithography. As discussed in the introduction, the primary motivation of this work is to extend the range of applications that can be covered by mask aligner photolithography by enhancing the resolution. The feature sizes in electronics and nano-optics are ever shrinking, increasing the complexity of fabrication routines. At the same time, back end of line electronics and micro-optics require a cost-efficient fabrication method at a competitive price.

The canonical task of photolithography is to replicate a desired pattern, encoded in a photomask, in a photosensitive material on top of a wafer. A mask aligner is a well-established alignment and exposure tool that relies on shadow printing. The photomask is brought into contact or close proximity of tens of micron. No additional optical components are situated between both photomask and the photoresist. Contact lithography offers the best resolution because the impact of diffraction is minimized. However, in high-volume manufacturing the intimate contact of photomask and photoresist is not desired, as possible damage decreases the lifetime and requires frequent photomask cleaning.

For all these reasons, we investigated several techniques to enhance the resolution of mask aligners working in the proximity mode. All these techniques can be categorized according to the fundamental properties of light and light propagation that they affect, i.e., polarization, direction, wavelength, phase, and amplitude. We discussed techniques based on modifications of the last three characteristics in this list.

First, we reviewed the fundamentals of advanced optical lithography, with the focus on the proximity mode of mask aligner lithography. As we rely heavily on a digital representation of light propagation, we introduced four methods to simulate light propagation through and behind photomasks and in optical systems.

In equivalence to optical microscopy, decreasing the wavelength reduces the impact of diffraction and allows to resolve smaller features. The resolution in mask aligner photolithography scales in good approximation with the square root of the wavelength. We demonstrated that the implementation of a frequency-quadrupled continuous wave laser source, emitting a wavelength of 193 nm, is well suited for this task. We investigated the performance of two concepts for laser beam shaping, the non-imaging and the imaging homogenizer. An additional rotating diffuser in the beam path diminishes the impact of the high coherence of the source. Using an amplitude photomask and chemically amplified photoresist, we reported on resolved features with a size of 1.75 μm at a proximity gap of 20 μm , compared to a resolution of about 3 μm when relying on illumination using the canonical mercury arc lamp.

The high coherence and the narrow linewidth of the laser source facilitates its application to Talbot lithography, i.e., the self-imaging effect of periodic structures. Decreasing the wavelength allows to shrink the feature size at a fixed proximity gap of 20 μm and simultaneously increases the depth of focus, enlarging the process window. We successfully demonstrated experimental prints with sub-micron periods, as required for the fabrication of optical metasurfaces working in the near-infrared regime.

Turning back to the canonical *i*-line illumination, we examined the application of rigorously optimized phase-shift masks to print dense periodic dot patterns in hexagonal arrangement, as for instance required in microfluidics and for the fabrication of biosensors. The design and optimization of the binary level phase-shift mask requires to assess the light propagation by a rigorous simulation method under oblique angles. The illumination with a well-defined angular spectrum allows to achieve a demagnification of the structure from the photomask to the photoresist. We successfully confirmed the performance in experimental prints, with an excellent agreement between optical simulations and scanning electron microscope images of the fabricated structures.

The aerial image of the illuminated photomask on the wafer suffers from image shape distortions due to diffraction at the mask features. By adding dedicated correction structures to the photomask design, we were able to partly counteract the detrimental effects manifesting as corner rounding or line-end shortening, also for non-Manhattan geometries. Our computational approach to optical proximity correction includes the simulation and optimization of the correction structure for a set of simple geometries. In addition, we showed in simulations that the process is quite insensitive to variations in the exposure dose or the proximity gap. Furthermore, we investigated a pixel-flip approach relying on quadratic correction features.

In the final chapter of the thesis, we proposed a novel class of photomasks, based on optical metasurfaces for wavefront manipulation. We discussed two designs that can readily be combined with existing mask aligners. Our first design contained the pattern encoded in the radii of TiO_2 cylinders with sub-wavelength dimensions arranged on a regular grid. This platform enables a 2π phase coverage at near-unity transmittance, as experimentally already demonstrated by the group of F. Capasso. The second hybrid approach additionally includes metal patches and rings that introduce a decent amount of absorption. This allowed to access almost the complete complex plane of transmission coefficients. Based on rigorous simulation methods, we discussed the design of the unit cells as well as an iterative algorithm to retrieve the photomask design, i.e., the radii of the nanocylinders. We demonstrated that metasurface photomasks are beneficial for printing arbitrary patterns, compared to canonical binary intensity and two-level phase-shift masks.

We conclude that the presented techniques and results extend the current capabilities of mask aligner photolithography. Sub-micron feature sizes for periodic structures as well as an improvement of the shape fidelity enable to address new application fields, in high-volume manufacturing previously only accessible via projection photolithography.

We envision that digital models of the production processes will gain in importance for feasibility studies, troubleshooting, and process development. One important issue is to improve the simulation of photoresist exposure, development, and etching steps, especially for thick photoresists. Upgrades on a system level require novel concepts of powerful light generation at deep ultraviolet wavelengths to facilitate rapid full-field exposures in mask aligners. Also soft factors as for instance the suppression of reflections, the resist chemistry, and mechanical stability have to be considered. In addition, efficient computational approaches to model the entire photolithographic process are required to

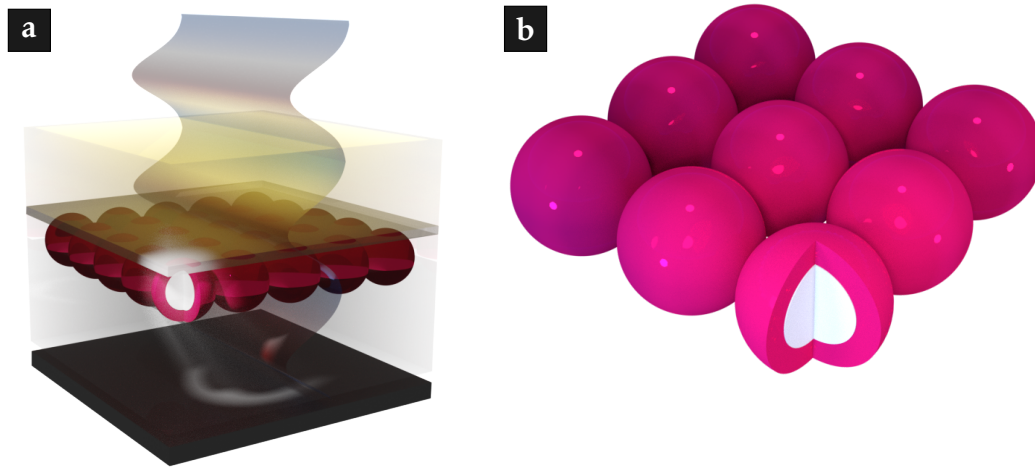


Figure 8.1: Artistic illustration of a metasurface for zeroth-order cancellation.
a Schematic view of the optical setup. The array of core-shell spheres has to be optimized in a way to cancel the zeroth order under plane wave illumination, similar to the rigorously optimized phase-shift mask discussed before.
b Detailed view of the dielectric core-shell particles, made from two concentric shells with different permittivities. The materials and the size of the concentric shells are degrees of freedom and hence are subject to optimization.

keep up with the growing complexity in pattern designs. Eventually, concepts of machine learning can be adapted to improve and speed up the optimization processes.

We anticipate an advancement of photomask technology towards implementing novel concepts of wavefront manipulation. Here, the ever-improving nanofabrication technology paves the way for more complex photomask structures at affordable prices. We envision a growing importance of tailored materials for light manipulation in photomasks. One possible example is illustrated in Fig. 8.1. A dense arrangement of so-called core-shell nanoparticles, i.e., concentric shells composed of two different materials, can be optimized in a way to cancel the zeroth order. The effect is similar to the rigorously optimized phase-shift masks discussed before, with the difference that the core-shell nanoparticles can be assembled via large-area fabrication methods as template patterning or self-assembly, enabling efficient photomask production.

With all these advancements leading to resolution enhancement, improved process stability, an enlarged process window, and in consequence a yield improvement, mask aligner photolithography will remain a relevant technology in the field of microfabrication in the future.

Bibliography

- [1] A. Vetter, C. Yan, R. Kirner, T. Scharf, W. Noell, R. Voelkel, and C. Rockstuhl, “Computational rule-based approach for corner correction of non-Manhattan geometries in mask aligner photolithography”, *Optics Express* **27**(22), 32523–32535, 2019, doi: 10.1364/OE.27.032523.
- [2] Y. Yun, A. Vetter, R. Stegmueller, S. Ferrari, W. H. P. Pernice, C. Rockstuhl, and C. Lee, “Superconducting nanowire single-photon spectrometer exploiting cascaded photonic crystal cavities”, *arXiv e-prints* arXiv:1908.01681, 2019.
- [3] S. Ferrari, V. Kovalyuk, A. Vetter, C. Lee, C. Rockstuhl, A. Semenov, G. Gol’tsman, and W. Pernice, “Analysis of the detection response of waveguide-integrated superconducting nanowire single-photon detectors at high count rate”, *Applied Physics Letters* **115**(10), 101104, 2019, doi: 10.1063/1.5113652.
- [4] M. Symeonidis, R. N. S. Suryadharma, R. Grillo, A. Vetter, C. Rockstuhl, T. Bürgi, and T. Scharf, “High-resolution interference microscopy with spectral resolution for the characterization of individual particles and self-assembled meta-atoms”, *Optics Express* **27**(15), 20990, 2019, doi: 10.1364/OE.27.020990.
- [5] Y. Augenstein, A. Vetter, B. V. Lahijani, H. P. Herzig, C. Rockstuhl, and M.-S. Kim, “Inverse photonic design of functional elements that focus Bloch surface waves”, *Light: Science & Applications* **7**(1), 104, 2018, doi: 10.1038/s41377-018-0106-x.
- [6] V. Kovalyuk, O. Kahl, S. Ferrari, A. Vetter, G. Lewes-Malandrakis, C. Nebel, A. Korneev, G. Goltsman, and W. Pernice, “On-chip single-photon spectrometer for visible and infrared wavelength range”, *Journal of Physics: Conference Series* **1124**(5), 2018, doi: 10.1088/1742-6596/1124/5/051045.
- [7] M. Bagiński, E. Tomczyk, A. Vetter, R. N. S. Suryadharma, C. Rockstuhl, and W. Lewandowski, “Achieving Highly Stable, Reversibly Reconfigurable Plasmonic Nanocrystal Superlattices through the Use of Semifluorinated Surface Ligands”, *Chemistry of Materials* **30**(22), 8201–8210, 2018, doi: 10.1021/acs.chemmater.8b03331.
- [8] M.-S. Kim, A. Vetter, C. Rockstuhl, B. V. Lahijani, M. Häyrynen, M. Kuittinen, M. Roussey, and H. P. Herzig, “Multiple self-healing Bloch surface wave beams generated by a two-dimensional fraxicon”, *Communications Physics* **1**(1), 63, 2018, doi: 10.1038/s42005-018-0065-9.
- [9] A. Vetter, R. Kirner, D. Opalevs, M. Scholz, P. Leisching, T. Scharf, W. Noell, C. Rockstuhl, and R. Voelkel, “Printing sub-micron structures using Talbot mask-aligner lithography with a 193 nm CW laser light source”, *Optics Express* **26**(17), 22218, 2018, doi: 10.1364/OE.26.022218.
- [10] J. Münzberg, A. Vetter, F. Beutel, W. Hartmann, S. Ferrari, W. H. P. Pernice, and C. Rockstuhl, “Superconducting nanowire single-photon detector implemented in a 2D photonic crystal cavity”, *Optica* **5**(5), 658, 2018, doi: 10.1364/OPTICA.5.000658.
- [11] R. Kirner, A. Vetter, D. Opalevs, C. Gilfert, M. Scholz, P. Leisching, T. Scharf, W. Noell, C. Rockstuhl, and R. Voelkel, “Mask-aligner lithography using a

- continuous-wave diode laser frequency-quadrupled to 193 nm”, *Optics Express* **26**(2), 730, 2018, doi: 10.1364/OE.26.000730.
- [12] O. Kahl, S. Ferrari, V. Kovalyuk, A. Vetter, G. Lewes-Malandrakis, C. Nebel, A. Korneev, G. Goltsman, and W. Pernice, “Spectrally multiplexed single-photon detection with hybrid superconducting nanophotonic circuits”, *Optica* **4**(5), 557, 2017, doi: 10.1364/OPTICA.4.000557.
- [13] S. Ferrari, V. Kovalyuk, W. Hartmann, A. Vetter, O. Kahl, C. Lee, A. Korneev, C. Rockstuhl, G. Goltsman, and W. Pernice, “Hot-spot relaxation time current dependence in niobium nitride waveguide-integrated superconducting nanowire single-photon detectors”, *Optics Express* **25**(8), 8739, 2017, doi: 10.1364/OE.25.008739.
- [14] S. Khasminskaya, F. Pyatkov, K. Słowik, S. Ferrari, O. Kahl, V. Kovalyuk, P. Rath, A. Vetter, F. Hennrich, M. M. Kappes, G. Goltsman, A. Korneev, C. Rockstuhl, R. Krupke, and W. H. P. Pernice, “Fully integrated quantum photonic circuit with an electrically driven light source”, *Nature Photonics* **10**(11), 727–732, 2016, doi: 10.1038/nphoton.2016.178.
- [15] A. Vetter, S. Ferrari, P. Rath, R. Alae, O. Kahl, V. Kovalyuk, S. Diewald, G. N. Goltsman, A. Korneev, C. Rockstuhl, and W. H. P. Pernice, “Cavity-Enhanced and Ultrafast Superconducting Single-Photon Detectors”, *Nano Letters* **16**(11), 7085–7092, 2016, doi: 10.1021/acs.nanolett.6b03344.
- [16] J. Szlachetka, A. Vetter, K. Slowik, C. Rockstuhl, and P. Kolenderski, “Nanostructural beam splitter (Conference Presentation)”, *Proc. SPIE* **11025**, Metamaterials XII, 11025X, 2019, doi: 10.1117/12.2520858.
- [17] J. Münzberg, A. Vetter, W. Hartmann, N. Gruhler, F. Beutel, S. Ferrari, C. Rockstuhl, and W. H. Pernice, “Cavity-Enhanced Superconducting Single Photon Detectors”, in *2018 20th International Conference on Transparent Optical Networks (ICTON)*, pages 1–4, IEEE, 2018, doi: 10.1109/ICTON.2018.8473663.
- [18] A. Vetter, D. Opalevs, M. Scholz, P. Leisching, R. Kirner, T. Scharf, W. Noell, C. Rockstuhl, and R. Voelkel, “Mask-aligner Talbot lithography using a 193 nm CW light source”, *Proc. SPIE* **10587**, Optical Microlithography XXXI, 105870W, 2018, doi: 10.1117/12.2296503.
- [19] R. Kirner, A. Vetter, D. Opalevs, M. Scholz, P. Leisching, T. Scharf, W. Noell, C. Rockstuhl, and R. Voelkel, “Enabling proximity mask-aligner lithography with a 193nm CW light source”, *Proc. SPIE* **10587**, Optical Microlithography XXXI, 105871f, 2018, doi: 10.1117/12.2297171.
- [20] D. Opalevs, M. Scholz, C. Gilfert, A. Vetter, R. Kirner, C. Rockstuhl, T. Scharf, R. Voelkel, R. K. Li, L. J. Liu, X. Y. Wang, P. Leisching, W. Noell, C. Chen, and J. Stuhler, “Semiconductor-based narrow-line and high-brilliance 193-nm laser system for industrial applications”, *Proc. SPIE* **10511**, Solid State Lasers XXVII: Technology and Devices, 105112C, 2018, doi: 10.1117/12.2290288.
- [21] S. Ferrari, A. Vetter, P. Rath, and W. H. P. Pernice, “Waveguide integrated superconducting single-photon detectors”, in *2016 18th International Conference on Transparent Optical Networks (ICTON)*, pages 1–3, IEEE, 2016, doi: 10.1109/ICTON.2016.7550616.
- [22] A. W. G. Pike, D. L. Hoffmann, M. Garcia-Diez, P. B. Pettitt, J. Alcolea, R. De Balbin, C. Gonzalez-Sainz, C. de las Heras, J. A. Lasheras, R. Montes, and J. Zilhao, “U-Series Dating of Paleolithic Art in 11 Caves in Spain”, *Science* **336**(6087), 1409–1413, 2012, doi: 10.1126/science.1219957.

- [23] A. Senefelder, *A complete course of lithography*, Printed for R. Ackermann, London, 1819.
- [24] A. Senefelder, *Vollständiges Lehrbuch der Steindruckerey*, Fleischmann, 1821.
- [25] J. Pennell and E. R. Penell, *Lithography & lithographers; some chapters in the history of the art, with technical remarks and suggestions*, London, T.F. Unwin, 1898.
- [26] B. W. Smith and K. Suzuki, *Microlithography: Science and Technology, Second Edition*, Optical science and engineering, CRC Press, 2007.
- [27] S. Landis, *Lithography*, ISTE, Wiley, 2013.
- [28] C. Mack, *Fundamental Principles of Optical Lithography*, John Wiley & Sons, Ltd, Chichester, UK, 2007, doi: 10.1002/9780470723876.
- [29] D. Englebart, "Microelectronics and the art of similitude", in *1960 IEEE International Solid-State Circuits Conference. Digest of Technical Papers*, pages 76–77, IEEE, 1960, doi: 10.1109/ISSCC.1960.1157297.
- [30] G. E. Moore, "Cramming more components onto integrated circuits", *Electronics* **38**(8), 114–117, 1965, doi: 10.1109/N-SSC.2006.4785860.
- [31] G. E. Moore, "Progress In Digital Integrated Electronics", *IEDM Tech. Digest* pages 11–13, 1975, doi: 10.1109/N-SSC.2006.4804410.
- [32] P. Horowitz and W. Hill, *The Art of Electronics*, Cambridge University Press, 2015.
- [33] A. K. K. Wong, *Optical imaging in projection microlithography*, SPIE Press, Bellingham, 2005, doi: 10.1117/3.612961.
- [34] B. J. Lin, *Optical Lithography: Here is why*, SPIE Press monograph, SPIE, 2010.
- [35] C. G. Willson, R. R. Dammel, and A. Reiser, "Photoresist materials: a historical perspective", *Proc. SPIE* **3049**, Advances in Resist Technology and Processing XIV, 1997, doi: 10.1117/12.275826.
- [36] L. M. Minsk, W. P. Van Deusen, and E. M. Robertson, "Photosensitization of polymeric cinnamic acid esters", U.S. patent 2,610,120, 1950.
- [37] L. M. Minsk, W. P. Van Deusen, and E. M. Robertson, "Photosensitization of polymeric cinnamic acid esters", U.S. patent 2,670,287, 1951.
- [38] R. Voelkel, "Wafer-scale micro-optics fabrication", *Advanced Optical Technologies* **1**(3), 135–150, 2012, doi: 10.1515/aot-2012-0013.
- [39] J. H. Bruning, "Optical lithography—thirty years and three orders of magnitude: the evolution of optical lithography tools", *Proc. SPIE* **3048**, Emerging Lithographic Technologies, 1997, doi: 10.2307/2348040.
- [40] J. Andrus and W. Bond, "Photoengraving in Transistor Fabrication", in F. Biondi, editor, *Transistor Technology, Vol. III*, pages 151–162, Princeton, NJ: D. Van Nostrand, 1958.
- [41] J. Nall and J. Lathrop, "Photolithographic fabrication techniques for transistors which are an integral part of a printed circuit", in *1957 International Electron Devices Meeting*, pages 117–117, IRE, 1957, doi: 10.1109/IEDM.1957.187078.
- [42] J. Hoerni, "Method of manufacturing semiconductor devices", U.S. patent 3,025,589, 1959.
- [43] R. N. Noyce, "Semiconductor device-and-lead structure", U.S. patent 2,981,877, 1959.

- [44] P. Siffert and E. Krimmel, *Silicon: Evolution and Future of a Technology*, Springer Berlin Heidelberg, 2013.
- [45] L. Stuerzebecher, F. Fuchs, U. D. Zeitner, and A. Tuennermann, “High-resolution proximity lithography for nano-optical components”, *Microelectronic Engineering* **132**, 120–134, 2015, doi: 10.1016/j.mee.2014.10.010.
- [46] M. Rothschild, “Projection optical lithography”, *Materials Today* **8**(2), 18–24, 2005, doi: 10.1016/S1369-7021(05)00698-X.
- [47] K. Ronse, “Optical lithography—a historical perspective”, *Comptes Rendus Physique* **7**(8), 844–857, 2006, doi: 10.1016/j.crhy.2006.10.007.
- [48] C. Wagner and N. Harned, “Lithography gets extreme”, *Nature Photonics* **4**(1), 24–26, 2010, doi: 10.1038/nphoton.2009.251.
- [49] N. Fu, Y. Liu, X. Ma, and Z. Chen, “EUV Lithography: State-of-the-Art Review”, *Journal of Microelectronic Manufacturing* **2**(2), 1–6, 2019, doi: 10.33079/jomm.19020202.
- [50] A. K. Wong, *Resolution Enhancement Techniques in Optical Lithography*, SPIE, 2001, doi: 10.1117/3.401208.
- [51] G. E. Moore, “Lithography and the future of Moore’s law”, in M. H. Bennett, editor, *Reporters, Markers, Dyes, Nanoparticles, and Molecular Probes for Biomedical Applications XI*, March, page 2, SPIE, 1995, doi: 10.1117/12.209195.
- [52] T. N. Theis and H.-S. P. Wong, “The End of Moore’s Law: A New Beginning for Information Technology”, *Computing in Science & Engineering* **19**(2), 41–50, 2017, doi: 10.1109/MCSE.2017.29.
- [53] R. Zoberbier, “White Paper – 50 years SUSS mask aligner”, 2013.
- [54] S. Partel, S. Zoppel, P. Hudek, A. Bich, U. Vogler, M. Hornung, and R. Voelkel, “Contact and proximity lithography using 193nm Excimer laser in Mask Aligner”, *Microelectronic Engineering* **87**(5-8), 936–939, 2010, doi: 10.1016/j.mee.2009.11.171.
- [55] R. Voelkel, U. Vogler, A. Bich, P. Pernet, K. J. Weible, M. Hornung, R. Zoberbier, E. Cullmann, L. Stuerzebecher, T. Harzendorf, and U. D. Zeitner, “Advanced mask aligner lithography: new illumination system”, *Optics Express* **18**(20), 20968–20978, 2010, doi: 10.1364/OE.18.020968.
- [56] T. Weichelt, U. Vogler, L. Stuerzebecher, R. Voelkel, and U. D. Zeitner, “Resolution enhancement for advanced mask aligner lithography using phase-shifting photomasks”, *Optics Express* **22**(13), 16310–16321, 2014, doi: 10.1364/OE.22.016310.
- [57] P. Rai-Choudhury, editor, *Handbook of microlithography, micromachining, and micro-fabrication*, volume 1 of *IEE materials & devices series ; SPIE Press monograph*, SPIE Optical Engineering Pr., Bellingham, Wash., 1997.
- [58] M. Grieves, “Digital Twin : Manufacturing Excellence through Virtual Factory Replication”, *White paper* 2014, doi: 10.1016/B978-0-12-382196-6.00017-0.
- [59] B. Arnold, “Shrinking possibilities”, *IEEE Spectrum* **46**(4), 26–56, 2009, doi: 10.1109/MSPEC.2009.4808761.
- [60] A. Sommerfeld, *Optics Lectures on Theoretical Physics, Vol. IV*, Academic Press INC, New York, 1954.
- [61] J. W. Goodman, *Introduction to Fourier Optics*, Roberts & Company Publishers, third edition, 2005.

- [62] J. Bernasconi, T. Scharf, U. Vogler, and H. P. Herzig, “High-power modular LED-based illumination systems for mask-aligner lithography”, *Optics Express* **26**(9), 11503–11512, 2018, doi: 10.1364/OE.26.011503.
- [63] Nichia Corporation, “Datasheet UV LED, NVSU233A(T)”, <https://www.nichia.co.jp/specification/products/led/NVSU233A-E.pdf>, 2016.
- [64] T. Weichelt, Y. Bourgin, and U. D. Zeitner, “Mask aligner lithography using laser illumination for versatile pattern generation”, *Optics Express* **25**(18), 20983–20992, 2017, doi: 10.1364/OE.25.020983.
- [65] R. M. M. Hasan and X. Luo, “Promising Lithography Techniques for Next-Generation Logic Devices”, *Nanomanufacturing and Metrology* **1**(2), 67–81, 2018, doi: 10.1007/s41871-018-0016-9.
- [66] B. L. Henke, J. A. Smith, and D. T. Attwood, “0.1-10-keV x-ray-induced electron emissions from solids - Models and secondary electron measurements”, *Journal of Applied Physics* **48**(5), 1852–1866, 2003, doi: 10.1063/1.323938.
- [67] Osram, “Mercury Short Arc Lamps HBO® for Microlithography”, <https://www.osram.com/pia/applications/industry/microlithography/index.jsp>, 2000.
- [68] H. Gross, *Handbook of Optical Systems, Volume 1, Fundamentals of Technical Optics*, Wiley-VCH, 2005.
- [69] S. Ishida and S. Hata, “LED light source, its manufacturing method, and LED-based photolithography apparatus and method”, U.S. patent 8,441,612 B2, 2013.
- [70] M. K. Yapici and I. Farhat, “UV-LED exposure system for low-cost photolithography”, Proc. SPIE **9052**, Optical Microlithography XXVII, 90521T, 2014, doi: 10.1117/12.2046123.
- [71] M. Erickstad, E. Gutierrez, and A. Groisman, “A low-cost low-maintenance ultraviolet lithography light source based on light-emitting diodes”, *Lab on a Chip* **15**(1), 57–61, 2015, doi: 10.1039/C4LC00472H.
- [72] T.-M. Huang, S.-T. Chang, H.-L. Tsay, M.-Y. Hsu, and F.-Z. Chen, “Uniformity of LED light illumination in application to direct imaging lithography”, Proc. SPIE **9954**, Fifteenth International Conference on Solid State Lighting and LED-based Illumination Systems, 99540Q, 2016, doi: 10.1117/12.2237441.
- [73] K. Hölz, J. Lietard, and M. M. Somoza, “High-Power 365 nm UV LED Mercury Arc Lamp Replacement for Photochemistry and Chemical Photolithography”, *ACS Sustainable Chemistry & Engineering* **5**(1), 828–834, 2017, doi: 10.1021/acssuschemeng.6b02175.
- [74] R. Winston, J. C. Minano, P. G. Benitez, W. Bortz, N. Shatz, and J. C. Bortz, *Nonimaging Optics*, Electronics & Electrical, Elsevier Science, 2005.
- [75] R. Voelkel and K. J. Weible, “Laser beam homogenizing: limitations and constraints”, Proc. SPIE **7102**, Optical Fabrication, Testing, and Metrology III, 71020J, 2008, doi: 10.1117/12.799400.
- [76] R. Voelkel, “Micro-optics: enabling technology for illumination shaping in optical lithography”, Proc. SPIE **9052**, Optical Microlithography XXVII, 90521U, 2014, doi: 10.1117/12.2046116.
- [77] A. Köhler, “Ein neues Beleuchtungsverfahren für mikrographische Zwecke”, *Zeitschrift für wissenschaftliche Mikroskopie und für mikroskopische Technik* **10**(4), 433–440, 1893.

- [78] F. M. Dickey, editor, *Laser Beam Shaping: Theory and Techniques*, CRC Press, 2017.
- [79] T. F. E. Henning, L. Unnebrink, and M. Scholl, "UV laser beam shaping by multifaceted beam integrators: fundamental principles and advanced design concepts", *Proc. SPIE* **2703**, Lasers as Tools for Manufacturing of Durable Goods and Microelectronics, 1996, doi: 10.1117/12.237772.
- [80] F. M. Dickey and T. E. Lizotte, *Laser Beam Shaping Applications*, CRC Press, 2017.
- [81] R. Voelkel, U. Vogler, A. Bich, K. J. Weible, M. Eisner, M. Hornung, P. Kaiser, R. Zoberbier, and E. Cullmann, "Illumination system for a microlithographic contact and proximity exposure apparatus", European Patent Application 2,253,997 A2, 2009.
- [82] SUSS MicroTec, "MO Exposure Optics® Technical Datasheet", www.suss.com/brochures-datasheets/mo-exposure-optics.pdf, 2018.
- [83] R. Voelkel, U. Vogler, A. Bramati, A. Erdmann, N. Ünal, U. Hofmann, M. Henemeyer, R. Zoberbier, D. Nguyen, and J. Brugger, "Lithographic process window optimization for mask aligner proximity lithography", *Proc. SPIE* **9052**, Opt. Microlithography XXVII, 90520G, 2014, doi: 10.1117/12.2046332.
- [84] W. H. Souder and P. Hidnert, "Measurements on the Thermal Expansion of Fused Silica", *Technical report*, 1926.
- [85] M. Rubin, "Optical properties of soda lime silica glasses", *Solar Energy Materials* **12**(4), 275–288, 1985, doi: 10.1016/0165-1633(85)90052-8.
- [86] M. Levenson, N. Viswanathan, and R. Simpson, "Improving resolution in photolithography with a phase-shifting mask", *IEEE Transactions on Electron Devices* **29**(12), 1828–1836, 1982, doi: 10.1109/T-ED.1982.21037.
- [87] G. A. Cirino, R. D. Mansano, P. Verdonck, L. Cescato, and L. G. Neto, "Diffractive phase-shift lithography photomask operating in proximity printing mode", *Optics Express* **18**(16), 16387–16405, 2010, doi: 10.1364/OE.18.016387.
- [88] P. Nussbaum, R. Völkel, H. P. Herzig, M. Eisner, and S. Haselbeck, "Design, fabrication and testing of microlens arrays for sensors and microsystems", *Pure and Applied Optics: Journal of the European Optical Society Part A* **6**(6), 617–636, 1997, doi: 10.1088/0963-9659/6/6/004.
- [89] J. M. J. Frechet, H. Ito, and C. Willson, "Sensitive Deep UV Resist Incorporation Chemical Amplification", in *Proceedings Microcircuit Engineering 1982, Grenoble*, page 260, 1982.
- [90] E. Reichmanis, F. M. Houlihan, O. Nalamasu, and T. X. Neenan, "Chemical amplification mechanisms for microlithography", *Chemistry of Materials* **3**(3), 394–407, 1991, doi: 10.1021/cm00015a009.
- [91] H. Ito, "Chemically amplified resists: past, present, and future", *Proc. SPIE* **3678**, Advances in Resist Technology and Processing XVI, 2, 1999, doi: 10.1117/12.350143.
- [92] MicroChemicals GmbH, "MicroChemicals - Grundlagen der Mikrostrukturierung", Technical paper, 2012.
- [93] J. Korka, "Standing Waves in Photoresists", *Appl. Opt.* **9**(4), 969–970, 1969, doi: 10.1364/AO.9.000969.
- [94] C. A. Mack, "Analytical expression for the standing wave intensity in photoresist", *Applied Optics* **25**(12), 1958–1961, 1986, doi: 10.1364/AO.25.001958.

- [95] H. Gross, *Handbook of Optical Systems Volume 3: Aberration Theory and Correction of Optical Systems Handbook*, volume 2, Wiley-VCH, 2005.
- [96] Y. Wei and R. L. Brainard, *Advanced Processes for 193-nm Immersion Lithography*, SPIE Press monograph, SPIE, 2009.
- [97] M. J. Bowden, “The Physics and Chemistry of the Lithographic Process”, *Journal of The Electrochemical Society* **128**(5), 195C, 1981, doi: 10.1149/1.2127577.
- [98] F. M. Schellenberg, “Resolution enhancement technology: the past, the present, and extensions for the future”, *Proc. SPIE* **5377**, Optical Microlithography XVII, 2004, doi: 10.1117/12.548923.
- [99] E. M. Catich and M. W. Gilroy, *The Origin of the Serif: Brush Writing & Roman Letters*, Catich Gallery, St. Ambrose University, second edition, 1991.
- [100] Eastman Kodak, “Techniques of Microphotography, Kodak Sales Service Publication P-52”, *Technical report*, Eastman Kodak, Rochester, NY, 1963.
- [101] B. E. A. Saleh and N. S. Subotic, “Pre-inverse filtering of distorted images”, *Applied Optics* **20**(22), 3912, 1981, doi: 10.1364/AO.20.003912.
- [102] K. M. Nashold and B. E. A. Saleh, “Image construction through diffraction-limited high-contrast imaging systems: an iterative approach”, *Journal of the Optical Society of America A* **2**(5), 635, 1985, doi: 10.1364/JOSAA.2.000635.
- [103] B. E. A. Saleh and K. M. Nashold, “Image construction: optimum amplitude and phase masks in photolithography”, *Applied Optics* **24**(10), 1432, 1985, doi: 10.1364/AO.24.001432.
- [104] F. M. Schellenberg, “A History of Resolution Enhancement Technology”, *Optical Review* **12**(2), 83–89, 2005, doi: 10.1007/s10043-004-0083-6.
- [105] X. Ma and G. R. Arce, *Computational lithography*, volume 77, John Wiley & Sons, 2011.
- [106] K. Motzek, S. Partel, A. Bramati, U. Hofmann, N. Ünal, M. Hennemeyer, M. Hornung, A. Heindl, M. Ruhland, A. Erdmann, and P. Hudek, “Mask aligner lithography simulation – From lithography simulation to process validation”, *Microelectronic Engineering* **98**, 121–124, 2012, doi: 10.1016/j.mee.2012.07.076.
- [107] K. Motzek, U. Vogler, M. Hennemeyer, M. Hornung, R. Voelkel, A. Erdmann, and B. Meliorisz, “Computational algorithms for optimizing mask layouts in proximity printing”, *Microelectronic Engineering* **88**(8), 2066–2069, 2011, doi: 10.1016/j.mee.2010.11.054.
- [108] K. Motzek, A. Bich, A. Erdmann, M. Hornung, M. Hennemeyer, B. Meliorisz, U. Hofmann, N. Ünal, R. Voelkel, S. Partel, and P. Hudek, “Optimization of illumination pupils and mask structures for proximity printing”, *Microelectronic Engineering* **87**(5-8), 1164–1167, 2010, doi: 10.1016/j.mee.2009.10.038.
- [109] R. Völkel, U. Vogler, A. Bramati, T. Weichelt, L. Stuerzebecher, U. D. Zeitner, K. Motzek, A. Erdmann, M. Hornung, and R. Zoberbier, “Advanced mask aligner lithography (AMALITH)”, *Proc. SPIE* **8326**, Optical Microlithography XXV, 83261Y, 2012, doi: 10.1117/12.916509.
- [110] K. Puthankovilakam, T. Scharf, H. P. Herzig, U. Vogler, and R. Voelkel, “Unified rule based correction for corners in proximity lithography mask using high resolution features”, *Microelectronic Engineering* **172**, 35–44, 2017, doi: 10.1016/j.mee.2017.03.001.

- [111] K. Motzek, S. Partel, U. Vogler, and A. Erdmann, "Numerical optimization of illumination and mask layout for the enlargement of process windows and for the control of photoresist profiles in proximity printing", *Proc. SPIE* **8171**, Physical Optics, 81710K, 2011, doi: 10.1117/12.896755.
- [112] R. Gerchberg and W. Saxton, "A practical algorithm for the determination of the phase from image and diffraction plane pictures", *Optik* **35**(2), 237–250, 1972.
- [113] F. Wyrowski and O. Bryngdahl, "Iterative Fourier-transform algorithm applied to computer holography", *Journal of the Optical Society of America A* **5**(7), 1058, 1988, doi: 10.1364/JOSAA.5.001058.
- [114] F. Wyrowski, "Diffractive optical elements: iterative calculation of quantized, blazed phase structures", *Journal of the Optical Society of America A* **7**(6), 961, 1990, doi: 10.1364/JOSAA.7.000961.
- [115] B. Walther, C. Helgert, C. Rockstuhl, and T. Pertsch, "Diffractive optical elements based on plasmonic metamaterials", *Applied Physics Letters* **98**(19), 191101, 2011, doi: 10.1063/1.3587622.
- [116] S. Bühling, F. Wyrowski, E.-B. Kley, A. J. M. Nellissen, L. Wang, and M. Dirkzwager, "Resolution enhanced proximity printing by phase and amplitude modulating masks", *Journal of Micromechanics and Microengineering* **11**(5), 603–611, 2001, doi: 10.1088/0960-1317/11/5/325.
- [117] L. G. Neto, G. A. Cirino, R. D. Mansano, P. S. Cardona, and P. Verdonck, "Hybrid phase and amplitude modulation proximity printing mask fabricated on DLC and SiO₂ substrates", *Proc. SPIE* **4984**, Micromachining Technology for Micro-Optics and Nano-Optics, 2003, doi: 10.1117/12.477830.
- [118] Y. Bourgin, D. Voigt, T. Käsebier, E.-B. Kley, and U. D. Zeitner, "Periodic sub-100nm structures fabricated by proximity i-line mask-aligner lithography (and self-aligned double patterning)", *Proc. SPIE* **9780**, Optical Microlithography XXIX, 978014, 2016, doi: 10.1117/12.2218610.
- [119] Y. Bourgin, D. Voigt, T. Käsebier, T. Siefke, E.-B. Kley, and U. D. Zeitner, "175 nm period grating fabricated by i-line proximity mask-aligner lithography", *Optics Letters* **42**(19), 3816–3819, 2017, doi: 10.1364/OL.42.003816.
- [120] H. Talbot, "LXXVI. Facts relating to optical science. No. IV", *Philosophical Magazine Series 3* **9**(56), 401–407, 1836, doi: 10.1080/14786443608649032.
- [121] L. Rayleigh, "XXV. On copying diffraction-gratings, and on some phenomena connected therewith", *Philosophical Magazine Series 5* **11**(67), 196–205, 1881, doi: 10.1080/14786448108626995.
- [122] K. Paturski, "The Self-Imaging Phenomenon and its Applications", volume 27 of *Progress in Optics*, pages 1–108, Elsevier, 1989, doi: 10.1016/S0079-6638(08)70084-2.
- [123] J. Wen, Y. Zhang, and M. Xiao, "The Talbot effect: recent advances in classical optics, nonlinear optics, and quantum optics", *Advances in Optics and Photonics* **5**(1), 83, 2013, doi: 10.1364/AOP.5.000083.
- [124] J. Eu and A. Lohmann, "Spatial filtering effects by means of hologram copying", *Optics Communications* **8**(3), 176–182, 1973, doi: 10.1016/0030-4018(73)90122-3.
- [125] J. Eu, C. Liu, and A. Lohmann, "Spatial filters for differentiation", *Optics Communications* **9**(2), 168–171, 1973, doi: 10.1016/0030-4018(73)90251-4.

- [126] S. K. Case, "Fourier processing in the object plane", *Optics Letters* **4**(9), 286–288, 1979, doi: 10.1364/OL.4.000286.
- [127] A. Lohmann and D. Silva, "An interferometer based on the Talbot effect", *Optics Communications* **2**(9), 413–415, 1971, doi: 10.1016/0030-4018(71)90055-1.
- [128] P. Chavel and T. C. Strand, "Range measurement using Talbot diffraction imaging of gratings", *Applied Optics* **23**(6), 862–871, 1984, doi: 10.1364/AO.23.000862.
- [129] A. W. Lohmann and J. A. Thomas, "Making an array illuminator based on the Talbot effect", *Applied Optics* **29**(29), 4337–4340, 1990, doi: 10.1364/AO.29.004337.
- [130] L. Soldano and E. Pennings, "Optical multi-mode interference devices based on self-imaging: principles and applications", *Journal of Lightwave Technology* **13**(4), 615–627, 1995, doi: 10.1109/50.372474.
- [131] M. R. Dennis, N. I. Zheludev, and F. J. García de Abajo, "The plasmon Talbot effect", *Optics Express* **15**(15), 9692–9700, 2007, doi: 10.1364/OE.15.009692.
- [132] K.-H. Luo, J. Wen, X.-H. Chen, Q. Liu, M. Xiao, and L.-A. Wu, "Second-order Talbot effect with entangled photon pairs", *Physical Review A* **80**(4), 043820, 2009, doi: 10.1103/PhysRevA.80.043820.
- [133] J. M. Burch, "Photographic Production of Gratings for Measurement", *Research* **13**(1), 2, 1960.
- [134] J. Burch, "II The Metrological Applications of Diffraction Gratings", *Progress in Optics* **2**, 73–108, 1963, doi: 10.1016/S0079-6638(08)70557-2.
- [135] H. Dammann, G. Groh, and M. Kock, "Restoration of Faulty Images of Periodic Objects by Means of Self-imaging", *Applied Optics* **10**(6), 1454–1455, 1971, doi: 10.1364/AO.10.001454.
- [136] K. Kodate, T. Kamiya, H. Takenaka, and H. Yanai, "Construction of Photolithographic Phase Gratings Using the Fourier Image Effect", *Applied Optics* **14**(2), 522–525, 1975, doi: 10.1364/AO.14.000522.
- [137] A. Isoyan, F. Jiang, Y. C. Cheng, F. Cerrina, P. Wachulak, L. Urbanski, J. Rocca, C. Menoni, and M. Marconi, "Talbot lithography: Self-imaging of complex structures", *Journal of Vacuum Science & Technology B: Microelectronics and Nanometer Structures* **27**(6), 2931, 2009, doi: 10.1116/1.3258144.
- [138] R. Edgar, "The Fresnel Diffraction Images of Periodic Structures", *Optica Acta: International Journal of Optics* **16**(3), 281–287, 1969, doi: 10.1080/713818186.
- [139] A. M. Hawryluk, R. M. Osgood, D. J. Ehrlich, and H. I. Smith, "Deep-ultraviolet spatial-period division using an excimer laser", *Optics Letters* **7**(9), 402–404, 1982, doi: 10.1364/OL.7.000402.
- [140] H. H. Solak, C. Dais, and F. Clube, "Displacement Talbot lithography: a new method for high-resolution patterning of large areas", *Optics Express* **19**(11), 10686–10691, 2011, doi: 10.1364/OE.19.010686.
- [141] H. H. Solak, C. Dais, F. Clube, and L. Wang, "Phase shifting masks in Displacement Talbot Lithography for printing nano-grids and periodic motifs", *Microelectronic Engineering* **143**, 74–80, 2015, doi: 10.1016/j.mee.2015.03.050.
- [142] P. Chausse and P. A. Shields, "'Double' displacement Talbot lithography: a new approach for periodic nanostructure patterning (Conference Presentation)", *Proc. SPIE* **10587**, Optical Microlithography XXXI, 2018, doi: 10.1117/12.2297416.

- [143] T. Sato, "Talbot effect immersion lithography by self-imaging of very fine grating patterns", *Journal of Vacuum Science & Technology B, Nanotechnology and Microelectronics: Materials, Processing, Measurement, and Phenomena* **30**(6), 06FG02, 2012, doi: 10.1116/1.4767440.
- [144] W. Li, V. Martinez-Esquiros, L. Urbanski, D. Patel, C. S. Menoni, M. C. Marconi, and A. Stein, "Defect-free fabrication of periodic structures using extreme ultraviolet Talbot lithography", *2013 IEEE Photonics Conference, IPC 2013* **604**, 635–636, 2013, doi: 10.1109/IPCon.2013.6656455.
- [145] D. Thomae, J. Maaß, O. Sandfuchs, A. Gatto, and R. Brunner, "Flexible mask illumination setup for serial multipatterning in Talbot lithography", *Applied Optics* **53**(9), 1775–1781, 2014, doi: 10.1364/AO.53.001775.
- [146] W. D. Montgomery, "Self-Imaging Objects of Infinite Aperture", *Journal of the Optical Society of America* **57**(6), 772, 1967, doi: 10.1364/JOSA.57.000772.
- [147] G. C. Sherman, "Application of the Convolution Theorem to Rayleigh's Integral Formulas", *Journal of the Optical Society of America* **57**(4), 546, 1967, doi: 10.1364/JOSA.57.000546.
- [148] M.-S. Kim, T. Scharf, C. Menzel, C. Rockstuhl, and H. P. Herzig, "Phase anomalies in Talbot light carpets of self-images", *Optics Express* **21**(1), 1287–1300, 2013, doi: 10.1364/OE.21.001287.
- [149] M. Born and E. Wolf, *Principles of Optics, 7th (expanded) ed*, Cambridge U. Press, Cambridge, UK, 1999.
- [150] T. Sato, "Focus position and depth of two-dimensional patterning by Talbot effect lithography", *Microelectronic Engineering* **123**, 80–83, 2014, doi: 10.1016/j.mee.2014.05.019.
- [151] J. Zhang and Y. Chen, "Optimal Design of Hexagonal Multiphase Talbot Array Illuminator Based on PPLN", *IEEE Journal of Quantum Electronics* **49**(5), 471–476, 2013, doi: 10.1109/JQE.2013.2244558.
- [152] S. Gupta, "Generalized spatial Talbot effect based on all-dielectric metasurfaces", *Optics Communications* **384**, 25–29, 2017, doi: 10.1016/j.optcom.2016.10.011.
- [153] Y. Bourgin, T. Käsebier, and U. D. Zeitner, "250 nm period grating transferred by proximity i-line mask-aligner lithography", *Optics Letters* **39**(6), 1665–1668, 2014, doi: 10.1364/OL.39.001665.
- [154] Y. Bourgin, T. Siefke, T. Käsebier, P. Genevée, A. Szeghalmi, E.-B. Kley, and U. D. Zeitner, "Double-sided structured mask for sub-micron resolution proximity i-line mask-aligner lithography", *Optics Express* **23**(13), 16628–16637, 2015, doi: 10.1364/OE.23.016628.
- [155] M. Okai, S. Tsuji, N. Chinone, and T. Harada, "Novel method to fabricate corrugation for a $\lambda/4$ -shifted distributed feedback laser using a grating photomask", *Applied Physics Letters* **55**(5), 415–417, 1989, doi: 10.1063/1.101882.
- [156] D. M. Tennant, T. Koch, P. Mulgrew, R. Gnall, F. Ostermeyer, and J.-M. Verdiell, "Characterization of near-field holography grating masks for optoelectronics fabricated by electron beam lithography", *Journal of Vacuum Science & Technology B: Microelectronics and Nanometer Structures* **10**(6), 2530, 1992, doi: 10.1116/1.586052.
- [157] D. Tennant, K. Feder, K. Dreyer, R. Gnall, T. Koch, U. Koren, B. Miller, and M. Young, "Phase grating masks for photonic integrated circuits fabricated by e-beam writing and dry etching: Challenges to commercial applications", *Microelectronic Engineering* **27**(1-4), 427–434, 1995, doi: 10.1016/0167-9317(94)00139-L.

- [158] M. Noguchi, M. Muraki, Y. Iwasaki, and A. Suzuki, "Subhalf-micron lithography system with phase-shifting effect", Proc. SPIE **1674**, Optical/Laser Microlithography V, 1992, doi: 10.1117/12.130312.
- [159] N. Shiraishi, S. Hirukawa, Y. Takeuchi, and N. Magome, "New imaging technique for 64M-DRAM", Proc. SPIE **1674**, Optical/Laser Microlithography V, 1992, doi: 10.1117/12.130364.
- [160] K. O. Hill, B. Malo, F. Bilodeau, D. C. Johnson, and J. Albert, "Bragg gratings fabricated in monomode photosensitive optical fiber by UV exposure through a phase mask", *Applied Physics Letters* **62**(10), 1035–1037, 1993, doi: 10.1063/1.108786.
- [161] E. Gamet, A. V. Tishchenko, and O. Parriaux, "Cancellation of the zeroth order in a phase mask by mode interplay in a high index contrast binary grating", *Applied Optics* **46**(27), 6719, 2007, doi: 10.1364/AO.46.006719.
- [162] L. Stuerzebecher, F. Fuchs, T. Harzendorf, S. Meyer, and U. D. Zeitner, "Application of rigorously optimized phase masks for the fabrication of binary and blazed gratings with diffractive proximity lithography", Proc. SPIE **8974**, Advanced Fabrication Technologies for Micro/Nano Optics and Photonics VII, 897415, 2014, doi: 10.1117/12.2037245.
- [163] B. Wang, "Cancellation of the zeroth order by a low-contrast grating", *Scientific Reports* **5**(1), 16501, 2015, doi: 10.1038/srep16501.
- [164] L. Stuerzebecher, T. Harzendorf, F. Fuchs, and U. D. Zeitner, "Wafer scale fabrication of submicron chessboard gratings using phase masks in proximity lithography", Proc. SPIE **8249**, Advanced Fabrication Technologies for Micro/Nano Optics and Photonics V, 82490R, 2012, doi: 10.1117/12.908737.
- [165] L. Stuerzebecher, F. Fuchs, T. Harzendorf, and U. D. Zeitner, "Pulse compression grating fabrication by diffractive proximity photolithography.", *Optics letters* **39**(4), 1042–5, 2014, doi: 10.1364/OL.39.001042.
- [166] J. Pomplun, S. Burger, L. Zschiedrich, and F. Schmidt, "Adaptive finite element method for simulation of optical nano structures", *physica status solidi (b)* **244**(10), 3419–3434, 2007, doi: 10.1002/pssb.200743192.
- [167] S. Burger, J. Pomplun, and F. Schmidt, *Finite Element Methods for Computational Nano-optics*, pages 837–843, Springer Netherlands, Dordrecht, 2012, doi: 10.1007/978-90-481-9751-4_17.
- [168] Y. Hao and R. Mittra, *The FDTD Method For Modeling Metamaterial*, Artech house, Boston/London, 2009.
- [169] A. Taflove, A. Oskooi, and S. G. Johnson, *Advances in FDTD Computational Electrodynamics: Photonics and Nanotechnology*, Artech house, 2013.
- [170] A. Christ and H. Hartnagel, "Three-Dimensional Finite-Difference Method for the Analysis of Microwave-Device Embedding", *IEEE Transactions on Microwave Theory and Techniques* **35**(8), 688–696, 1987, doi: 10.1109/TMTT.1987.1133733.
- [171] P. Vincent, *Differential Methods*, pages 101–121, Springer Berlin Heidelberg, Berlin, Heidelberg, 1980, doi: 10.1007/978-3-642-81500-3_4.
- [172] E. Popov and M. Nevière, "Maxwell equations in Fourier space: fast-converging formulation for diffraction by arbitrary shaped, periodic, anisotropic media", *Journal of the Optical Society of America A* **18**(11), 2886, 2001, doi: 10.1364/JOSAA.18.002886.

- [173] G. Schmidt and B. H. Kleemann, "Integral equation methods from grating theory to photonics: an overview and new approaches for conical diffraction", *Journal of Modern Optics* **58**(5-6), 407–423, 2011, doi: 10.1080/09500340.2010.538734.
- [174] T. Paul, *Light Propagation in Optical Metamaterials – A Bloch Modal Approach*, Ph.D. thesis, Friedrich-Schiller Universität Jena, 2012.
- [175] H. Kogelnik, "Coupled Wave Theory for Thick Hologram Gratings", *Bell System Technical Journal* **48**(9), 2909–2947, 1969, doi: 10.1002/j.1538-7305.1969.tb01198.x.
- [176] M. G. Moharam and T. K. Gaylord, "Rigorous coupled-wave analysis of planar-grating diffraction", *Journal of the Optical Society of America* **71**(7), 811, 1981, doi: 10.1364/JOSA.71.000811.
- [177] E. Noponen and J. Turunen, "Eigenmode method for electromagnetic synthesis of diffractive elements with three-dimensional profiles", *Journal of the Optical Society of America A* **11**(9), 2494, 1994, doi: 10.1364/JOSAA.11.002494.
- [178] F. Bloch, "Über die Quantenmechanik der Elektronen in Kristallgittern", *Zeitschrift für Physik* **52**(7-8), 555–600, 1929, doi: 10.1007/BF01339455.
- [179] L. Li, "Use of Fourier series in the analysis of discontinuous periodic structures", *Journal of the Optical Society of America A* **13**(9), 1870, 1996, doi: 10.1364/JOSAA.13.001870.
- [180] L. Li, "New formulation of the Fourier modal method for crossed surface-relief gratings", *Journal of the Optical Society of America A* **14**(10), 2758, 1997, doi: 10.1364/JOSAA.14.002758.
- [181] N. P. K. Cotter, T. W. Preist, and J. R. Sambles, "Scattering-matrix approach to multilayer diffraction", *Journal of the Optical Society of America A* **12**(5), 1097, 1995, doi: 10.1364/JOSAA.12.001097.
- [182] C. J. Bouwkamp, "Diffraction Theory", *Reports on Progress in Physics* **17**(1), 302, 1954, doi: 10.1088/0034-4885/17/1/302.
- [183] C. Rockstuhl, "Script for the lecture on Theoretical Optics", 2015, Institute of Theoretical Solid State Physics, Institute of Nanotechnology, Karlsruhe Institute of Technology (KIT), Germany.
- [184] R. F. Henry and P. W. U. Graefe, *Zero padding as a means of improving definition of computed spectra*, Manuscript report series, Published for Environment Canada by Dept. of Energy, Mines and Resources, Marine Sciences Branch, 1971.
- [185] Genisys GmbH, <https://genisys-gmbh.com/lab.html>, 2019.
- [186] F. Shen and A. Wang, "Fast-Fourier-transform based numerical integration method for the Rayleigh-Sommerfeld diffraction formula", *Applied Optics* **45**(6), 1102, 2006, doi: 10.1364/AO.45.001102.
- [187] E. Hecht, *Optics*, Addison-Wesley, Reading Massachusetts, 2002.
- [188] F. Wyrowski and M. Kuhn, "Introduction to field tracing", *Journal of Modern Optics* **58**(5-6), 449–466, 2011, doi: 10.1080/09500340.2010.532237.
- [189] N. G. Douglas, A. R. Jones, and F. J. van Hoesel, "Ray-based simulation of an optical interferometer", *Journal of the Optical Society of America A* **12**(1), 124, 1995, doi: 10.1364/JOSAA.12.000124.
- [190] N. Lindlein and H. P. Herzig, "Design and modeling of a miniature system containing micro-optics", *Proc. SPIE* **4437**, Gradient Index, Miniature, and Diffractive Optical Systems II, 2001, doi: 10.1117/12.448143.

- [191] N. Lindlein, "Simulation of micro-optical systems including microlens arrays", *Journal of Optics A: Pure and Applied Optics* **4**(4), 351, 2002, doi: 10.1088/1464-4258/4/4/351.
- [192] C. Wheatstone, "On the prismatic decomposition of electrical light", *Phil. Mag* **7**, 299, 1835.
- [193] W. Elenbaas, *The high pressure mercury vapour discharge*, volume 2, North-Holland publishing company, 1951.
- [194] N. G. Basov, V. A. Danilychev, Y. M. Popov, and D. D. Khodkevich, "Laser operating in the vacuum region of the spectrum by excitation of liquid xenon with an electron beam", *JETP lett* **12**(10), 329–331, 1970.
- [195] D. Basting and G. Marowsky, editors, *Excimer Laser Technology*, Springer Berlin Heidelberg, Berlin, Heidelberg, 2005, doi: 10.1007/b137894.
- [196] K. Jain, C. Willson, and B. Lin, "Ultrafast deep UV Lithography with excimer lasers", *IEEE Electron Device Letters* **3**(3), 53, 1982, doi: 10.1109/EDL.1982.25476.
- [197] K. Jain, "Advances In Excimer Laser Lithography", *Proc. SPIE* **774**, Lasers in Microlithography, 1987, doi: 10.1117/12.940396.
- [198] T. Saito, T. Matsunaga, K.-i. Mitsuhashi, K. Terashima, T. Ohta, A. Tada, T. Ishihara, M. Yoshino, H. Tsushima, T. Enami, H. Tomaru, and T. Igarashi, "Ultrabroadbandwidth 4-kHz ArF excimer laser for 193-nm lithography", *Proc. SPIE* **4346**, Optical Microlithography XIV, 2001, doi: 10.1117/12.435658.
- [199] V. B. Fleurov, D. J. Colon III, D. J. W. Brown, P. O'Keeffe, H. Besaucele, A. I. Ershov, F. Trintchouk, T. Ishihara, P. Zambon, R. J. Rafac, and A. Lukashev, "Dual-chamber ultra line-narrowed excimer light source for 193-nm lithography", *Proc. SPIE* **5040**, Optical Microlithography XVI, 2003, doi: 10.1117/12.485358.
- [200] M. Mizuguchi, H. Hosono, H. Kawazoe, and T. Ogawa, "Color center formation and time-resolved photoluminescence for ArF excimer laser irradiation in CaF₂ single crystals", *Proc. SPIE* **3424**, Inorganic Optical Materials, 1998, doi: 10.1117/12.323756.
- [201] R. E. Schenker, L. Eichner, H. Vaidya, S. Vaidya, and W. G. Oldham, "Degradation of fused silica at 193 nm and 213 nm", *Proc. SPIE* **2440**, Optical/Laser Microlithography VIII, 1995, doi: 10.1117/12.209323.
- [202] J. M. Algots, R. Sandstrom, W. N. Partlo, P. Maroevic, E. Eva, M. Gerhard, R. Linder, and F. Stietz, "Compaction and rarefaction of fused silica with 193-nm excimer laser exposure", *Proc. SPIE* **5040**, Optical Microlithography XVI, 2003, doi: 10.1117/12.485530.
- [203] R. Delmdahl, "The excimer laser: Precision engineering", *Nature Photonics* **4**(5), 286, 2010, doi: 10.1038/nphoton.2010.106.
- [204] M. P. Lee and R. K. Hanson, "Calculations of O₂ absorption and fluorescence at elevated temperatures for a broadband argon—fluoride laser source at 193 nm", *Journal of Quantitative Spectroscopy and Radiative Transfer* **36**(5), 425–440, 1986, doi: 10.1016/0022-4073(86)90098-1.
- [205] M. Scholz, D. Opalevs, P. Leisching, W. Kaenders, G. Wang, X. Wang, R. Li, and C. Chen, "A bright continuous-wave laser source at 193 nm", *Applied Physics Letters* **103**(5), 051114, 2013, doi: 10.1063/1.4817786.

- [206] C. Chen, Y. Wang, Y. Xia, B. Wu, D. Tang, K. Wu, Z. Wenrong, L. Yu, and L. Mei, "New development of nonlinear optical crystals for the ultraviolet region with molecular engineering approach", *Journal of Applied Physics* **77**(6), 2268, 1995, doi: 10.1063/1.358814.
- [207] D. Tang, Y. Xia, B. Wu, and C. Chen, "Growth of a new UV nonlinear optical crystal: $\text{KBe}_2(\text{BO}_3)\text{F}_2$ ", *Journal of Crystal Growth* **222**(1-2), 125, 2001, doi: 10.1016/S0022-0248(00)00850-2.
- [208] R. V. Pound, "Electronic frequency stabilization of microwave oscillators", *Review of Scientific Instruments* **17**(11), 490–505, 1946.
- [209] R. W. P. Drever, J. L. Hall, F. V. Kowalski, J. Hough, G. M. Ford, A. J. Munley, and H. Ward, "Laser phase and frequency stabilization using an optical resonator", *Applied Physics B Photophysics and Laser Chemistry* **31**(2), 97, 1983, doi: 10.1007/BF00702605.
- [210] J. Lu, G. Wang, Z. Xu, C. Chen, J. Wang, C. Zhang, and Y. Liu, "High-efficiency fourth-harmonic generation of KBBF crystal", *Optics Communications* **200**(1-6), 415–418, 2001, doi: 10.1016/S0030-4018(01)01654-6.
- [211] J. C. Dainty, *Laser speckle and related phenomena*, volume 9, Springer science & business Media, 2013.
- [212] J. W. Goodman, *Speckle Phenomena in Optics : Theory and Applications*, Roberts & Co, 2007.
- [213] B.-H. Liao and C.-C. Lee, "Antireflection coatings for deep ultraviolet optics deposited by magnetron sputtering from Al targets", *Optics Express* **19**(8), 7507–7512, 2011, doi: 10.1364/OE.19.007507.
- [214] D. Li, D. P. Kelly, R. Kirner, and J. T. Sheridan, "Speckle orientation in paraxial optical systems", *Applied Optics* **51**(4), A1, 2012, doi: 10.1364/AO.51.0000A1.
- [215] G. J. Swanson, "Binary optics technology: Theoretical limits on the diffraction efficiency of multilevel diffractive optical elements", *Technical report*, M.I.T. Lincoln Laboratory, 1991.
- [216] K. E. Chong, I. Staude, A. James, J. Dominguez, S. Liu, S. Campione, G. S. Subramania, T. S. Luk, M. Decker, D. N. Neshev, I. Brener, and Y. S. Kivshar, "Polarization-Independent Silicon Metadevices for Efficient Optical Wavefront Control", *Nano Letters* **15**(8), 5369–5374, 2015, doi: 10.1021/acs.nanolett.5b01752.
- [217] T. Sannomiya, O. Scholder, K. Jefimovs, C. Hafner, and A. B. Dahlin, "Investigation of Plasmon Resonances in Metal Films with Nanohole Arrays for Biosensing Applications", *Small* **7**(12), 1653, 2011, doi: 10.1002/smll.201002228.
- [218] M. Lampton, "The Microchannel Image Intensifier", *Scientific American* **245**(5), 62, 1981.
- [219] A. Nesci, R. Dändliker, M. Salt, and H. Herzig, "Measuring amplitude and phase distribution of fields generated by gratings with sub-wavelength resolution", *Optics Communications* **205**(4-6), 229–238, 2002, doi: 10.1016/S0030-4018(02)01371-8.
- [220] C. Rockstuhl, I. Marki, T. Scharf, M. Salt, H. Peter Herzig, and R. Dändliker, "High Resolution Interference Microscopy: A Tool for Probing Optical Waves in the Far-Field on a Nanometric Length Scale", *Current Nanoscience* **2**(4), 337–350, 2006, doi: 10.2174/157341306778699383.

- [221] M.-S. Kim, T. Scharf, C. Menzel, C. Rockstuhl, and H. P. Herzig, “Talbot images of wavelength-scale amplitude gratings”, *Optics Express* **20**(5), 4903–4920, 2012, doi: 10.1364/OE.20.004903.
- [222] K. E. Chong, L. Wang, I. Staude, A. R. James, J. Dominguez, S. Liu, G. S. Subramania, M. Decker, D. N. Neshev, I. Brener, and Y. S. Kivshar, “Efficient Polarization-Insensitive Complex Wavefront Control Using Huygens’ Metasurfaces Based on Dielectric Resonant Meta-atoms”, *ACS Photonics* **3**(4), 514–519, 2016, doi: 10.1021/acphotonics.5b00678.
- [223] M. Decker, I. Staude, M. Falkner, J. Dominguez, D. N. Neshev, I. Brener, T. Pertsch, and Y. S. Kivshar, “High-Efficiency Dielectric Huygens’ Surfaces”, *Advanced Optical Materials* **3**(6), 813–820, 2015, doi: 10.1002/adom.201400584.
- [224] G. M. Whitesides, “The origins and the future of microfluidics”, *Nature* **442**(7101), 368–373, 2006, doi: 10.1038/nature05058.
- [225] B. Meliorisz, P. Evanschitzky, and A. Erdmann, “Simulation of proximity and contact lithography”, *Microelectronic Engineering* **84**(5-8), 733–736, 2007, doi: 10.1016/j.mee.2007.01.125.
- [226] A. Bramati, U. Vogler, B. Meliorisz, K. Motzek, M. Hornung, and R. Voelkel, “Simulation tools for advanced mask aligner lithography”, Proc. SPIE **8167**, Optical Design and Engineering IV, 81670U, 2011, doi: 10.1117/12.897572.
- [227] C. A. Mack, “Development of Positive Photoresists”, *Journal of The Electrochemical Society* **134**(1), 148, 1987, doi: 10.1149/1.2100396.
- [228] L. J. V. Miranda, “PySwarms, a research-toolkit for Particle Swarm Optimization in Python”, *Journal of Open Source Software* **3**(21), 2018, doi: 10.21105/joss.00433.
- [229] O. D. Miller, *Photonic Design: From Fundamental Solar Cell Physics to Computational Inverse Design*, Ph.D. thesis, Cambridge, 2013, doi: 10.1017/CBO9781107415324.004.
- [230] Y. Granik, “Solving inverse problems of optical microlithography”, Proc. SPIE **5754**, Optical Microlithography XVIII, 2005, doi: 10.1117/12.600141.
- [231] Y. Granik, “Fast pixel-based mask optimization for inverse lithography”, *Journal of Micro/Nanolithography, MEMS, and MOEMS* **5**(4), 043002, 2006, doi: 10.1117/1.2399537.
- [232] X. Ma and G. R. Arce, “Pixel-based simultaneous source and mask optimization for resolution enhancement in optical lithography”, *Optics Express* **17**(7), 5783–5793, 2009, doi: 10.1364/OE.17.005783.
- [233] X. Ma, S. Jiang, J. Wang, B. Wu, Z. Song, and Y. Li, “A fast and manufacture-friendly optical proximity correction based on machine learning”, *Microelectronic Engineering* **168**, 15–26, 2017, doi: 10.1016/j.mee.2016.10.006.
- [234] N. Otsu, “A Threshold Selection Method from Gray-Level Histograms”, *IEEE Transactions on Systems, Man, and Cybernetics* **9**(1), 62–66, 1979, doi: 10.1109/TSMC.1979.4310076.
- [235] G. Pitruzzello and T. F. Krauss, “Photonic crystal resonances for sensing and imaging”, *Journal of Optics* **20**(7), 073004, 2018, doi: 10.1088/2040-8986/aac75b.
- [236] D. Zhang, R. Wang, Y. Xiang, Y. Kuai, C. Kuang, R. Badugu, Y. Xu, P. Wang, H. Ming, X. Liu, and J. R. Lakowicz, “Silver Nanowires for Reconfigurable Bloch Surface Waves”, *ACS Nano* **11**(10), 10446–10451, 2017, doi: 10.1021/acsnano.7b05638.

- [237] J. Polo and A. Lakhtakia, "Surface electromagnetic waves: A review", *Laser & Photonics Reviews* **5**(2), 234–246, 2011, doi: 10.1002/lpor.200900050.
- [238] W. L. Barnes, A. Dereux, and T. W. Ebbesen, "Surface plasmon subwavelength optics", *Nature* **424**(6950), 824–830, 2003, doi: 10.1038/nature01937.
- [239] Y. Gao, Q. Gan, Z. Xin, X. Cheng, and F. J. Bartoli, "Plasmonic Mach–Zehnder Interferometer for Ultrasensitive On-Chip Biosensing", *ACS Nano* **5**(12), 9836–9844, 2011, doi: 10.1021/nn2034204.
- [240] M. Li, S. K. Cushing, and N. Wu, "Plasmon-enhanced optical sensors: a review", *The Analyst* **140**(2), 386–406, 2015, doi: 10.1039/C4AN01079E.
- [241] A. S. Baburin, A. S. Kalmykov, R. V. Kirtaev, D. V. Negrov, D. O. Moskalev, I. A. Ryzhikov, P. N. Melentiev, I. A. Rodionov, and V. I. Balykin, "Toward a theoretically limited SPP propagation length above two hundred microns on an ultra-smooth silver surface [Invited]", *Optical Materials Express* **8**(11), 3254, 2018, doi: 10.1364/OME.8.003254.
- [242] K. M. McPeak, S. V. Jayanti, S. J. P. Kress, S. Meyer, S. Iotti, A. Rossinelli, and D. J. Norris, "Plasmonic Films Can Easily Be Better: Rules and Recipes", *ACS Photonics* **2**(3), 326–333, 2015, doi: 10.1021/ph5004237.
- [243] P. Yeh, A. Yariv, and C.-S. Hong, "Electromagnetic propagation in periodic stratified media I General theory*", *Journal of the Optical Society of America* **67**(4), 423, 1977, doi: 10.1364/JOSA.67.000423.
- [244] B. V. Lahijani, N. Descharmes, R. Barbey, G. D. Osowiecki, V. J. Wittwer, O. Razskazovskaya, T. Südmeyer, and H. P. Herzig, "Optical surface waves on one-dimensional photonic crystals: investigation of loss mechanisms and demonstration of centimeter-scale propagation", arXiv:1907.00187, 2019.
- [245] F. Michelotti, R. Rizzo, A. Sinibaldi, P. Munzert, C. Wächter, and N. Danz, "Design rules for combined label-free and fluorescence Bloch surface wave biosensors", *Optics Letters* **42**(14), 2798–2801, 2017, doi: 10.1364/OL.42.002798.
- [246] R. Rizzo, M. Alvaro, N. Danz, L. Napione, E. Descrovi, S. Schmieder, A. Sinibaldi, S. Rana, R. Chandrawati, P. Munzert, T. Schubert, E. Maillart, A. Anopchenko, P. Rivolo, A. Mascioletti, E. Förster, F. Sonntag, M. M. Stevens, F. Bussolino, and F. Michelotti, "Bloch surface wave enhanced biosensor for the direct detection of Angiopoietin-2 tumor biomarker in human plasma", *Biomedical Optics Express* **9**(2), 529, 2018, doi: 10.1364/BOE.9.000529.
- [247] B. Kuswandi, Nuriman, J. Huskens, and W. Verboom, "Optical sensing systems for microfluidic devices: A review", *Analytica Chimica Acta* **601**(2), 141–155, 2007, doi: 10.1016/j.aca.2007.08.046.
- [248] A. Occhicone, A. Sinibaldi, F. Sonntag, P. Munzert, N. Danz, and F. Michelotti, "A novel technique based on Bloch surface waves sustained by one-dimensional photonic crystals to probe mass transport in a microfluidic channel", *Sensors and Actuators B: Chemical* **247**, 532–539, 2017, doi: 10.1016/j.snb.2017.03.041.
- [249] M.-S. Kim, B. V. Lahijani, and H. P. Herzig, "Stepwise Luneburg Lens for Bloch Surface Waves", *Applied Sciences* **8**(2), 245, 2018, doi: 10.3390/app8020245.
- [250] M.-S. Kim, B. Vosoughi Lahijani, N. Descharmes, J. Straubel, F. Negredo, C. Rockstuhl, M. Häyrynen, M. Kuittinen, M. Roussey, and H. P. Herzig, "Subwavelength Focusing of Bloch Surface Waves", *ACS Photonics* **4**(6), 1477–1483, 2017, doi: 10.1021/acsp Photonics.7b00245.

- [251] M. Kadic, G. W. Milton, M. van Hecke, and M. Wegener, “3D metamaterials”, *Nature Reviews Physics* **1**(3), 198–210, 2019, doi: 10.1038/s42254-018-0018-y.
- [252] B. Hassani and E. Hinton, “A review of homogenization and topology optimization I - Homogenization theory for media with periodic structure”, *Computers and Structures* **69**(6), 707–717, 1998, doi: 10.1016/S0045-7949(98)00131-X.
- [253] A. Alù, “First-principles homogenization theory for periodic metamaterials”, *Physical Review B* **84**(7), 075153, 2011, doi: 10.1103/PhysRevB.84.075153.
- [254] D. R. Smith, W. J. Padilla, D. C. Vier, S. C. Nemat-Nasser, and S. Schultz, “Composite Medium with Simultaneously Negative Permeability and Permittivity”, *Physical Review Letters* **84**(18), 4184–4187, 2000, doi: 10.1103/PhysRevLett.84.4184.
- [255] R. A. Shelby, D. Smith, and S. Schultz, “Experimental Verification of a Negative Index of Refraction”, *Science* **292**(5514), 77–79, 2001, doi: 10.1126/science.1058847.
- [256] D. R. Smith, J. B. Pendry, and M. Wiltshire, “Metamaterials and Negative Refractive Index”, *Science* **305**(5685), 788–792, 2004, doi: 10.1126/science.1096796.
- [257] W. J. Padilla, A. J. Taylor, C. Highstrete, M. Lee, and R. D. Averitt, “Dynamical Electric and Magnetic Metamaterial Response at Terahertz Frequencies”, *Physical Review Letters* **96**(10), 107401, 2006, doi: 10.1103/PhysRevLett.96.107401.
- [258] W. Cai, U. K. Chettiar, A. V. Kildishev, and V. M. Shalaev, “Optical cloaking with metamaterials”, *Nature Photonics* **1**(4), 224–227, 2007, doi: 10.1038/nphoton.2007.28.
- [259] N. Liu, H. Guo, L. Fu, S. Kaiser, H. Schweizer, and H. Giessen, “Three-dimensional photonic metamaterials at optical frequencies”, *Nature Materials* **7**(1), 31–37, 2008, doi: 10.1038/nmat2072.
- [260] T. Ergin, N. Stenger, P. Brenner, J. B. Pendry, and M. Wegener, “Three-Dimensional Invisibility Cloak at Optical Wavelengths”, *Science* **328**(5976), 337–339, 2010, doi: 10.1126/science.1186351.
- [261] C. M. Soukoulis and M. Wegener, “Past achievements and future challenges in the development of three-dimensional photonic metamaterials”, *Nature Photonics* **52**(2), 47–50, 2011, doi: 10.1038/nphoton.2011.154.
- [262] H. Chen and C. T. Chan, “Acoustic cloaking in three dimensions using acoustic metamaterials”, *Applied Physics Letters* **91**(18), 183518, 2007, doi: 10.1063/1.2803315.
- [263] T. Frenzel, J. David Brehm, T. Bückmann, R. Schittny, M. Kadic, and M. Wegener, “Three-dimensional labyrinthine acoustic metamaterials”, *Applied Physics Letters* **103**(6), 061907, 2013, doi: 10.1063/1.4817934.
- [264] S. A. Cummer, J. Christensen, and A. Alù, “Controlling sound with acoustic metamaterials”, *Nature Reviews Materials* **1**(3), 16001, 2016, doi: 10.1038/natrevmats.2016.1.
- [265] M. Kadic, T. Bückmann, N. Stenger, M. Thiel, and M. Wegener, “On the practicability of pentamode mechanical metamaterials”, *Applied Physics Letters* **100**(19), 191901, 2012, doi: 10.1063/1.4709436.
- [266] T. Frenzel, M. Kadic, and M. Wegener, “Three-dimensional mechanical metamaterials with a twist”, *Science* **358**(6366), 1072–1074, 2017, doi: 10.1126/science.aao4640.
- [267] D. Lu and Z. Liu, “Hyperlenses and metalenses for far-field super-resolution imaging”, *Nature Communications* **3**(1), 1205, 2012, doi: 10.1038/ncomms2176.

- [268] J. Sun, T. Xu, and N. M. Litchinitser, "Experimental Demonstration of Demagnifying Hyperlens", *Nano Letters* **16**(12), 7905–7909, 2016, doi: 10.1021/acs.nanolett.6b04175.
- [269] J. Sun and N. M. Litchinitser, "Toward Practical, Subwavelength, Visible-Light Photolithography with Hyperlens", *ACS Nano* **12**(1), 542–548, 2018, doi: 10.1021/acsnano.7b07185.
- [270] N. Engheta, "Thin absorbing screens using metamaterial surfaces", in *IEEE Antennas and Propagation Society International Symposium (IEEE Cat. No.02CH37313)*, pages 392–395, IEEE, 2002, doi: 10.1109/APS.2002.1016106.
- [271] N. Yu and F. Capasso, "Flat optics with designer metasurfaces", *Nature Materials* **13**(2), 139–150, 2014, doi: 10.1038/nmat3839.
- [272] H.-T. Chen, A. J. Taylor, and N. Yu, "A review of metasurfaces: physics and applications", *Reports on Progress in Physics* page 76401, 2016, doi: 10.1088/0034-4885/79/7/076401.
- [273] S. M. Kamali, E. Arbabi, A. Arbabi, and A. Faraon, "A review of dielectric optical metasurfaces for wavefront control", arXiv:1804.09802, 2018.
- [274] J. Y. Rhee, Y. J. Yoo, K. W. Kim, Y. J. Kim, and Y. P. Lee, "Metamaterial-based perfect absorbers", *Journal of Electromagnetic Waves and Applications* **28**(13), 1541–1580, 2014, doi: 10.1080/09205071.2014.944273.
- [275] M. Decker and I. Staude, "Resonant dielectric nanostructures: a low-loss platform for functional nanophotonics", *Journal of Optics* **18**(10), 103001, 2016, doi: 10.1088/2040-8978/18/10/103001.
- [276] S. Jahani and Z. Jacob, "All-dielectric metamaterials", *Nature Nanotechnology* **11**(1), 23–36, 2016, doi: 10.1038/nnano.2015.304.
- [277] A. Krasnok, R. Savelev, D. Baranov, and P. Belov, "All-dielectric nanophotonics: fundamentals, fabrication, and applications", arXiv:1610.05363, 2016.
- [278] D. G. Baranov, D. A. Zuev, S. I. Lepeshov, O. V. Kotov, A. E. Krasnok, A. B. Evlyukhin, and B. N. Chichkov, "All-dielectric nanophotonics: the quest for better materials and fabrication techniques", *Optica* **4**(7), 814–825, 2017, doi: 10.1364/OP-TICA.4.000814.
- [279] I. Staude and J. Schilling, "Metamaterial-inspired silicon nanophotonics", *Nature Publishing Group* **11**(5), 274–284, 2017, doi: 10.1038/nphoton.2017.39.
- [280] F. Capasso, "The future and promise of flat optics: a personal perspective", *Nanophotonics* **7**(6), 953–957, 2018, doi: 10.1515/nanoph-2018-0004.
- [281] L. Huang, S. Zhang, and T. Zentgraf, "Metasurface holography: from fundamentals to applications", *Nanophotonics* **7**(6), 1169–1190, 2018, doi: 10.1515/nanoph-2017-0118.
- [282] F. Ding, A. Pors, and S. I. Bozhevolnyi, "Gradient metasurfaces: a review of fundamentals and applications", *Reports on Progress in Physics* **81**(2), 026401, 2018, doi: 10.1088/1361-6633/aa8732.
- [283] S. Chang, X. Guo, and X. Ni, "Optical Metasurfaces: Progress and Applications", *Annual Review of Materials Research* **48**(1), 279–302, 2018, doi: 10.1146/annurev-matsci-070616-124220.
- [284] M. Khorasaninejad and F. Capasso, "Metalenses: Versatile multifunctional photonic components", *Science* **358**(6367), 2017, doi: 10.1126/science.aam8100.

- [285] L. Huang, X. Chen, H. Mühlenbernd, G. Li, B. Bai, Q. Tan, G. Jin, T. Zentgraf, and S. Zhang, “Dispersionless Phase Discontinuities for Controlling Light Propagation”, *Nano Letters* **12**(11), 5750–5755, 2012, doi: 10.1021/nl303031j.
- [286] J. P. Balthasar Mueller, N. A. Rubin, R. C. Devlin, B. Groever, and F. Capasso, “Metasurface Polarization Optics: Independent Phase Control of Arbitrary Orthogonal States of Polarization”, *Phys. Rev. Lett.* **118**, 113901, 2017, doi: 10.1103/PhysRevLett.118.113901.
- [287] X. Ni, A. V. Kildishev, and V. M. Shalaev, “Metasurface holograms for visible light”, *Nature Communications* **4**, 2807, 2013, doi: 10.1038/ncomms3807.
- [288] D. Wen, S. Chen, F. Yue, K. Chan, M. Chen, M. Ardron, K. F. Li, P. W. H. Wong, K. W. Cheah, E. Y. B. Pun, G. Li, S. Zhang, and X. Chen, “Metasurface Device with Helicity-Dependent Functionality”, *Advanced Optical Materials* **4**(2), 321–327, 2016, doi: 10.1002/adom.201500498.
- [289] N. Meinzer, W. L. Barnes, and I. R. Hooper, “Plasmonic meta-atoms and metasurfaces”, *Nature Photonics* **8**(12), 889–898, 2014, doi: 10.1038/nphoton.2014.247.
- [290] J. Zhang, M. ElKabbash, R. Wei, S. C. Singh, B. Lam, and C. Guo, “Plasmonic metasurfaces with 42.3% transmission efficiency in the visible”, *Light: Science and Applications* **8**(1), 2019, doi: 10.1038/s41377-019-0164-8.
- [291] R. D. Richtmyer, “Dielectric Resonators”, *Journal of Applied Physics* **10**(6), 391–398, 1939, doi: 10.1063/1.1707320.
- [292] I. Staude, A. E. Miroshnichenko, M. Decker, N. T. Fofang, S. Liu, E. Gonzales, J. Dominguez, T. S. Luk, D. N. Neshev, I. Brener, and Y. Kivshar, “Tailoring directional scattering through magnetic and electric resonances in subwavelength silicon nanodisks”, *ACS Nano* **7**(9), 7824–7832, 2013, doi: 10.1021/nn402736f.
- [293] E. Rusak, I. Staude, M. Decker, J. Sautter, A. E. Miroshnichenko, D. A. Powell, D. N. Neshev, and Y. S. Kivshar, “Hybrid nanoantennas for directional emission enhancement”, *Applied Physics Letters* **105**(22), 2014, doi: 10.1063/1.4903219.
- [294] R. Guo, E. Rusak, I. Staude, J. Dominguez, M. Decker, C. Rockstuhl, I. Brener, D. N. Neshev, and Y. S. Kivshar, “Multipolar Coupling in Hybrid Metal-Dielectric Metasurfaces”, *ACS Photonics* **3**(3), 349–353, 2016, doi: 10.1021/acsp Photonics.6b00012.
- [295] A. B. Evlyukhin, A. I. Kuznetsov, S. M. Novikov, J. Beermann, C. Reinhardt, R. Kiyani, S. I. Bozhevolnyi, and B. N. Chichkov, “Optical properties of spherical gold mesoparticles”, *Applied Physics B* **106**(4), 841–848, 2012, doi: 10.1007/s00340-011-4727-5.
- [296] W. Zhao, H. Jiang, B. Liu, J. Song, Y. Jiang, C. Tang, and J. Li, “Dielectric Huygens’ Metasurface for High-Efficiency Hologram Operating in Transmission Mode”, *Scientific Reports* **6**, 30613, 2016, doi: 10.1038/srep30613.
- [297] M. Khorasaninejad, A. Y. Zhu, C. Roques-Carmes, W. T. Chen, J. Oh, I. Mishra, R. C. Devlin, and F. Capasso, “Polarization-Insensitive Metalenses at Visible Wavelengths”, *Nano Letters* **16**(11), 7229–7234, 2016, doi: 10.1021/acs.nanolett.6b03626.
- [298] P. Lalanne and P. Chavel, “Metalenses at visible wavelengths: past, present, perspectives”, *Laser & Photonics Reviews* **11**(3), 1600295, 2017, doi: 10.1002/lpor.201600295.
- [299] P. Genevet, F. Capasso, F. Aieta, M. Khorasaninejad, and R. Devlin, “Recent advances in planar optics: from plasmonic to dielectric metasurfaces”, *Optica* **4**(1), 139, 2017, doi: 10.1364/OPTICA.4.000139.

- [300] P. Lalanne, S. Astilean, P. Chavel, E. Cambril, and H. Launois, “Blazed binary subwavelength gratings with efficiencies larger than those of conventional échelette gratings”, *Opt. Lett.* **23**(14), 1081–1083, 1998, doi: 10.1364/OL.23.001081.
- [301] P. Lalanne, S. Astilean, P. Chavel, E. Cambril, and H. Launois, “Design and fabrication of blazed binary diffractive elements with sampling periods smaller than the structural cutoff”, *Journal of the Optical Society of America A* **16**(5), 1143, 1999, doi: 10.1364/JOSAA.16.001143.
- [302] P. Lalanne, “Waveguiding in blazed-binary diffractive elements”, *Journal of the Optical Society of America A* **16**(10), 2517, 1999, doi: 10.1364/JOSAA.16.002517.
- [303] S. J. Byrnes, A. Lenef, F. Aieta, and F. Capasso, “Designing large, high-efficiency, high-numerical-aperture, transmissive meta-lenses for visible light”, *Optics Express* **24**(5), 5110–5124, 2016, doi: 10.1364/OE.24.005110.
- [304] L. Hsu, M. Dupré, A. Ndao, J. Yellowhair, and B. Kanté, “Local phase method for designing and optimizing metasurface devices”, *Optics Express* **25**(21), 24974, 2017, doi: 10.1364/OE.25.024974.
- [305] Y. Li and M. Hong, “Diffractive Efficiency Optimization in Metasurface Design via Electromagnetic Coupling Compensation”, *Materials* **12**(7), 1005, 2019, doi: 10.3390/ma12071005.
- [306] A. Olk and D. Powell, “Accurate Metasurface Synthesis Incorporating Near-Field Coupling Effects”, *Physical Review Applied* **11**(6), 064007, 2019, doi: 10.1103/PhysRevApplied.11.064007.
- [307] M. V. Berry, “Quantal Phase Factors Accompanying Adiabatic Changes”, *Proceedings of the Royal Society A: Mathematical, Physical and Engineering Sciences* **392**(1802), 45–57, 1984, doi: 10.1098/rspa.1984.0023.
- [308] G. Biener, A. Niv, V. Kleiner, and E. Hasman, “Formation of helical beams by use of Pancharatnam–Berry phase optical elements”, *Optics Letters* **27**(21), 1875, 2002, doi: 10.1364/OL.27.001875.
- [309] C. Menzel, C. Rockstuhl, and F. Lederer, “Advanced Jones calculus for the classification of periodic metamaterials”, *Physical Review A* **82**(5), 053811, 2010, doi: 10.1103/PhysRevA.82.053811.
- [310] M. Kang, T. Feng, H.-T. Wang, and J. Li, “Wave front engineering from an array of thin aperture antennas”, *Optics Express* **20**(14), 15882, 2012, doi: 10.1364/oe.20.015882.
- [311] Y. Deng, X. Wang, Z. Gong, K. Dong, S. Lou, N. Pégard, K. B. Tom, F. Yang, Z. You, L. Waller, and J. Yao, “All-Silicon Broadband Ultraviolet Metasurfaces”, *Advanced Materials* **30**(38), 1–6, 2018, doi: 10.1002/adma.201802632.
- [312] N. Yu, P. Genevet, M. A. Kats, F. Aieta, J.-P. Tetienne, F. Capasso, and Z. Gaburro, “Light Propagation with Phase Discontinuities: Generalized Laws of Reflection and Refraction”, *Science* **334**(6054), 333–337, 2011, doi: 10.1126/science.1210713.
- [313] F. Aieta, P. Genevet, N. Yu, M. A. Kats, Z. Gaburro, and F. Capasso, “Out-of-plane reflection and refraction of light by anisotropic optical antenna metasurfaces with phase discontinuities”, *Nano Letters* **12**(3), 1702–1706, 2012, doi: 10.1021/nl300204s.
- [314] S. Larouche and D. R. Smith, “Reconciliation of generalized refraction with diffraction theory”, *Optics Letters* **37**(12), 2391, 2012, doi: 10.1364/OL.37.002391.

- [315] W. T. Chen, A. Y. Zhu, J. Sisler, Z. Bharwani, and F. Capasso, "A broadband achromatic polarization-insensitive metalens consisting of anisotropic nanostructures", *Nature Communications* **10**(1), 355, 2019, doi: 10.1038/s41467-019-08305-y.
- [316] R. C. Devlin, M. Khorasaninejad, W. T. Chen, J. Oh, and F. Capasso, "Broadband high-efficiency dielectric metasurfaces for the visible spectrum", *Proceedings of the National Academy of Sciences* **113**(38), 10473–10478, 2016, doi: 10.1073/pnas.1611740113.
- [317] B. Groever, W. T. Chen, and F. Capasso, "Meta-Lens Doublet in the Visible Region", *Nano Letters* **17**(8), 4902–4907, 2017, doi: 10.1021/acs.nanolett.7b01888.
- [318] W. T. Chen, A. Y. Zhu, M. Khorasaninejad, Z. Shi, V. Sanjeev, and F. Capasso, "Immersion Meta-Lenses at Visible Wavelengths for Nanoscale Imaging", *Nano Letters* **17**(5), 3188–3194, 2017, doi: 10.1021/acs.nanolett.7b00717.
- [319] M. Khorasaninejad, W. T. Chen, J. Oh, and F. Capasso, "Super-Dispersive Off-Axis Meta-Lenses for Compact High Resolution Spectroscopy", *Nano Letters* **16**(6), 3732–3737, 2016, doi: 10.1021/acs.nanolett.6b01097, PMID: 27119987.
- [320] M. Khorasaninejad, Z. Shi, A. Y. Zhu, W. T. Chen, V. Sanjeev, A. Zaidi, and F. Capasso, "Achromatic Metalens over 60 nm Bandwidth in the Visible and Metalens with Reverse Chromatic Dispersion", *Nano Letters* **17**(3), 1819–1824, 2017, doi: 10.1021/acs.nanolett.6b05137.
- [321] M. Decker, W. T. Chen, T. Nobis, A. Y. Zhu, M. Khorasaninejad, Z. Bharwani, F. Capasso, and J. Petschulat, "Imaging Performance of Polarization-Insensitive Metalenses", *ACS Photonics* **6**(6), 1493–1499, 2019, doi: 10.1021/acsphotonics.9b00221.
- [322] B. H. Chen, P. C. Wu, V. C. Su, Y. C. Lai, C. H. Chu, I. C. Lee, J. W. Chen, Y. H. Chen, Y. C. Lan, C. H. Kuan, and D. P. Tsai, "GaN Metalens for Pixel-Level Full-Color Routing at Visible Light", *Nano Letters* **17**(10), 6345–6352, 2017, doi: 10.1021/acs.nanolett.7b03135.
- [323] N. K. Emani, E. Khaidarov, R. Paniagua-Domínguez, Y. H. Fu, V. Valuckas, S. Lu, X. Zhang, S. T. Tan, H. V. Demir, and A. I. Kuznetsov, "High-efficiency and low-loss gallium nitride dielectric metasurfaces for nanophotonics at visible wavelengths", *Applied Physics Letters* **111**(22), 2017, doi: 10.1063/1.5007007.
- [324] Z. Guo, H. Xu, K. Guo, F. Shen, H. Zhou, Q. Zhou, J. Gao, and Z. Yin, "High-efficiency visible transmitting polarizations devices based on the GaN metasurface", *Nanomaterials* **8**(5), 2018, doi: 10.3390/nano8050333.
- [325] A. S. Barker and M. Ilegems, "Infrared Lattice Vibrations and Free-Electron Dispersion in GaN", *Physical Review B* **7**(2), 743–750, 1973, doi: 10.1103/PhysRevB.7.743.
- [326] S. M. Kamali, A. Arbabi, E. Arbabi, Y. Horie, and A. Faraon, "Decoupling optical function and geometrical form using conformal flexible dielectric metasurfaces", *Nature Communications* **7**(1), 11618, 2015, doi: 10.1038/ncomms11618.
- [327] E. Arbabi, A. Arbabi, S. M. Kamali, Y. Horie, and A. Faraon, "Multiwavelength polarization-insensitive lenses based on dielectric metasurfaces with meta-molecules", *Optica* **3**(6), 628, 2016, doi: 10.1364/OPTICA.3.000628.
- [328] J. D. Joannopoulos, S. G. Johnson, J. N. Winn, and R. D. Meade, *Photonic crystals: molding the flow of light*, Princeton University Press, 2011.
- [329] E. H. Anderson, C. M. Horwitz, and H. I. Smith, "Holographic lithography with thick photoresist", *Applied Physics Letters* **43**(9), 874–875, 1983, doi: 10.1063/1.94533.

- [330] M. Campbell, D. N. Sharp, M. T. Harrison, R. G. Denning, and A. J. Turberfield, "Fabrication of photonic crystals for the visible spectrum by holographic lithography", *Nature* **404**(6773), 53–56, 2000, doi: 10.1038/35003523.
- [331] B. R. Brown and A. W. Lohmann, "Complex Spatial Filtering with Binary Masks", *Applied Optics* **5**(6), 967, 1966, doi: 10.1364/AO.5.000967.
- [332] A. W. Lohmann and D. P. Paris, "Binary Fraunhofer Holograms, Generated by Computer", *Applied Optics* **6**(10), 1739, 1967, doi: 10.1364/AO.6.001739.
- [333] F. Wyrowski and O. Bryngdahl, "Iterative Fourier-transform algorithm applied to computer holography", *Journal of the Optical Society of America A* **5**(7), 1058, 1988, doi: 10.1364/JOSAA.5.001058.
- [334] F. Wyrowski and O. Bryngdahl, "Digital holography as part of diffractive optics", *Reports on Progress in Physics* **54**(12), 1481–1571, 1991, doi: 10.1088/0034-4885/54/12/001.
- [335] F. Wyrowski, "Design theory of diffractive elements in the paraxial domain", *Journal of the Optical Society of America A* **10**(7), 1553, 1993, doi: 10.1364/josaa.10.001553.
- [336] F. Fetthauer, C. Stroot, and O. Bryngdahl, "On the quantization of holograms with the iterative Fourier transform algorithm", *Optics Communications* **136**(1-2), 7–10, 1997, doi: 10.1016/S0030-4018(96)00674-8.
- [337] J. Zhang, N. Pégard, J. Zhong, H. Adesnik, and L. Waller, "3D computer-generated holography by non-convex optimization", *Optica* **4**(10), 1306, 2017, doi: 10.1364/OP-TICA.4.001306.
- [338] F. Wyrowski, "Diffraction efficiency of analog and quantized digital amplitude holograms: analysis and manipulation", *Journal of the Optical Society of America A* **7**(3), 383, 1990, doi: 10.1364/JOSAA.7.000383.
- [339] B. E. A. Saleh and M. C. Teich, *Fundamentals of Photonics*, Wiley Series in Pure and Applied Optics, Wiley, 2007.
- [340] O. Ripoll, V. Kettunen, and H. P. Herzig, "Review of iterative Fourier-transform algorithms for beam shaping applications", *Optical Engineering* **43**(11), 2549–2556, 2004, doi: 10.1117/1.1804543.
- [341] R. C. Gonzalez and R. E. Woods, *Digital Image Processing*, International Edition, Prentice Hall, 2002.
- [342] G. Yoon, D. Lee, K. T. Nam, and J. Rho, "Pragmatic metasurface hologram at visible wavelength: the balance between diffraction efficiency and fabrication compatibility", *ACS Photonics* **5**(5), 1643–1647, 2018, doi: 10.1021/acsp Photonics.7b01044.
- [343] A. She, S. Zhang, S. Shian, D. R. Clarke, and F. Capasso, "Large area metalenses: design, characterization, and mass manufacturing", *Optics Express* **26**(2), 1573, 2018, doi: 10.1364/OE.26.001573.
- [344] M. Mansouree and A. Arbabi, "Large-scale Metasurface Design using the Adjoint Sensitivity Technique", in *Conference on Lasers and Electro-Optics*, volume 6, page FF1F.7, OSA, Washington, D.C., 2018, doi: 10.1364/CLEO_QELS.2018.FF1F.7.
- [345] Y. Lee, S.-J. Kim, J.-G. Yun, C. Kim, S.-Y. Lee, and B. Lee, "Electrically tunable multifunctional metasurface for integrating phase and amplitude modulation based on hyperbolic metamaterial substrate", *Optics Express* **26**(24), 32063, 2018, doi: 10.1364/OE.26.032063.

- [346] A. She, S. Zhang, S. Shian, D. R. Clarke, and F. Capasso, “Adaptive metalenses with simultaneous electrical control of focal length, astigmatism, and shift”, *Science Advances* **4**(2), 2018, doi: 10.1126/sciadv.aap9957.
- [347] A. Forouzmmand, M. M. Salary, G. Kafaie Shirmanesh, R. Sokhoyan, H. A. Atwater, and H. Mosallaei, “Tunable all-dielectric metasurface for phase modulation of the reflected and transmitted light via permittivity tuning of indium tin oxide”, *Nanophotonics* **8**(3), 415–427, 2019, doi: 10.1515/nanoph-2018-0176.
- [348] A. Rahimzadegan, D. Arslan, R. N. S. Suryadharma, S. Fasold, M. Falkner, T. Pertsch, I. Staude, and C. Rockstuhl, “Disorder-Induced Phase Transitions in the Transmission of Dielectric Metasurfaces”, *Physical Review Letters* **122**(1), 015702, 2019, doi: 10.1103/PhysRevLett.122.015702.
- [349] L. Huang, H. Mühlenbernd, X. Li, X. Song, B. Bai, Y. Wang, and T. Zentgraf, “Broadband Hybrid Holographic Multiplexing with Geometric Metasurfaces”, *Advanced Materials* **27**(41), 6444–6449, 2015, doi: 10.1002/adma.201502541.
- [350] A. Arbabi, Y. Horie, M. Bagheri, and A. Faraon, “Dielectric metasurfaces for complete control of phase and polarization with subwavelength spatial resolution and high transmission”, *Nature Nanotechnology* **10**(11), 937–943, 2015, doi: 10.1038/nnano.2015.186.
- [351] B. Wang, F. Dong, Q.-T. Li, D. Yang, C. Sun, J. Chen, Z. Song, L. Xu, W. Chu, Y.-F. Xiao, Q. Gong, and Y. Li, “Visible-Frequency Dielectric Metasurfaces for Multiwavelength Achromatic and Highly Dispersive Holograms”, *Nano Letters* **16**(8), 5235–5240, 2016, doi: 10.1021/acs.nanolett.6b02326.
- [352] B. Wang, B. Quan, J. He, Z. Xie, X. Wang, J. Li, Q. Kan, and Y. Zhang, “Wavelength de-multiplexing metasurface hologram”, *Scientific Reports* **6**, 35657, 2016, doi: 10.1038/srep35657.
- [353] I. Staude, T. Pertsch, and Y. S. Kivshar, “All-Dielectric Resonant Meta-Optics Lightens up”, *ACS Photonics* **6**(4), 802–814, 2019, doi: 10.1021/acsp Photonics.8b01326.
- [354] D. Tennant, *Limits of Conventional Lithography*, Springer New York, 1999.
- [355] R. Garcia, A. W. Knoll, and E. Riedo, “Advanced scanning probe lithography”, *Nature Nanotechnology* **9**(8), 577–587, 2014, doi: 10.1038/nnano.2014.157.
- [356] C. W. Gwyn, R. Stulen, D. Sweeney, and D. Attwood, “Extreme ultraviolet lithography”, *Journal of Vacuum Science & Technology B: Microelectronics and Nanometer Structures* **16**(6), 3142, 1998, doi: 10.1116/1.590453.
- [357] P. D. Bisschop, “Stochastic effects in EUV lithography: random, local CD variability, and printing failures”, *Journal of Micro/Nanolithography, MEMS, and MOEMS* **16**(04), 1, 2017, doi: 10.1117/1.JMM.16.4.041013.
- [358] S. Kawata, H.-B. Sun, T. Tanaka, and K. Takada, “Finer features for functional microdevices”, *Nature* **412**(6848), 697–698, 2001, doi: 10.1038/35089130.
- [359] M. Deubel, G. von Freymann, M. Wegener, S. Pereira, K. Busch, and C. M. Soukoulis, “Direct laser writing of three-dimensional photonic-crystal templates for telecommunications”, *Nature Materials* **3**(7), 444–447, 2004, doi: 10.1038/nmat1155.
- [360] W. Haske, V. W. Chen, J. M. Hales, W. Dong, S. Barlow, S. R. Marder, and J. W. Perry, “65 nm feature sizes using visible wavelength 3-D multiphoton lithography”, *Optics Express* **15**(6), 3426, 2007, doi: 10.1364/OE.15.003426.

- [361] J. Fischer and M. Wegener, “Three-dimensional optical laser lithography beyond the diffraction limit”, *Laser & Photonics Reviews* **7**(1), 22–44, 2012, doi: 10.1002/lpor.201100046.
- [362] E. Yablonovitch and R. B. Vrijen, “Optical projection lithography at half the Rayleigh resolution limit by two-photon exposure”, *Optical Engineering* **38**(2), 334, 1999, doi: 10.1117/1.602092.
- [363] Nanoscribe data sheet, http://www.nanoscribe.de/files/7914/0169/2326/DataSheet_Photonic_Professional.pdf, 2018.
- [364] J. Fischer, G. von Freymann, and M. Wegener, “The Materials Challenge in Diffraction-Unlimited Direct-Laser-Writing Optical Lithography”, *Advanced Materials* **22**(32), 3578–3582, 2010, doi: 10.1002/adma.201000892.
- [365] J. Fischer and M. Wegener, “Three-dimensional direct laser writing inspired by stimulated-emission-depletion microscopy [Invited]”, *Optical Materials Express* **1**(4), 614, 2011, doi: 10.1364/OME.1.000614.
- [366] T. Bückmann, N. Stenger, M. Kadic, J. Kaschke, A. Frölich, T. Kennerknecht, C. Eberl, M. Thiel, and M. Wegener, “Tailored 3D Mechanical Metamaterials Made by Dip-in Direct-Laser-Writing Optical Lithography”, *Advanced Materials* **24**(20), 2710–2714, 2012, doi: 10.1002/adma.201200584.
- [367] A. Jesacher and M. J. Booth, “Parallel direct laser writing in three dimensions with spatially dependent aberration correction”, *Optics Express* **18**(20), 21090, 2010, doi: 10.1364/oe.18.021090.
- [368] E. H. Waller and G. von Freymann, “Multi foci with diffraction limited resolution”, *Optics Express* **21**(18), 21708, 2013, doi: 10.1364/oe.21.021708.
- [369] L. Yang, Y. Hu, J. Chu, W. Huang, U. Hinze, J. Li, A. El-Tamer, and B. N. Chichkov, “Parallel direct laser writing of micro-optical and photonic structures using spatial light modulator”, *Optics and Lasers in Engineering* **70**, 26–32, 2015, doi: 10.1016/j.optlaseng.2015.02.006.
- [370] A. N. Boto, P. Kok, D. S. Abrams, S. L. Braunstein, C. P. Williams, and J. P. Dowling, “Quantum Interferometric Optical Lithography: Exploiting Entanglement to Beat the Diffraction Limit”, *Physical Review Letters* **85**(13), 2733–2736, 2000, doi: 10.1103/PhysRevLett.85.2733.
- [371] P. Kok, A. N. Boto, D. S. Abrams, C. P. Williams, S. L. Braunstein, and J. P. Dowling, “Quantum-interferometric optical lithography: Towards arbitrary two-dimensional patterns”, *Physical Review A* **63**(6), 063407, 2001, doi: 10.1103/PhysRevA.63.063407.
- [372] G. Björk, L. L. Sánchez-Soto, and J. Söderholm, “Entangled-State Lithography: Tailoring Any Pattern with a Single State”, *Physical Review Letters* **86**(20), 4516–4519, 2001, doi: 10.1103/PhysRevLett.86.4516.
- [373] M. D’Angelo, M. V. Chekhova, and Y. Shih, “Two-Photon Diffraction and Quantum Lithography”, *Physical Review Letters* **87**(1), 013602, 2001, doi: 10.1103/PhysRevLett.87.013602.
- [374] P. Kok, “Research summary Optical Quantum Lithography”, <http://www.pieterkok.staff.shef.ac.uk/index.php?nav=research&sub=litho>, 2019.
- [375] T. Chang, M. Mankos, K. Y. Lee, and L. P. Muray, “Multiple electron-beam lithography”, *Microelectronic Engineering* **57–58**, 117–135, 2001, doi: 10.1016/S0167-9317(01)00528-7.

- [376] Y. Chen, "Nanofabrication by electron beam lithography and its applications: A review", *Microelectronic Engineering* **135**, 57–72, 2015, doi: 10.1016/j.mee.2015.02.042.
- [377] G. D. Boer, M. P. Dansberg, R. Jager, J. J. M. Peijster, E. Slot, S. W. H. K. Steenbrink, and M. J. Wieland, "MAPPER: progress toward a high-volume manufacturing system", Proc. SPIE **8680**, Alternative Lithographic Technologies V, 86800O, 2013, doi: 10.1117/12.2011486.
- [378] M. Esashi, A. Kojima, N. Ikegami, H. Miyaguchi, and N. Koshida, "Development of massively parallel electron beam direct write lithography using active-matrix nanocrystalline-silicon electron emitter arrays", *Microsystems & Nanoengineering* **1**(1), 15029, 2015, doi: 10.1038/micronano.2015.29.
- [379] G. Y. Liu, S. Xu, and Y. Qian, "Nanofabrication of self-assembled monolayers using scanning probe lithography", *Accounts of Chemical Research* **33**(7), 457–466, 2000, doi: 10.1021/ar980081s.
- [380] A. A. Tseng, A. Notargiacomo, and T. P. Chen, "Nanofabrication by scanning probe microscope lithography: A review", *Journal of Vacuum Science & Technology B: Microelectronics and Nanometer Structures* **23**(3), 877, 2005, doi: 10.1116/1.1926293.
- [381] A. Houel, D. Tonneau, N. Bonnail, H. Dallaporta, and V. I. Safarov, "Direct patterning of nanostructures by field-induced deposition from a scanning tunneling microscope tip", *Journal of Vacuum Science & Technology B: Microelectronics and Nanometer Structures* **20**(6), 2337, 2002, doi: 10.1116/1.1520548.
- [382] D. M. Eigler and E. K. Schweizer, "Positioning single atoms with a scanning tunnelling microscope", *Nature* **344**(6266), 524–526, 1990, doi: 10.1038/344524a0.
- [383] H. J. Mamin and D. Rugar, "Thermomechanical writing with an atomic force microscope tip", *Applied Physics Letters* **61**(8), 1003–1005, 1992, doi: 10.1063/1.108460.
- [384] S. C. Minne, J. D. Adams, G. Yaralioglu, S. R. Manalis, A. Atalar, and C. F. Quate, "Centimeter scale atomic force microscope imaging and lithography", *Applied Physics Letters* **73**(12), 1742–1744, 1998, doi: 10.1063/1.122263.
- [385] K. Salaita, Y. Wang, and C. A. Mirkin, "Applications of dip-pen nanolithography", *Nature Nanotechnology* **2**(3), 145–155, 2007, doi: 10.1038/nnano.2007.39.
- [386] C. A. Mirkin, "The Power of the Pen: Development of Massively Parallel Dip-Pen Nanolithography", *ACS Nano* **1**(2), 79–83, 2007, doi: 10.1021/nn700228m.
- [387] S. Y. Chou, P. R. Krauss, and P. J. Renstrom, "Imprint of sub-25 nm vias and trenches in polymers", *Applied Physics Letters* **67**(21), 3114–3116, 1995, doi: 10.1063/1.114851.
- [388] S. Y. Chou, "Nanoimprint lithography", *Journal of Vacuum Science & Technology B: Microelectronics and Nanometer Structures* **14**(6), 4129, 1996, doi: 10.1116/1.588605.
- [389] L. J. Guo, "Nanoimprint Lithography: Methods and Material Requirements", *Advanced Materials* **19**(4), 495–513, 2007, doi: 10.1002/adma.200600882.
- [390] H. Schiff, "Nanoimprint lithography: An old story in modern times? A review", *Journal of Vacuum Science & Technology B: Microelectronics and Nanometer Structures* **26**(2), 458, 2008, doi: 10.1116/1.2890972.
- [391] B. J. Wiley, D. Qin, and Y. Xia, "Nanofabrication at High Throughput and Low Cost", *ACS Nano* **4**(7), 3554–3559, 2010, doi: 10.1021/nn101472p.

- [392] S. Y. Chou, "Sub-10 nm imprint lithography and applications", *Journal of Vacuum Science & Technology B: Microelectronics and Nanometer Structures* **15**(6), 2897, 1997, doi: 10.1116/1.589752.
- [393] S. I. Association, "International Technology Roadmap for Semiconductors, 2003 edition, Lithography", *ITRS* page <http://www.itrs.net>, 2003.
- [394] Y. Yao, H. Liu, Y. Wang, Y. Li, B. Song, R. P. Wang, M. L. Povinelli, and W. Wu, "Nanoimprint-defined, large-area meta-surfaces for unidirectional optical transmission with superior extinction in the visible-to-infrared range", *Optics Express* **24**(14), 15362, 2016, doi: 10.1364/OE.24.015362.
- [395] M. Iwanaga, "Large-area metasurfaces produced with nm precision by UV nanoimprint lithography", *2016 Progress In Electromagnetics Research Symposium, PIERS 2016 - Proceedings* **3**, 1857–1861, 2016, doi: 10.1109/PIERS.2016.7734815.
- [396] S. V. Makarov, V. Milichko, E. V. Ushakova, M. Omelyanovich, A. Cerdan Pasaran, R. Haroldson, B. Balachandran, H. Wang, W. Hu, Y. S. Kivshar, and A. A. Zakhidov, "Multifold Emission Enhancement in Nanoimprinted Hybrid Perovskite Metasurfaces", *ACS Photonics* **4**(4), 728–735, 2017, doi: 10.1021/acsphotonics.6b00940.
- [397] M. J. Lercel, H. G. Craighead, A. N. Parikh, K. Seshadri, and D. L. Allara, "Sub-10 nm lithography with self-assembled monolayers", *Applied Physics Letters* **68**(11), 1504–1506, 1996, doi: 10.1063/1.115680.
- [398] G. M. Whitesides, "Self-Assembly at All Scales", *Science* **295**(5564), 2418–2421, 2002, doi: 10.1126/science.1070821.
- [399] J. C. Love, L. A. Estroff, J. K. Kriebel, R. G. Nuzzo, and G. M. Whitesides, "Self-Assembled Monolayers of Thiolates on Metals as a Form of Nanotechnology", *Chemical Reviews* **105**(4), 1103–1170, 2005, doi: 10.1021/cr0300789.
- [400] Y. S. Jung, J. B. Chang, E. Verploegen, K. K. Berggren, and C. A. Ross, "A Path to Ultranarrow Patterns Using Self-Assembled Lithography", *Nano Letters* **10**(3), 1000–1005, 2010, doi: 10.1021/nl904141r.
- [401] S. M. George, "Atomic Layer Deposition: An Overview", *Chemical Reviews* **110**(1), 111–131, 2010, doi: 10.1021/cr900056b.
- [402] Homepage of the NOLOSS Project, <https://www.nolossproject.eu/>.

Appendix

A Documentation of contributions by co-authors

This section once states clearly which contributions to the results have been made by colleagues and co-authors whom I would like to thank for her invaluable support and availability.

1. TOPTICA PHOTONICS Lochhamer Schlag 19, 82166 Graefelfing (Munich), Germany (D. Opalevs, C. Gilfert, M. Scholz, P. Leisching): Developing the optical setup for the 193 nm laser, Figs. 4.4 to 4.7.
2. Raoul Kirner, SUSS Microoptics SA, Rogues-Terres 61, 2068 Hauterive, Switzerland, raoul.kirner@suss.com: Beam shaping optics and the corresponding optical simulations, leading to Figs. 4.9 to 4.12 and 4.19.
3. Jeremy Béguelin, SUSS Microoptics SA, Rogues-Terres 61, 2068 Hauterive, Switzerland, jeremy.beguelin@suss.com: White light interferometer image and goniometric measurements, Fig. 4.8.
4. Yannick Bourgin, Uwe Zeitner, and Tina Weichelt, Fraunhofer IOF, Albert-Einstein-Straße 7, 07745 Jena, Germany, uwe.zeitner@iof.fraunhofer.de: Design and fabrication of rigorously optimized phase-shift mask presented in Chapter 5.
5. Y. Augenstein, Institute of Theoretical Solid State Physics, KIT Karlsruhe, Germany, yannick.augenstein@kit.edu, B. V. Lahijani and M.-S. Kim, École Polytechnique Fédérale Lausanne, Route Cantonale, 1015 Lausanne, Switzerland: Simulations and measurements leading to Figs. 6.16b and 6.17.

B Next-generation lithography

This section looks beyond the horizon of canonical optical lithography, as applied to modern semiconductor fabrication nowadays. In the future, other techniques may emerge, complementing or even replacing optical lithography at DUV wavelengths. The following short summary makes no claim to be exhaustive, and rather aims to give a glimpse at possible future developments. We divide the techniques into two categories, depending on whether they are related to optics or not. Despite the overwhelming multitude of approaches to nanofabrication, Tennant observed in 1999 that all fabrication technologies follow a simple scaling law [354],

$$r = k_T \cdot A^{1/5} \tag{B.1}$$

with r the resolution in nm, A the areal throughput in nm^2/s , and $k_T \sim 0.75$ a constant empirically found by Tennant. In other words, an improvement in the resolution affects the throughput to the power of five. Tennant's law strikingly illustrates the tradeoff between resolution and throughput in methods of modern nanofabrication, as illustrated in Fig. B.1 for the techniques discussed here.

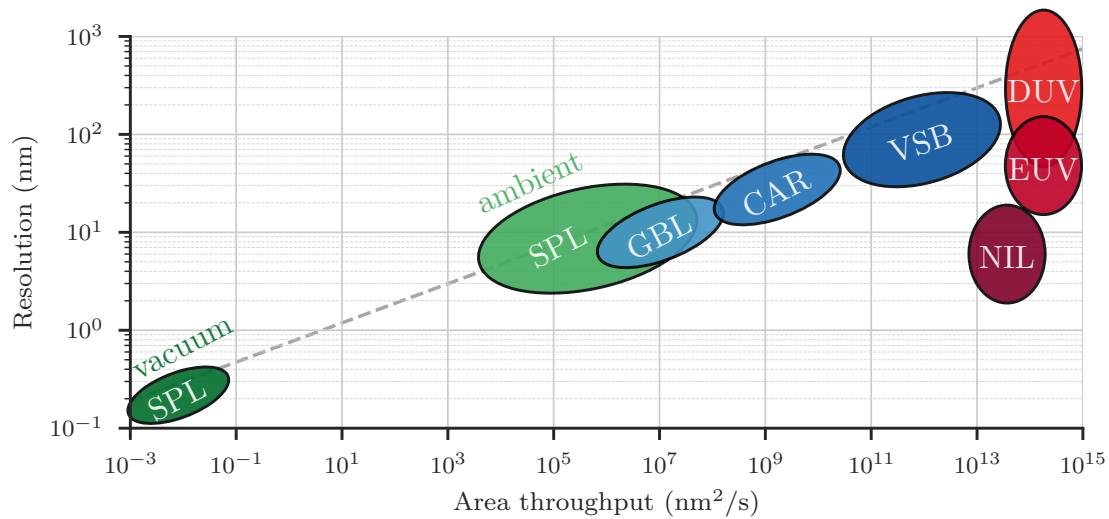


Figure B.1: Tennant's law in micro- and nanofabrication shows the relationship between resolution and areal throughput, scaling with Eq. (B.1) (dashed gray line). We discuss only 2D area techniques, not including volumetric fabrication methods as 3D additive manufacturing.

Abbreviations: Scanning probe lithography (SPL), chemically amplified resist (CAR), Gaussian beam lithography (GBL), variable shaped beam (VSB), deep ultraviolet (DUV), extreme ultraviolet (EUV), and nanoimprint lithography (NIL). Adapted from [354, 355].

B.1 Future trends in optical lithography

The continuing trend of wavelength reduction, following Eq. (2.21), culminates in the development and recent market launch of EUV lithography [48, 356], centered around a wavelength of 13.5 nm. Optics in this regime requires a fundamentally different approach: The generation of light relies on a laser-produced plasma, beam shaping and steering as well as the photomask requires reflective catoptric systems, and everything has to be operated under vacuum conditions due to spurious absorption in the atmosphere. Due to the significantly increased photon energy compared to DUV lithography, secondary electrons and photoelectrons are generated upon light absorption in the resist and the substrate, effectively smearing out the image. Many properties in the EUV are reminiscent of X-ray lithography, where the resolution is basically limited by these effects [66]. With the higher photon energy, a smaller number of photons is required to achieve a certain exposure dose. Stochastic variations in the absorption of the photons arise, which can ultimately result in individual small features not being printed at all [357]. In addition, shot noise adds to this variation, further reducing the critical dimension uniformity. These problems can be circumvented using higher doses, however, at the price of reducing the throughput. Following Eq. (2.22), further increasing the NA imposes in particular issues regarding the DOF. Despite these challenges, this technology is believed to have the potential for a further shrinkage in feature size at high volume production [48], especially upon implementing high-NA systems, and is driving Moore's law.

Other interesting approaches to high resolution optical lithography move on from classical linear optics, and aim to surpass the associated resolution limit relying on nonlinear and quantum properties of light. Multiphoton lithography relies on the polymerization of a photoresist upon nonlinear absorption of tightly focused photons [358–361]. A common additive manufacturing scheme working in three dimensions exploits two-photon absorption (TPA) [362]. In a small volume around the focus, a *voxel*, eventually the threshold for multiphoton polymerization is surpassed [359]. Scanning the focus through the resist generates 3D structures, with the nonlinear process enabling feature sizes

well below the Abbe diffraction limit [361]. Commercially available systems claim a lateral resolution below 200 nm, with a slightly increased voxel size in axial direction below 1000 nm [363]. Several approaches resulting in resolution enhancement have been demonstrated, for instance using stimulated emission depletion (STED)-assisted DLW [364, 365] and dip-in DLW [366]. Bottleneck for nanofabrication is the serial writing process, with several ideas towards parallel DLW demonstrated [367–369].

Quantum lithography takes the concept of multiphoton lithography one step further and includes quantum effects to beat the classical diffraction limit [370–373]. For an intuitive understanding of the concept perceived by Kok and co-workers, let's consider the famous double-slit experiment, in many aspects similar to the discussion concerning Figs. 2.10 and 2.13. In the classical wave picture, we understand the emerging pattern behind the double-slit as the interference of waves passing the slits, with the width of the interference fringes approximately proportional to the wavelength. In a quantum-optical picture, we now consider single photons, which can take all possible paths through one of the slits [374]. In the limit of many photons, we obtain again the same interference pattern as in the wave-optical picture. The sum of single-photon interference intensities leads to the overall observed interference pattern.

The concept of quantum lithography now relies on the *entanglement* of photons, in our example two photons. The two-mode state of a double-slit with possible paths a and b for two identical photons is

$$\frac{|2\rangle_a |0\rangle_b + |0\rangle_a |2\rangle_b}{\sqrt{2}}, \quad (\text{B.2})$$

that means their paths are entangled. This is reminiscent of the Hong-Ou-Mandel (HOM) effect, and indeed HOM interference was exploited for the first demonstration of quantum lithography [373].

In essence, the two photons behave as a single entity, provided a TPA process is involved. The path-entangled photons behave as one photon with twice the energy (and hence half the wavelength), improving the resolution over classical lithography. This concept can be extended to NOON states, many-body entangled states with $[|N\rangle_a |0\rangle_b + |0\rangle_a |N\rangle_b]/\sqrt{2}$, as well as splitting of the states, $[|N-m\rangle_a |m\rangle_b + |m\rangle_a |N-m\rangle_b]/\sqrt{2}$ with integer $m < N$, for arbitrary patterns [374]. Prerequisite for this quantum lithographic scheme are suitable photoresists, sensitive to the absorption of N photons.

B.2 High volume non-optical fabrication

The chief advantage of optical lithography is the parallel structuring approach, enabling the pattern transfer with high information density. Extending the realm of discussion to alternative lithographic techniques, such approaches frequently outperform optical lithography in terms of resolution. The sequential approach of such serial scanning methods, however, can be only applied to rapid prototyping and master generation, and is restricted for the use in high volume fabrication. To have an overview over the available possibilities for nanofabrication, we briefly summarize sophisticated approaches to scale up such methods, relying on either electrons, an ensemble of sharp tips in scanning probe lithography (SPL), self-organization of matter on a nanoscale, or imprint techniques, showing the potential to complement and eventually replace optical lithography in high volume fabrication.

E-beam lithography, relying on the scanning of a Gaussian electron beam over or projecting elementary shapes (rectangles, triangles) on a suitable resist in vacuum, is the prevalent

tool for maskmaking and a competitor for high volume direct wafer writing [375,376]. The resolution is restricted by aberrations of the electron optics and the spread of secondary electrons generated by the impinging beam, leading to a proximity effect [376]. For this maskless technology, the writing speed is inherently limited by the beam current, the equivalent to the light source intensity in optical lithography. However, increasing the beam current facilitates electron-electron interactions, reducing the beam quality and ultimately the resolution. The industrial standard is to use many beams in parallel, greatly increasing the throughput, while adding complexity to the system [375, 377, 378].

Scanning probe lithography can be divided into two basic techniques, scanning tunneling microscope (STM) and atomic force microscopy (AFM) lithography, and three categories, i.e., the modification, the addition, or the removal of material on a surface [355, 379, 380]. In STM lithography, a sharp voltage-biased metallic tip is brought within atomic range of a surface, enabling electron tunneling over the gap. A resist can be exposed by forming an e-beam in miniature in a similar fashion as in e-beam lithography. The voltages are several orders of magnitude lower than in e-beam lithography, but the currents are increased by about three orders of magnitude [380]. The highly localized current does not diverge and allows a high resolution. Multi-tip STM lithography multiplies the throughput of one individual single tip. Material deposition, the second category, is implemented by field-induced atom transfer from the tip to the substrate, for example demonstrated for a Pt tip [381]. For the removal of material, typically decomposition processes are initiated through e-beam heating. For completeness, STM also enables the accurate positioning of single atoms, as demonstrated by the seminal work of Eigler and Schweizer [382], showing only limited use for large-scale fabrication.

Considering AFM-related lithographic methods, primarily thermal and thermochemical induced effects have attracted the interest of the community [355]. In the thermal SPL, a resistively heated tip introduces the removal of a suitable material [383], for instance polymers resistive to heat or molecular glass resists. The modification is highly localized at the contact area between AFM tip and the surface. In thermochemical SPL, the heat is used to induce changes in the chemistry of the material. Despite the limited throughput in SPL (compare Fig. B.1), the use of parallel probes promises a route for upscaling [384]. A major benefit of SPL is the ability to image the surface in-situ, for instance during the retrace step, operating in the established AFM mode. Adding material in SPL is also a mature technology, for example relying on dip-pen nanolithography (DPN) [385]. The operation of 55 000 levers in parallel have been demonstrated, replicating the same structure over a 2D array [386].

In contrast to SPL, nanoimprint lithography (NIL) is a parallel printing technique, promising decent resolution at high throughput (compare Fig. B.1) [387–391]. NIL relies on a stamp transferring the pattern to the substrate, by pressing a hard mold containing the structure as a topography into a soft polymer cast [389]. A thin residual layer protecting the substrate is subsequently removed in an anisotropic etch step, for instance using RIE. Promising properties of NIL are an excellent resolution: Already over two decades ago, the printing of sub-10 nm holes in a periodic arrangement has been demonstrated [392]. High aspect ratios have been shown as well as UV curable casts. It allows the fabrication of multi-level DOEs in one iteration, whereas optical lithography requires several steps. In addition, the mold can be reused thousands of times, compensating the costs for creating a high-resolution mold, and renders NIL a cost-effective technique. Nanoimprint is since 2003 part of the International Technology Roadmap for Semiconductors [393], and is successfully used for instance for the large-area fabrication of MSs [376, 394–396]. Remaining problems of NIL revolve around achieving a high yield by reducing defect formation.

All techniques discussed so far rely on the top-down approach, inherently limited by

either the diffraction limit or the nanoscopic size of the probe. Fundamentally different are self-assembled or self-organized structures that emerge in a bottom-up fabrication approach, applicable on greatly varying length scales [397–400]. As a manufacturer, one relies on the interaction of fundamental building blocks, for instance chemical and biological processes or electrostatic forces. Such self-guided fabrication or directed self-assembly enables the generation of complex 3D materials, while regularly suffering from limited process control and defect formation.

In summary, several techniques such as NIL and EUV are on the verge of becoming an alternative to canonical DUV optical lithography as a high resolution and cost-effective fabrication tool. Nevertheless, optical lithography remains the tool of choice for high throughput fabrication at decent resolution.

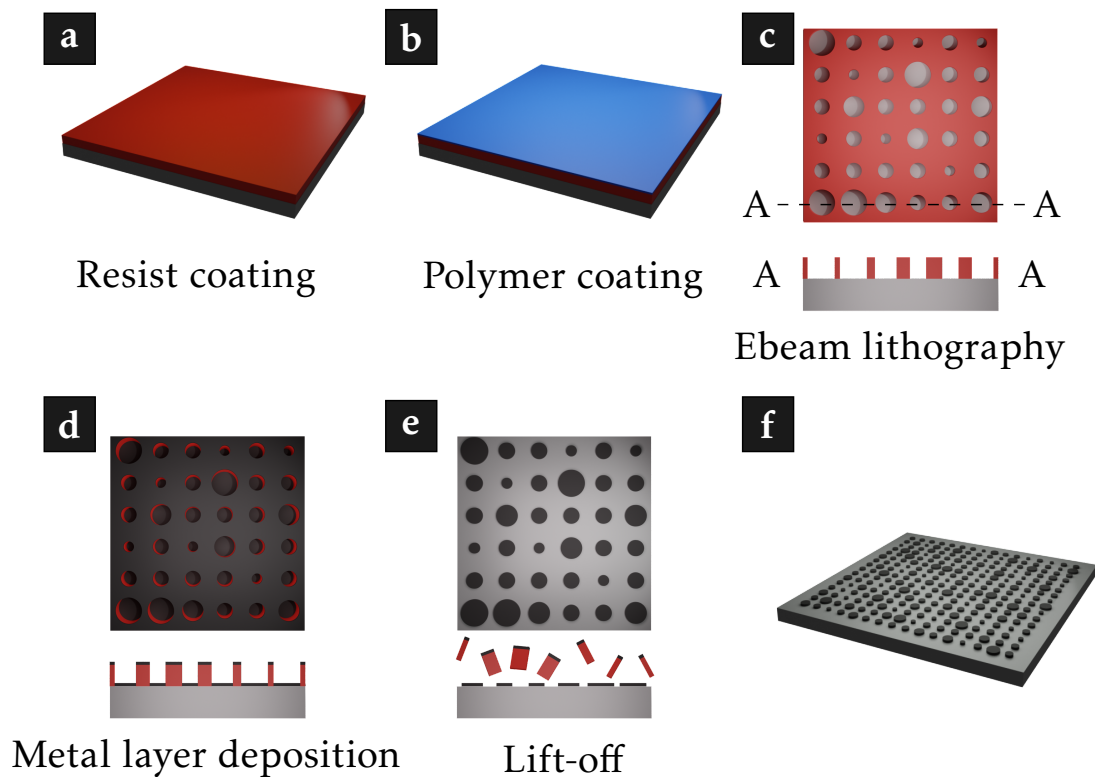


Figure C.2: Schematic of metal absorber fabrication.

a – b Spincoating ebeam resist and a conducting polymer (*Espacer*[®]).

c Ebeam lithography, using a positive resist (for instance PMMA, shown in red). The volume of the absorber structure is removed in the development step.

d Metal layer deposition via ebeam physical vapor deposition.

e Lift-off in acetone. The resist and the metal layer on top of it is removed.

f Final absorber structure. The next step is to add the phase modulation using dielectric structures, see Fig. C.3.

C A route to experimental realization of hybrid UV metasurfaces

In this section we discuss a possible fabrication procedure for the metasurfaces discussed in Chapter 7. The most complex case, the hybrid metasurface, would first require to add the plasmonic absorber layer (Appendix C.1), followed by the dielectric nanocylinder array (Appendix C.2). For the phase-only metasurface, the first step is omitted.

C.1 Fabrication of the plasmonic absorber layer

For the plasmonic absorber layer, we propose to use a standard lift-off process [34], as illustrated in Fig. C.2. First, a ebeam resist (for example a thin PMMA double layer) is spincoated on the fused silica substrate, followed by the coating of a conducting polymer (for example *Espacer*[®]) to prevent charging effects during ebeam lithography. The positive photoresist is exposed with the pattern corresponding to the distribution of absorbers. With the PMMA double layer, where the bottom resist has a higher sensitivity during exposure, a so-called undercut is created. Following resist development, the chromium metal layer is deposited on the substrate and the photoresist. Using a highly directional method (for instance ebeam physical vapor deposition) prevents the coverage on the resist sidewalls. Together with the undercut, this facilitates a dedicated lift-off step, where the photoresist and the metal on top of it is removed in a solvent. Having finished the metal absorber layer, the next step is to fabricate the dielectric nanocylinders.

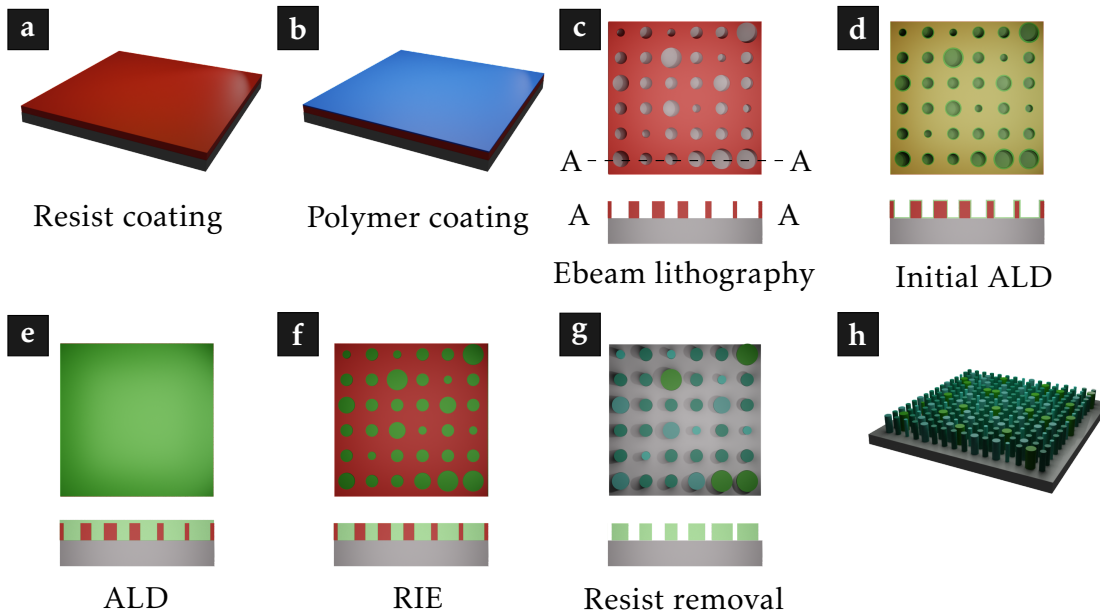


Figure C.3: Schematic of TiO_2 metasurface fabrication. Adapted from [316].

a – b Spincoating ebeam resist and a conducting polymer (*EsSpacer*[®]).

c Ebeam lithography, using a positive resist (ZEP 520A, shown in red). The volume of the nanocylinders is removed in the development step.

d – e Atomic layer deposition (ALD) of TiO_2 (green). The layer is overgrown until a flat surface is obtained.

f Reactive-ion etching (RIE) of the TiO_2 down to the photoresist layer.

g – h A removal of the ebeam resist results in the desired metasurface.

C.2 Fabrication of the dielectric nanocylinder array

The task at hand is to fabricate the dielectric nanocylinders with a challenging height-to-width ratio > 10 . Early publications relied on RIE of the TiO_2 layer [301], but suffer from slanted sidewalls and considerable sidewall roughness which limit the diffraction efficiency. Considerable improvement is achieved following the fabrication procedure outlined in [316]. Here, the basic idea is to use atomic layer deposition (ALD) on top of the structured ebeam resist. ALD is a conformal deposition technique which allows high height-to-width ratios and an exact control over the layer thickness, and a uniform film featuring a reduced defect density and surface roughness with respect to alternative deposition techniques [316, 401].

Figure C.3 illustrates the individual fabrication steps. The lithographic patterning of the positive photoresist creates the cylindrical volumes that are subsequently filled up by ALD. One important parameter is the temperature during the ALD process, which has to be below the glass transition temperature of the photoresist to prevent shape modifications. As depicted in Fig. C.3e, the TiO_2 is grown beyond the height of the photoresist to obtain a void-free volume. Subsequently, the overgrown layer is etched away using RIE, and the resist is removed in a solvent.

In this process, the resist thickness defines the final height of the nanocylinders. The absorber patch underneath the nanocylinder, as depicted in Fig. 7.7b, might induce small variations in the height of the nanocylinders, which can be fully taken into account in the simulations.

Acknowledgments

Inspiring three years of research have finally reached an end, and I'd like to say 'thank you' to everyone who contributed with support, help, comments, advice, ideas, and encouraging words. The plethora of projects within my doctoral thesis led to the unique opportunity to meet, collaborate with, and learn from inspiring people along the way.

First and foremost, I would like to thank my doctorate supervisor, Professor Carsten Rockstuhl, for offering such an exciting project, for all the stimulating discussions and the wonderful collaboration within a myriad of projects and topics. Carsten always gave me the opportunity to realize my own concepts and ideas, and had the patience to guide me through every topic.

Second, I sincerely thank Professor Martin Wegener for being the second referee of this doctoral thesis.

I acknowledge the European Union for the funding in the early-stage researcher project *NOLOSS*, part of the research & innovation Marie Skłodowska-Curie Actions. In my personal opinion, the objective of the marvelous opportunity I was offered here is described best by the objective of the project, "to prepare and train young researchers for the challenges of modern optics technology" [402].

My sincerest thanks to Toralf Scharf for initiating the *NOLOSS* project and all the work related to it. The project lives from all the meetings, discussing a variety of topics with many different project partners. Furthermore, thank you, Toralf, for being an excellent landlord over one and a half years in Neuchâtel, leading to fruitful discussions in the hallway or at dinner not always concerning only administrative issues.

Special thanks to Reinhard Völkel and Wilfried Noell at SUSS MicroOptics (SMO). As my industrial partner in this project, I spend half my PhD time in Switzerland with SMO. I am grateful to you for all the great ideas we were able to work on, and the productive atmosphere. I learned numerous things in the area of optical simulation, fabrication, and metrology. Thank you for your support!

NOLOSS is a team project, with 15 early-stage researchers, four universities, and nine industrial beneficiaries. Thank you all for the great time we shared at project meetings and conferences!

In addition, I would like to thank:

- The Institute of Nanotechnology, where I was employed most of my PhD time, and the Institute of Theoretical Solid State Physics, where I worked for the final four months.
- Raoul Kirner for our cooperation and his help at SMO over all the years. Without your support, progress would have been incredibly slow, and I really enjoyed working together. Thanks for your work on the prototype mask aligner setup.
- Jeremy Beguelin for all the help regarding metrology and many hours cycling the Jura mountains.
- Stefan Nanz for the fruitful hours preparing for the PhD examination.
- Silvia Diewald for her invaluable support and help, operating the e-beam lithography with great care and precision, and discussing the fabrication procedures and results.

- Martin Eisner for his support and for sharing a ride to Germany.
- Radius N.S. Suryadharma for the excellent food he cooks and his hospitality, especially in MBA weeks.
- Julian Münzberg, a master student I had the pleasure to supervise, for his great work on single-photon detectors in 2D photonic crystals.
- Yannick Augenstein, a master student at the time, and Babak Vosoughi Lahijani for their work and the collaboration on the inverse design of Bloch surface waves.
- The colleagues at *Toptica Photonics*, especially Matthias Scholz, Dmitrijs Opvarevs, and Patrick Leisching, for provision of the 193 nm laser source and useful insights in fruitful discussions.
- Wolfram Pernice and Simone Ferrari at the University of Münster, for the ongoing cooperation on cavity-integrated single-photon detectors.
- Myun-Sik Kim for the great work he performed on the topic of Bloch surface waves.
- Cedric Droguet for his help concerning the prototype mask aligner.
- Chen Yan and Jérôme Borboën for many helpful ideas and discussions.
- Nico Gruhler for his help on nanofabrication.
- All colleagues all over Europe, cooperating on countless topics, for their dedication and great results.
- Raoul, Chang, Aso, Marvin, and Carsten for proofreading the thesis and your valuable feedback which ended up significantly improving the thesis.
- My office colleagues at KIT and SMO for many interesting discussions and the productive environment.
- All group members at KIT for having a great time with stimulating discussions, in lunch breaks, at table tennis, playing lasertag, having dinner, and various other activities after work.
- The secretaries of TFP and INT for help with administrative issues, especially sending samples all over Europe.
- The SMO soccer team for many close matches near the lake.
- All colleagues at SMO for a great and productive time in Switzerland.
- The Karlsruhe School of Optics and Photonics (KSOP) for the financial support and a myriad of insightful workshops, and the team of the KSOP for all the help. Special thanks to Guillaume Gomard, my KSOP mentor, for inspiring discussions and helpful comments.
- All friends and fellow students in Karlsruhe, Münster, Neuchâtel, Dublin, Erlangen, and Lauchheim for many joyful hours during all those years.
- My parents and my brother for their help, support, feedback, and motivation I am happy to receive.
- Veronika for your love and words of encouragement, also in difficult times, and all the joyful and memorable moments we have shared together.

Thank you all!

Curriculum Vitae

Andreas Vetter

Löhestraße 63
91054 Erlangen
+49 176 47391579
andreas.m.vetter@gmail.com



Personal Data

Name Vetter
Prenome Andreas
Date of Birth 9th of August, 1989
Place of Birth Ellwangen/Germany
Citizenship German

Education

- August 2016 – **PhD student**, *SUSS Microoptics and Karlsruhe Institute of Technology (KIT)*, EU project
- November 2019 *NOLOSS*, nolossproject.eu, graduated *summa cum laude* (with distinction)
- August 2016 – February 2017 and September 2017 – August 2018: *SUSS Microoptics*
February 2017 – August 2017 and September 2018 – November 2019: *KIT*
- January 2017 – **MBA Fundamentals Program**, *HECTOR School of Engineering & Management*, Final
September 2018 Grade: 1.3 (First-Class Honours)
- November 2013 – **Master of Physics**, *Karlsruhe Institute of Technology*, Departement of Physics, Final
May 2016 Grade: 1.0 (First-Class Honours)
 - Focus of study: Photonics and Nanotechnology.
 - Master thesis: *Superconducting nanowire single-photon detectors implemented using perfect absorber concepts*, Professor Carsten Rockstuhl and Professor Wolfram Pernice, Karlsruhe Institute of Technology (KIT) and University of Münster.
- August 2014 – **Exchange program**, *Trinity College Dublin/Ireland*
- December 2014 ◦ Research project on the influence of electric charging on nanoparticle growth by pulsed laser deposition.
◦ Modules on bio-physics and nanophotonics.
- October 2010 – **Bachelor of Physics**, *Karlsruhe Institute of Technology*, Departement of Physics, Final
November 2013 Grade: 1.2 (First-Class Honours)
- September 2000 – **Abitur**, *General qualification for university entrance*, *Kopernikus Gymnasium Wasseralfingen*,
June 2009 Final Grade: 1.0 (First-Class Honours)

Teaching

- October 2018 – **Tutor of two seminars**, *Experimental Physics A*, Prof. Schimmel, Departement of Physics
- February 2019 Karlsruhe Institute of Technology
- April 2017 – **Tutor**, *Theoretical Quantum Mechanics I*, Prof. Schmalian, Departement of Physics
- July 2017 Karlsruhe Institute of Technology

Practical Experiences

- April 2015 – **Tutor**, *physics lab for beginners of the Departement of Physics*, experiments in the field of vacuum engineering, Karlsruhe Institute of Technology
- March 2016
- October 2012 – **Tutor**, *physics lab for beginners of the Departement of Physics*, various experiments in the field of optics and electronics, Karlsruhe Institute of Technology
- July 2014
- October 2013 – **Scientific assistant**, *Nanostructure Service Laboratory*, Center for Functional Nanostructures (CFN), Karlsruhe Institute of Technology
- March 2014
 - Optical and ebeam lithography in clean room environment.
 - Preparation of samples for scanning tunneling microscopy.
- April 2010 – **Industrial internship**, *LOBO® electronic GmbH, Aalen*
- August 2010
 - Manufacturing and service of laser show equipment.
 - Responsible for several projects comprising applications of modern multimedia and show design
- July 2009 – **Community service**, *Welfare Center St. Elisabeth/Lauchheim*
- March 2010

